

COPERNICUS SPACE COMPONENT SENTINEL OPTICAL IMAGING
MISSION PERFORMANCE CLUSTER SERVICE

Data Quality Report

Sentinel-3 OLCI

August 2023

OPT-MPC

Copernicus Sentinel



Optical Mission Performance Cluster

Ref.: OMPC.ACR.DQR.03.08-2023

Issue: 1.0

Date: 11/09/2023

Contract: 4000136252/21/I-BG

Customer: ESA	Document Ref.: OMPC.ACR.DQR.03.08-2023
Contract No.: 4000136252/21/I-BG	Date: 11/09/2023
	Issue: 1.0

Project:	COPERNICUS SPACE COMPONENT SENTINEL OPTICAL IMAGING MISSION PERFORMANCE CLUSTER SERVICE		
Title:	Data Quality Report - OLCI		
Author(s):	OLCI ESL team		
Approved by:	L. Bourg, OPT-MPC OLCI ESL Coordinator S. Clerc, OPT-MPC Optical ESL Coordinator	Authorized by	C. Hénocq, OPT-MPC S3 Technical Manager
Distribution:	ESA, EUMETSAT, published in Sentinel Online		
Accepted by ESA	S. Dransfeld, ESA TO		
Filename	OMPC.ACR.DQR.03.08-2023 - i1r0 - OLCI DQR August 2023.docx		

Disclaimer

The views expressed herein can in no way be taken to reflect the official opinion of the European Space Agency or the European Union.



Table of content

TABLE OF CONTENT	IV
LIST OF FIGURES	VI
LIST OF TABLES	XIII
1 PROCESSING BASELINE VERSION.....	1
1.1 Sentinel3-A	1
1.2 Sentinel3-B	1
2 INSTRUMENT MONITORING	2
2.1 CCD temperatures	2
2.1.1 OLCI-A	2
2.1.2 OLCI-B	4
2.2 Radiometric Calibration.....	5
2.2.1 Dark Offsets [OLCI-L1B-CV-230].....	8
2.2.3 Instrument response and degradation modelling [OLCI-L1B-CV-250]	18
2.2.4 Ageing of nominal diffuser [OLCI-L1B-CV-240].....	36
2.2.5 Updating of calibration ADF [OLCI-L1B-CV-260].....	36
2.3 Spectral Calibration [OLCI-L1B-CV-400]	36
2.3.1 OLCI-A.....	36
2.3.2 OLCI-B	40
2.4 Signal to Noise assessment [OLCI-L1B-CV-620].....	45
2.4.1 SNR from Radiometric calibration data	45
2.5 Geometric Calibration/Validation.....	51
2.5.1 OLCI-A.....	51
2.5.2 OLCI-B	54
3 OLCI LEVEL 1 PRODUCT VALIDATION	58
3.1 [OLCI-L1B-CV-300], [OLCI-L1B-CV-310] – Radiometric Validation	58
3.1.1 S3ETRAC Service	58
3.1.2 Radiometric validation with DIMITRI.....	60
3.1.3 Radiometric validation with OSCAR	65
3.1.4 OSCAR Glitter results	68
3.1.5 Radiometric validation with Moon observations: LIME results	69
4 LEVEL 2 LAND PRODUCTS VALIDATION.....	70
4.1 [OLCI-L2LRF-CV-300].....	70
4.1.1 Routine extractions.....	70
4.1.2 Comparisons with MERIS MGVI and MTCI climatology.....	80
4.1.3 Comparisons with GBOV (Ground-Based Observations for Validation) data v3	80
4.1.4 OLCI-A.....	81
4.1.5 OLCI-B	89



4.1.6	TAYLOR DIAGRAM RESULTS	95
4.1.7	Sentinel-3A and 3B biophysical variables inter-annual variability results	96
4.2	[OLCI-L2LRF-CV-410 & OLCI-L2LRF-CV-420] – Cloud Masking & Surface Classification for Land Products.....	98
4.2.1	Sky Camera based validation – prototype results July 2023	99
5	VALIDATION OF INTEGRATED WATER VAPOUR OVER LAND & WATER	107
6	LEVEL 2 SYN PRODUCTS VALIDATION	110
6.1	SYN L2 SDR products	110
6.2	SY_2_VGP, SY_2_VG1 and SY_2_V10 products	110
6.3	SYN L2 AOD NTC products	114
7	EVENTS	116
8	APPENDIX A	117

List of Figures

Figure 1: long term monitoring of OLCI-A CCD temperatures using minimum value (top), time averaged values (middle), and maximum value (bottom) provided in the annotations of the Radiometric Calibration Level 1 products, for the shutter frames, all radiometric calibrations so far except the first one (absolute orbit 183) for which the instrument was not yet thermally stable. ----- 2

Figure 2: Same as Figure 1 for diffuser frames.----- 3

Figure 3: long term monitoring of OLCI-B CCD temperatures using minimum value (top), time averaged values (middle), and maximum value (bottom) provided in the annotations of the Radiometric Calibration Level 1 products, for the Shutter frames, all radiometric calibrations so far except the first one (absolute orbit 167) for which the instrument was not yet thermally stable. ----- 4

Figure 4: same as Figure 3 for diffuser frames.----- 5

Figure 5: Sun azimuth angles during acquired OLCI-A Radiometric Calibrations (diffuser frame) on top of nominal yearly cycle (black curve). Diffuser 1 with diamonds, diffuser 2 with crosses. Different colours correspond to different years of acquisition (see the legend inside the figure).----- 6

Figure 6: same as Figure 5 for OLCI-B.----- 6

Figure 7: OLCI-A Sun geometry during radiometric Calibrations on top of characterization ones (diffuser frame)----- 7

Figure 8: same as Figure 7 for OLCI-B----- 7

Figure 9: Dark Offset table for band Oa06 with (red) and without (black) HEP filtering (Radiometric Calibration of 22 July 2017). The strong HEP event near pixel 400 has been detected and removed by the HEP filtering.----- 8

Figure 10: OLCI-A Dark Offset for band Oa1 (top) and Oa21 (bottom), all radiometric calibrations so far except the first one (orbit 183) for which the instrument was not thermally stable yet.----- 9

Figure 11: map of OLCI-A periodic noise for the 5 cameras, for band Oa21. X-axis is detector number (East part, from 540 to 740, where the periodic noise occurs), Y-axis is the orbit number. Y-axis range is focused on the most recent 5000 orbits. The counts have been corrected from the West detectors mean value (not affected by periodic noise) in order to remove mean level gaps and consequently to have a better visualisation of the long term evolution of the periodic noise structure. At the beginning of the mission the periodic noise for band Oa21 had strong amplitude in camera 2, 3 and 5 compared to camera 1 and 4. However PN evolved through the mission and these discrepancies between cameras have been reduced. At the time of this Cyclic Report Camera 2 still shows a slightly higher PN than other cameras. ----- 10

Figure 12: same as Figure 11 for smear band.----- 11

Figure 13: OLCI-A Dark Current for band Oa1 (top) and Oa21 (bottom), all radiometric calibrations so far except the first one (orbit 183) for which the instrument was not thermally stable yet.----- 12

Figure 14: left column: ACT mean on 400 first detectors of OLCI-A Dark Current coefficients for spectral band Oa01 (top) and Oa21 (bottom). Right column: same as left column but for Standard deviation instead of mean. We see an increase of the DC level as a function of time especially for band Oa21.----- 12

Figure 15: OLCI-A Dark current increase rates with time (in counts per year) vs. band (left) and vs. band width (right)----- 13

Figure 16: OLCI-B Dark Offset for band Oa1 (top) and Oa21 (bottom), all radiometric calibrations so far except the first one (orbit 167) for which the instrument was not thermally stable yet.----- 14

Figure 17: OLCI-B map of periodic noise for the 5 cameras, for band Oa21. X-axis is detector number (East part, from 540 to 740, where the periodic noise occurs), Y-axis is the orbit number. The counts have been corrected from the West detectors mean value (not affected by periodic noise) in order to remove mean level gaps and consequently to have a better visualization of the long term evolution of the periodic noise structure. ----- 15

Figure 18: same as Figure 17 for smear band. ----- 15

Figure 19: OLCI-B Dark Current for band Oa1 (top) and Oa21 (bottom), all radiometric calibrations so far except the first one (orbit 167) for which the instrument was not thermally stable yet. ----- 16

Figure 20: left column: ACT mean on 400 first detectors of OLCI-B Dark Current coefficients for spectral band Oa01 (top) and Oa21 (bottom). Right column: same as left column but for Standard deviation instead of mean. We see an increase of the DC level as a function of time especially for band Oa21. ----- 17

Figure 21: OLCI-B Dark Current increase rates with time (in counts per year) vs. band (left) and vs. band width (right)----- 17

Figure 22: OLCI-A Gain Coefficients for band Oa1 (top) and Oa21 (bottom), derived using the in-flight BRDF model. The dataset is made of all diffuser 1 radiometric calibrations since orbit 979. ----- 18

Figure 23: camera averaged gain relative evolution with respect to calibration of 25/04/2016 (change of OLCI channel settings), as a function of elapsed time since the beginning of the mission; one curve for each band (see colour code on plots), one plot for each module. The diffuser ageing is taken into account.-- 19

Figure 24: OLCI-B Gain Coefficients for band Oa1 (top) and Oa21 (bottom), derived using the in-flight BRDF model. The dataset is made of all diffuser 1 radiometric calibrations since orbit 758. ----- 20

Figure 25: OLCI-B camera averaged gain relative evolution with respect to first calibration after channel programming change (18/06/2018), as a function of elapsed time since the beginning of the mission; one curve for each band (see colour code on plots), one plot for each module. The diffuser ageing is taken into account. ----- 21

Figure 26: RMS performance of the OLCI-A Gain Model of the current processing baseline as a function of orbit. ----- 23

Figure 27: RMS performance of the OLCI-A Gain Model of the previous Processing Baseline as a function of orbit.----- 23

Figure 28: OLCI-A Camera-averaged instrument evolution since channel programming change (25/04/2016) and up to the most recent calibration (28/08/2023) versus wavelength. ----- 24

Figure 29: For the 5 cameras: OLCI-A Evolution model performance, as camera-average and standard deviation of ratio of Model over Data vs. wavelength, for each orbit of the test dataset, including 5 calibrations in extrapolation, with a colour code for each calibration from blue (oldest) to red (most recent).----- 25

Figure 30: OLCI-A evolution model performance, as ratio of Model over Data vs. pixels, all cameras side by side, over the whole current calibration dataset (since instrument programming update), including 5 calibrations in extrapolation, channels Oa1 to Oa6. ----- 26

Figure 31: same as Figure 30 for channels Oa7 to Oa14. ----- 27

Figure 32: same as Figure 30 for channels Oa15 to Oa21.----- 28

Figure 33: RMS performance of the OLCI-B Gain Model of the current processing baseline as a function of orbit. ----- 29


	Optical MPC Data Quality Report –Sentinel-3 OLCI August 2023	Ref.: OMPC.ACR.DQR.03.08-2023 Issue: 1.0 Date: 11/09/2023 Page: viii
---	---	---

Figure 34: RMS performance of the OLCI-B Gain Model of the previous processing baseline as a function of orbit (please note the different vertical scale with respect to Figure 33).----- 30

Figure 35: OLCI-B Camera-averaged instrument evolution since channel programming change (18/06/2018) and up to most recent calibration (11/08/2023) versus wavelength. ----- 31

Figure 36: For the 5 cameras: OLCI-B Evolution model performance, as camera-average and standard deviation of ratio of Model over Data vs. wavelength, for each orbit of the test dataset, including 4 calibrations in extrapolation, with a colour code for each calibration from blue (oldest) to red (most recent). ----- 32

Figure 37: OLCI-B evolution model performance, as ratio of Model over Data vs. pixels, all cameras side by side, over the whole current calibration dataset (since instrument programming update), including 4 calibrations in extrapolation, channels Oa1 to Oa6. ----- 33

Figure 38: same as Figure 37 for channels Oa7 to Oa14. ----- 34

Figure 39: same as for channels Oa15 to Oa21. ----- 35

Figure 40: OLCI-A across track spectral calibration from all S02/S03 sequences since the beginning of the mission. Top plot is spectral line 1, middle plot is spectral line 2 and bottom plot spectral line 3. The nominal spectral calibration is plotted as a red horizontal dotted line and the on-ground spectral calibration as a red thick line. ----- 37

Figure 41: OLCI-A camera averaged spectral calibration evolution as a function of time since launch (all spectral S02/S03 calibrations since the beginning of the mission are included). The data are normalized with the first Spectral Calibration of the plot. ----- 38

Figure 42: OLCI-A across track spectral calibration from all S09 sequences since the beginning of the mission. The used features are the atmospheric oxygen at 759nm and the Fraunhofer lines at 485nm, 656nm and 854nm. The nominal spectral calibration is plotted as a red dotted line. ----- 39

Figure 43: OLCI-A camera averaged spectral calibration evolution as a function of orbit number from S09 calibrations since the 4th of May 2016. The last calibration for S09 is from 11 August 2023. For each camera, the spectral evolution corresponding derived from spectral lines at 485 nm, 656 nm, 770 nm and 854 nm have been averaged. The data are normalized with the first Spectral Calibration of the plot. ----- 40

Figure 44: OLCI-B across track spectral calibration from all S02/S03 sequences since the beginning of the mission. Top plot is spectral line 1, middle plot is spectral line 2 and bottom plot spectral line 3. The nominal spectral calibration is plotted as a red dotted line and the on-ground spectral calibration as a red thick line.----- 41

Figure 45: OLCI-B camera averaged spectral calibration evolution as a function of time since launch (all spectral S02/S03 calibrations since the beginning of the mission are included). The data are normalized with the first Spectral Calibration. ----- 42

Figure 46: OLCI-B across track spectral calibration from all (few during commissioning have been left out for the sake of clearness) S09 sequences since the beginning of the mission. The used features are the atmospheric oxygen at 759nm and the Fraunhofer lines at 485nm, 656nm and 854nm. The nominal spectral calibration is plotted as a red dotted line. ----- 43

Figure 47: OLCI-B camera averaged spectral calibration evolution as a function of orbit number since launch from S09 calibrations since the beginning of the mission. The last calibration for S09 is from 21 August 2023. For each camera, the spectral evolution corresponding derived from spectral lines at 485 nm, 656 nm, 770 nm and 854 nm have been averaged. The data are normalized with the first Spectral Calibration. ----- 44

Figure 48: OLCI-A Signal to Noise ratio as a function of the spectral band for the 5 cameras. These results have been computed from radiometric calibration data. All calibrations except first one (orbit 183) are presents with the colours corresponding to the orbit number (see legend). The SNR is very stable with time: the curves for all orbits are almost superimposed. The dashed curve is the ESA requirement.----- 45

Figure 49: long-term stability of the SNR estimates from Calibration data, example of channel Oa1. ---- 46

Figure 50: OLCI-B Signal to Noise ratio as a function of the spectral band for the 5 cameras. These results have been computed from radiometric calibration data. All calibrations except first one (orbit 167) are presents with the colours corresponding to the orbit number (see legend). The SNR is very stable with time: the curves for all orbits are almost superimposed. The dashed curve is the ESA requirement.----- 48

Figure 51: long-term stability of the OLCI-B SNR estimates from Calibration data, example of channel Oa1. ----- 49

Figure 52: overall OLCI-A georeferencing RMS performance time series (left) and number of validated control points corresponding to the performance time series (right) over the whole monitoring period 51

Figure 53: across-track (left) and along-track (right) OLCI-A georeferencing biases time series for Camera 1. Blue line is the average, black lines are average plus and minus 1 sigma.----- 52

Figure 54: same as Figure 53 for Camera 2. ----- 52

Figure 55: same as Figure 53 for Camera 3. ----- 52

Figure 56: same as Figure 53 for Camera 4. ----- 53

Figure 57: same as Figure 53 for Camera 5. ----- 53

Figure 58: OLCI-A spatial across-track misregistration at each camera transition (left) and maximum amplitude of the across-track error within each camera (left). ----- 53

Figure 59: OLCI-A spatial along-track misregistration at each camera transition (left) and maximum amplitude of the along-track error within each camera (left). ----- 54

Figure 60: overall OLCI-B georeferencing RMS performance time series over the whole monitoring period (left) and corresponding number of validated control points (right)----- 54

Figure 61: across-track (left) and along-track (right) OLCI-B georeferencing biases time series for Camera 1. ----- 55

Figure 62: same as Figure 61 for Camera 2. ----- 55

Figure 63: same as Figure 61 for Camera 3. ----- 55

Figure 64: same as Figure 61 for Camera 4. ----- 56

Figure 65: same as Figure 61 for Camera 5. ----- 56

Figure 66: OLCI-B spatial across-track misregistration at each camera transition (left) and maximum amplitude of the across-track error within each camera (left). ----- 56

Figure 67: OLCI-B spatial along-track misregistration at each camera transition (left) and maximum amplitude of the along-track error within each camera (left). ----- 57

Figure 68: summary of S3ETRAC products generation for OLCI-A (number of OLCI-A L1 products Ingested, blue – number of S3ETRAC extracted products generated, green – number of S3ETRAC runs without generation of output product (data not meeting selection requirements), yellow – number of runs ending in error, red, one plot per site type).----- 59

Figure 69: summary of S3ETRAC products generation for OLCI-B (number of OLCI-B L1 products Ingested, yellow – number of S3ETRAC extracted products generated, blue – number of S3ETRAC runs without

generation of output product (data not meeting selection requirements), green – number of runs ending in error, red, one plot per site type).----- 60

Figure 70: Time-series of the elementary ratios (observed/simulated) signal from OLCI-A for (top to bottom) bands Oa03 and Oa17 respectively over January – August 2023 from the six PICS Cal/Val sites. Dashed-green and orange lines indicate the 2% and 5% respectively. Error bars indicate the desert methodology uncertainty.----- 61

Figure 71: Time-series of the elementary ratios (observed/simulated) signal from OLCI-B for (top to bottom) bands Oa08 and Oa17 respectively over – August 2023 from the six PICS Cal/Val sites. Dashed-green and orange lines indicate the 2% and 5% respectively. Error bars indicate the desert methodology uncertainty.----- 62

Figure 72: The estimated gain values for OLCI-A and OLCI-B over the 6 PICS sites identified by CEOS over the period January 2023- August 2023 as a function of wavelength. Dashed-green and orange lines indicate the 2% and 5% respectively. Error bars indicate the desert methodology uncertainty.----- 63

Figure 73: The estimated gain values for OLCI-A and OLCI-B from Glint, Rayleigh and PICS methods over the period January 2022- End August 2023 as a function of wavelength. We use the gain value of Oa8 from PICS-Desert method as reference gain for Glint method. Dashed-green and orange lines indicate the 2% and 5% respectively. Error bars indicate the method uncertainties.----- 64

Figure 74: Ratio of observed TOA reflectance to simulated one for (black) MERIS, (pale-green) S2A/MSI, (white) S2B/MSI, (blue) S3A/OLCI, (green) S3B/OLCI, (red) S3A/SLSTR-NADIR, and (cyan) S3B/SLSTR-NADIR averaged over the six PICS test sites over different periods as a function of wavelength.----- 65

Figure 75: OSCAR Rayleigh S3A and S3B Calibration results as a function of wavelength for June 2023. The results are obtained with a new climatology derived from CMEMS OLCI monthly CHL products. ----- 66

Figure 76: OSCAR Rayleigh OLCI-A and OLCI-B Calibration results as a function of wavelength for all acquisitions of 2023. The results are obtained with a new climatology derived from CMEMS OLCI monthly CHL products.----- 67

Figure 77: OSCAR Glitter OLCI-A & OLCI-B Calibration results as a function of wavelength for August 2023. The results are obtained with a new climatology derived from CMEMS OLCI monthly CHL products.---- 68

Figure 78: OSCAR Glitter OLCI-A & OLCI-B Calibration results as a function of wavelength for all acquisitions of 2023. The results are obtained with a new climatology derived from CMEMS OLCI monthly CHL products.----- 69

Figure 79: DeGeb time series over current report period ----- 70

Figure 80: ITCat time series over current report period----- 71

Figure 81: ITlsp time series over current report period ----- 71

Figure 82: ITSro time series over current report period----- 72

Figure 83: ITTra time series over current report period ----- 72

Figure 84: SPAlI time series over current report period ----- 73

Figure 85: UKNFo time series over current report period ----- 73

Figure 86: USNe1 time series over current report period ----- 74

Figure 87: USNe2 time series over current report period ----- 74

Figure 88: USNe3 time series over current report period ----- 75

Figure 89: DeGeb time series over current report period ----- 75

Figure 90: ITCat time series over current report period----- 76

Figure 91: ITIsp time series over current report period ----- 76

Figure 92: ITSro time series over current report period----- 77

Figure 93: ITTra time series over current report period----- 77

Figure 94: SPAlI time series over current report period ----- 78

Figure 95: UKNFo time series over current report period ----- 78

Figure 96: USNe1 time series over current report period ----- 79

Figure 97: USNe2 time series over current report period ----- 79

Figure 98: USNe3 time series over current report period ----- 80

Figure 99: Time series of OLCI-A GIFAPAR (blue-sky) and four methods for the Bartlett site. ----- 82

Figure 100: Time series of OLCI-A GIFAPAR (blue-sky) and four methods for the CPER site. ----- 83

Figure 101: Time series of OLCI-A GIFAPAR (blue-sky) and four methods for the Guanica site. ----- 83

Figure 102: Time series of OLCI-A GIFAPAR (blue-sky) and four methods for the Hainich site.----- 84

Figure 103: Time series of OLCI-A GIFAPAR (blue-sky) and four methods for the Harvard site. ----- 84

Figure 104: Time series of OLCI-A GIFAPAR (blue-sky) and four methods for the Jornada site. ----- 85

Figure 105: Time series of OLCI-A GIFAPAR (blue-sky) and four methods for the Moab site. ----- 85

Figure 106: Time series of OLCI-A GIFAPAR (blue-sky) and four methods for the Oak site. ----- 86

Figure 107: Time series of OLCI-A GIFAPAR (blue-sky) and four methods for the Ordway site. ----- 86

Figure 108: Time series of OLCI-A GIFAPAR (blue-sky) and four methods for the Smithsonian site. ----- 87

Figure 109: Time series of OLCI-A GIFAPAR (blue-sky) and four methods for the Steigerwaldt site. ----- 87

Figure 110: Time series of OLCI-A GIFAPAR (blue-sky) and four methods for the Talladega site. ----- 88

Figure 111: Time series of OLCI-A GIFAPAR (blue-sky) and four methods for the Tumbarumba site. ----- 88

Figure 112: Time series of OLCI-B GIFAPAR (blue-sky) and four methods for the Bartlett site.----- 89

Figure 113: Time series of OLCI-B GIFAPAR (blue-sky) and four methods for the CPER site. ----- 89

Figure 114: Time series of OLCI-B GIFAPAR (blue-sky) and four methods for the Guanica site. ----- 90

Figure 115: Time series of OLCI-B GIFAPAR (blue-sky) and four methods for the Hainich site.----- 90

Figure 116: Time series of OLCI-B GIFAPAR (blue-sky) and four methods for the Harvard site. ----- 91

Figure 117: Time series of OLCI-B GIFAPAR (blue-sky) and four methods for the Jornada site. ----- 91

Figure 118: Time series of OLCI-B GIFAPAR (blue-sky) and four methods for the Moab site. ----- 92

Figure 119: Time series of OLCI-B GIFAPAR (blue-sky) and four methods for the Oak site. ----- 92

Figure 120: Time series of OLCI-B GIFAPAR (blue-sky) and four methods for the Ordway site. ----- 93

Figure 121: Time series of OLCI-B GIFAPAR (blue-sky) and four methods for the Smithsonian site. ----- 93

Figure 122: Time series of OLCI-B GIFAPAR (blue-sky) and four methods for the Steigerwaldt site. ----- 94

Figure 123: Time series of OLCI-B GIFAPAR (blue-sky) and four methods for the Talladega site. ----- 94

Figure 124: Time series of OLCI-B GIFAPAR (blue-sky) and four methods for the Tumbarumba site. ----- 95

Figure 125: Time series of monthly mean GIFAPAR (left) and OTCI (right) for S3A (top) and S3B (bottom) for Smithsonian SCBI. ----- 97


	Optical MPC Data Quality Report –Sentinel-3 OLCI August 2023	Ref.: OMPC.ACR.DQR.03.08-2023 Issue: 1.0 Date: 11/09/2023 Page: xii
---	---	--

Figure 126: Time series of monthly mean GIFAPAR (left) and OTCI (right) for S3A (top) and S3B (bottom) for Zigzag Creek.----- 98

Figure 127: Temperature and cloud cover Rome, August 2023 (source: <https://world-weather.info/forecast/italy/rome/August-2023/>)----- 99

Figure 128: Cloud observations and precipitation Rome, August 2023 (source: <https://weatherspark.com/h/m/71779/2023/6/Historical-Weather-in-August-2023-in-Rome-Italy>) ---- 100

Figure 129: Sky camera acquisitions over Rome during Sentinel-3 OLCI overpass ----- 101

Figure 130: Classified sky camera acquisitions over Rome during Sentinel-3 OLCI overpass ----- 101

Figure 131: Confusion matrix showing validation results for OLCI L2 cloud screening including margin against SC1 automated classification. ----- 102

Figure 132: Confusion matrix showing validation results for OLCI L2 cloud screening excluding margin against SC1 automated classification ----- 102

Figure 133: Temperature and cloud cover Valencia, August 2023 (source: <https://world-weather.info/forecast/spain/valencia/August-2023/>) ----- 103

Figure 134: Cloud observations and precipitation Valencia, August 2023 (source: <https://weatherspark.com/h/m/42614/2023/6/Historical-Weather-in-August-2023-in-Valencia-Spain#Figures-CloudCover>)----- 104

Figure 135: Sky camera acquisitions over Valencia during Sentinel-3 OLCI overpass ----- 105

Figure 136: Classified sky camera acquisitions over Valencia during Sentinel-3 OLCI overpass ----- 105

Figure 137: Confusion matrix showing validation results for OLCI L2 cloud screening including margin against SC1 automated classification ----- 106

Figure 138: Confusion matrix showing validation results for OLCI L2 cloud screening excluding margin against SC1 automated classification ----- 106

Figure 139: Upper: Scatter plot of the IWV products, derived from OLCI (A left, B right) above land and from SUOMI NET GNSS measurements. Middle: Histogram of the difference between OLCI (A: left, B: right) and GNSS (blue: original OLCI, orange: bias corrected OLCI). Lower: Positions of the GNSS (A: left, B: right). ----- 108

Figure 140: Temporal evolution of different quality measures for OLCI A (left) and OLCI B (right) with respect to SUOMI Net. From top to bottom: systematic deviation factor, bias, root mean squared difference (with and without bias correction), explained variance (number in boxes are the numbers of matchups) ----- 109

Figure 141: Scatter density plots between SY_V10 S3A (top) or S3B (bottom) and PROBA-V C2 S10-TOC for BLUE, RED, NIR and SWIR bands (left to right), August/2023 vs. August/2019----- 111

Figure 142: Temporal evolution of APU statistics between SY_2_V10 S3A (left) or S3B (right) and PROBA-V S10-TOC for BLUE, RED, NIR and SWIR bands (top to bottom), January/2021 - June/2023 (S3 SYN VGT) vs. January/2017 - August/2019 (PROBA-V)----- 112

Figure 143: Temporal evolution of APU statistics between S3A_SY_2_V10 and S3B_SY_2_V10 for BLUE, RED, NIR and SWIR bands (top to bottom), January/2021 - August/2023 ----- 113

Figure 144: For S3A, for the period May-June, for years 2020 to 2023 separately, scatter density plots for aAOD and syAOD and corresponding validation statistics. ----- 114

Figure 145: Globally, for S3A, scatter density plots for matchups between syAOD and aAOD for the period 2020.01-2023.04 (left) and 2020.01-2023.06 (right) for matchups with SZA>78. ----- 115

List of Tables

Table 1: OLCI-A SNR figures as derived from Radiometric Calibration data. Figures are given for each camera (time average and standard deviation), and for the whole instrument. The requirement and its reference radiance level are recalled (in $\text{mW}\cdot\text{sr}^{-1}\cdot\text{m}^{-2}\cdot\text{nm}^{-1}$). ----- 47

Table 2: OLCI-B SNR figures as derived from Radiometric Calibration data. Figures are given for each camera (time average and standard deviation), and for the whole instrument. The requirement and its reference radiance level are recalled (in $\text{mW}\cdot\text{sr}^{-1}\cdot\text{m}^{-2}\cdot\text{nm}^{-1}$). ----- 50

Table 3: S3ETRAC Rayleigh Calibration sites----- 66

Table 4. OSCAR Rayleigh calibration results for S3A and S3B (average and standard deviation over all 2023 acquisitions) over all scenes currently (re)processed with the new climatology and observed difference (in %) between OLCIA and OLCIB----- 67

Table 5: OSCAR Glitter calibration results for OLCI-A and OLCI-B (average and standard deviation over all acquisitions of 2023) currently processed with the new climatology and observed difference (in %) ---- 69

Table 6: GBOV validation sites analysed in monthly reports ----- 81

1 Processing Baseline Version

1.1 Sentinel3-A

IPF	IPF / Processing Baseline version	Date of deployment
OL1	06.17 / OL__L1_.003.03.00 (with uncertainties activated)	25/07/2023
OL2 LAND	06.18 / OL__L2L.002.11.02	25/07/2023
SY2	06.25 / SYN_L2_.002.18.01	25/07/2023
SY2_VGS	06.12 / SYN_L2V.002.09.01	25/07/2023
SY2_AOD	01.08 / AOD_NTC.002.08.01	25/07/2023

1.2 Sentinel3-B

IPF	IPF / Processing Baseline version	Date of deployment
OL1	06.17 / OL__L1_.003.03.00 (with uncertainties activated)	18/07/2023
OL2 Land	06.18 / OL__L2L.002.11.02	18/07/2023
SY2	06.25 / SYN_L2_.002.18.01	18/07/2023
SY2_VGS	06.12 / SYN_L2V.002.09.01	18/07/2023
SY2_AOD	01.08 / AOD_NTC.002.08.01	18/07/2023

2 Instrument monitoring

2.1 CCD temperatures

2.1.1 OLCI-A

The long-term monitoring of the CCD temperatures is based on Radiometric Calibration Annotations (see Figure 1). Variations are very small (0.09 C peak-to-peak) and no trend can be identified. Data from current reporting period (rightmost data points) do not show any specificity.

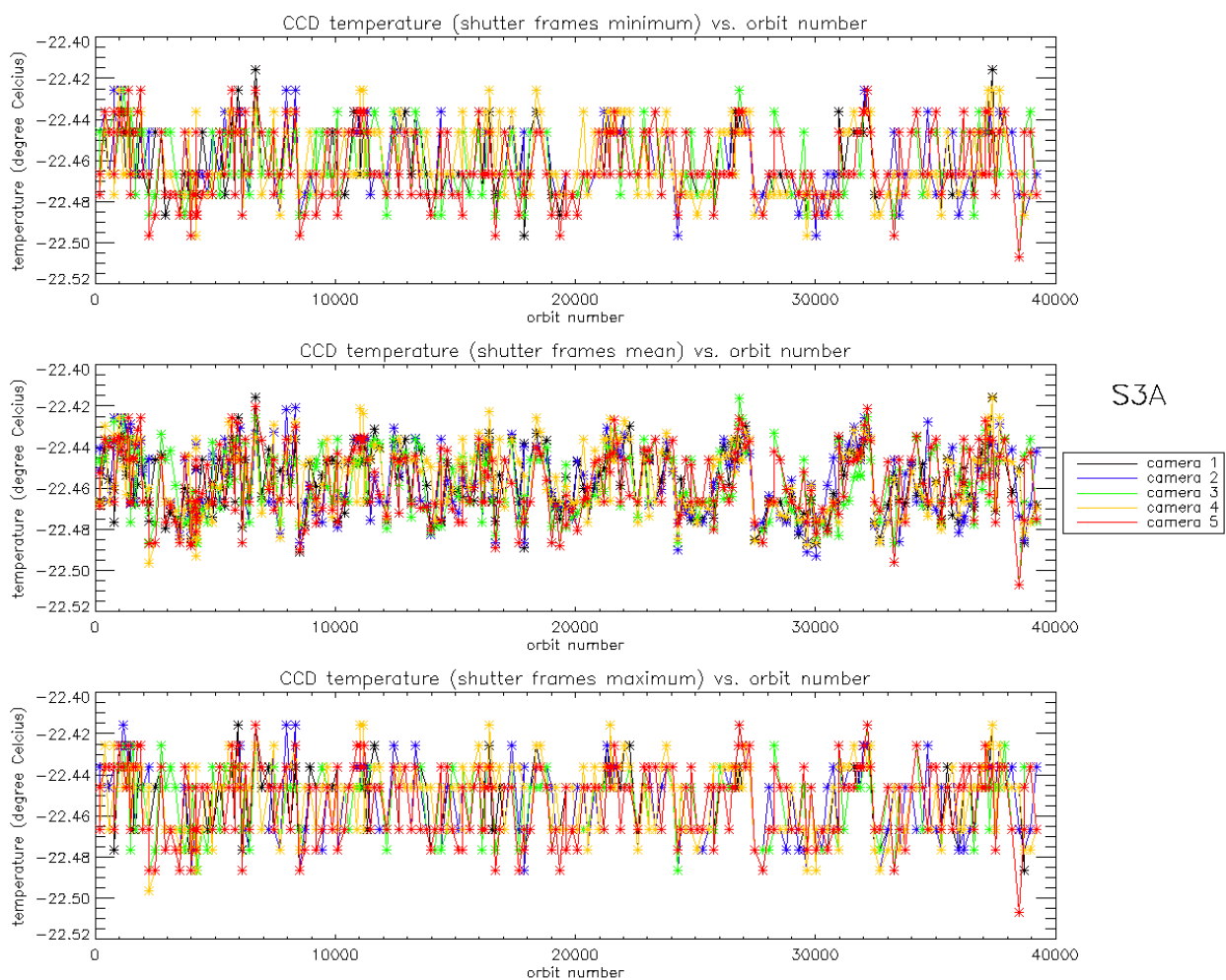


Figure 1: long term monitoring of OLCI-A CCD temperatures using minimum value (top), time averaged values (middle), and maximum value (bottom) provided in the annotations of the Radiometric Calibration Level 1 products, for the shutter frames, all radiometric calibrations so far except the first one (absolute orbit 183) for which the instrument was not yet thermally stable.

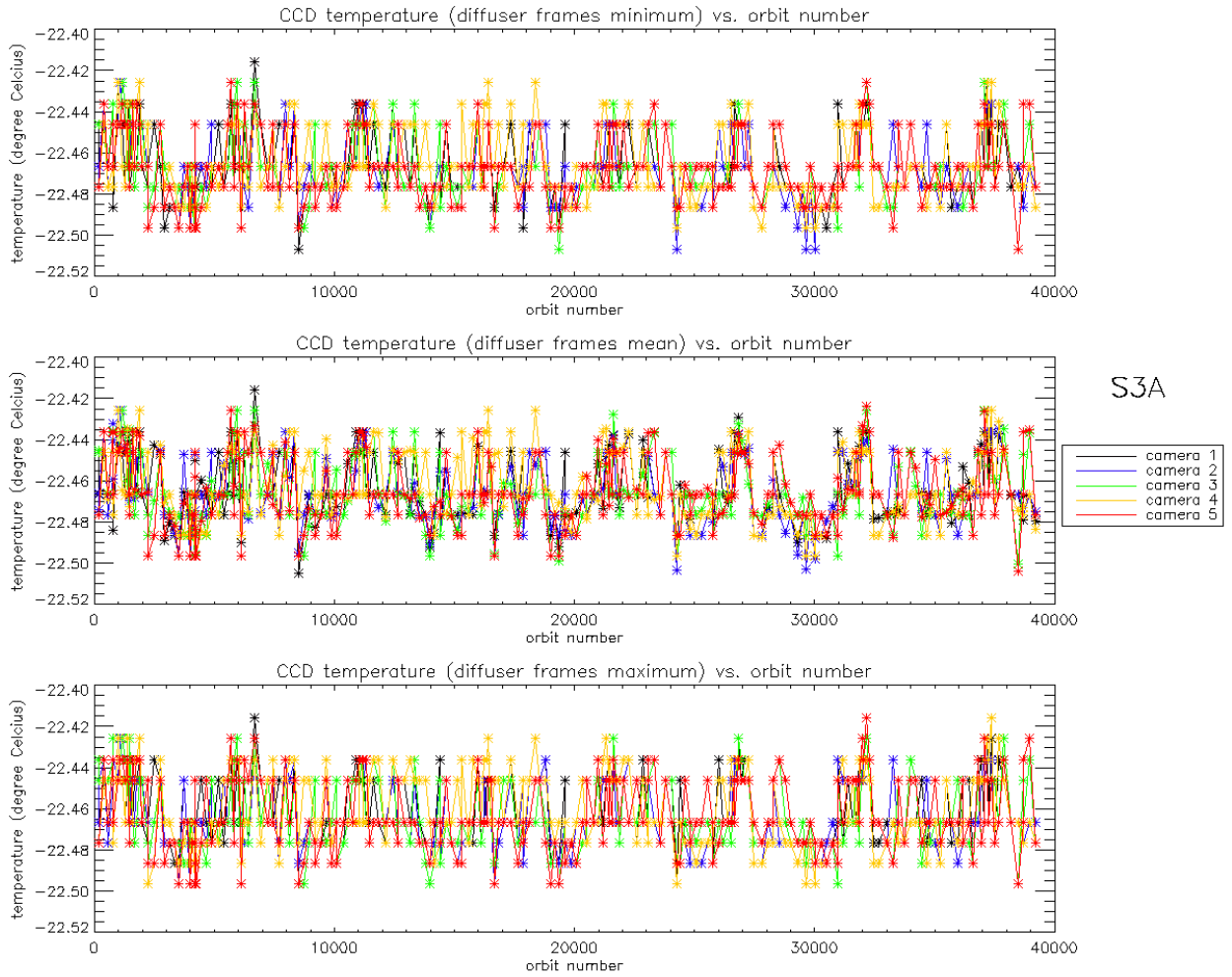


Figure 2: Same as Figure 1 for diffuser frames.

2.1.2 OLCI-B

As for OLCI-A, the variations of CCD temperature are very small (0.08 C peak-to-peak) and no trend can be identified. Data from current reporting period (rightmost data points) do not show any specificity.

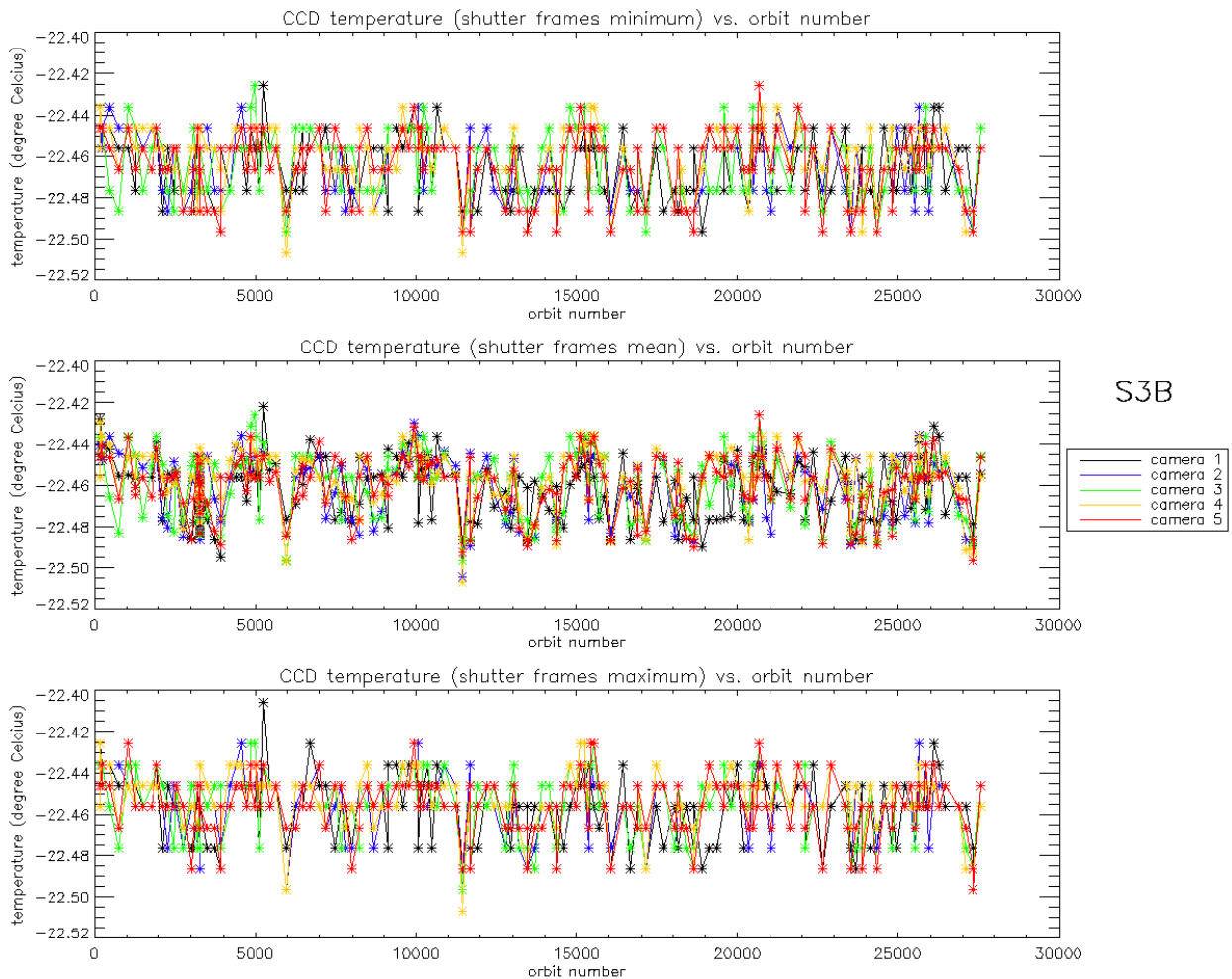


Figure 3: long term monitoring of OLCI-B CCD temperatures using minimum value (top), time averaged values (middle), and maximum value (bottom) provided in the annotations of the Radiometric Calibration Level 1 products, for the Shutter frames, all radiometric calibrations so far except the first one (absolute orbit 167) for which the instrument was not yet thermally stable.

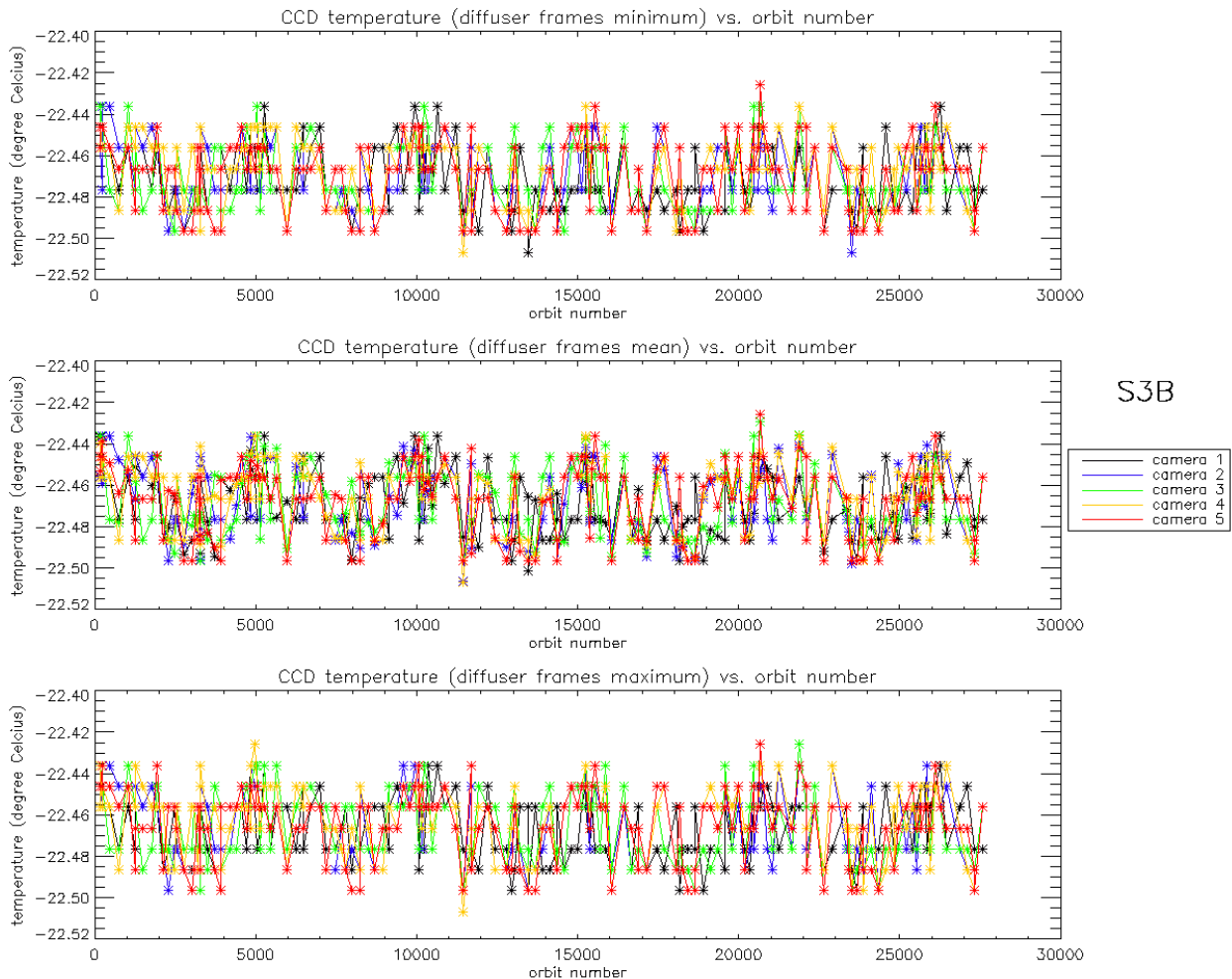


Figure 4: same as Figure 3 for diffuser frames.

2.2 Radiometric Calibration

For OLCI-A, two Radiometric Calibration sequences have been acquired during the reported period:

- ❖ S01 sequence (diffuser 1) on 09/08/2023 00:15 to 00:17 (absolute orbit 38931)
- ❖ S01 sequence (diffuser 1) on 28/08/2023 18:55 to 18:57 (absolute orbit 39213)

For OLCI-B, one Radiometric Calibration sequence have been acquired during the reported period:

- ❖ S01 sequence (diffuser 1) on 11/08/2023 10:31 to 10:33 (absolute orbit 27572)

The acquired Sun azimuth angles are presented on Figure 5 for OLCI-A and Figure 6 for OLCI-B, on top of the nominal values without Yaw Manoeuvre (i.e. with nominal Yaw Steering control of the satellite).

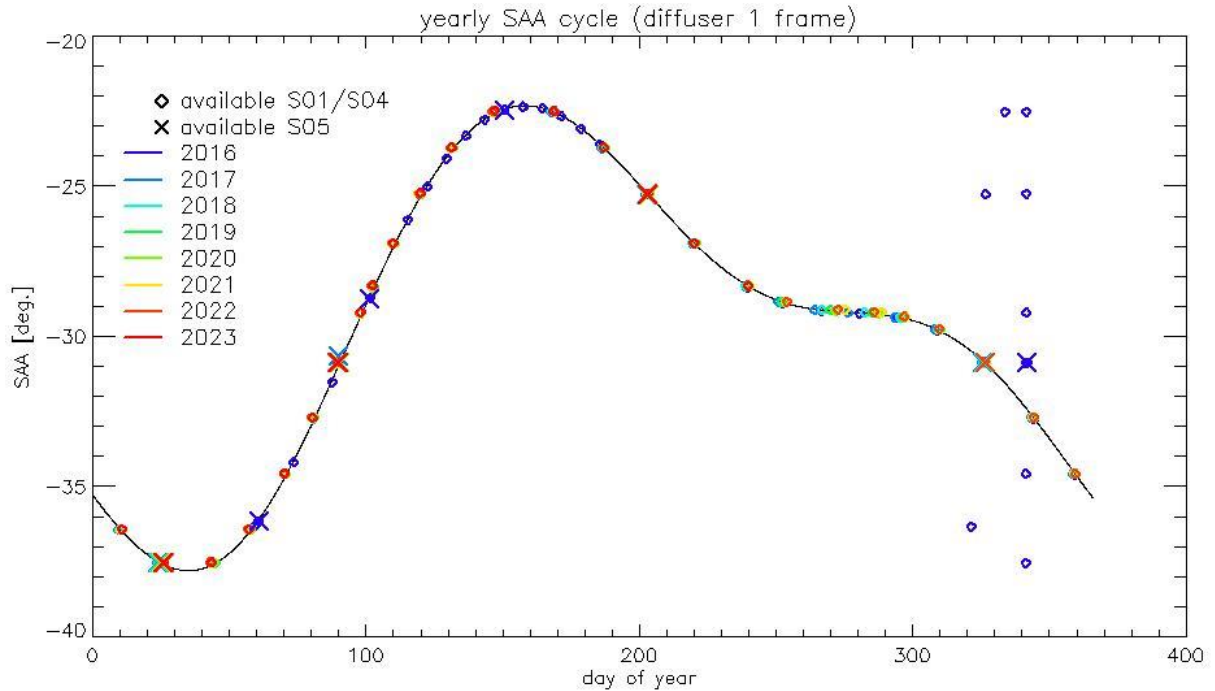


Figure 5: Sun azimuth angles during acquired OLCI-A Radiometric Calibrations (diffuser frame) on top of nominal yearly cycle (black curve). Diffuser 1 with diamonds, diffuser 2 with crosses. Different colours correspond to different years of acquisition (see the legend inside the figure).

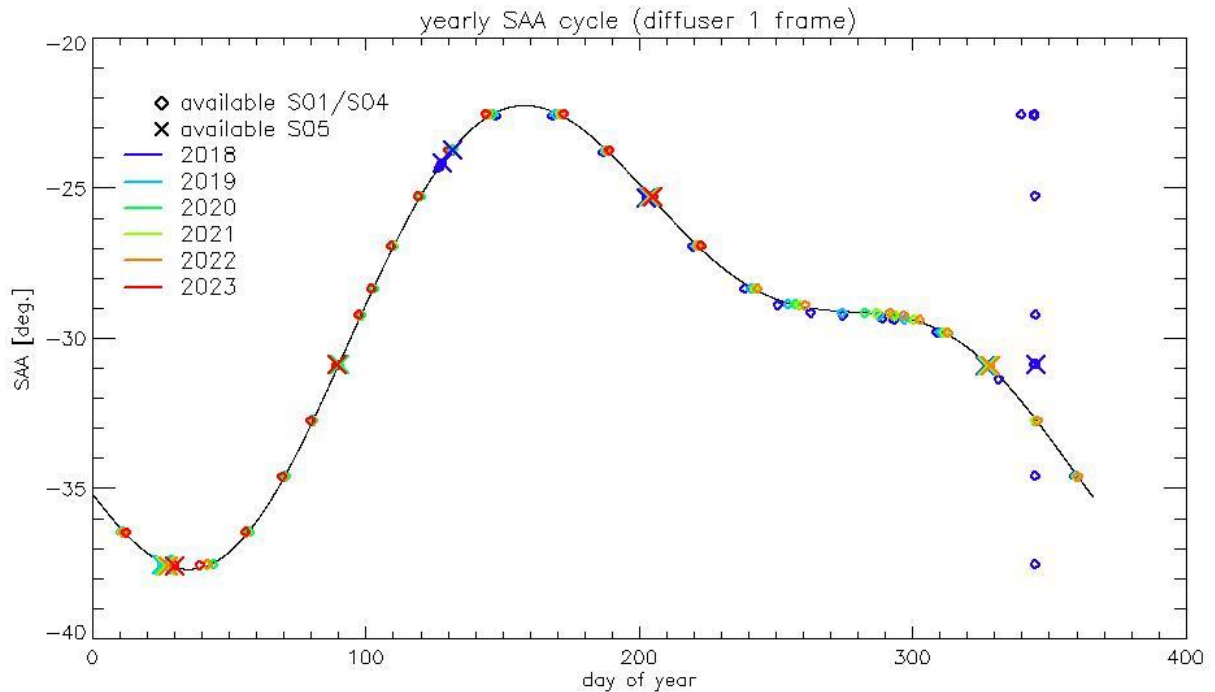


Figure 6: same as Figure 5 for OLCI-B.

Sun Zenith Angles as a function of Sun Azimuth Angles are presented in Figure 7 for OLCI-A and Figure 8 for OLCI-B.

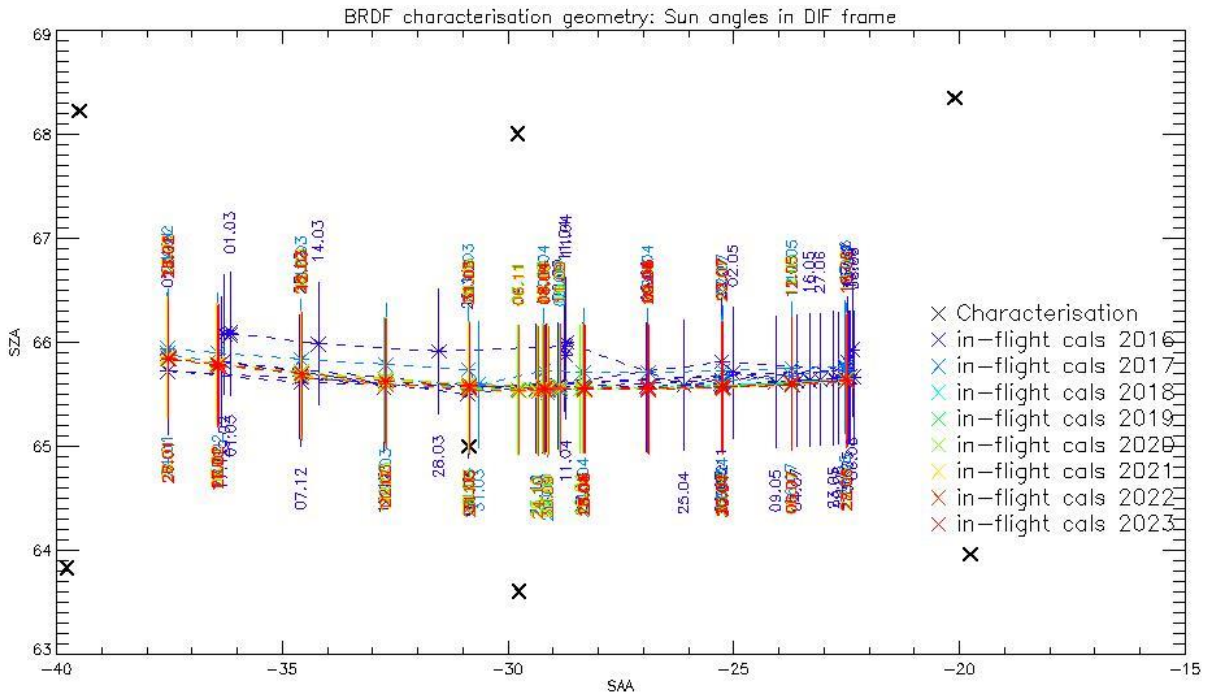


Figure 7: OLCI-A Sun geometry during radiometric Calibrations on top of characterization ones (diffuser frame)

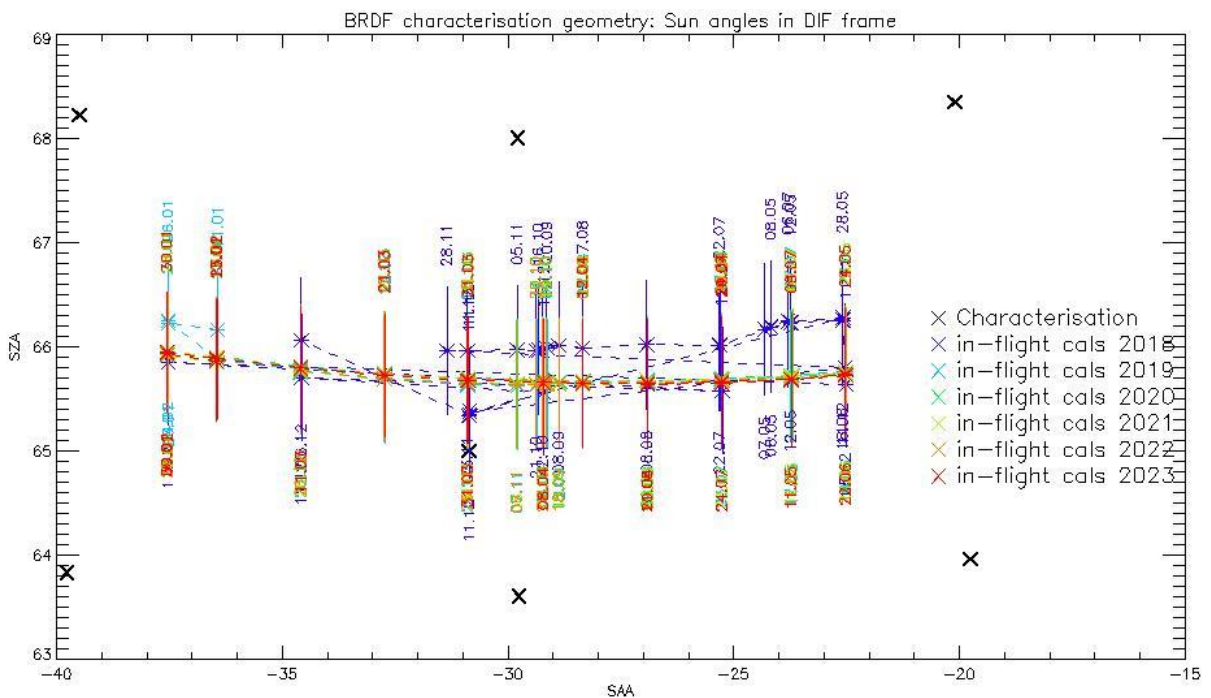


Figure 8: same as Figure 7 for OLCI-B

2.2.1 Dark Offsets [OLCI-L1B-CV-230]

Note about the High Energy Particles:

The filtering of High Energy Particle (HEP) events from radiometric calibration data has been implemented (for shutter frames only) in a post processor, allowing generating Dark Offset and Dark Current tables computed on filtered data. The post-processor starts from IPF intermediate data (corrected counts), applies the HEP detection and filtering and finally computes the Dark Offset and Dark Current tables the same way as IPF. An example of the impact of HEP filtering is given in Figure 9.

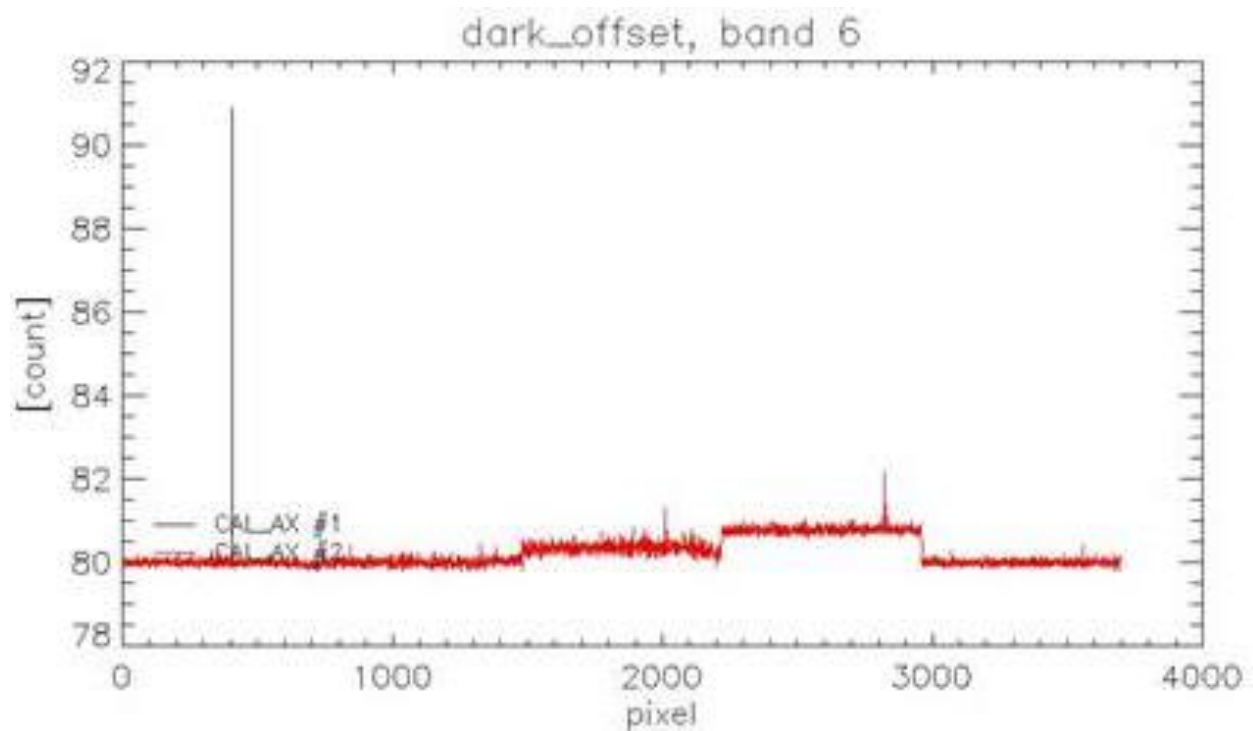


Figure 9: Dark Offset table for band Oa06 with (red) and without (black) HEP filtering (Radiometric Calibration of 22 July 2017). The strong HEP event near pixel 400 has been detected and removed by the HEP filtering.

All results presented below in this section have been obtained using the HEP filtered Dark Offset and Dark Current tables.

2.2.1.2 OLCI-A

Dark offsets

Dark offsets are continuously affected by the global offset induced by the Periodic Noise on the OCL (Offset Control Loop) convergence. Current reporting period calibrations are affected the same way as others. The amplitude of the shift varies with band and camera from virtually nothing (e.g. camera 2, band Oa1) to up to 5 counts (Oa21, camera 3). The Periodic Noise itself comes on top of the global shift with its known signature: high frequency oscillations with a rapid damp. This effect remains more or less stable with time in terms of amplitude, frequency and decay length, but its phase varies with time, introducing the global offset mentioned above.

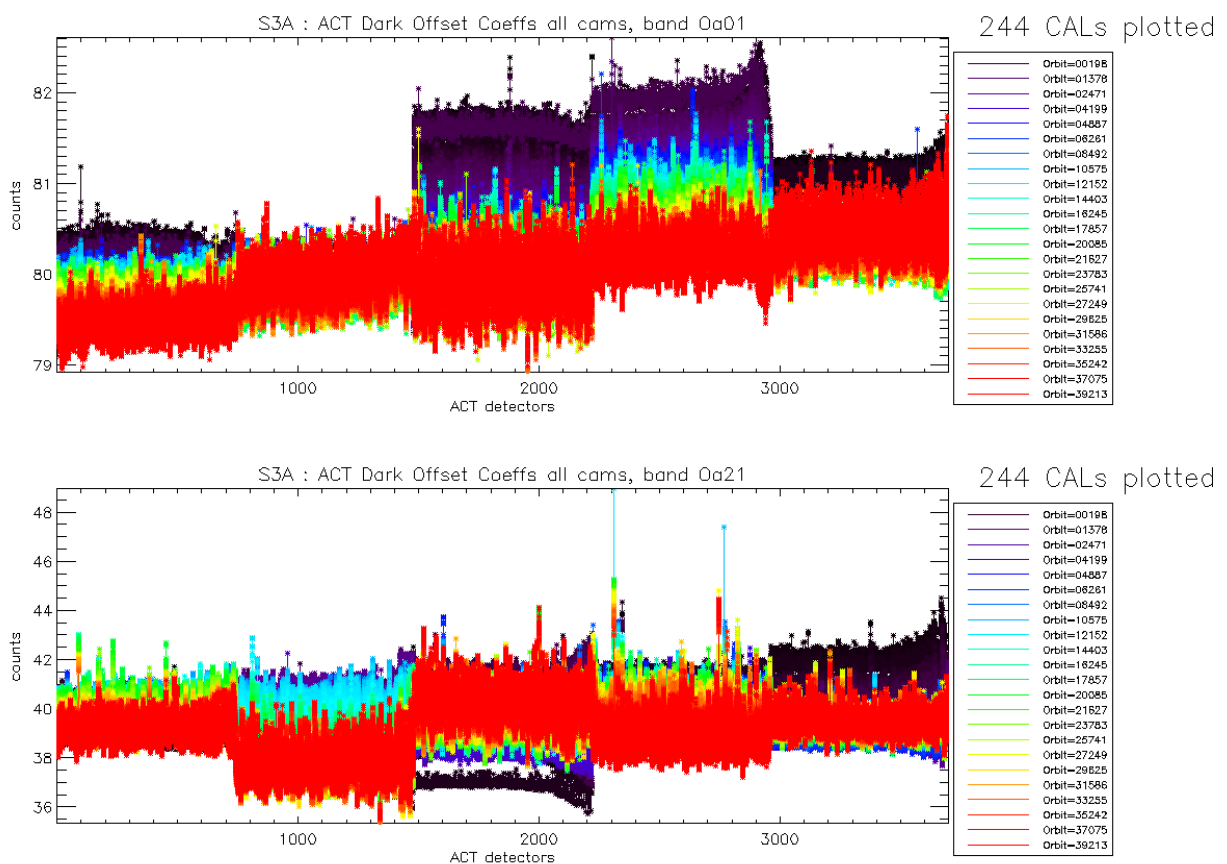


Figure 10: OLCI-A Dark Offset for band Oa1 (top) and Oa21 (bottom), all radiometric calibrations so far except the first one (orbit 183) for which the instrument was not thermally stable yet.

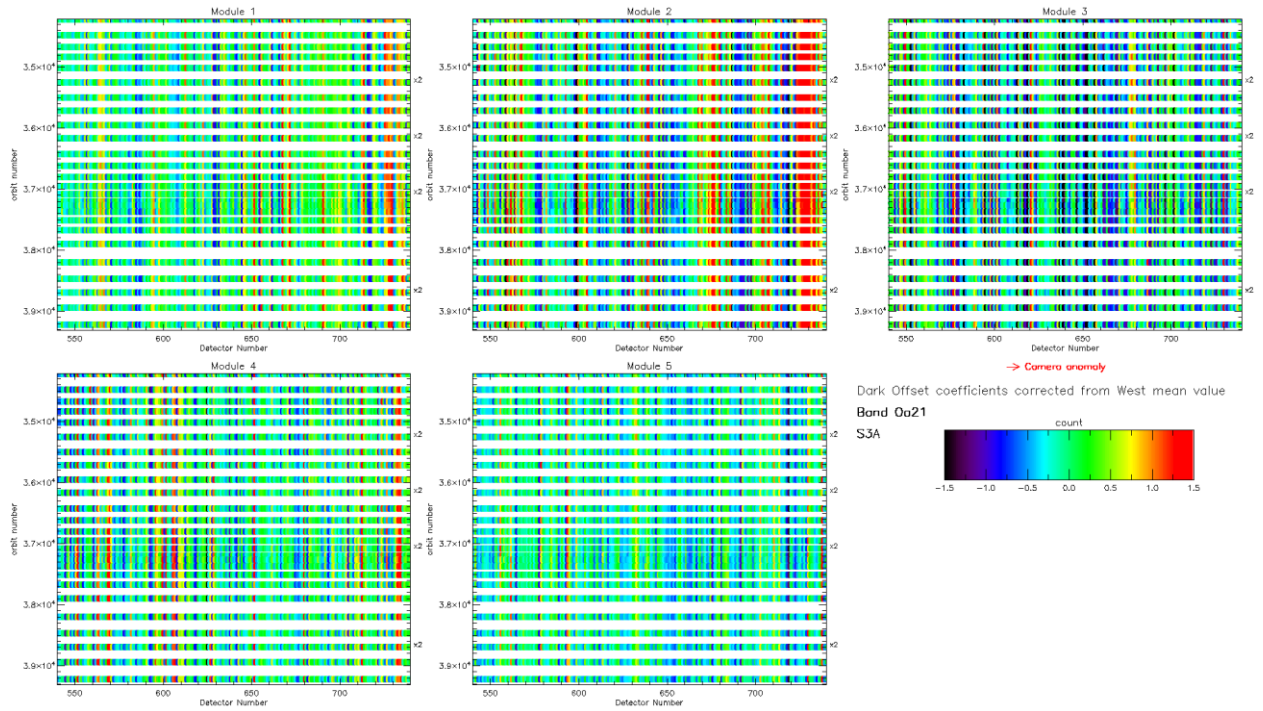


Figure 11: map of OLCI-A periodic noise for the 5 cameras, for band Oa21. X-axis is detector number (East part, from 540 to 740, where the periodic noise occurs), Y-axis is the orbit number. Y-axis range is focused on the most recent 5000 orbits. The counts have been corrected from the West detectors mean value (not affected by periodic noise) in order to remove mean level gaps and consequently to have a better visualisation of the long term evolution of the periodic noise structure. At the beginning of the mission the periodic noise for band Oa21 had strong amplitude in camera 2, 3 and 5 compared to camera 1 and 4. However PN evolved through the mission and these discrepancies between cameras have been reduced. At the time of this Cyclic Report Camera 2 still shows a slightly higher PN than other cameras.

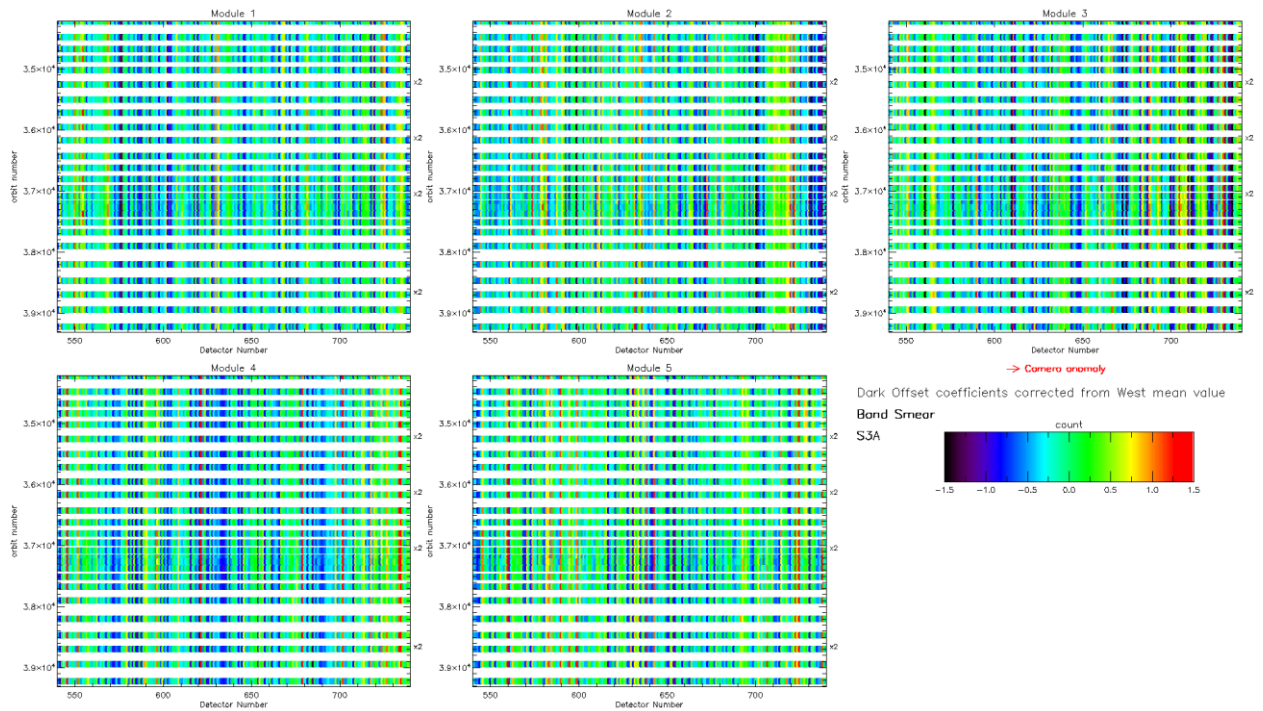


Figure 12: same as Figure 11 for smear band.

Figure 11 and Figure 12 show the so-called ‘map of periodic noise’ in the 5 cameras, for respectively band 21 and smear band. These maps have been computed from the dark offsets after removal of the mean level of the WEST detectors (not impacted by PN) in order to remove mean level gaps from one CAL to the other and consequently to highlight the shape of the PN. Maps are focused on the last 200 EAST detectors where PN occurs and on a time range covering only the last 5000 orbits in order to better visualize the CALs of the current reporting period.

Figure 11 and Figure 12 show that at this stage of the mission the PN is very stable in all cameras. There is no special behaviour noticed during the reporting period.

Dark Currents

Dark Currents (Figure 13) are not affected by the global offset of the Dark Offsets, thanks to the clamping to the average blind pixels value. However, the oscillations of Periodic Noise remain visible. There is no significant evolution of this parameter during the current reporting period except the small regular increase (almost linear), for all detectors, since the beginning of the mission (see Figure 14).

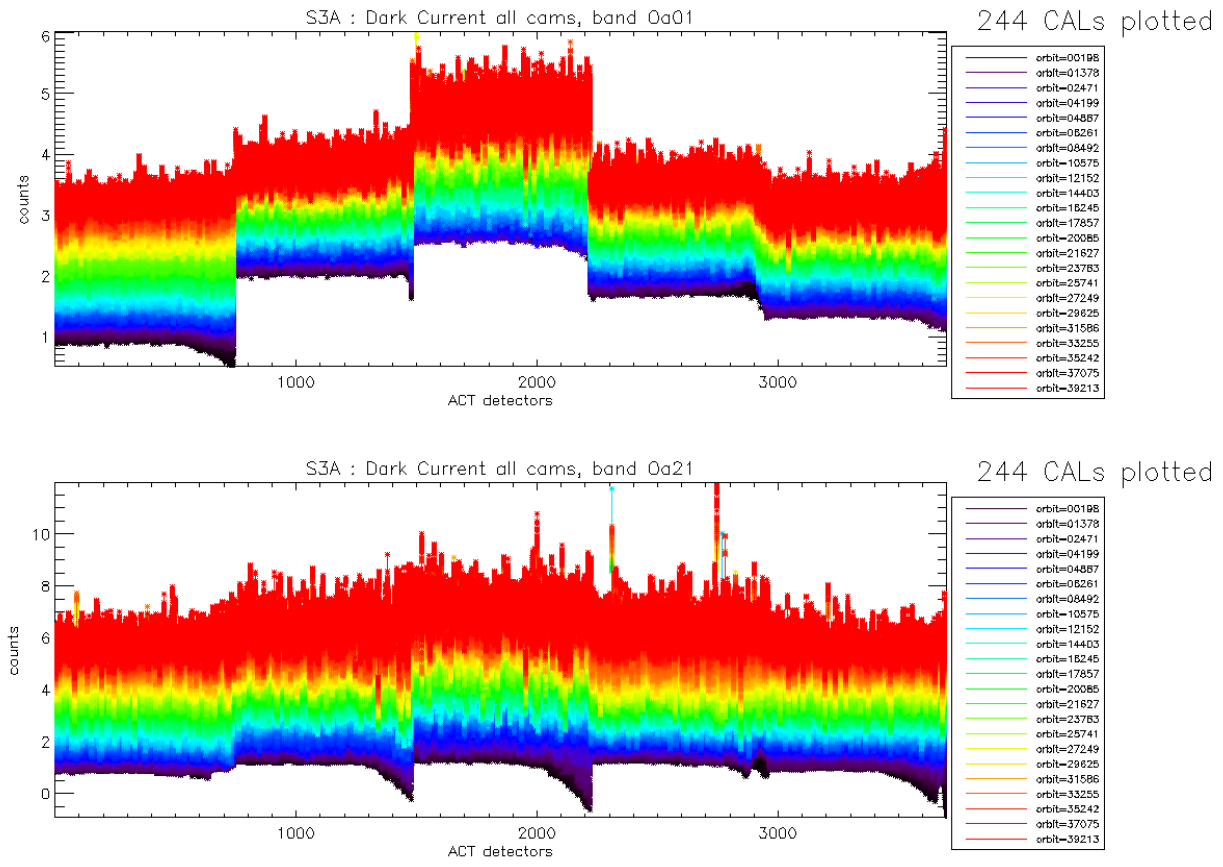


Figure 13: OLCI-A Dark Current for band Oa1 (top) and Oa21 (bottom), all radiometric calibrations so far except the first one (orbit 183) for which the instrument was not thermally stable yet.

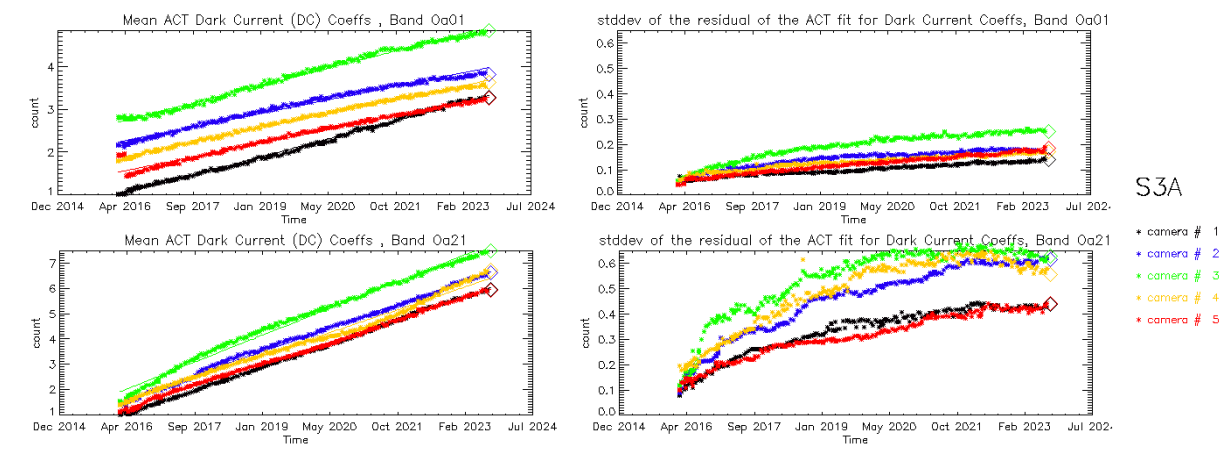


Figure 14: left column: ACT mean on 400 first detectors of OLCI-A Dark Current coefficients for spectral band Oa01 (top) and Oa21 (bottom). Right column: same as left column but for Standard deviation instead of mean. We see an increase of the DC level as a function of time especially for band Oa21.

A possible explanation of the regular increase of DC could be the increase of the number of hot pixels which is more important in Oa21 because this band is made of more CCD lines than band Oa01 and thus receives more cosmic rays impacts. It is known that cosmic rays degrade the structure of the CCD, generating more and more hot pixels at long term scales. Indeed, when computing the time slopes of the spatially averaged Dark Current as a function of band, i.e. the slopes of curves in left plots of Figure 14, one can see that Oa21 is by far the most affected, followed by the smear band (Figure 15, left); when plotting these slopes against total band width (in CCD rows, regardless of the number of micro-bands), the correlation between the slope values and the width becomes clear (Figure 15, right).

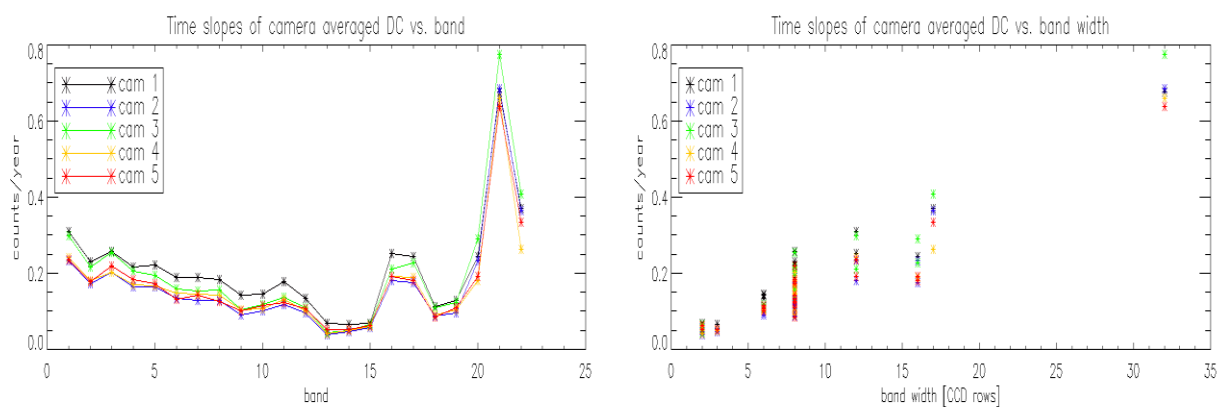


Figure 15: OLCI-A Dark current increase rates with time (in counts per year) vs. band (left) and vs. band width (right)

2.2.1.3 OLCI-B

Dark Offsets

Dark offsets for OLCI-B show a similar behaviour than for OLCI-A: mean level gaps between different orbits, induced by the presence of a pseudo periodic noise on the east edge of the cameras with a drifting phase.

Evolution of OLCI-B Dark Offset coefficients for band Oa01 and Oa21 are represented in Figure 16.

The periodic noise maps are shown for band Oa21 and smear band respectively in Figure 17 and Figure 18. As it happened for OLCI-A after a few thousands of orbits, the strong periodic noise phase and amplitude drift, present at the very beginning of the mission is now showing a clear stabilization.

Despite this overall stabilization, small evolutions are still noticeable in some bands/camera, like for example camera 1 in band Oa21 (upper left map in Figure 17) or in camera 1 band smear (upper left map in Figure 18).

Globally, OLCI-B PN is slightly less stabilized than OLCI-A PN.

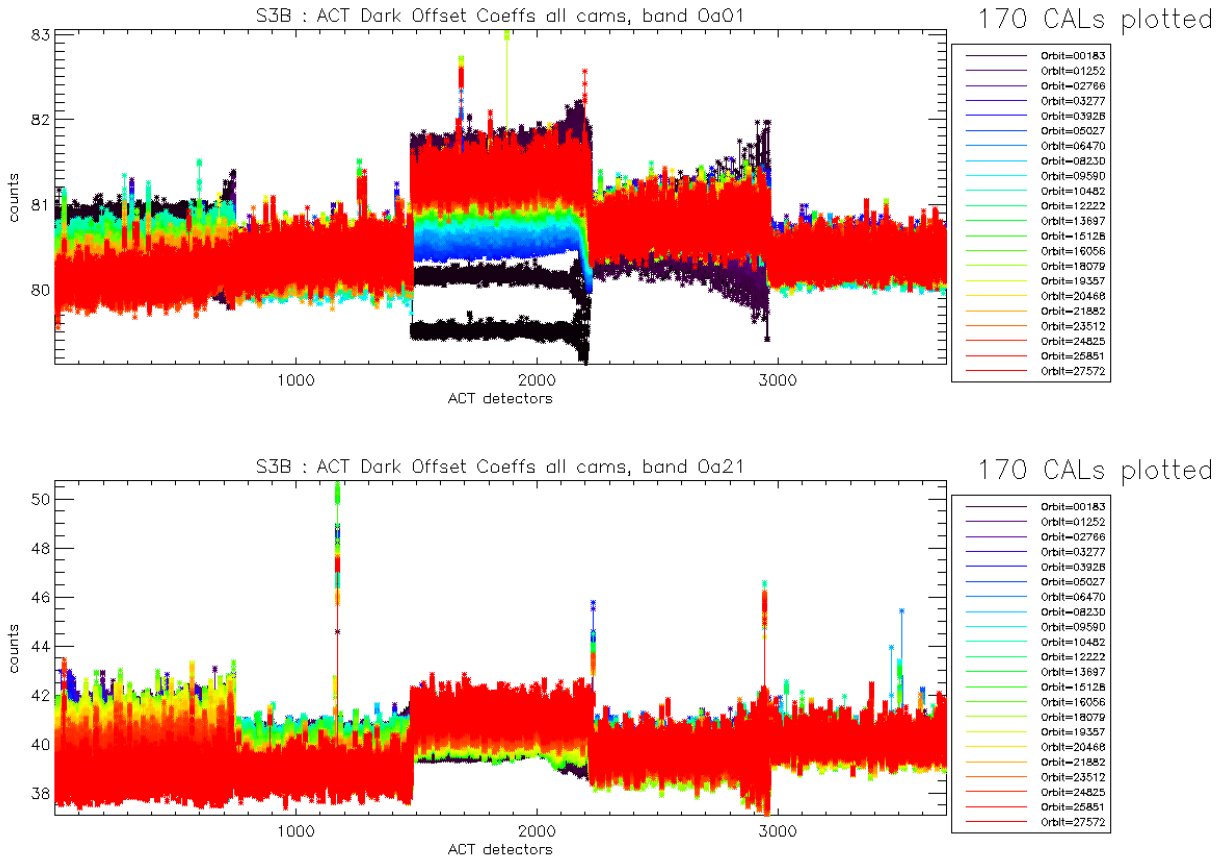


Figure 16: OLCI-B Dark Offset for band Oa1 (top) and Oa21 (bottom), all radiometric calibrations so far except the first one (orbit 167) for which the instrument was not thermally stable yet.

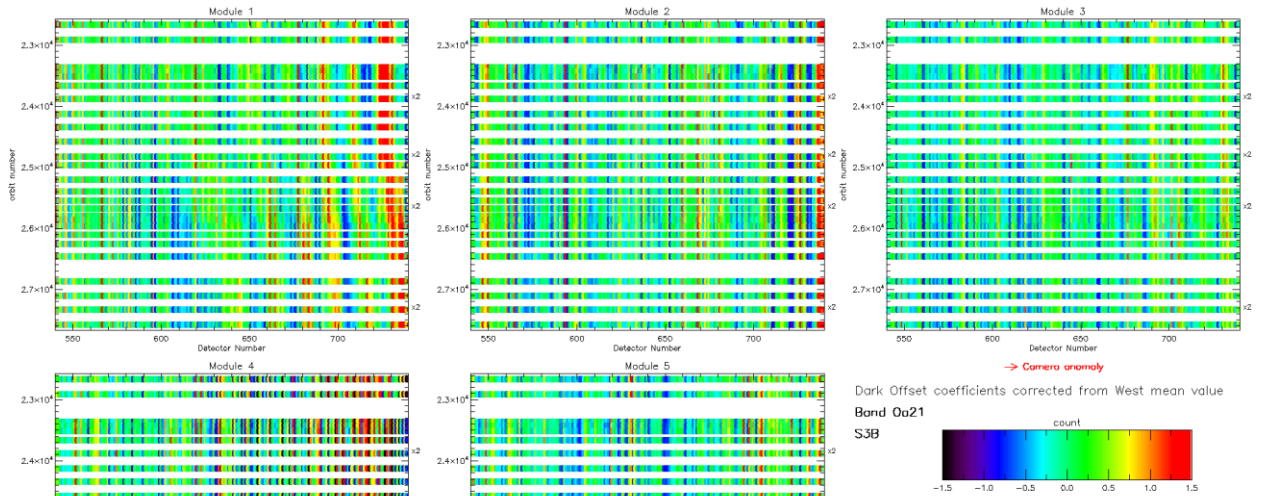


Figure 17: OLCI-B map of periodic noise for the 5 cameras, for band Oa21. X-axis is detector number (East part, from 540 to 740, where the periodic noise occurs), Y-axis is the orbit number. The counts have been corrected from the West detectors mean value (not affected by periodic noise) in order to remove mean level gaps and consequently to have a better visualization of the long term evolution of the periodic noise structure.

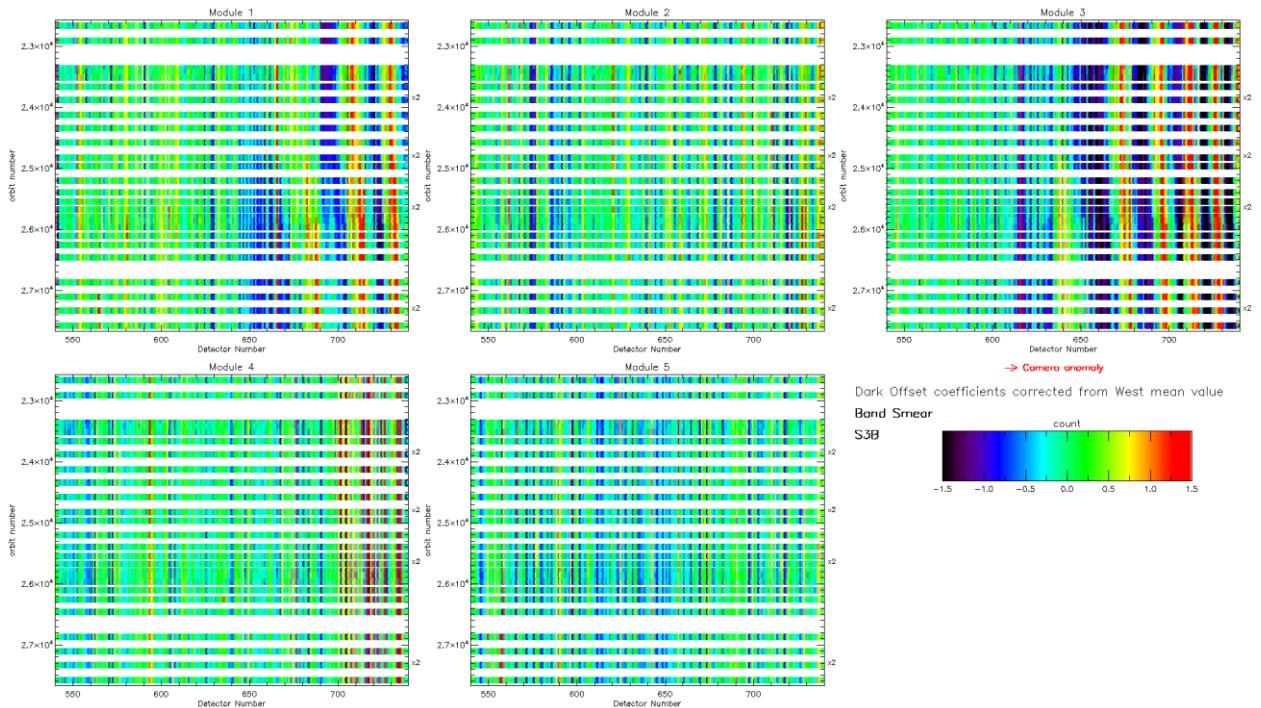


Figure 18: same as Figure 17 for smear band.

Dark Currents

As for OLCI-A there is no significant evolution of the Dark Current coefficients (Figure 19) during the current reporting period except the small regular increase (almost linear), for all detectors, since the beginning of the mission (see Figure 20) probably due to an increase of hot pixels (see Figure 21).

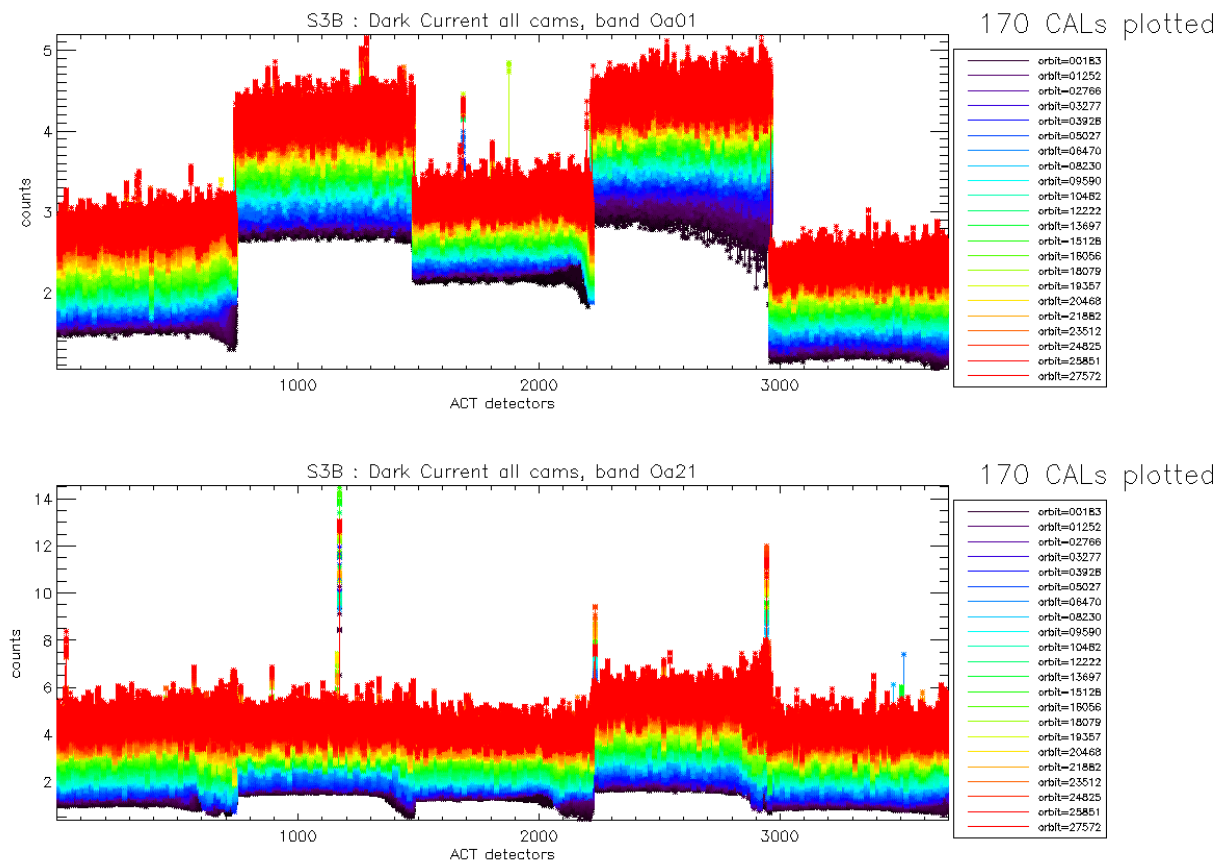


Figure 19: OLCI-B Dark Current for band Oa1 (top) and Oa21 (bottom), all radiometric calibrations so far except the first one (orbit 167) for which the instrument was not thermally stable yet.

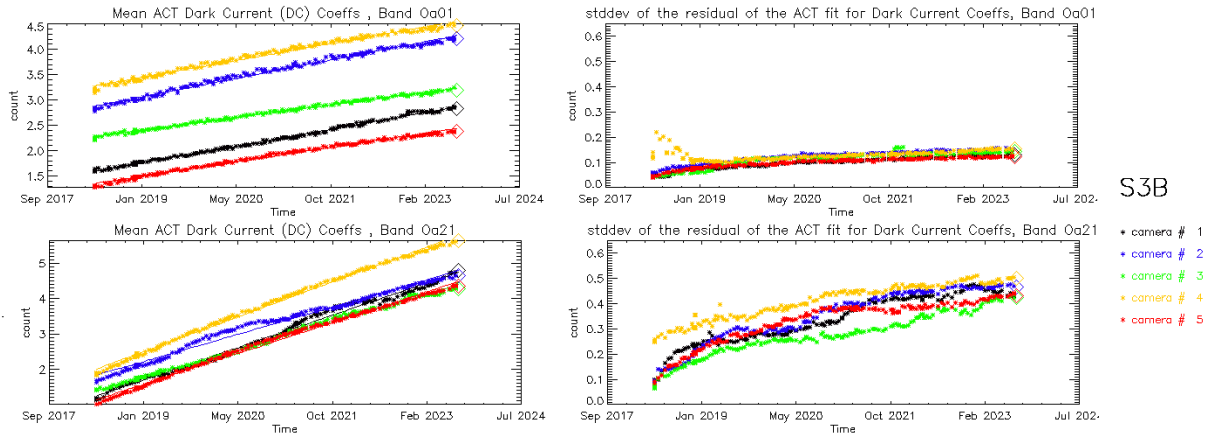


Figure 20: left column: ACT mean on 400 first detectors of OLCI-B Dark Current coefficients for spectral band Oa01 (top) and Oa21 (bottom). Right column: same as left column but for Standard deviation instead of mean. We see an increase of the DC level as a function of time especially for band Oa21.

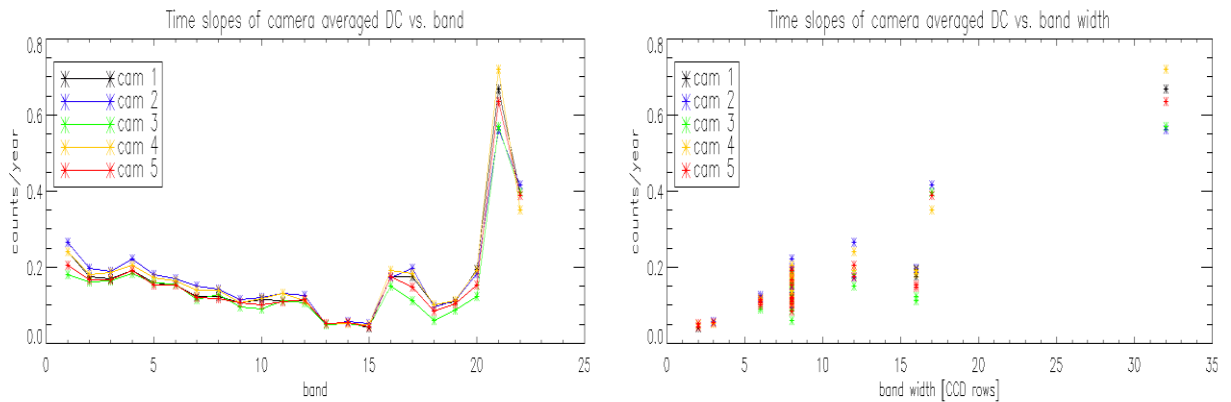


Figure 21: OLCI-B Dark Current increase rates with time (in counts per year) vs. band (left) and vs. band width (right)

2.2.3 Instrument response and degradation modelling [OLCI-L1B-CV-250]

2.2.3.1 Instrument response monitoring

2.2.3.1.1 OLCI-A

Figure 22 shows the gain coefficients of every pixel for two OLCI-A channels, Oa1 (400 nm) and Oa21 (1020 nm), highlighting the significant evolution of the instrument response since early mission.

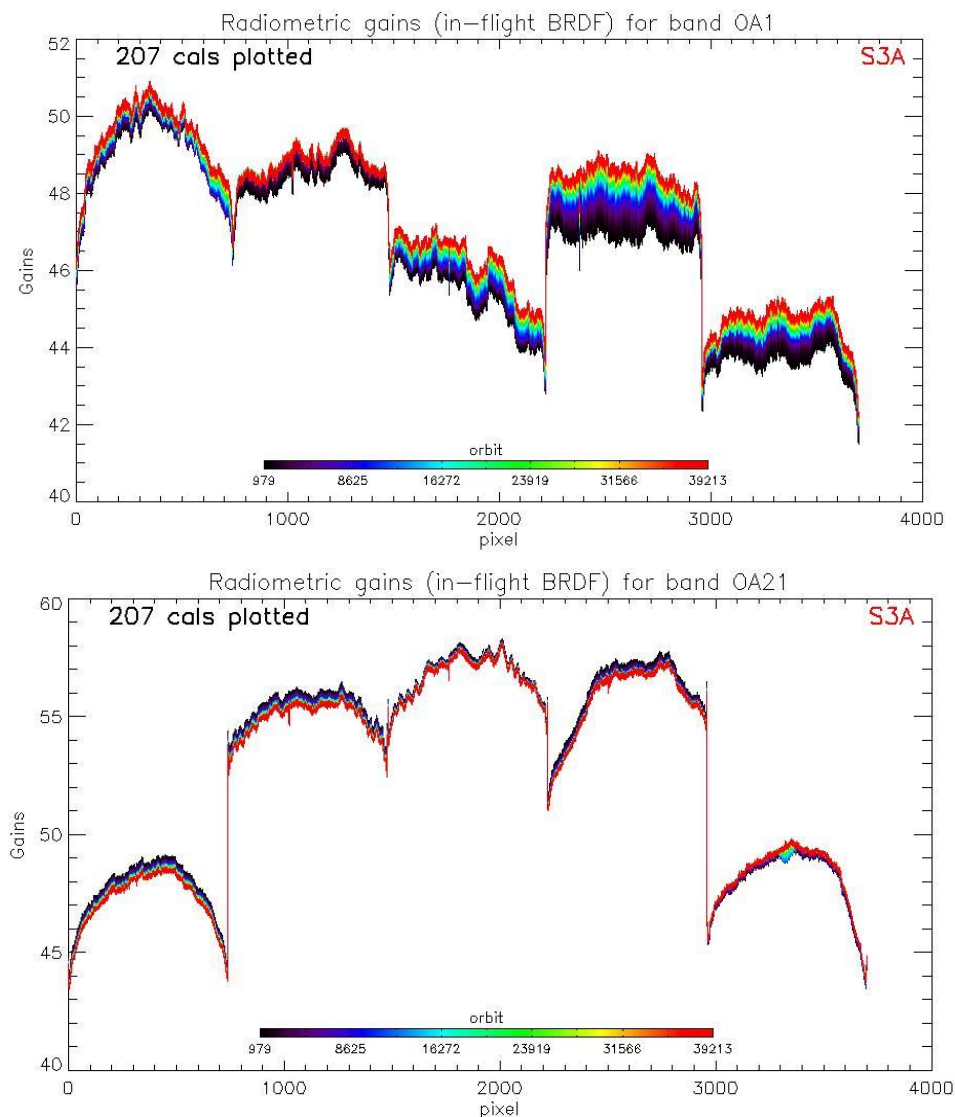


Figure 22: OLCI-A Gain Coefficients for band Oa1 (top) and Oa21 (bottom), derived using the in-flight BRDF model. The dataset is made of all diffuser 1 radiometric calibrations since orbit 979.

Figure 23 displays a summary of the time evolution of the cross-track average of the gains (in-flight BRDF, taking into account the diffuser ageing), for each module, relative to a given reference calibration (the 25/04/2016, change of OLCI channel settings). It shows that, if a significant evolution occurred during the early mission, the trends tend in general to stabilize, with some exceptions (e.g. band 1 of camera 1 and 4, bands 2 & 3 of camera 5).

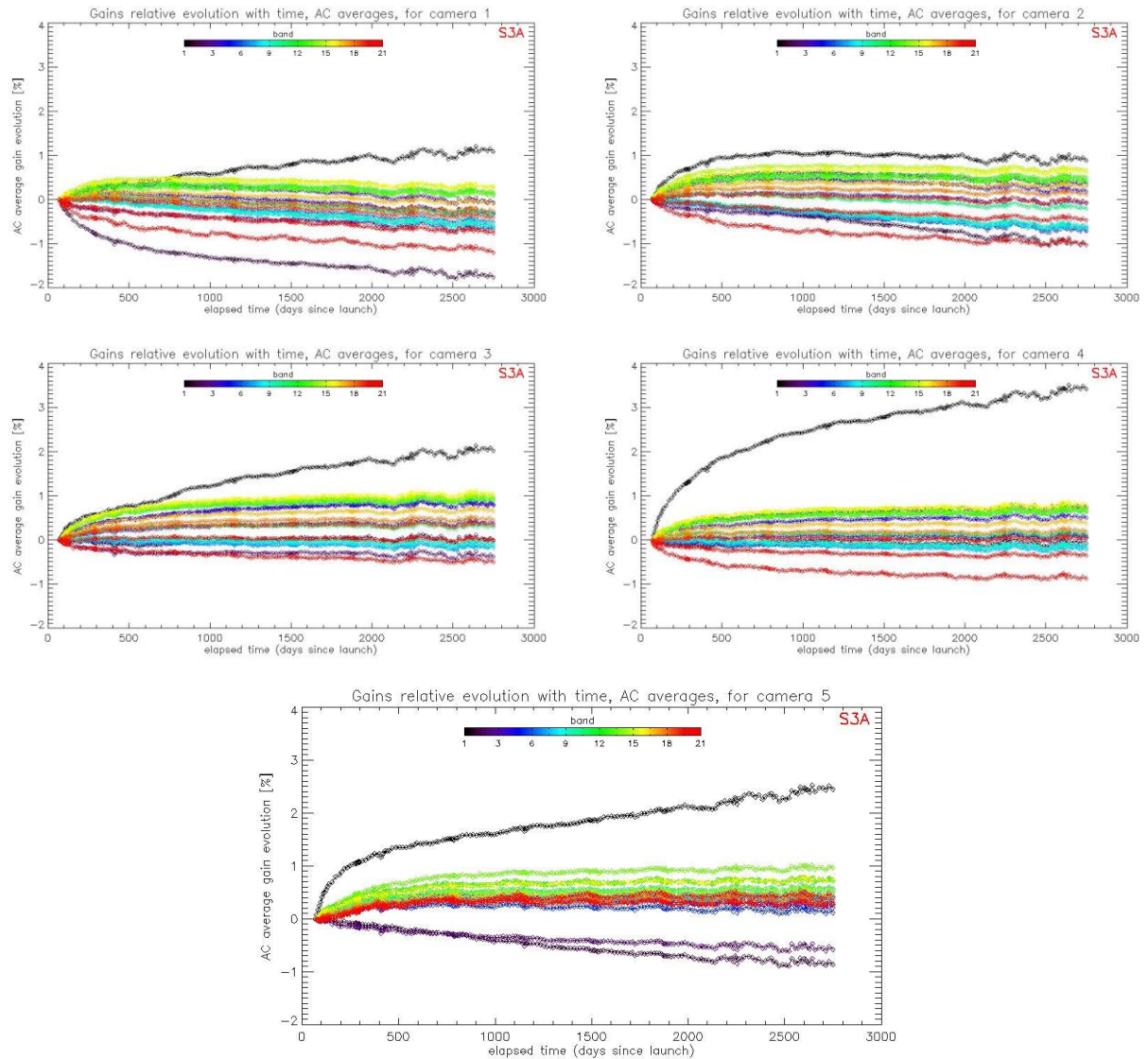


Figure 23: camera averaged gain relative evolution with respect to calibration of 25/04/2016 (change of OLCI channel settings), as a function of elapsed time since the beginning of the mission; one curve for each band (see colour code on plots), one plot for each module. The diffuser ageing is taken into account.

2.2.3.1.2 OLCI-B

Figure 24 shows the gain coefficients of every pixel for two OLCI-B channels, Oa1 (400 nm) and Oa21 (1020 nm), highlighting the significant evolution of the instrument response since early mission.

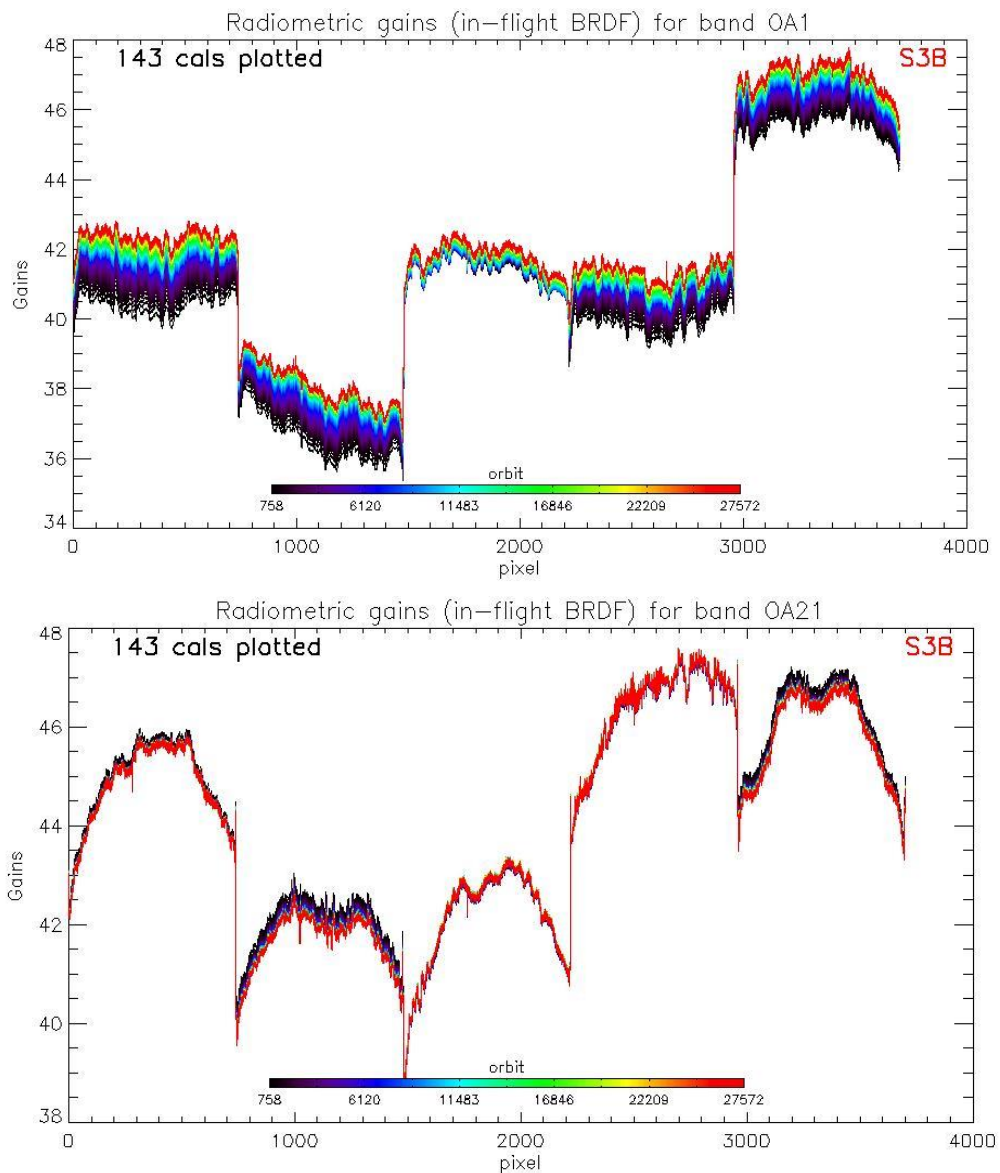


Figure 24: OLCI-B Gain Coefficients for band Oa1 (top) and Oa21 (bottom), derived using the in-flight BRDF model. The dataset is made of all diffuser 1 radiometric calibrations since orbit 758.

Figure 25 displays a summary of the time evolution of the cross-track average of the gains (in-flight BRDF, taking into account diffuser ageing), for each module, relative to a given reference calibration (first calibration after channel programming change: 18/06/2018). It shows that, if a significant evolution occurred during the early mission, the trends tend to stabilize. The large amount of points near elapsed

time = 220 days is due to the yaw manoeuvre campaign. The slight discontinuity near “day 920 since launch” is due to the upgrade of the Ageing model.

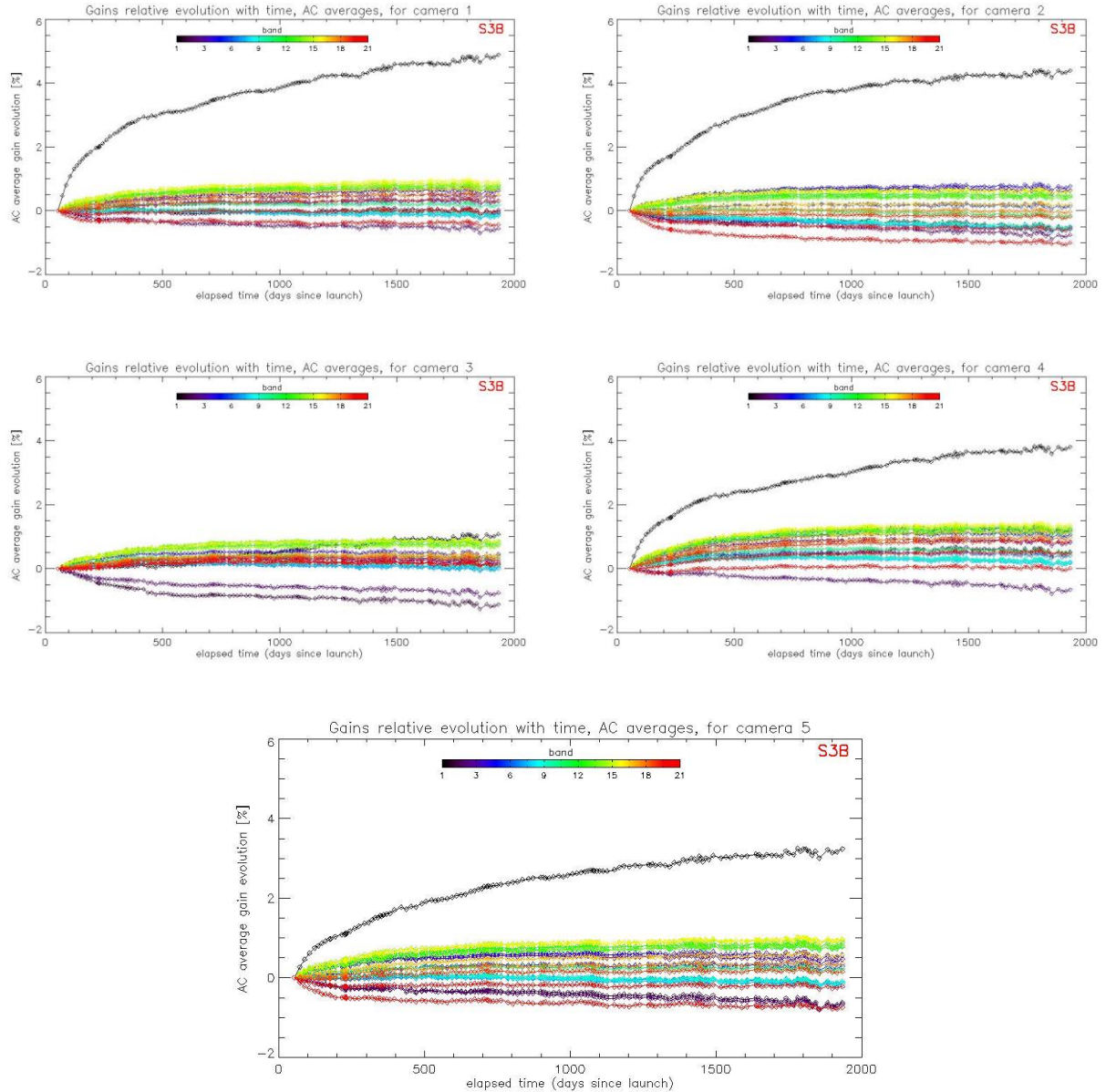



Figure 25: OLCI-B camera averaged gain relative evolution with respect to first calibration after channel programming change (18/06/2018), as a function of elapsed time since the beginning of the mission; one curve for each band (see colour code on plots), one plot for each module. The diffuser ageing is taken into account.

 <p>OPT-MPC Optical Mission Performance Cluster</p>	<p>Optical MPC</p> <p>Data Quality Report –Sentinel-3 OLCI</p> <p>August 2023</p>	<p>Ref.: OMPC.ACR.DQR.03.08-2023</p> <p>Issue: 1.0</p> <p>Date: 11/09/2023</p> <p>Page: 22</p>
---	--	--

2.2.3.2 Instrument evolution modelling

2.2.3.2.1 OLCI-A

A new OLCI-A Radiometric Gain Model has been put in operations at PDGS the 18/07/2023 (Processing Baseline 3.23). This model has been derived on the basis of an extended (compared to the previous model) Radiometric Calibration dataset, going from 11/04/2016 to 28/05/2023. It includes the correction of the diffuser ageing for the six bluest bands (Oa1 to Oa6) for which it is clearly measurable. The model performance over the complete dataset (including the 5 calibrations in extrapolation over about 3 months) remains better than about 0.13% for all bands. The previous model, trained on a Radiometric Dataset limited to 30/04/2022, shows a clear drift of the model with respect to most recent data (Figure 27), that motivated the change. Comparison of the two figures shows the improvement brought by the updated model over almost all the mission. Performance shown on Figure 26 adopts, as for OLCI-B, the multiple model approach, i.e. different models (two for OLCI-A since this new PB, three for OLCI-B since PB 1.57) are used to cover the whole mission (red dashed line on Figure 26), each model being fitted on a partial dataset (green dashed line on Figure 26) whose coverage is optimized to provide best performance.

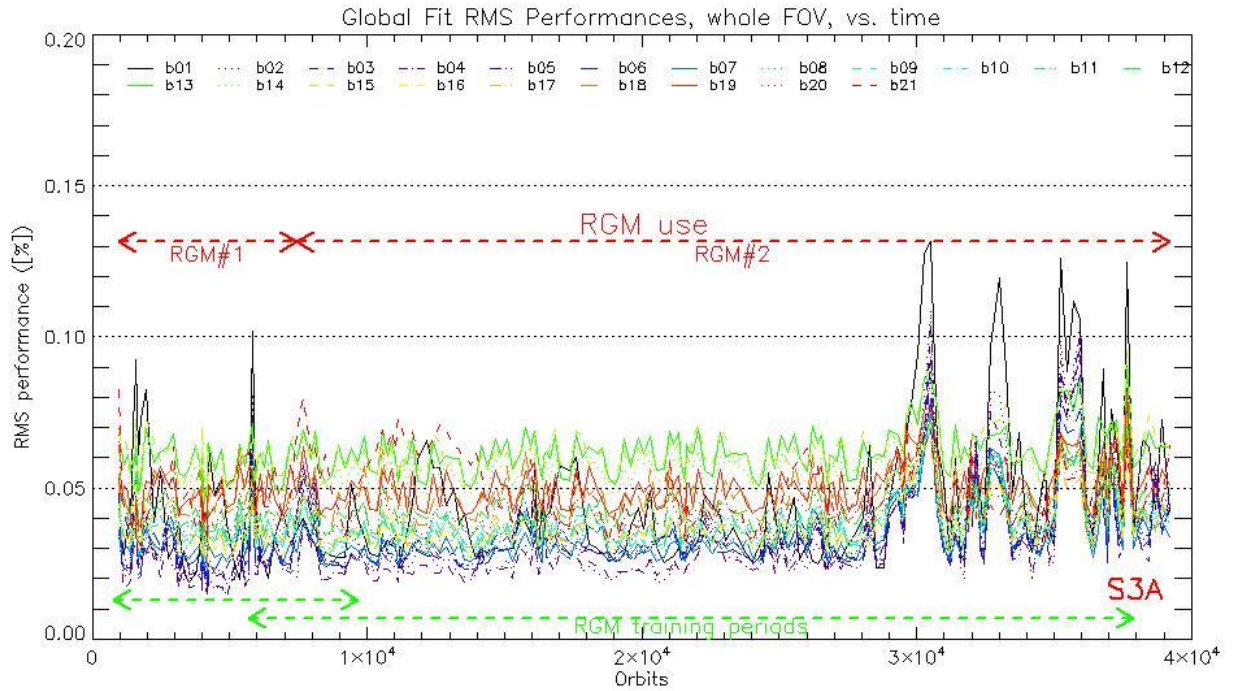


Figure 26: RMS performance of the OLCI-A Gain Model of the current processing baseline as a function of orbit.

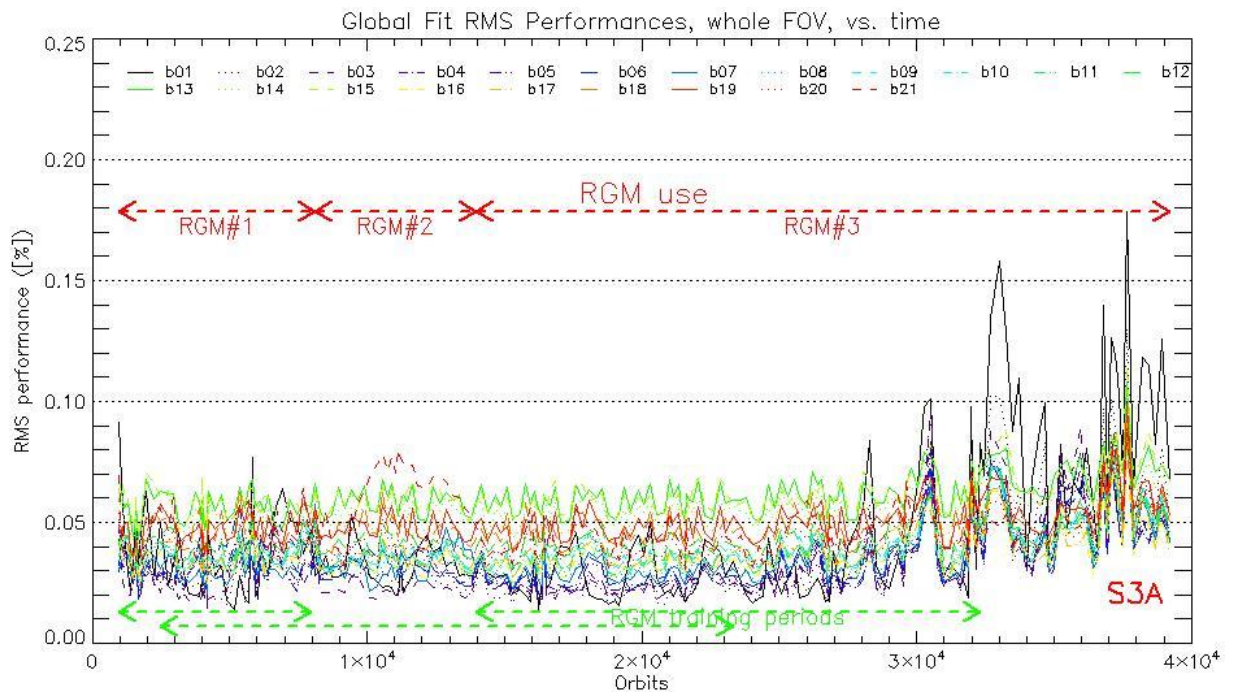


Figure 27: RMS performance of the OLCI-A Gain Model of the previous Processing Baseline as a function of orbit.

The overall instrument evolution since channel programming change (25/04/2016) is shown on Figure 28.

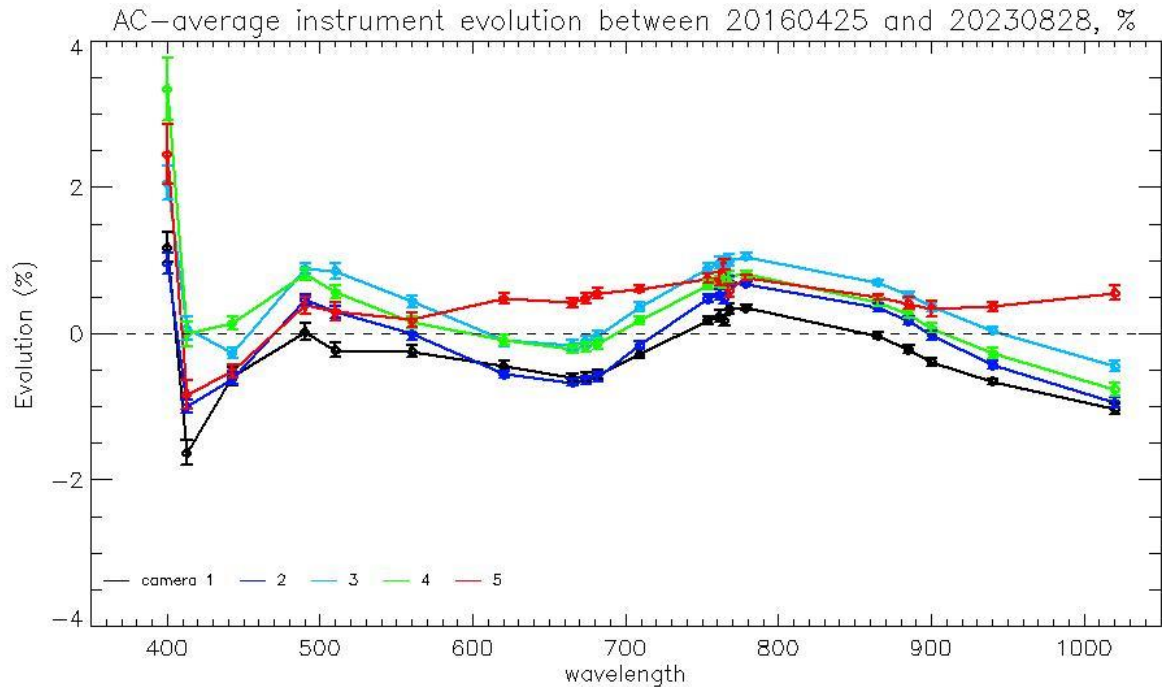


Figure 28: OLCI-A Camera-averaged instrument evolution since channel programming change (25/04/2016) and up to the most recent calibration (28/08/2023) versus wavelength.

The overall per camera performance, as a function of wavelength, and at each orbit is shown on Figure 29 as the average and standard deviation of the model over data ratio.

Finally, Figure 30 to Figure 32 show the detail of the model performance, with across-track plots of the model over data ratios at each orbit, one plot for each channel.

Comparisons of Figure 30 to Figure 32 with their counterparts in DQR of July 2022 clearly demonstrate the improvement brought by the new model whatever the level of detail.

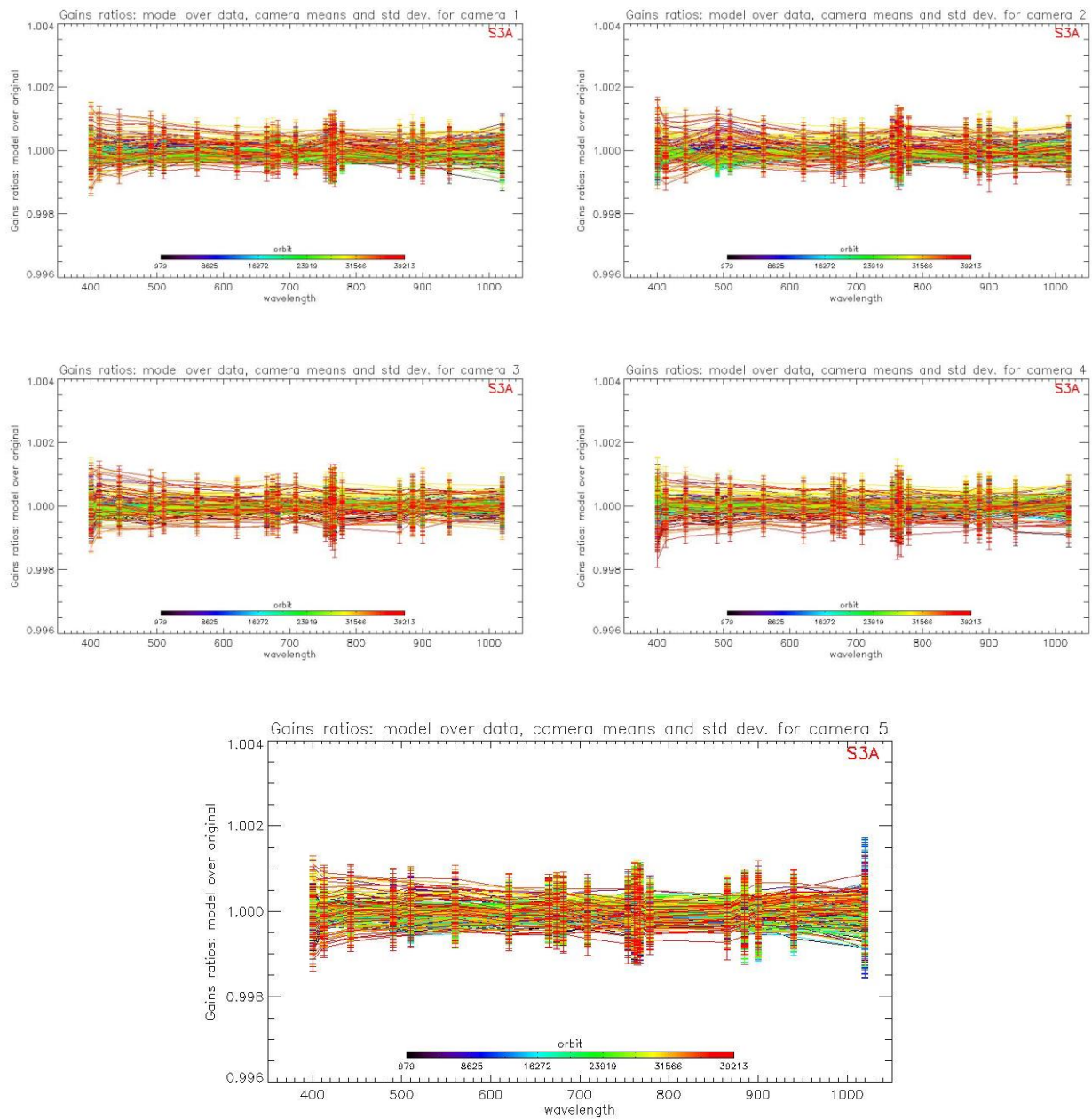


Figure 29: For the 5 cameras: OLCI-A Evolution model performance, as camera-average and standard deviation of ratio of Model over Data vs. wavelength, for each orbit of the test dataset, including 5 calibrations in extrapolation, with a colour code for each calibration from blue (oldest) to red (most recent).

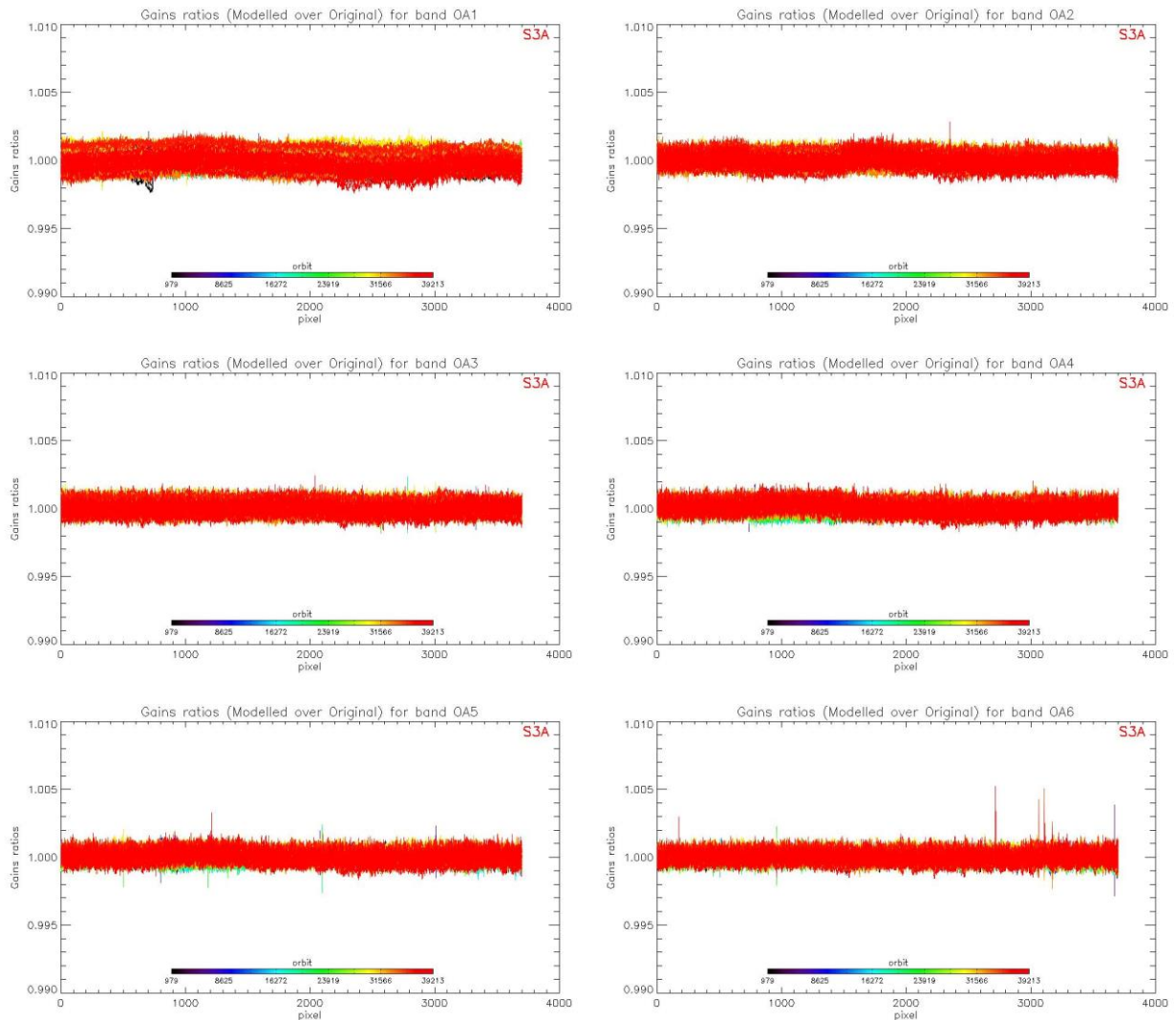


Figure 30: OLCI-A evolution model performance, as ratio of Model over Data vs. pixels, all cameras side by side, over the whole current calibration dataset (since instrument programming update), including 5 calibrations in extrapolation, channels Oa1 to Oa6.

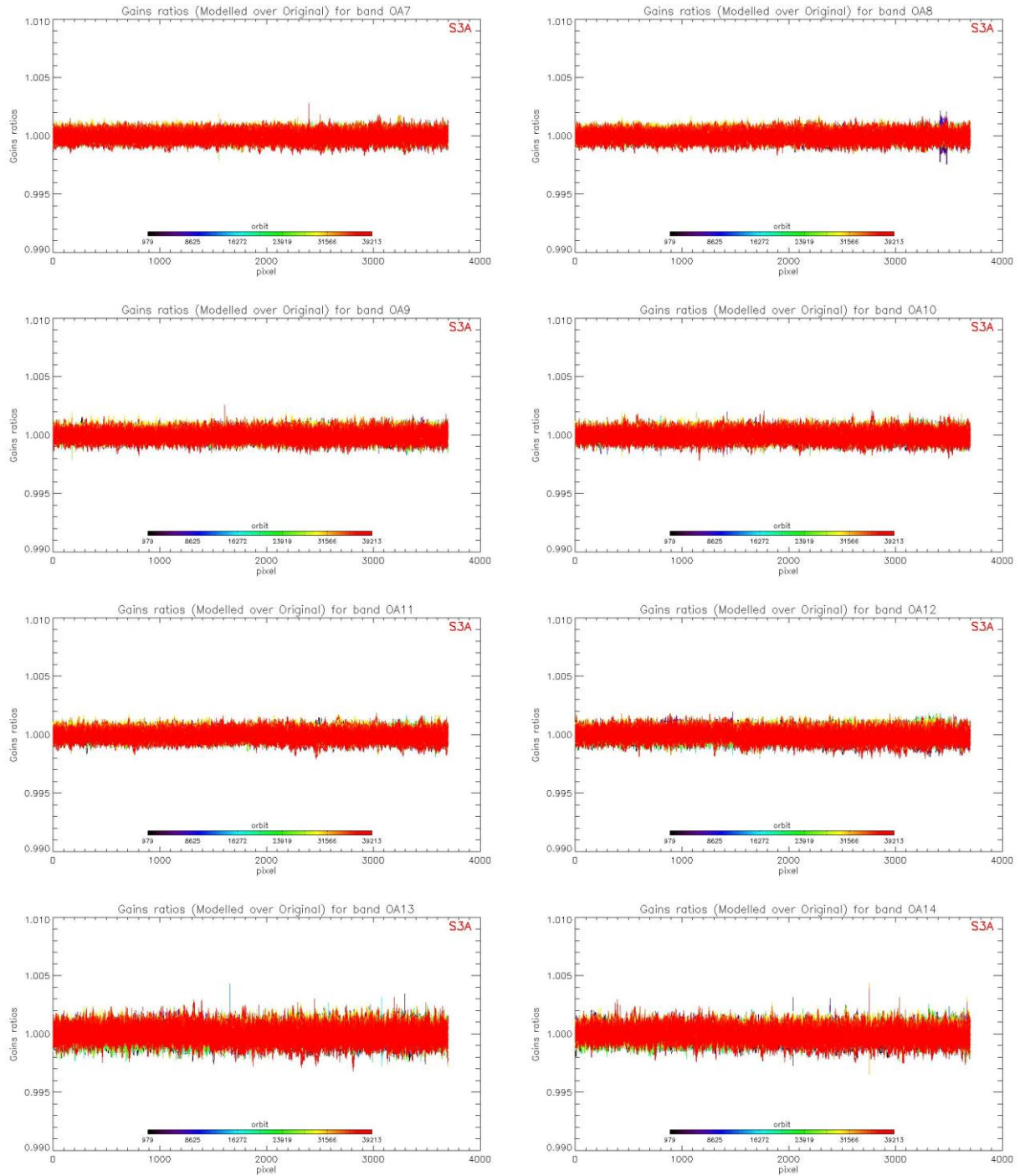


Figure 31: same as Figure 30 for channels Oa7 to Oa14.

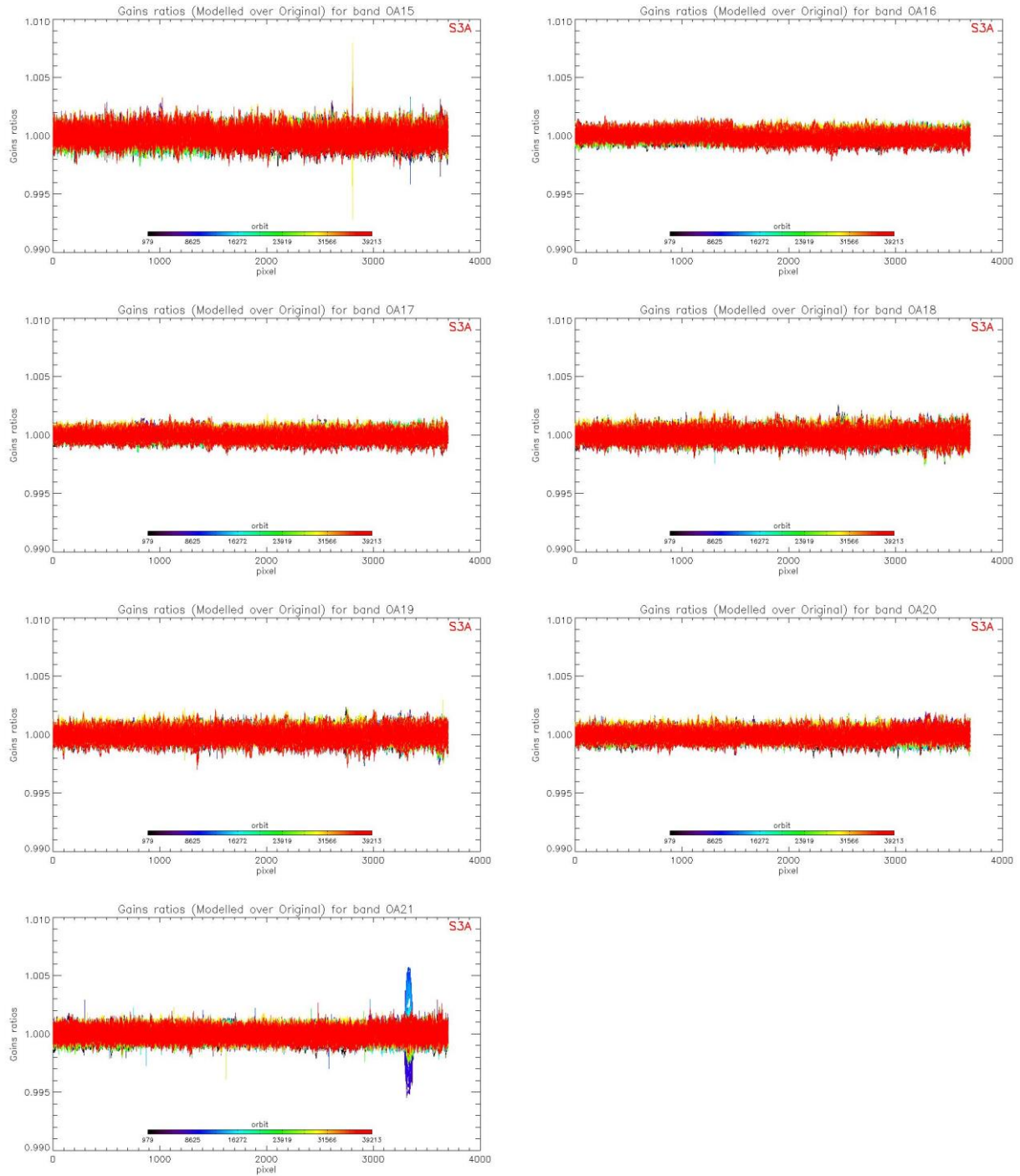


Figure 32: same as Figure 30 for channels Oa15 to Oa21.

2.2.3.2.2 OLCI-B

A new OLCI-B Radiometric Gain Model has been put in operations at PDGS on 25/07/2023 (Processing Baseline 3.23). This model has been derived on the basis of an extended Radiometric Calibration dataset (from 08/05/2018 to 24/05/2023). It includes the correction of the diffuser ageing for the five bluest bands (Oa1 to Oa5) for which it is clearly measurable. The model performance over the complete dataset (including 4 calibrations in extrapolation over about 3 months) is illustrated in Figure 33. It remains better than about 0.11% when averaged over the whole field of view for all bands at the exception of a spike near orbit 26500 reaching about up to 0.20 % for Oa02. The previous model, trained on a Radiometric Dataset limited to 29/04/2022, shows a significant drift of the model with respect to most recent data (Figure 34). Comparison of the two figures shows the improvement brought by the updated Model over all the mission.

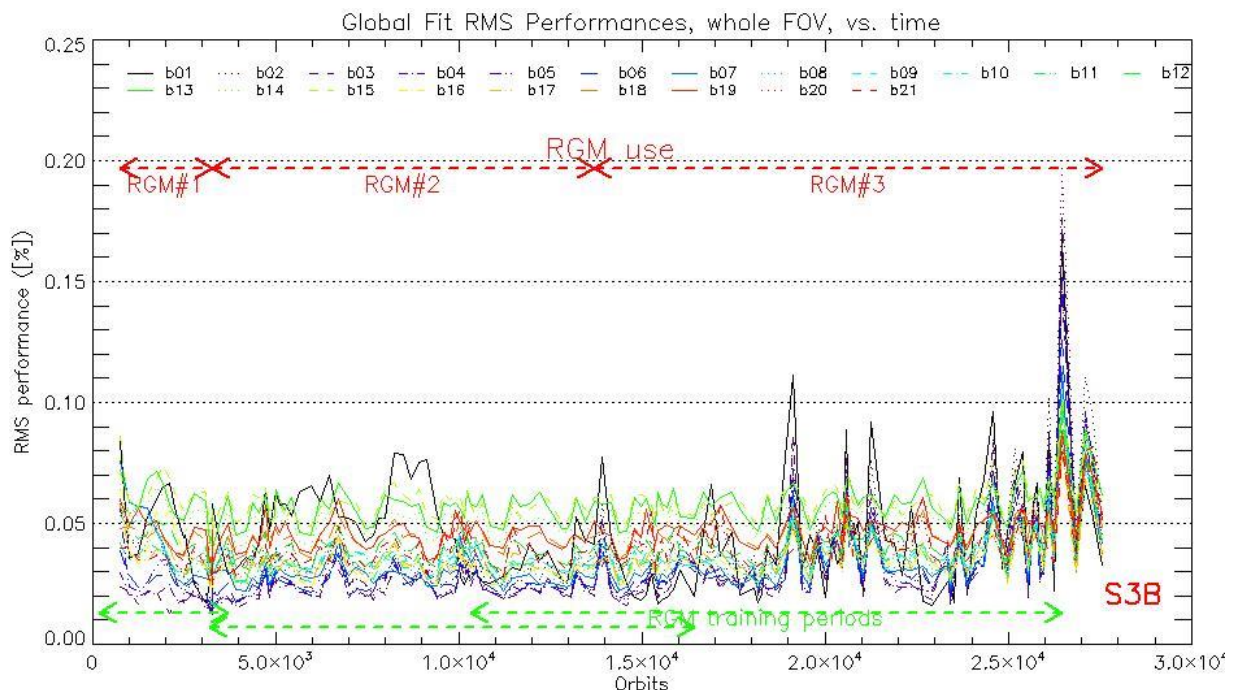


Figure 33: RMS performance of the OLCI-B Gain Model of the current processing baseline as a function of orbit.

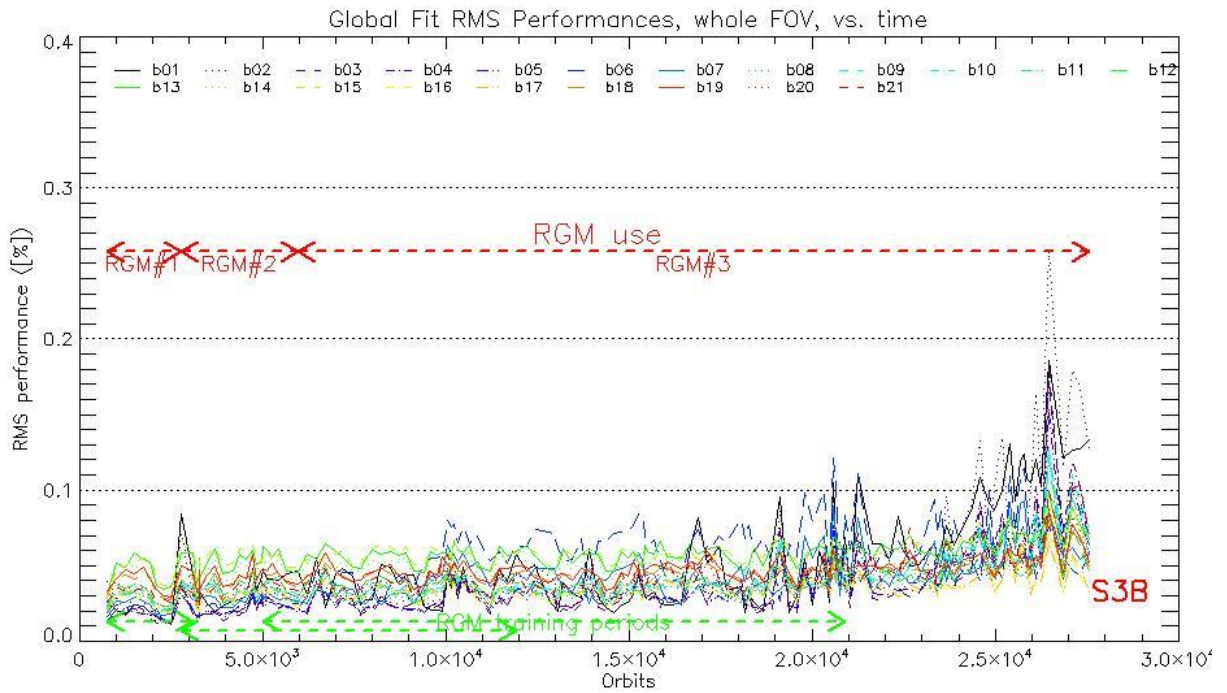


Figure 34: RMS performance of the OLCI-B Gain Model of the previous processing baseline as a function of orbit (please note the different vertical scale with respect to Figure 33).

The overall instrument evolution since channel programming change (18/06/2018) is shown on Figure 35.

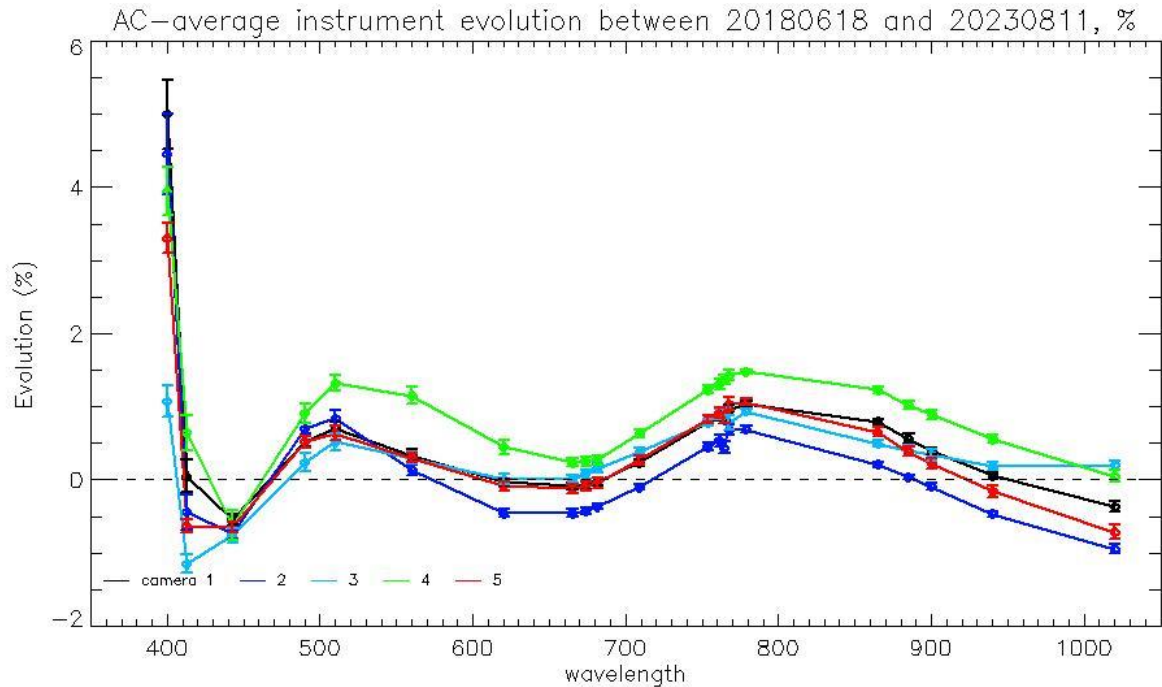


Figure 35: OLCI-B Camera-averaged instrument evolution since channel programming change (18/06/2018) and up to most recent calibration (11/08/2023) versus wavelength.

The overall per camera performance, as a function of wavelength, and at each orbit is shown on Figure 36 as the average and standard deviation of the model over data ratio.

Finally, Figure 37 to Figure 39 show the detail of the model performance, with across-track plots of the model over data ratios at each orbit, one plot for each channel.

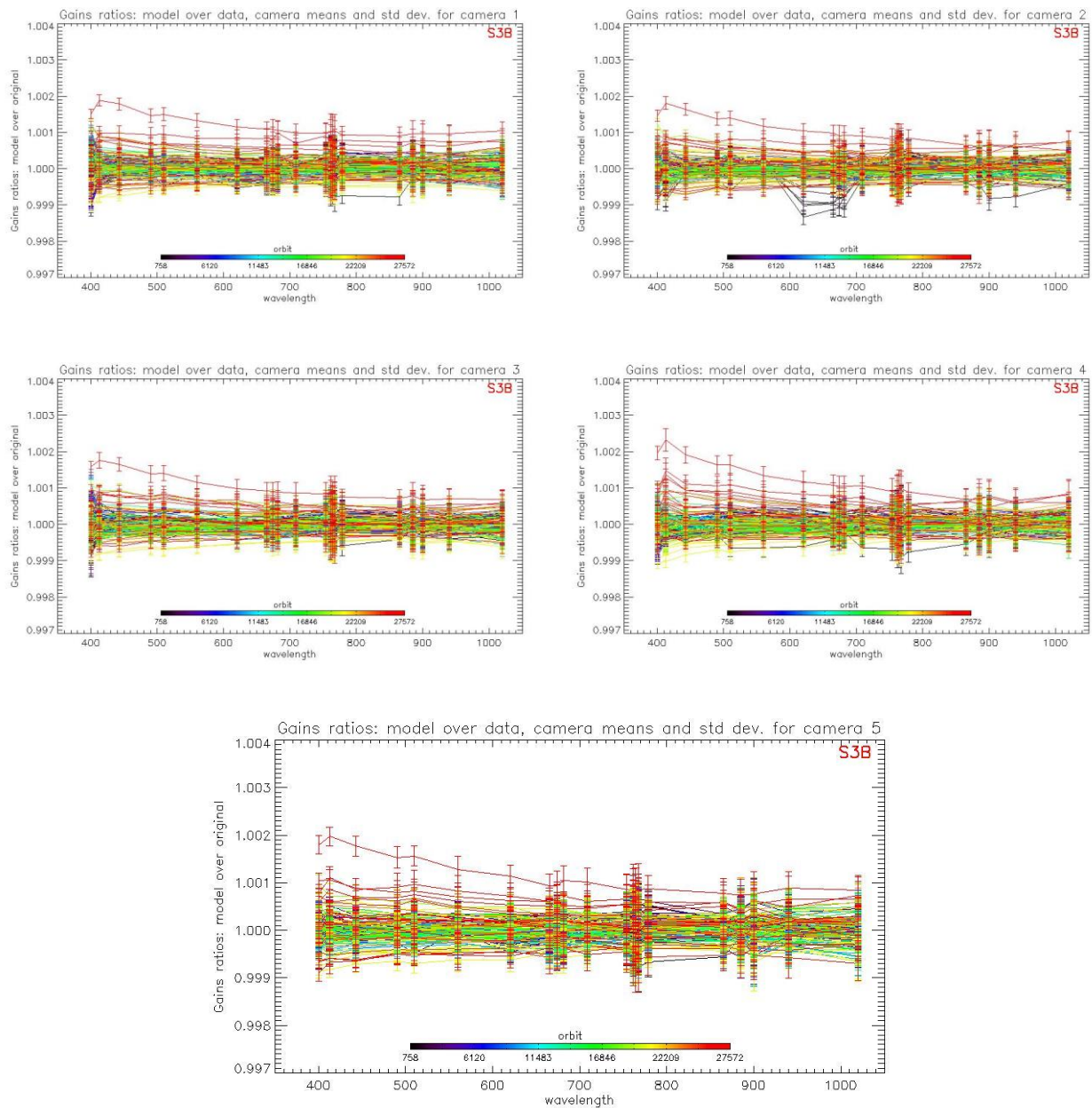


Figure 36: For the 5 cameras: OLCI-B Evolution model performance, as camera-average and standard deviation of ratio of Model over Data vs. wavelength, for each orbit of the test dataset, including 4 calibrations in extrapolation, with a colour code for each calibration from blue (oldest) to red (most recent).

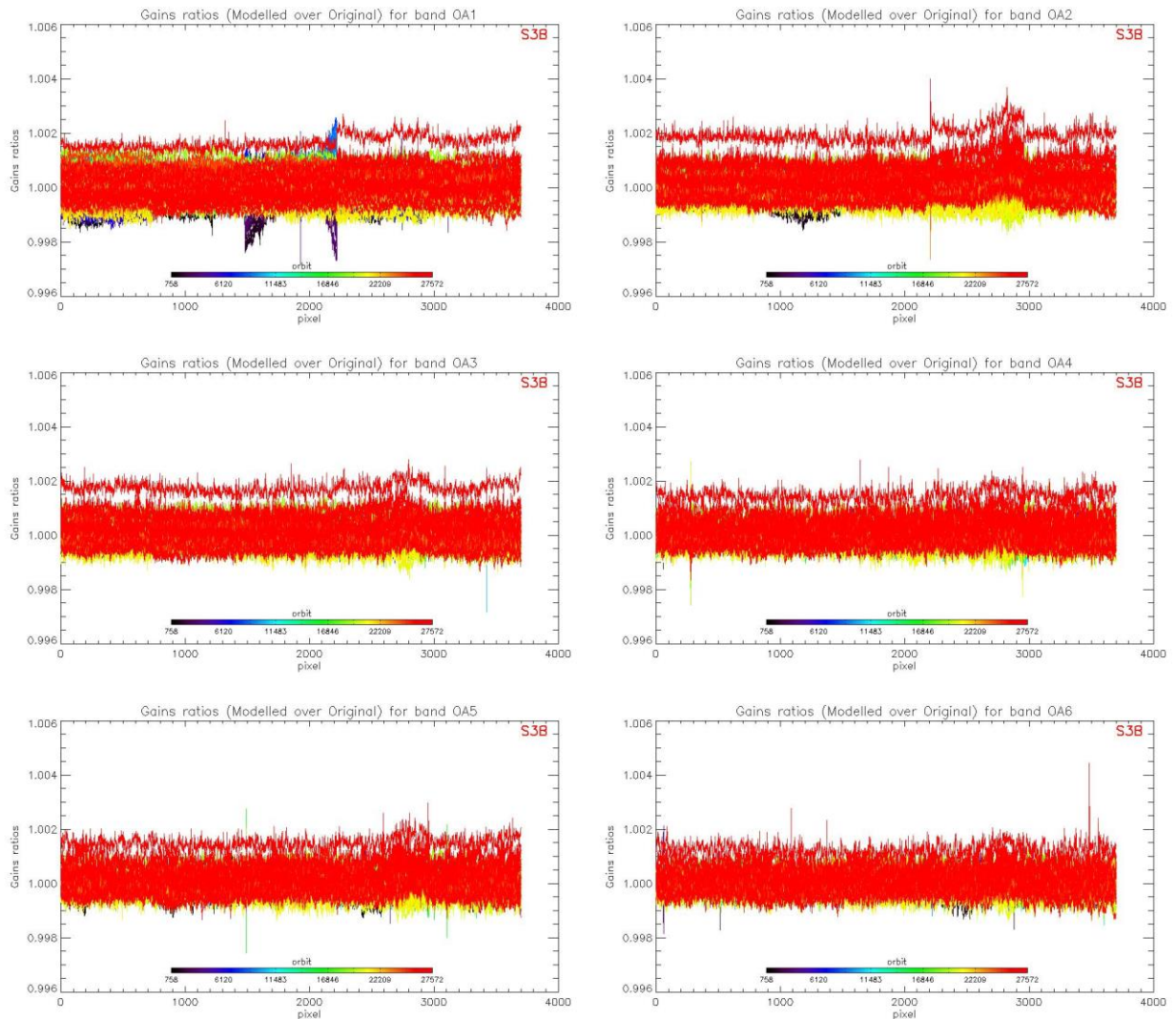


Figure 37: OLCI-B evolution model performance, as ratio of Model over Data vs. pixels, all cameras side by side, over the whole current calibration dataset (since instrument programming update), including 4 calibrations in extrapolation, channels Oa1 to Oa6.

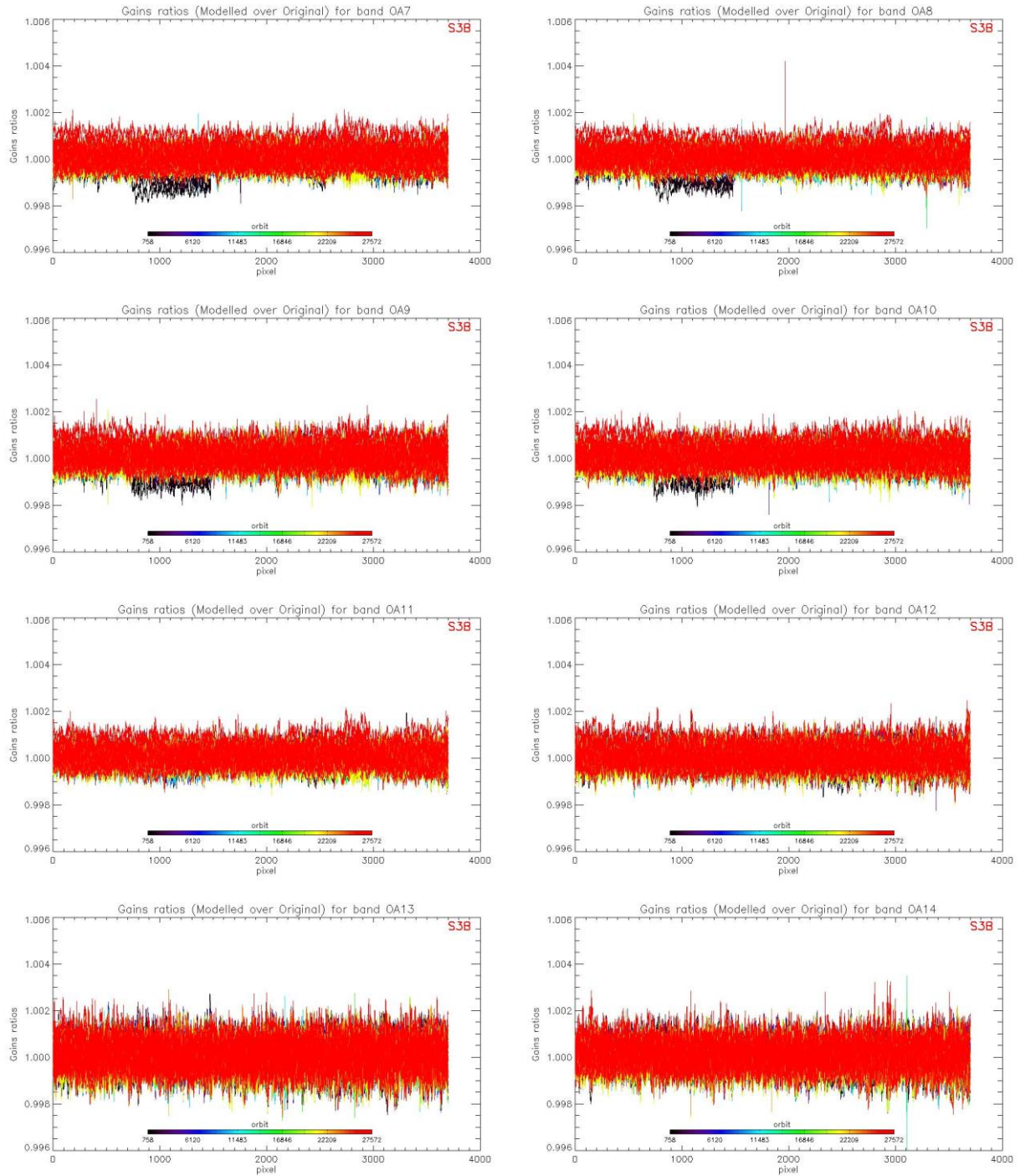


Figure 38: same as Figure 37 for channels Oa7 to Oa14.

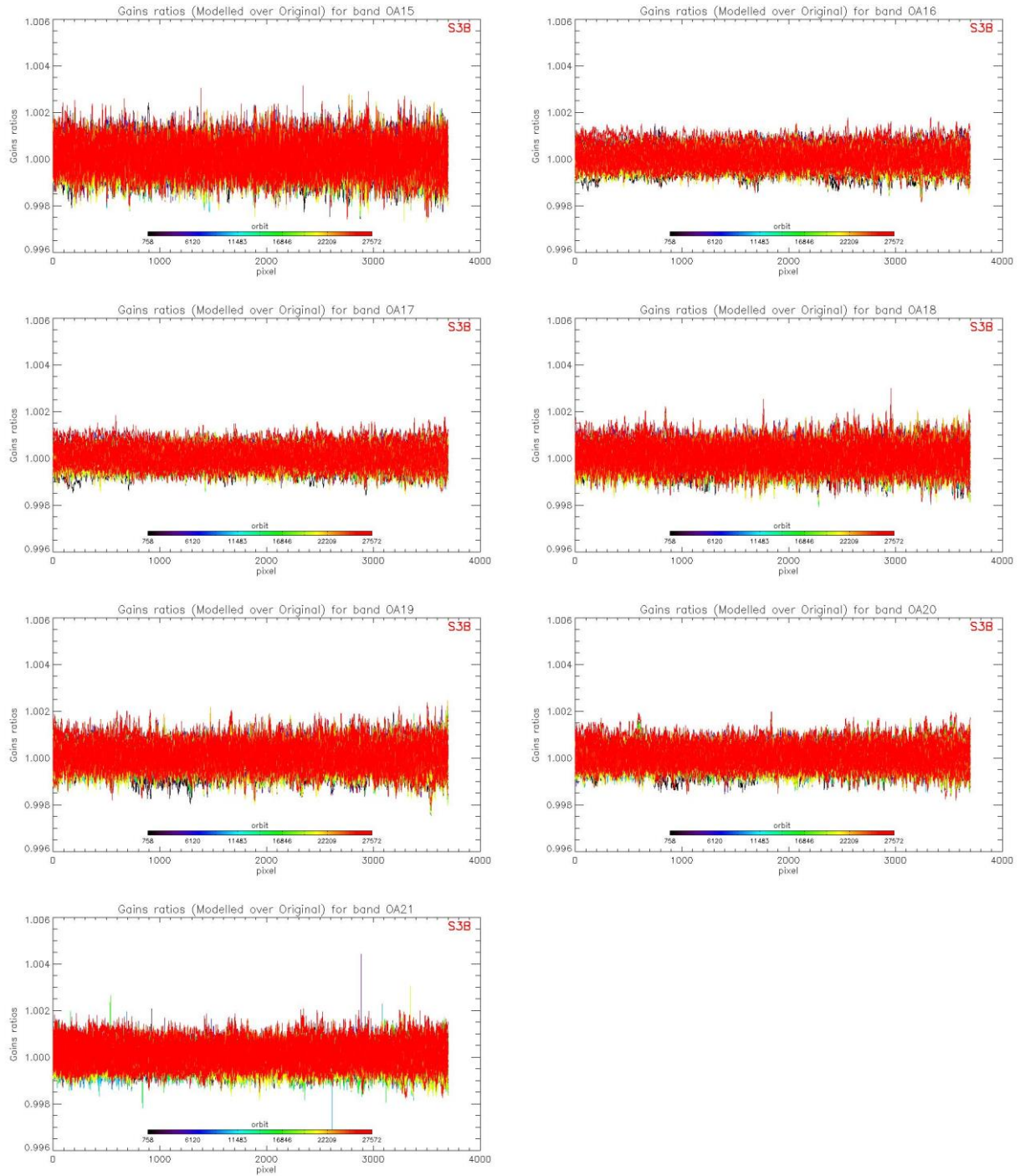
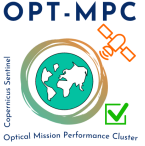


Figure 39: same as for channels Oa15 to Oa21.

	Optical MPC Data Quality Report –Sentinel-3 OLCI August 2023	Ref.: OMPC.ACR.DQR.03.08-2023 Issue: 1.0 Date: 11/09/2023 Page: 36
---	---	---

2.2.4 Ageing of nominal diffuser [OLCI-L1B-CV-240]

2.2.4.1 OLCI-A

There has been no calibration sequence S05 (reference diffuser) for OLCI-A during the current reported period.

Consequently, the last ageing results, presented in July 2023 report, stay valid.

2.2.4.2 OLCI-B

There has been no calibration sequence S05 (reference diffuser) for OLCI-B during the current reported period.

Consequently, the last ageing results, presented in July 2023 report, stay valid.

2.2.5 Updating of calibration ADF [OLCI-L1B-CV-260]

2.2.5.1 OLCI-A

No CAL_AX ADF has been delivered to PDGS during the report period for OLCI-A.

2.2.5.2 OLCI-B

No CAL_AX ADF has been delivered to PDGS during the report period for OLCI-B.

2.3 Spectral Calibration [OLCI-L1B-CV-400]

2.3.1 OLCI-A

There has been one S02+S03 Spectral Calibration for OLCI-A in the current reported period:

- ❖ S02 sequence (diffuser 1) on 11/08/2023 11:10 to 11:12 (absolute orbit 38966)
- ❖ S03 sequence (Erbium doped diffuser) on 11/08/2023 12:51 to 12:53 (absolute orbit 38967)

and one Spectral calibration S09:

- ❖ S09 sequence on 11/08/2023 09:04:44 to 09:04:49 (absolute orbit 38965)

The S02/S03 data have been processed and analysed to assess OLCI-A spectral long-term evolution. The absolute results are presented in Figure 40 while its long-term evolution is presented Figure 41.

The processing of the S09 calibration sequence (spectral calibration using O₂ absorption and Fraunhofer lines) is illustrated in Figure 43.

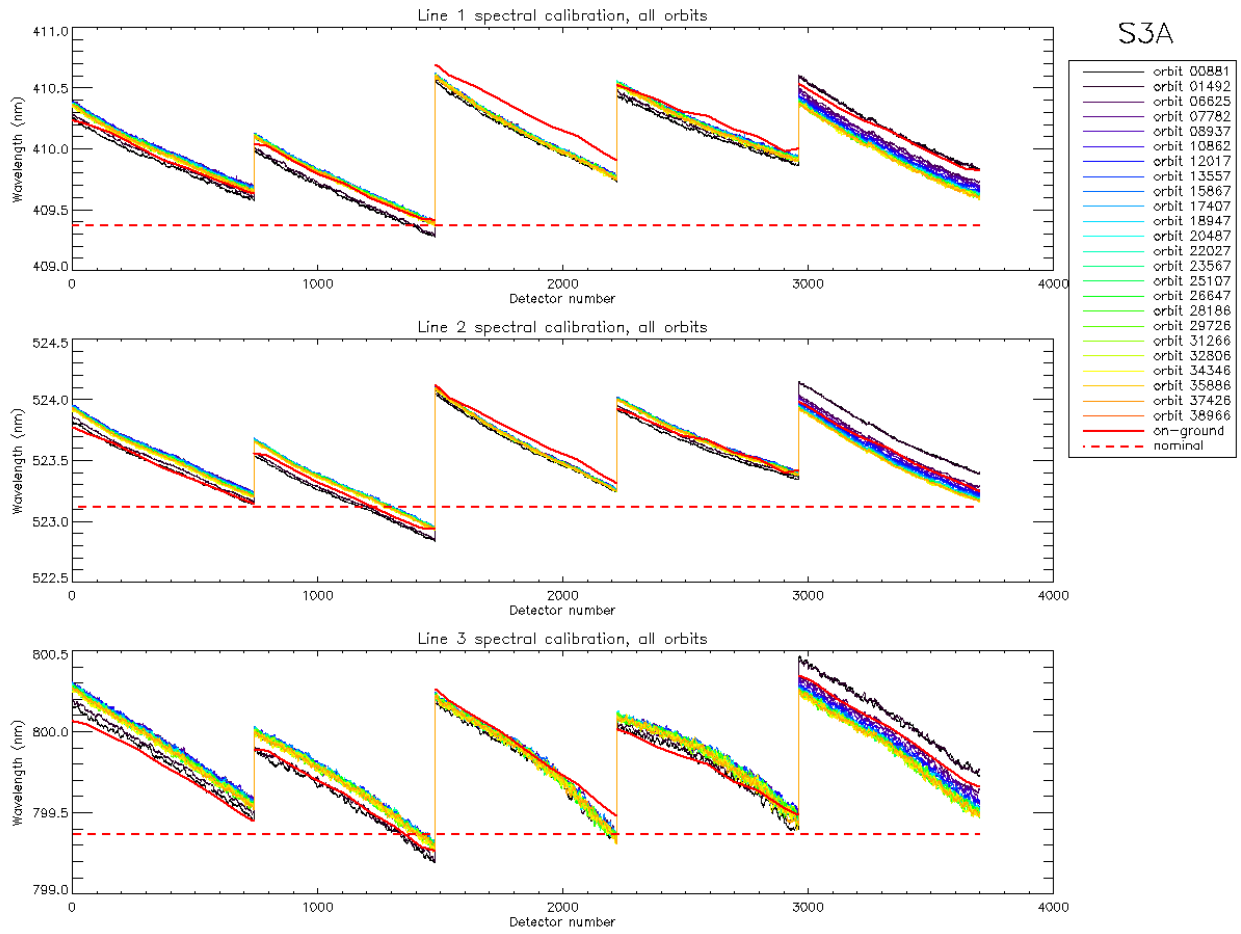


Figure 40: OLCI-A across track spectral calibration from all S02/S03 sequences since the beginning of the mission. Top plot is spectral line 1, middle plot is spectral line 2 and bottom plot spectral line 3. The nominal spectral calibration is plotted as a red horizontal dotted line and the on-ground spectral calibration as a red thick line.

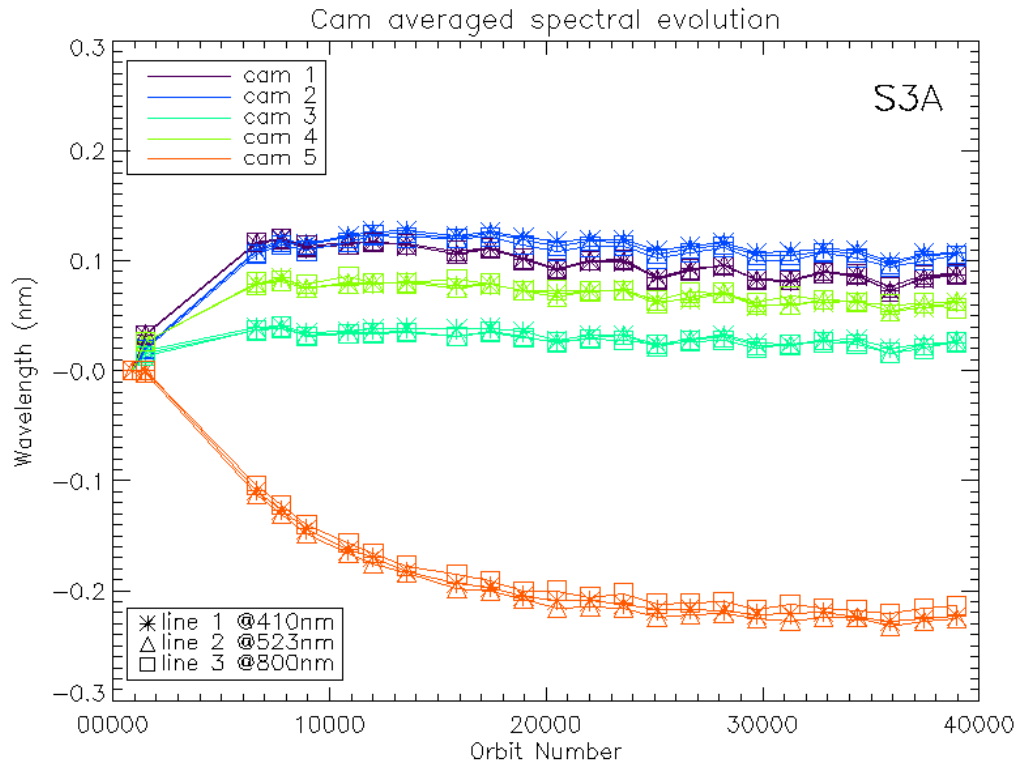


Figure 41: OLCI-A camera averaged spectral calibration evolution as a function of time since launch (all spectral S02/S03 calibrations since the beginning of the mission are included). The data are normalized with the first Spectral Calibration of the plot.

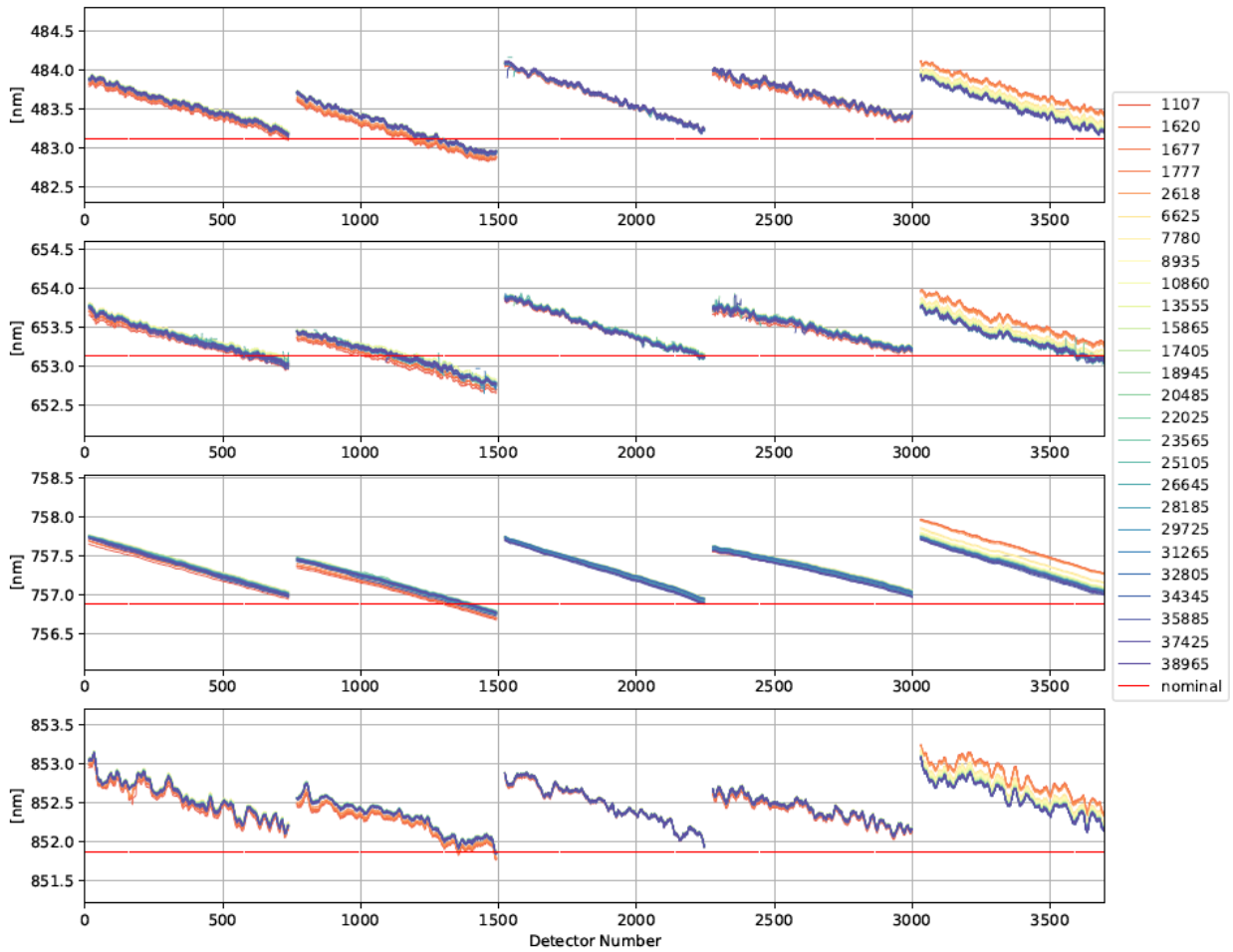


Figure 42: OLCI-A across track spectral calibration from all S09 sequences since the beginning of the mission. The used features are the atmospheric oxygen at 759nm and the Fraunhofer lines at 485nm, 656nm and 854nm. The nominal spectral calibration is plotted as a red dotted line.

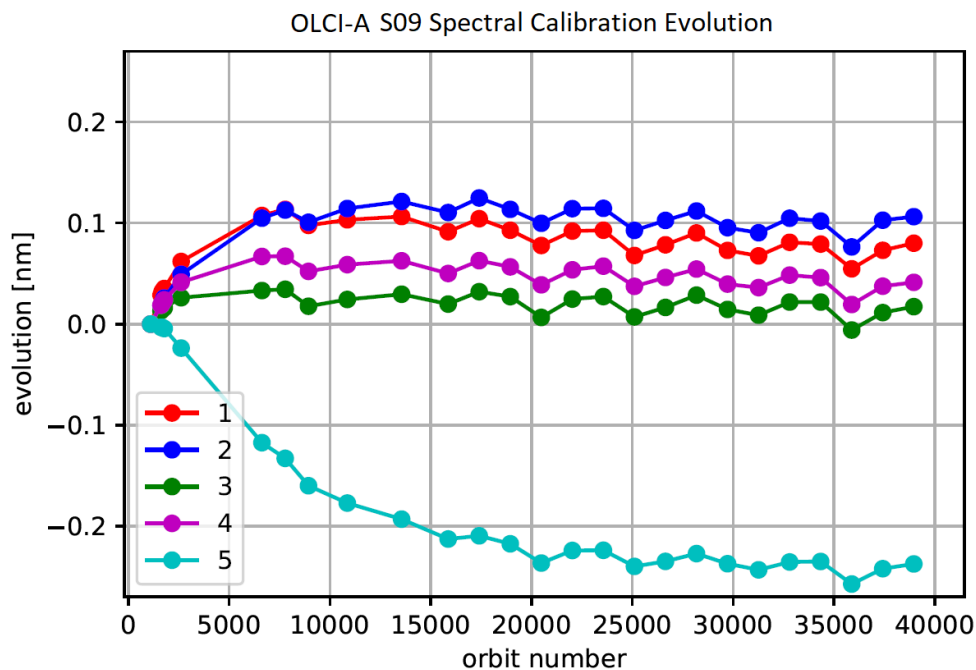


Figure 43: OLCI-A camera averaged spectral calibration evolution as a function of orbit number from S09 calibrations since the 4th of May 2016. The last calibration for S09 is from 11 August 2023. For each camera, the spectral evolution corresponding derived from spectral lines at 485 nm, 656 nm, 770 nm and 854 nm have been averaged. The data are normalized with the first Spectral Calibration of the plot.

We see that the long term evolution of the spectral calibration obtained with sequence S09 (Figure 43) is in rather good agreement with the one obtained with sequence S02/S03 (Figure 41). Indeed, for camera 1, 2, 3 and 4, we observe for the two methods a positive trend of the spectral calibration at the beginning of the mission, which is now rather stabilized (in fact a very small long-term negative trend is now visible), and for camera 5, an obvious negative trend since almost the beginning of the mission which is also stabilizing but more progressively. In all cases, the spectral calibration drift since the beginning of the mission is smaller than ≈ 0.23 nm and the change with respect to the values included in the Auxiliary Data files is less than 0.1 nm. However, camera 5 still evolves but with a slower rate; only further monitoring will allow to assess the need for an evolution of the Auxiliary Parameters impacted by the instrument spectral model, reflecting the current or future state of the instrument.

2.3.2 OLCI-B

There has been one S02+S03 Spectral Calibration for OLCI-B in the reporting period:

- ❖ S02 sequence (diffuser 1) on 21/08/2023 11:13 to 11:15 (absolute orbit 27715)
- ❖ S03 sequence (Erbium doped diffuser) on 21/08/2023 12:54 to 12:56 (absolute orbit 27716)

and one Spectral calibration S09:

- ❖ S09 sequence on 21/08/2023 09:07:00 to 09:07:06 (absolute orbit 27714)

The S02/S03 data have been processed and analyzed to assess OLCI-B spectral long-term evolution. The absolute results are presented in Figure 44, while its long term evolution is presented on Figure 45. The processing of the S09 calibration sequence (spectral calibration using O2 absorption and Fraunhofer lines) is now available and presented in Figure 46 and Figure 47.

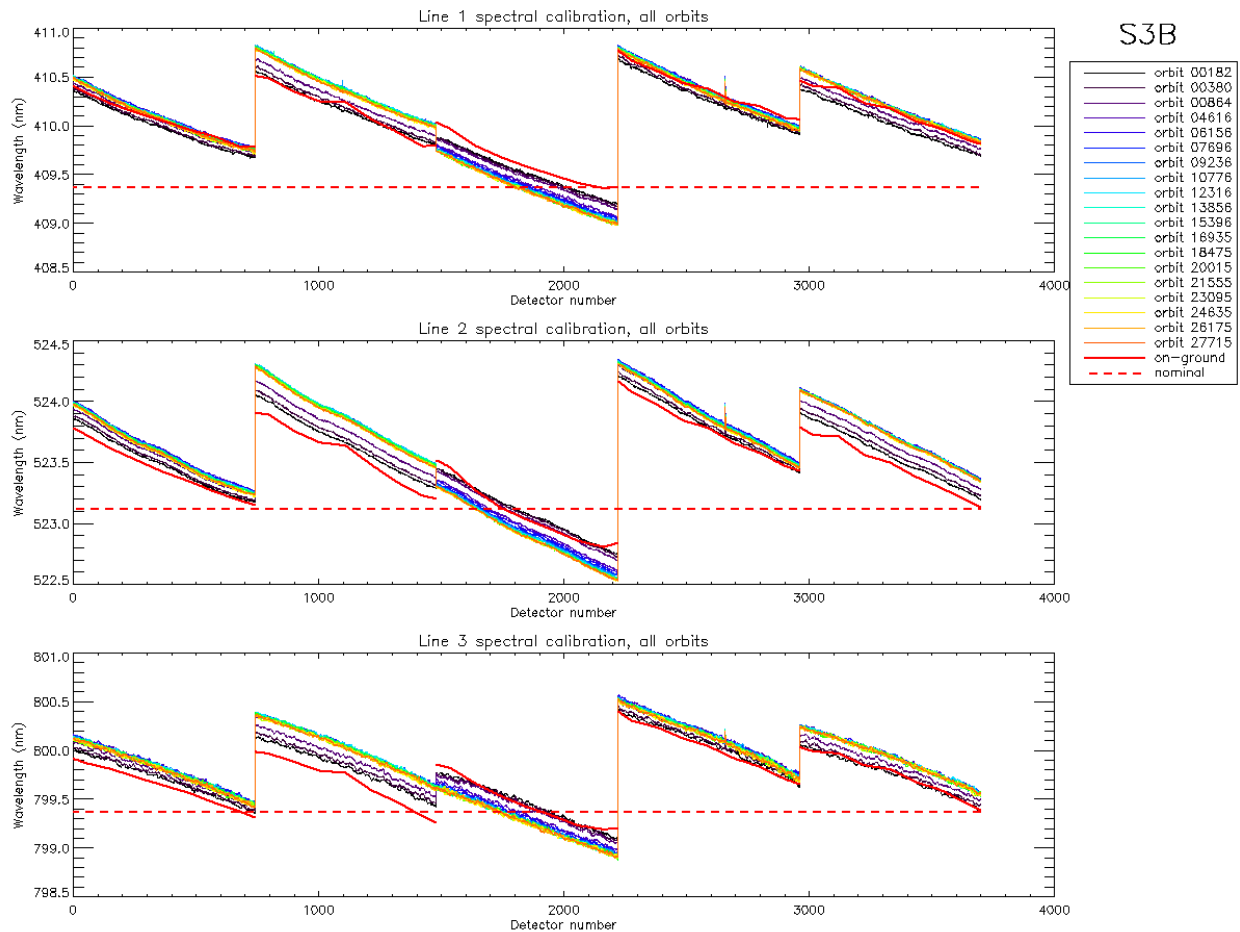


Figure 44: OLCI-B across track spectral calibration from all S02/S03 sequences since the beginning of the mission. Top plot is spectral line 1, middle plot is spectral line 2 and bottom plot spectral line 3. The nominal spectral calibration is plotted as a red dotted line and the on-ground spectral calibration as a red thick line.

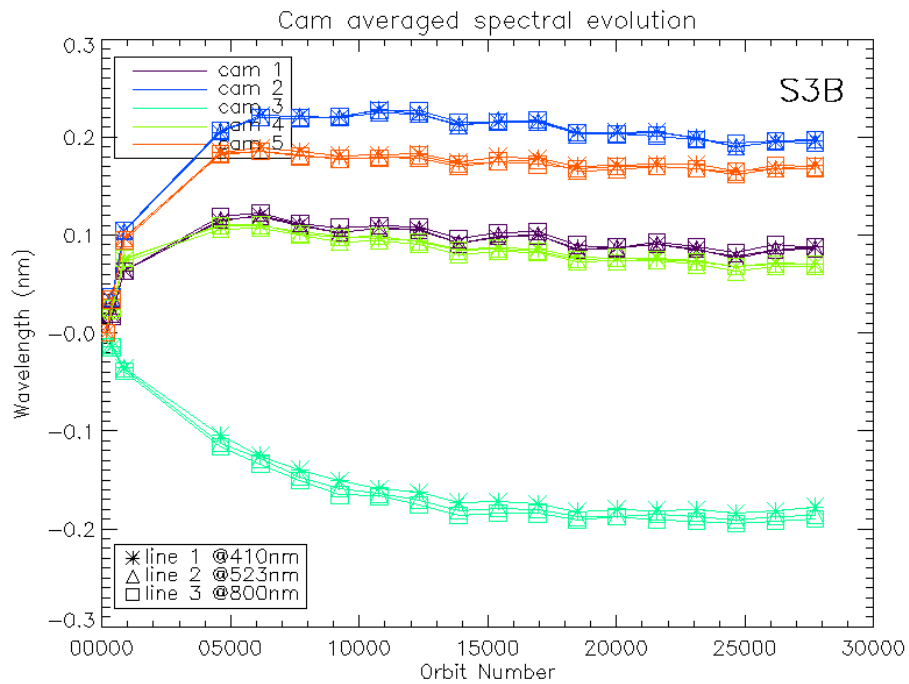


Figure 45: OLCI-B camera averaged spectral calibration evolution as a function of time since launch (all spectral S02/S03 calibrations since the beginning of the mission are included). The data are normalized with the first Spectral Calibration.

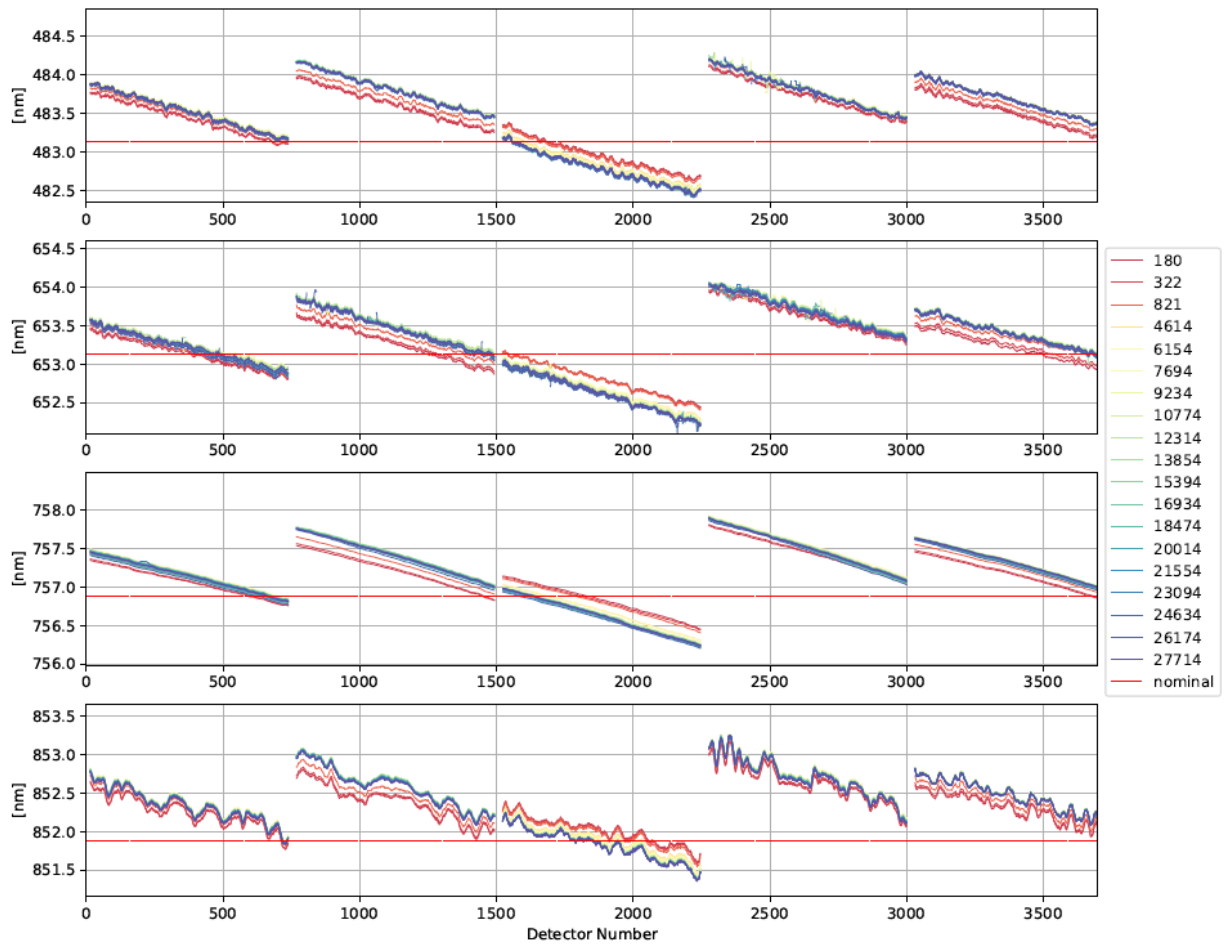


Figure 46: OLCI-B cross track spectral calibration from all (few during commissioning have been left out for the sake of clearness) S09 sequences since the beginning of the mission. The used features are the atmospheric oxygen at 759nm and the Fraunhofer lines at 485nm, 656nm and 854nm. The nominal spectral calibration is plotted as a red dotted line.

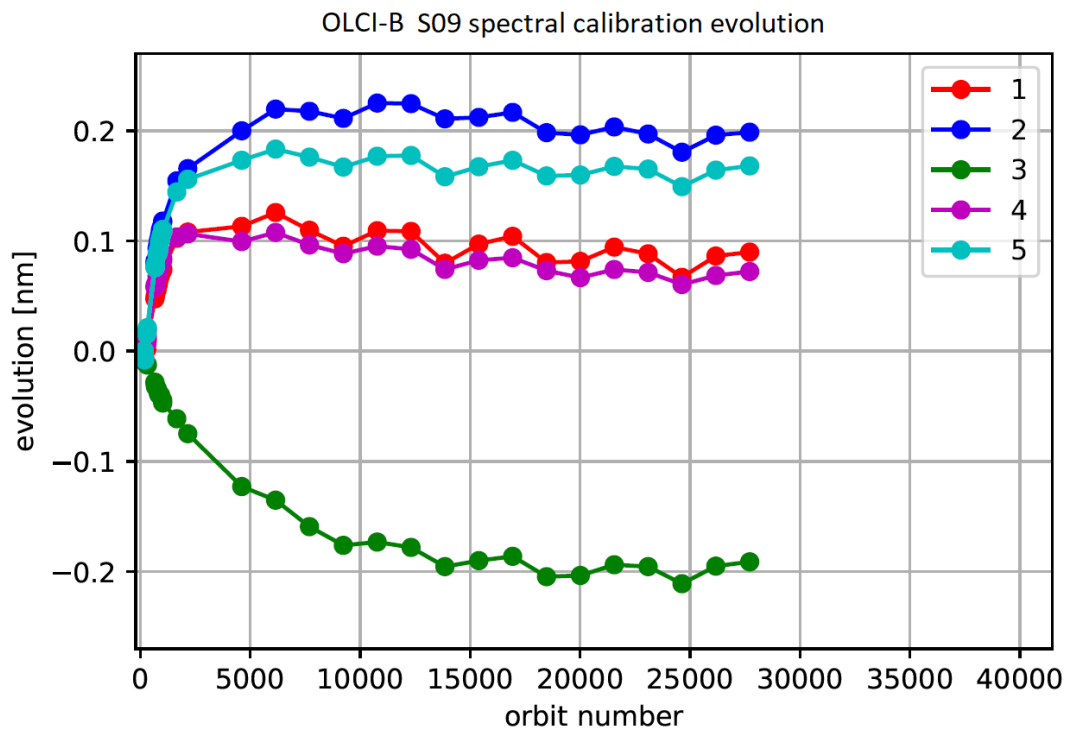


Figure 47: OLCI-B camera averaged spectral calibration evolution as a function of orbit number since launch from S09 calibrations since the beginning of the mission. The last calibration for S09 is from 21 August 2023. For each camera, the spectral evolution corresponding derived from spectral lines at 485 nm, 656 nm, 770 nm and 854 nm have been averaged. The data are normalized with the first Spectral Calibration.

Figure 44 to Figure 47 show that:

- ❖ As for OLCI-A camera 5, the wavelength calibration drift of OLCI-B camera 3 goes in the opposite direction than for the other cameras.
- ❖ It seems that the quick positive drift of the early mission has stabilized for camera 1, 2, 4 and 5 and a very small long-term negative drift is now visible. The stabilization for camera 3 is now also clearly visible even though it took more time to stabilize than for other cameras.
- ❖ The results obtained with the S02/S03 method and the one obtained with the S09 method are rather similar.

The spectral calibration drift is smaller than ≈ 0.23 nm for all cases.

2.4 Signal to Noise assessment [OLCI-L1B-CV-620]

2.4.1 SNR from Radiometric calibration data

2.4.1.1 OLCI-A

SNR computed for all calibration data (S01, S04 and S05 sequences) as a function of band number is presented in Figure 48.

SNR computed for all calibration data as a function of orbit number for band Oa01 (the less stable band) is presented in Figure 49.

There is no significant evolution of this parameter during the current reporting period and the ESA requirement is fulfilled for all bands.

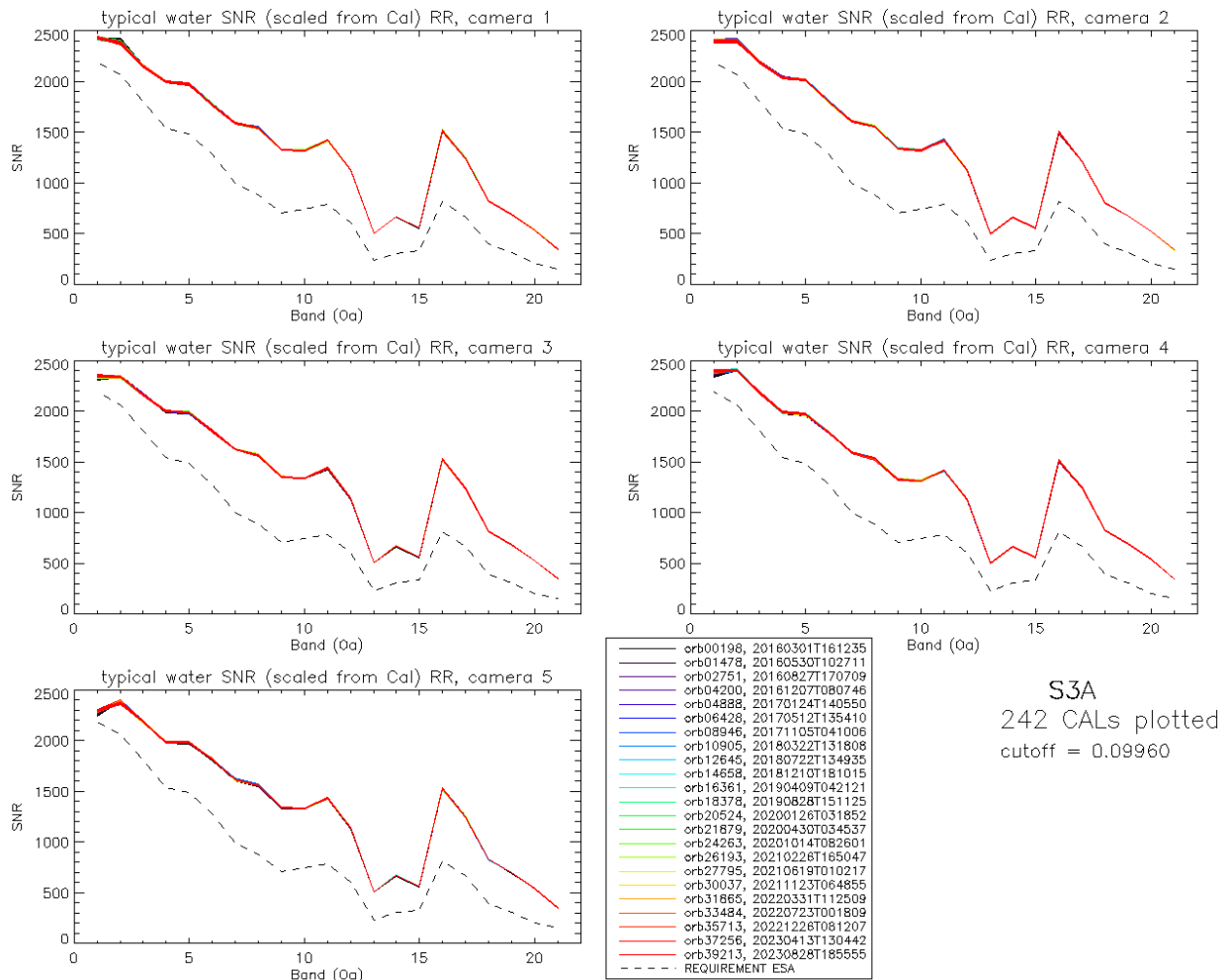


Figure 48: OLCI-A Signal to Noise ratio as a function of the spectral band for the 5 cameras. These results have been computed from radiometric calibration data. All calibrations except first one (orbit 183) are presents with the colours corresponding to the orbit number (see legend). The SNR is very stable with time: the curves for all orbits are almost superimposed. The dashed curve is the ESA requirement.

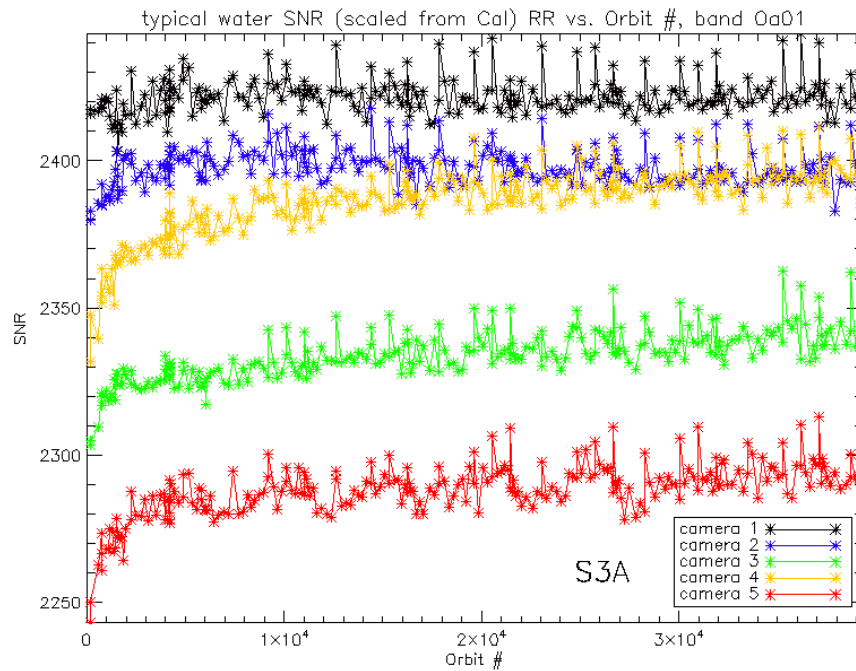


Figure 49: long-term stability of the SNR estimates from Calibration data, example of channel Oa01.

The mission averaged SNR figures are provided in Table 1 below, together with their radiance reference level. According to the OLCI SNR requirements, these figures are valid at these radiance levels and at Reduced Resolution (RR, 1.2 km). They can be scaled to other radiance levels assuming shot noise (CCD sensor noise) is the dominating term, i.e. radiometric noise can be considered Gaussian with its standard deviation varying as the square root of the signal; in other words: $SNR(L) = SNR(L_{ref}) \cdot \sqrt{\frac{L}{L_{ref}}}$. Following the same assumption, values at Full Resolution (300m) can be derived from RR ones as 4 times smaller.

Table 1: OLCI-A SNR figures as derived from Radiometric Calibration data. Figures are given for each camera (time average and standard deviation), and for the whole instrument. The requirement and its reference radiance level are recalled (in $mW.sr^{-1}.m^{-2}.nm^{-1}$).

nm	L _{ref}	SNR	C1		C2		C3		C4		C5		All	
	LU	RQT	avg	std	avg	std	avg	std	avg	std	avg	std	avg	std
400.000	63.0	2188	2421	6.2	2397	6.3	2333	8.5	2385	12.0	2288	9.2	2365	7.0
412.000	74.1	2061	2386	9.6	2402	7.8	2339	5.0	2400	5.0	2379	9.4	2381	6.0
442.000	65.6	1811	2157	6.2	2195	6.2	2163	5.0	2185	4.3	2193	6.0	2179	4.3
490.000	51.2	1541	1999	4.8	2036	4.8	1998	4.3	1984	4.4	1988	4.4	2001	3.1
510.000	44.4	1488	1978	5.3	2014	4.9	1986	4.5	1967	4.3	1985	4.2	1986	3.3
560.000	31.5	1280	1775	4.7	1802	4.1	1803	4.8	1794	3.9	1819	3.3	1798	3.0
620.000	21.1	997	1590	4.1	1608	4.3	1624	3.2	1593	3.3	1615	3.3	1606	2.5
665.000	16.4	883	1545	4.2	1556	4.6	1566	3.9	1533	3.6	1561	3.6	1552	3.0
674.000	15.7	707	1328	3.4	1336	3.8	1350	2.8	1323	3.3	1343	3.3	1336	2.4
681.000	15.1	745	1319	3.7	1325	3.4	1337	2.7	1314	2.5	1334	3.3	1326	2.2
709.000	12.7	785	1420	4.1	1420	4.0	1435	3.4	1414	3.5	1431	3.0	1424	2.7
754.000	10.3	605	1127	3.1	1121	2.8	1136	3.1	1125	2.5	1139	2.6	1130	2.1
761.000	6.1	232	502	1.1	499	1.1	505	1.1	501	1.1	508	1.3	503	0.8
764.000	7.1	305	663	1.5	658	1.5	668	2.0	662	1.5	670	2.0	664	1.2
768.000	7.6	330	558	1.4	554	1.2	563	1.3	557	1.3	564	1.2	559	0.9
779.000	9.2	812	1516	4.6	1498	4.4	1527	5.0	1512	4.8	1527	4.7	1516	4.0
865.000	6.2	666	1243	3.5	1213	3.4	1240	3.8	1247	3.5	1250	2.7	1239	2.7
885.000	6.0	395	823	1.7	801	1.6	814	1.9	824	1.5	831	1.6	819	1.1
900.000	4.7	308	690	1.6	673	1.3	683	1.6	693	1.5	698	1.4	688	1.0
940.000	2.4	203	534	1.2	522	1.2	525	1.0	539	1.1	542	1.3	532	0.7
1020.000	3.9	152	345	0.9	337	0.8	348	0.7	345	0.8	351	0.8	345	0.5

2.4.1.2 OLCI-B

SNR computed for all OLCI-B calibration data (S01, S04 (but not the dark-only S04) and S05 sequences) as a function of band number is presented in Figure 50.

SNR computed for all OLCI-B calibration data as a function of orbit number for band Oa01 (the less stable band) is presented in Figure 51.

As for OLCI-A the SNR is very stable in time. There is no significant evolution of this parameter during the current reporting and the ESA requirement is fulfilled for all bands.

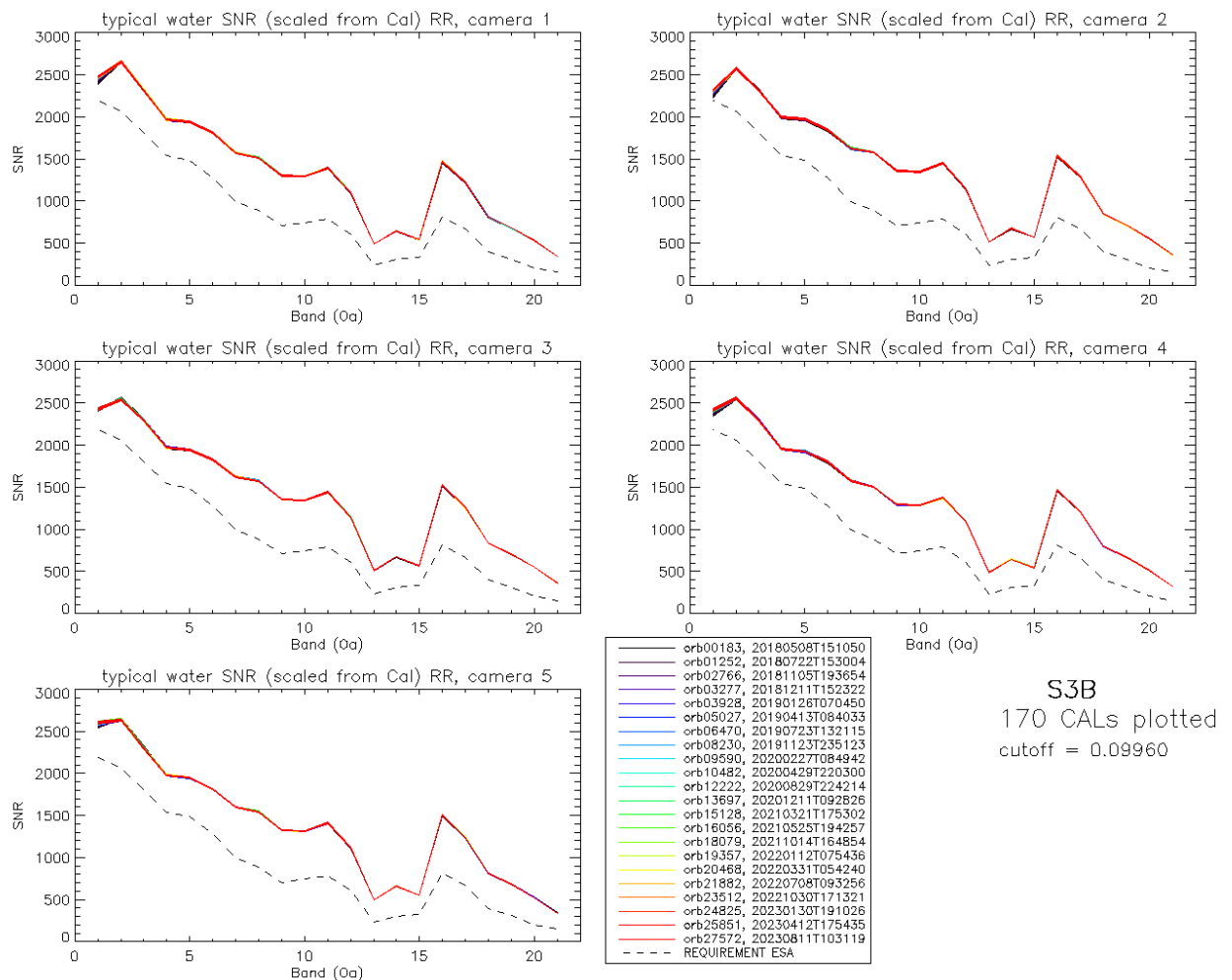


Figure 50: OLCI-B Signal to Noise ratio as a function of the spectral band for the 5 cameras. These results have been computed from radiometric calibration data. All calibrations except first one (orbit 167) are presents with the colours corresponding to the orbit number (see legend). The SNR is very stable with time: the curves for all orbits are almost superimposed. The dashed curve is the ESA requirement.

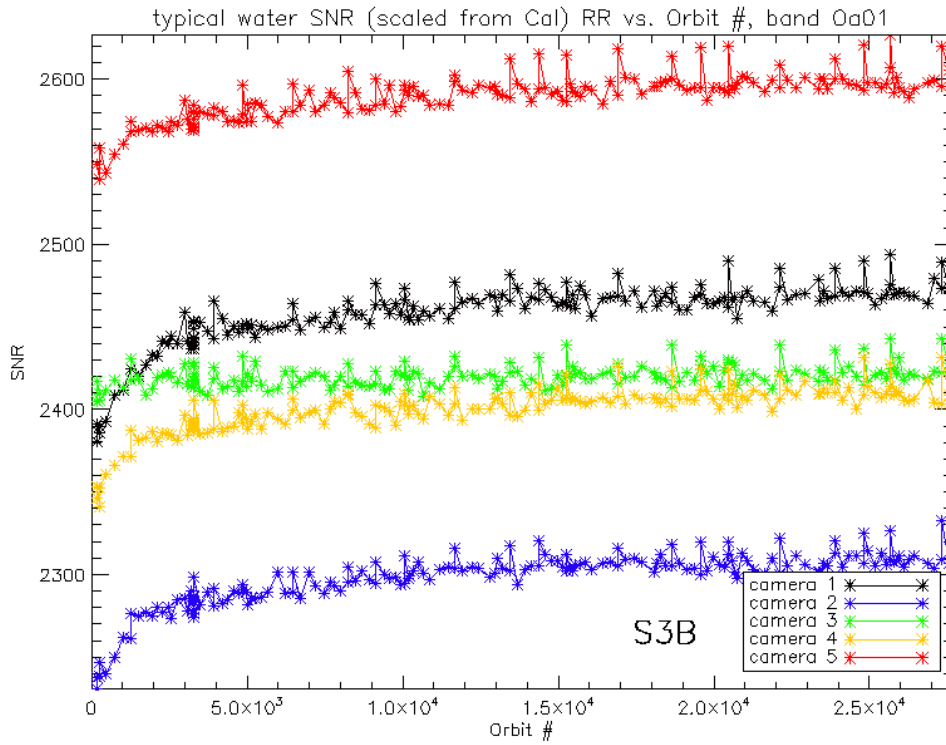


Figure 51: long-term stability of the OLCI-B SNR estimates from Calibration data, example of channel Oa1.

Table 2: OLCI-B SNR figures as derived from Radiometric Calibration data. Figures are given for each camera (time average and standard deviation), and for the whole instrument. The requirement and its reference radiance level are recalled (in $mW.sr^{-1}.m^{-2}.nm^{-1}$).

nm	L _{ref}	SNR	C1		C2		C3		C4		C5		All	
			avg	std	avg	std	avg	std	avg	std	avg	std	avg	std
400.000	63.0	2188	2458	18.6	2297	16.5	2420	6.8	2400	14.0	2589	14.3	2433	13.1
412.000	74.1	2061	2654	7.1	2569	6.6	2542	8.9	2550	6.5	2636	7.9	2590	5.8
442.000	65.6	1811	2323	6.8	2315	6.5	2298	7.1	2301	7.1	2307	6.8	2309	5.9
490.000	51.2	1541	1966	4.8	1990	5.6	1971	5.1	1952	4.7	1979	4.5	1972	3.9
510.000	44.4	1488	1939	4.8	1968	6.0	1942	5.0	1925	4.9	1952	4.8	1945	4.1
560.000	31.5	1280	1813	4.7	1848	4.8	1829	4.6	1805	4.7	1817	3.9	1822	3.5
620.000	21.1	997	1572	4.3	1626	4.6	1624	3.9	1576	3.6	1600	3.6	1600	3.0
665.000	16.4	883	1513	4.1	1578	3.8	1573	3.8	1501	3.0	1546	3.6	1542	2.8
674.000	15.7	707	1300	3.9	1358	3.6	1353	3.1	1292	2.7	1328	2.9	1326	2.4
681.000	15.1	745	1293	3.5	1347	3.3	1343	3.0	1285	2.8	1316	2.9	1317	2.2
709.000	12.7	785	1390	4.0	1447	4.0	1443	4.1	1373	2.9	1412	3.7	1413	3.0
754.000	10.3	605	1096	3.5	1143	3.6	1142	3.3	1089	2.8	1116	3.1	1117	2.8
761.000	6.1	232	488	1.2	509	1.2	509	1.4	486	1.2	498	1.3	498	0.9
764.000	7.1	305	643	1.6	673	2.0	672	1.8	641	1.8	658	1.8	657	1.5
768.000	7.6	330	541	1.4	568	1.4	564	1.3	541	1.3	555	1.5	554	1.0
779.000	9.2	812	1467	4.1	1535	4.6	1527	5.1	1468	4.0	1507	4.1	1501	3.7
865.000	6.2	666	1221	3.5	1288	3.7	1258	3.6	1206	3.5	1238	2.8	1242	2.7
885.000	6.0	395	808	2.2	848	1.9	834	1.9	799	1.8	815	2.1	821	1.5
900.000	4.7	308	679	1.5	714	1.9	704	1.7	670	1.5	683	1.5	690	1.2
940.000	2.4	203	527	1.3	549	1.6	551	1.2	510	1.1	522	1.3	532	0.9
1020.000	3.9	152	336	0.8	358	1.2	358	0.8	318	0.7	338	0.9	342	0.6

2.5 Geometric Calibration/Validation

2.5.1 OLCI-A

OLCI-A georeferencing performance is compliant since the introduction of MPC Geometric Calibration, put in production on the 14th of March 2018. It has however significantly improved after its last full revision of GCMs (Geometric Calibration Models, or platform to instrument alignment quaternions) and IPPVMs (Instrument Pixels Pointing Vectors) both derived using the GeoCal Tool and put in production on 30/07/2019.

The following figures (Figure 52 to Figure 57) show time series of the overall RMS performance (requirement criterion) and of the across-track and along-track biases for each camera. New plots (Figure 58 and Figure 59) introduce monitoring of the performance homogeneity within the field of view: georeferencing errors in each direction at camera transitions (difference between last pixel of camera N and first pixel of camera N+1) and within a given camera (maximum bias minus minimum inside each camera). The performance improvement since the 30/07/2019 is significant on most figures: the global RMS value decreases from around 0.35 to about 0.2 (Figure 52), the across-track biases decrease significantly for all cameras (Figure 53 to Figure 57), the along-track bias reduces for at least camera 3 (Figure 55) and the field of view homogeneity improves drastically (Figure 58 and Figure 59, but also reduction of the dispersion – distance between the ± 1 sigma lines – in Figure 53 to Figure 57).

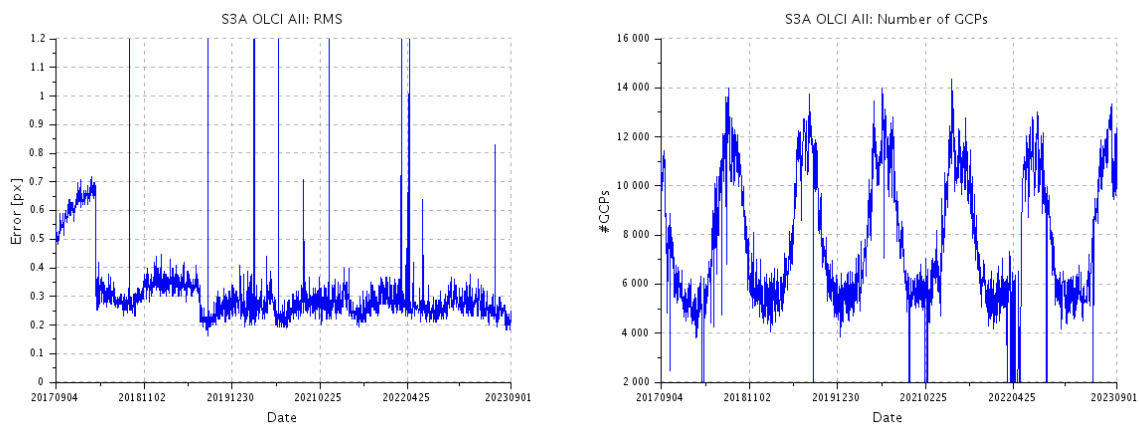


Figure 52: overall OLCI-A georeferencing RMS performance time series (left) and number of validated control points corresponding to the performance time series (right) over the whole monitoring period

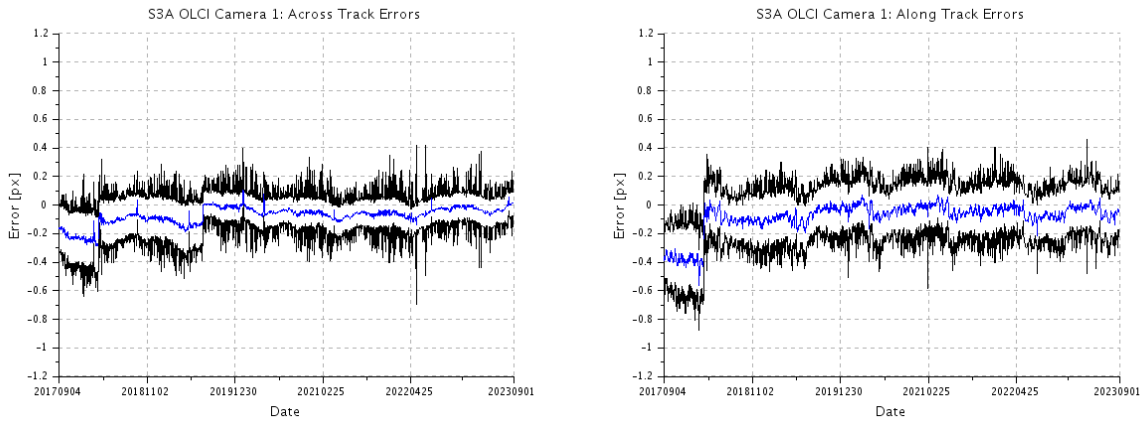


Figure 53: cross-track (left) and along-track (right) OLCI-A georeferencing biases time series for Camera 1. Blue line is the average, black lines are average plus and minus 1 sigma.

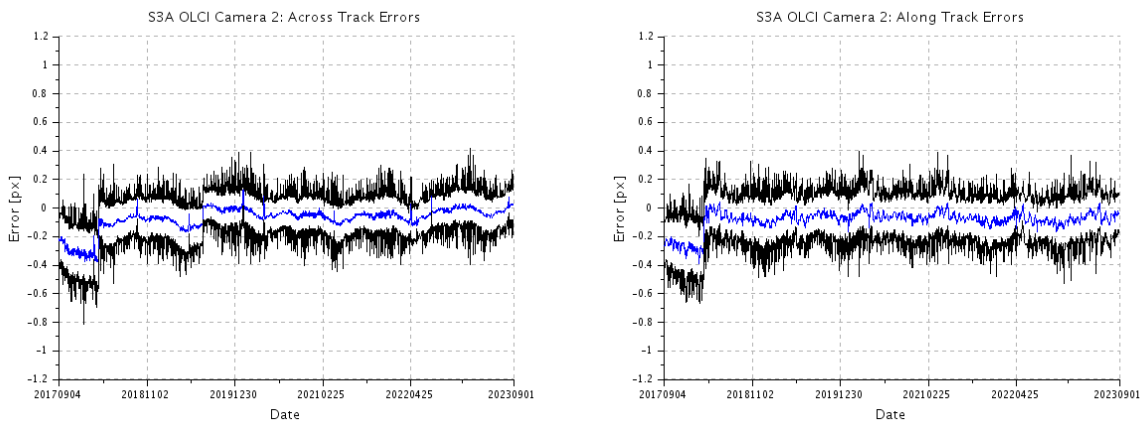


Figure 54: same as Figure 53 for Camera 2.

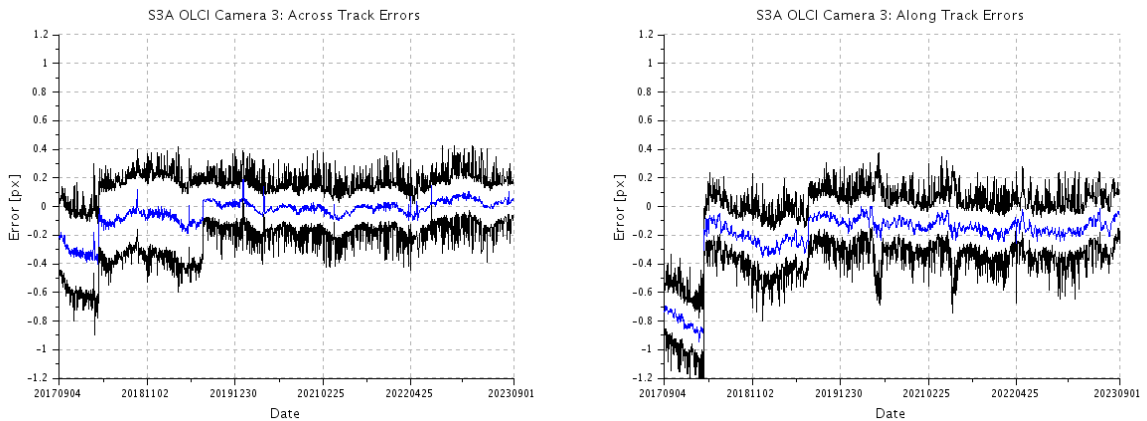


Figure 55: same as Figure 53 for Camera 3.

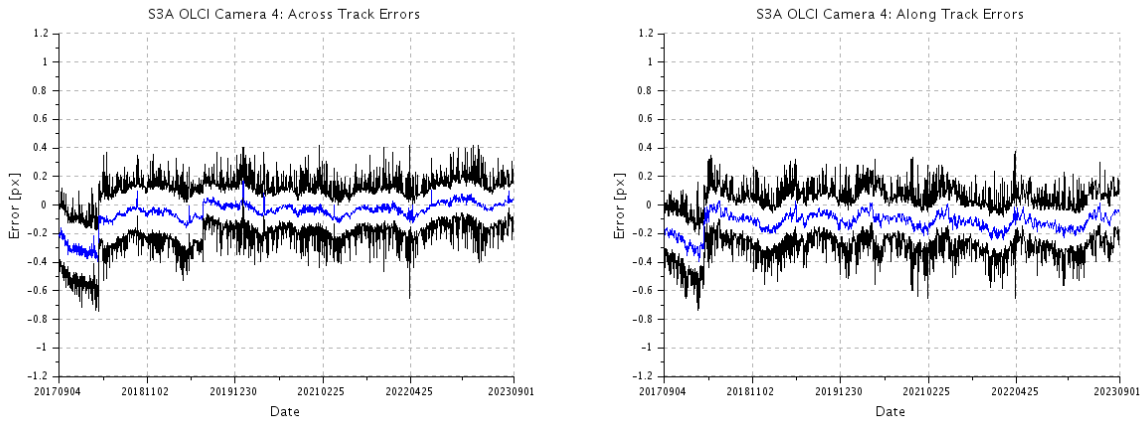


Figure 56: same as Figure 53 for Camera 4.

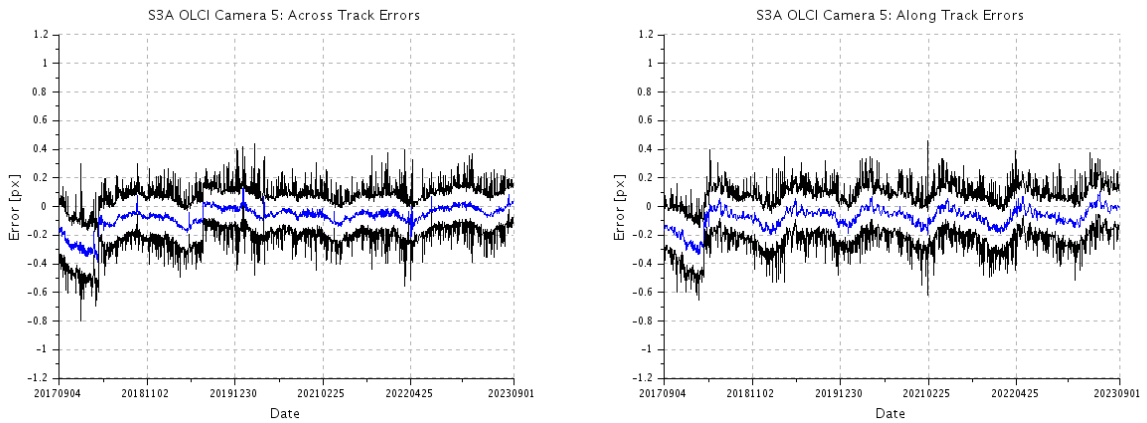


Figure 57: same as Figure 53 for Camera 5.

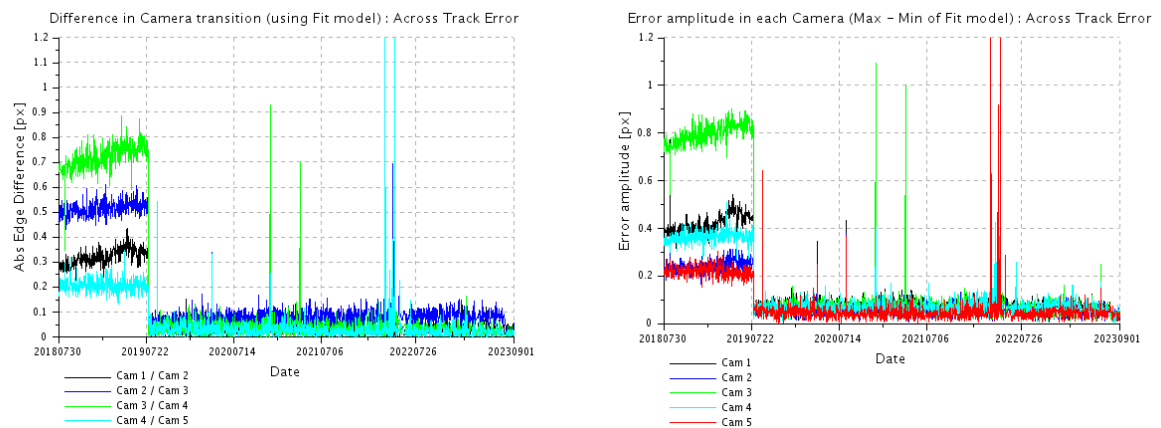


Figure 58: OLCI-A spatial across-track misregistration at each camera transition (left) and maximum amplitude of the across-track error within each camera (left).

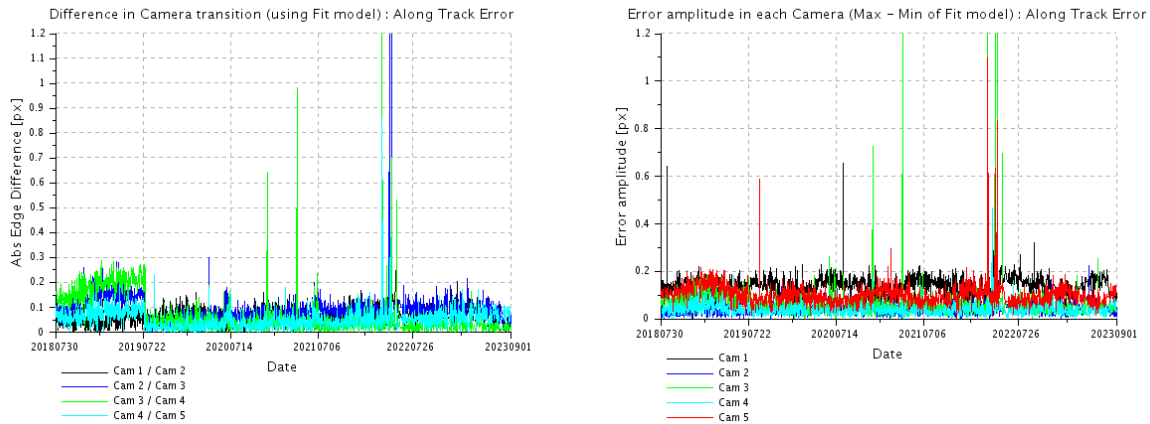


Figure 59: OLCI-A spatial along-track misregistration at each camera transition (left) and maximum amplitude of the along-track error within each camera (left).

2.5.2 OLCI-B

Georeferencing performance of OLCI-B improved significantly with the fourth geometric calibration introduced the 30/07/2019. However, the instrument pointing is still evolving, in particular for camera 2 (Figure 66) and a new geometric calibration has been done and introduced in the processing chain on the 16th of April 2020. Its impact is significant on the along-track biases of all cameras (Figure 61 to Figure 65), but also on the continuity at camera interfaces (Figure 66, left) and on intra-camera homogeneity (Figure 66, right). Since then, further adjustments to the geometric calibration have been introduced, mainly to correct the along-track drifts. The most recent was put in production on 29/07/2021 and its effect can be seen e.g. on left graphs of Figure 62, Figure 63 and Figure 65 (across-track biases of cameras 2, 3 & 5).

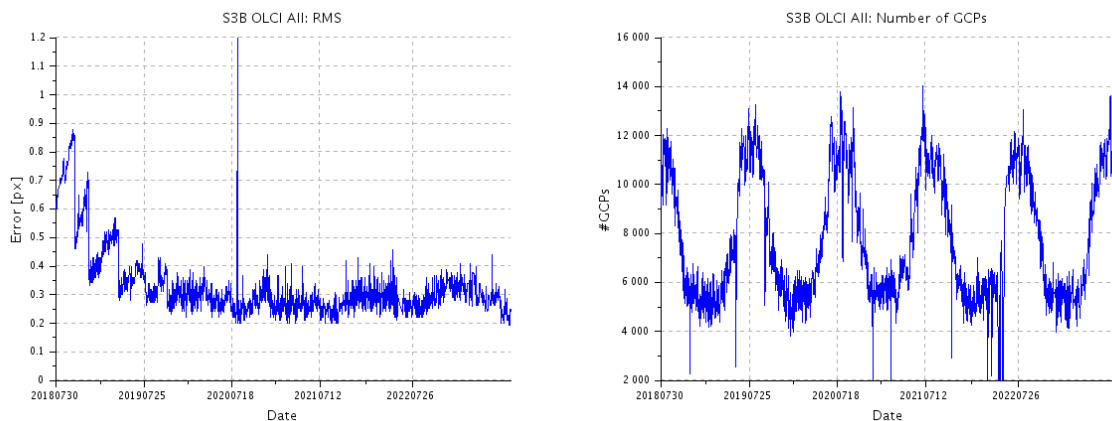


Figure 60: overall OLCI-B georeferencing RMS performance time series over the whole monitoring period (left) and corresponding number of validated control points (right)

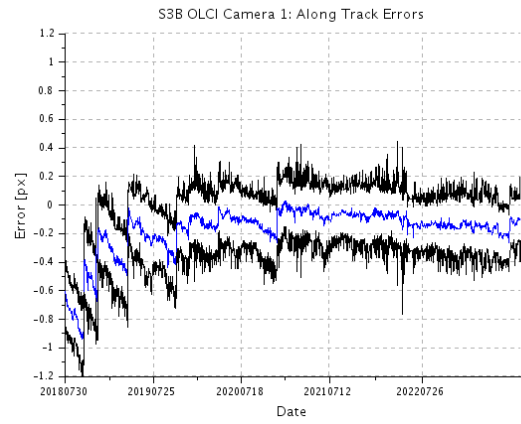
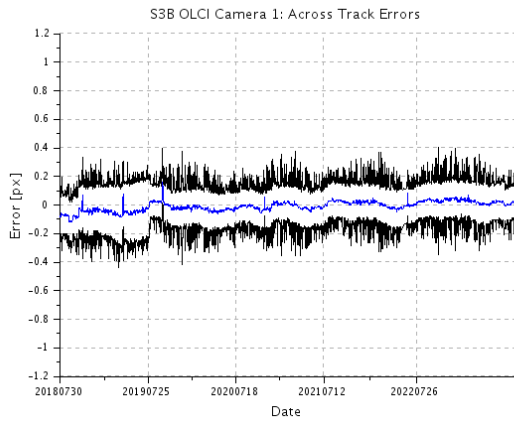


Figure 61: across-track (left) and along-track (right) OLCI-B georeferencing biases time series for Camera 1.

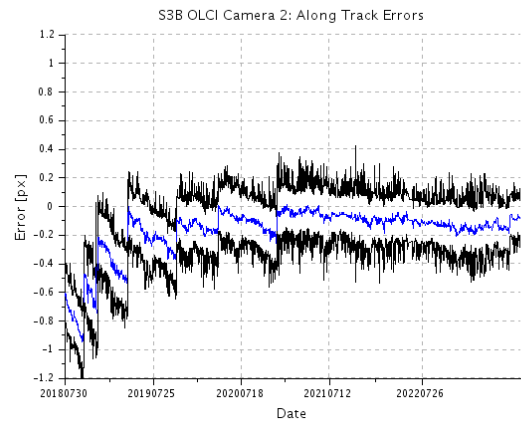
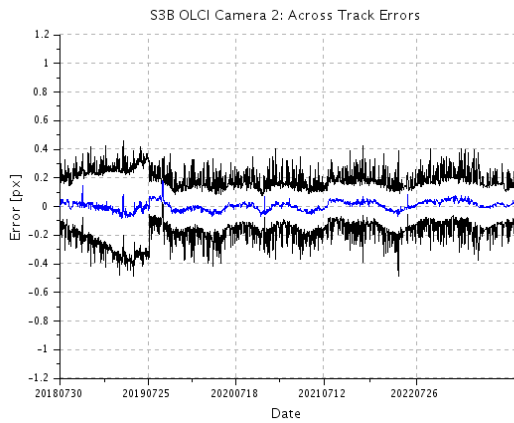


Figure 62: same as Figure 61 for Camera 2.

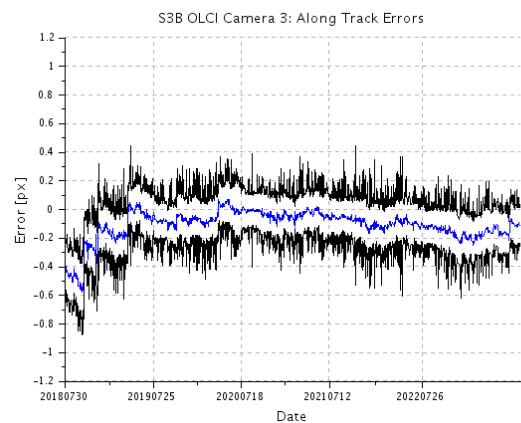
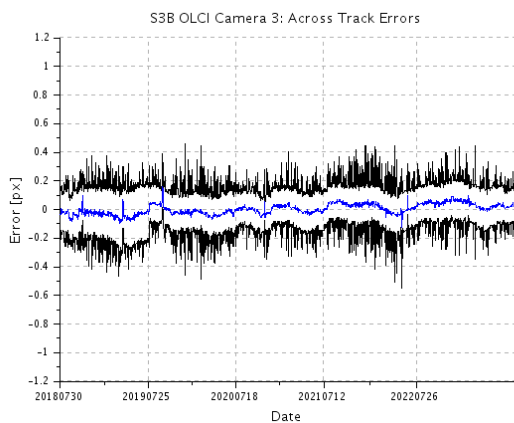


Figure 63: same as Figure 61 for Camera 3.

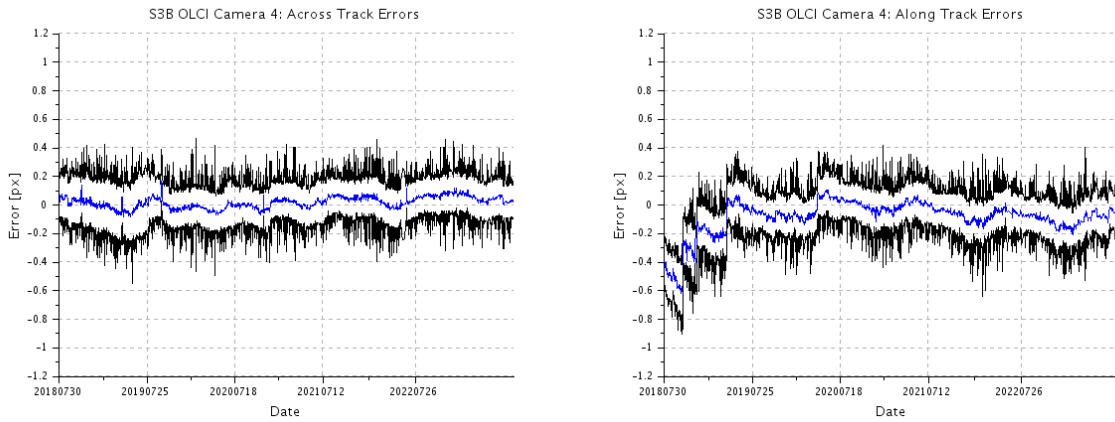


Figure 64: same as Figure 61 for Camera 4.

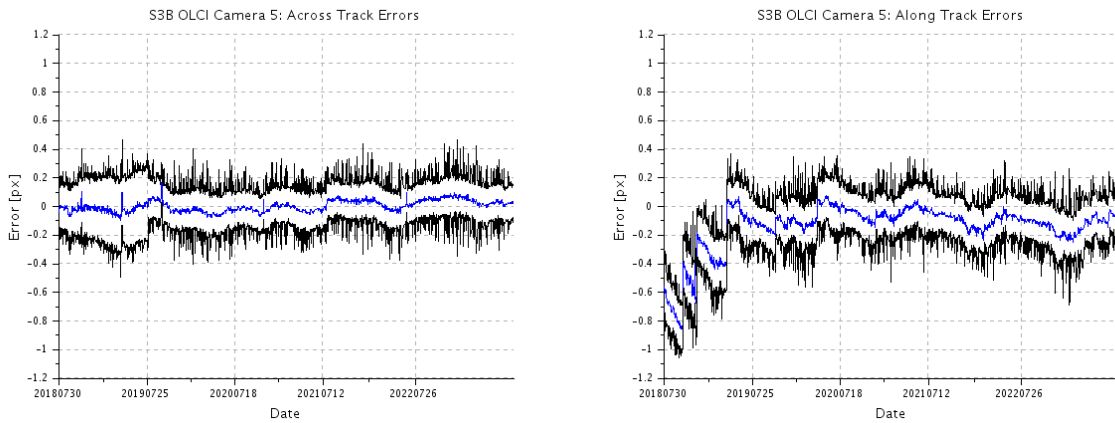


Figure 65: same as Figure 61 for Camera 5.

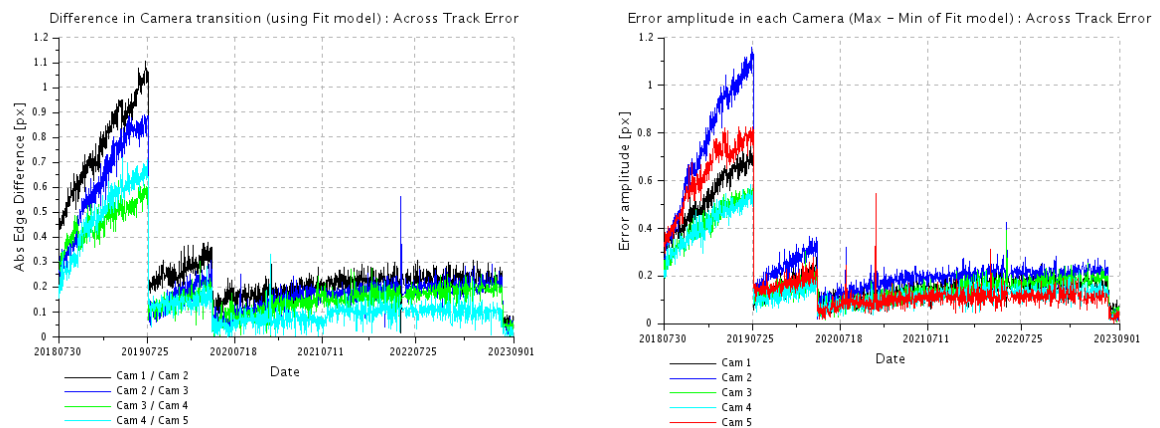


Figure 66: OLCI-B spatial across-track misregistration at each camera transition (left) and maximum amplitude of the across-track error within each camera (left).

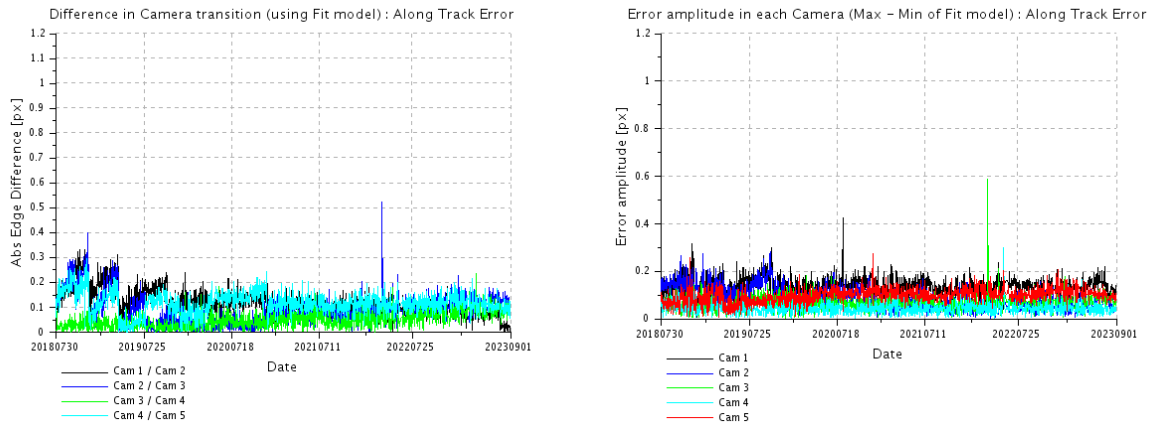



Figure 67: OLCI-B spatial along-track misregistration at each camera transition (left) and maximum amplitude of the along-track error within each camera (left).

	<p>Optical MPC</p> <p>Data Quality Report –Sentinel-3 OLCI</p> <p>August 2023</p>	<p>Ref.: OMPC.ACR.DQR.03.08-2023</p> <p>Issue: 1.0</p> <p>Date: 11/09/2023</p> <p>Page: 58</p>
---	--	--

3 OLCI Level 1 Product validation

3.1 [OLCI-L1B-CV-300], [OLCI-L1B-CV-310] – Radiometric Validation

3.1.1 S3ETRAC Service

Activities done

The S3ETRAC service extracts OLCI L1 RR and SLSTR L1 RBT data and computes associated statistics over 49 sites corresponding to different surface types (desert, snow, ocean maximizing Rayleigh signal, ocean maximizing sunglint scattering and deep convective clouds). The S3ETRAC products are used for the assessment and monitoring of the L1 radiometry (optical channels) by the ESLs.

All details about the S3ETRAC/OLCI and S3ETRAC/SLSTR statistics are provided on the S3ETRAC website <http://s3etrac.acri.fr/index.php?action=generalstatistics>.

- ❖ Number of OLCI products processed by the S3ETRAC service
- ❖ Statistics per type of target (DESERT, SNOW, RAYLEIGH, SUNGLINT and DCC)
- ❖ Statistics per sites
- ❖ Statistics on the number of records

For illustration, we provide below statistics on the number of S3ETRAC/OLCI records generated per type of targets (DESERT, SNOW, RAYLEIGH, SUNGLINT and DCC) for both OLCI-A (Figure 68) and OLCI-B (Figure 69).

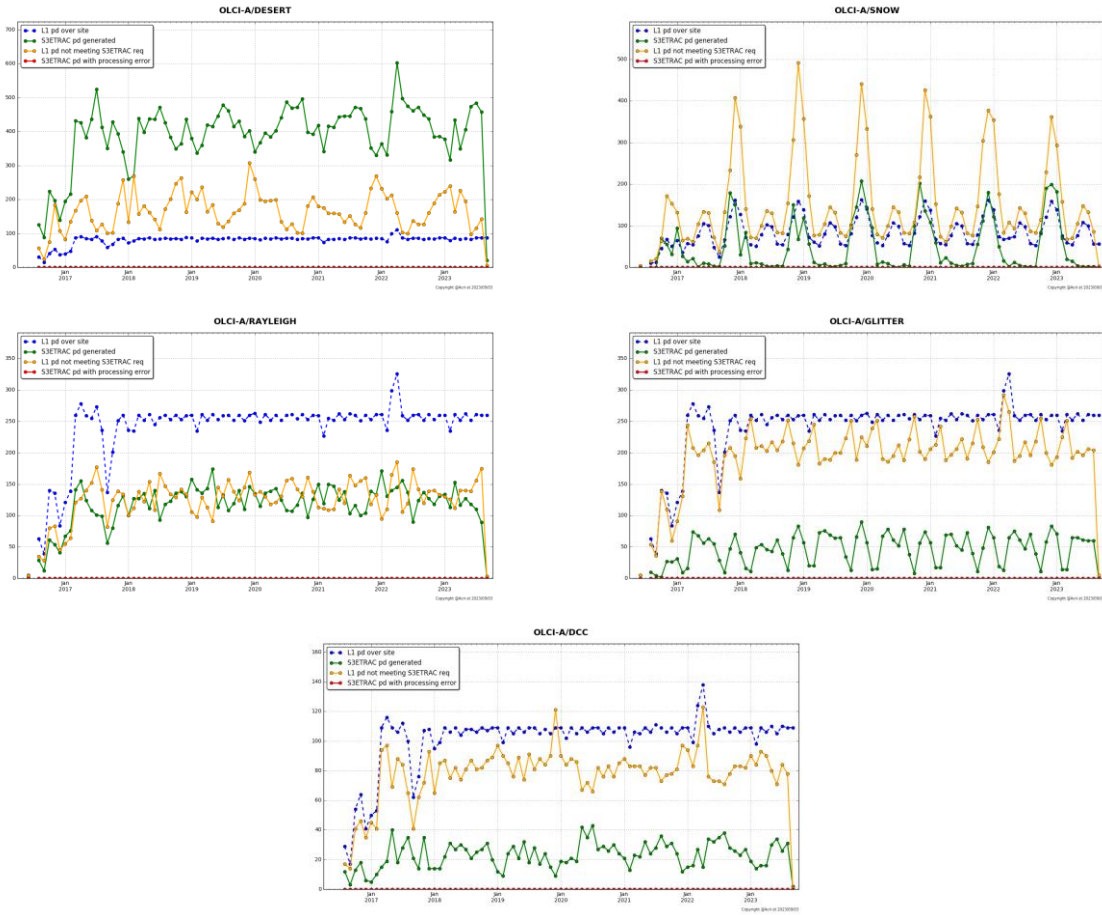


Figure 68: summary of S3ETRAC products generation for OLCI-A (number of OLCI-A L1 products Ingested, blue – number of S3ETRAC extracted products generated, green – number of S3ETRAC runs without generation of output product (data not meeting selection requirements), yellow – number of runs ending in error, red, one plot per site type).

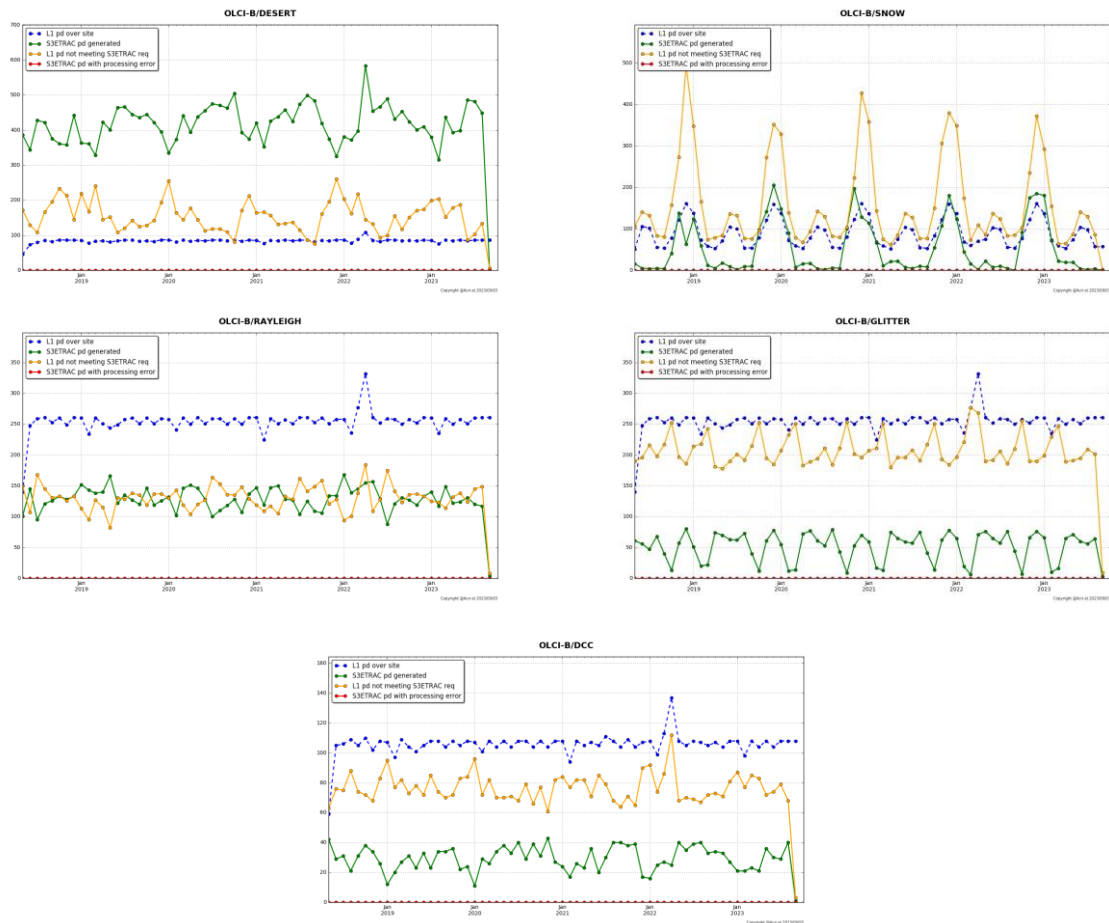


Figure 69: summary of S3ETRAC products generation for OLCI-B
(number of OLCI-B L1 products Ingested, yellow – number of S3ETRAC extracted products generated, blue – number of S3ETRAC runs without generation of output product (data not meeting selection requirements), green – number of runs ending in error, red, one plot per site type).

3.1.2 Radiometric validation with DIMITRI

OLCI-A and OLCI-B L1B radiometry verification has been processed as follow:

- ❖ The verification is performed over Ocean-sites and over Desert-sites **until the 30th of August 2023**.
- ❖ All results from OLCI-A and OLCI-B over Rayleigh, Glint and PICS are consistent with the previous reporting period over the used CalVal sites.
- ❖ Good stability of both sensors OLCI-A and OLCI-B could be observed, nevertheless the time-series average shows higher reflectance from OLCI-A.
- ❖ Bands with high gaseous absorption are excluded.

3.1.2.1 Verification and Validation over PICS

1. The ingestion of all the available L1B-LN1-NT products from OLCI-A and OLCI-B over the 6 desert CalVal-sites (Algeria3 & 5, Libya 1 & 4 and Mauritania 1 & 2) has been performed until the **30th of August 2023**.
2. The results are consistent over all the six used PICS sites (Figure 70 and Figure 71). Both sensors show a good stability over the analysed period.
3. The temporal average over the period **January - 30th of August 2023** of the elementary ratios (observed reflectance to the simulated one) for **OLCI-A** shows gain values between 2-4% over all the VNIR bands (Figure 72). Unlikely, the temporal average over the same period of the elementary ratios for **OLCI-B** shows gain values within 2% (mission requirements) over the VNIR spectral range (Figure 72). The spectral bands with significant absorption from water vapor and O₂ (Oa11, Oa13, Oa14, Oa15 and Oa20) are excluded.

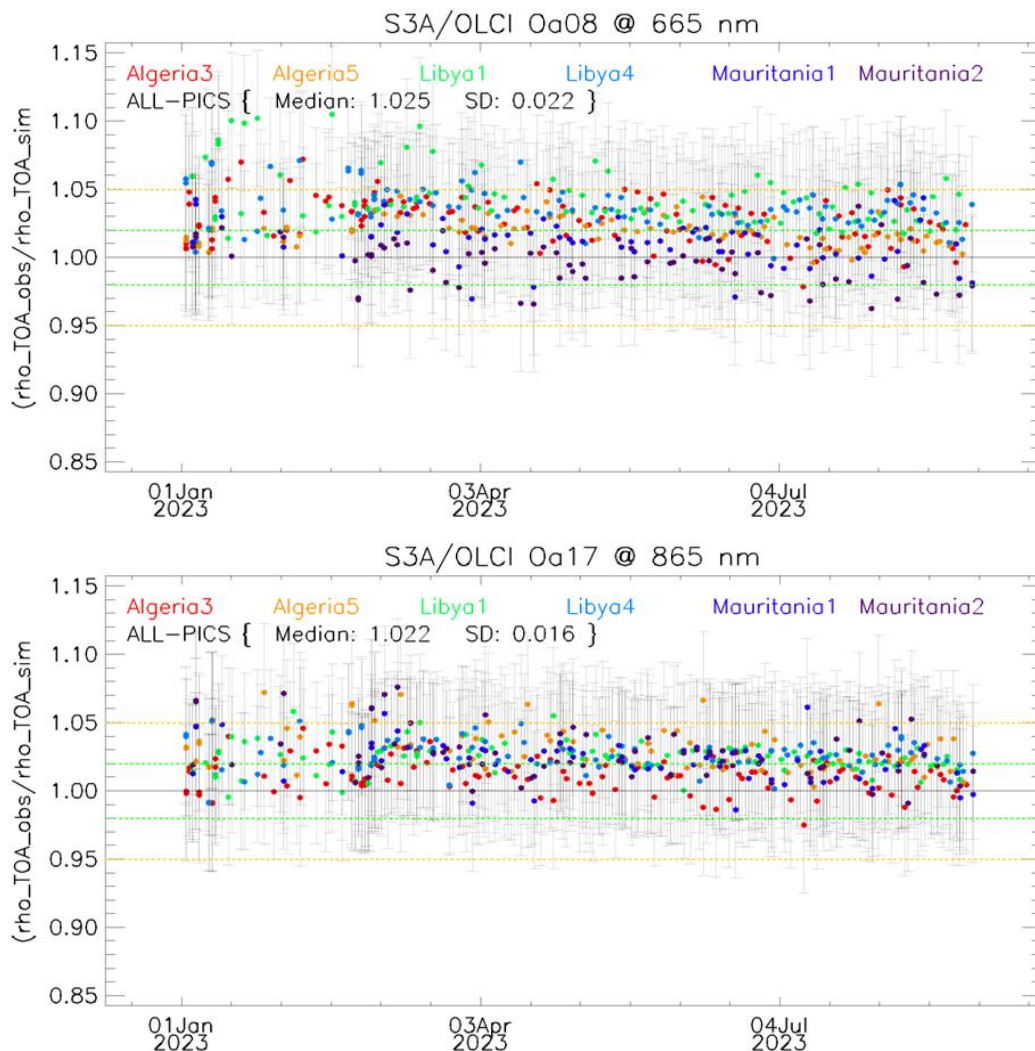


Figure 70: Time-series of the elementary ratios (observed/simulated) signal from OLCI-A for (top to bottom) bands Oa03 and Oa17 respectively over January – August 2023 from the six PICS Cal/Val sites. Dashed-green and orange lines indicate the 2% and 5% respectively. Error bars indicate the desert methodology uncertainty.

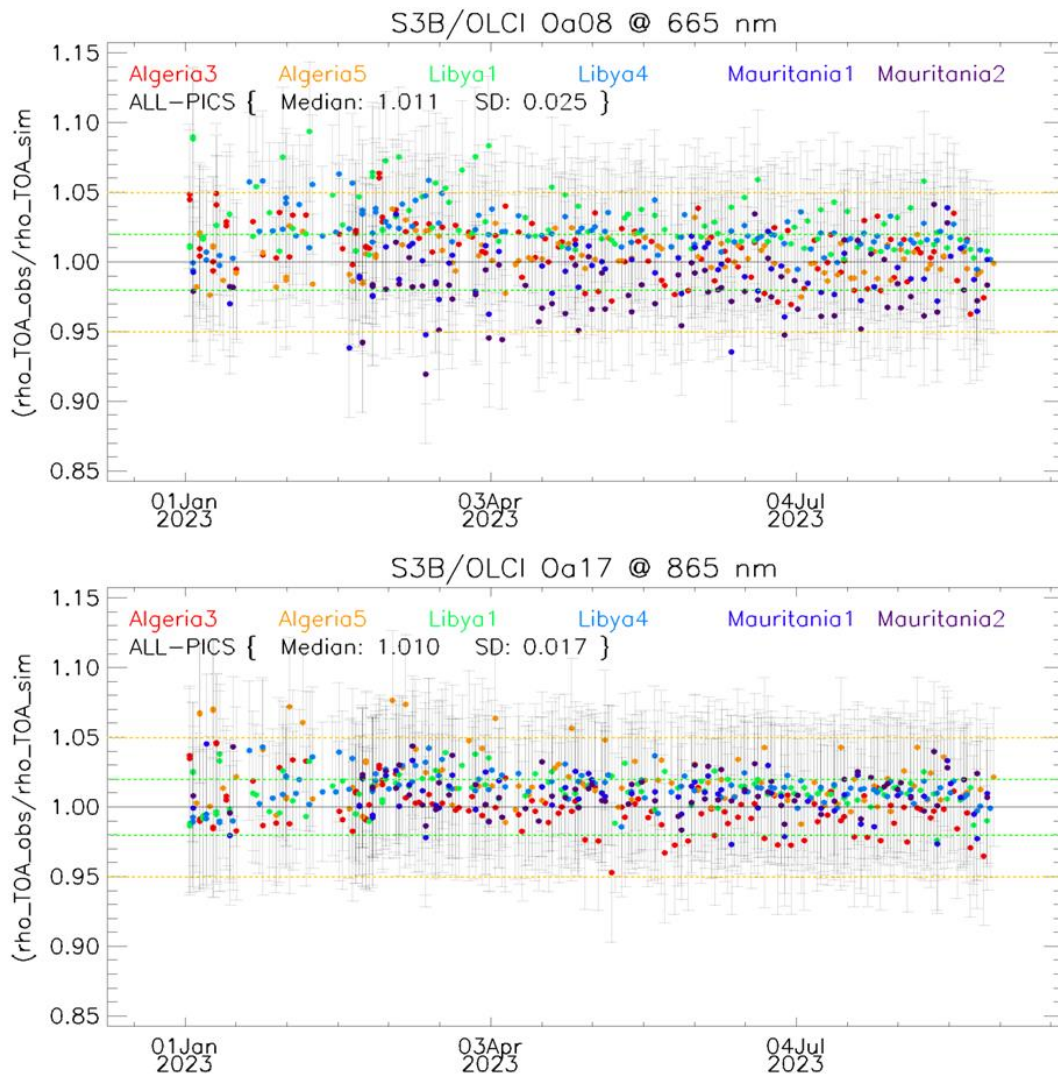


Figure 71: Time-series of the elementary ratios (observed/simulated) signal from OLCI-B for (top to bottom) bands Oa08 and Oa17 respectively over – August 2023 from the six PICS Cal/Val sites. Dashed-green and orange lines indicate the 2% and 5% respectively. Error bars indicate the desert methodology uncertainty.

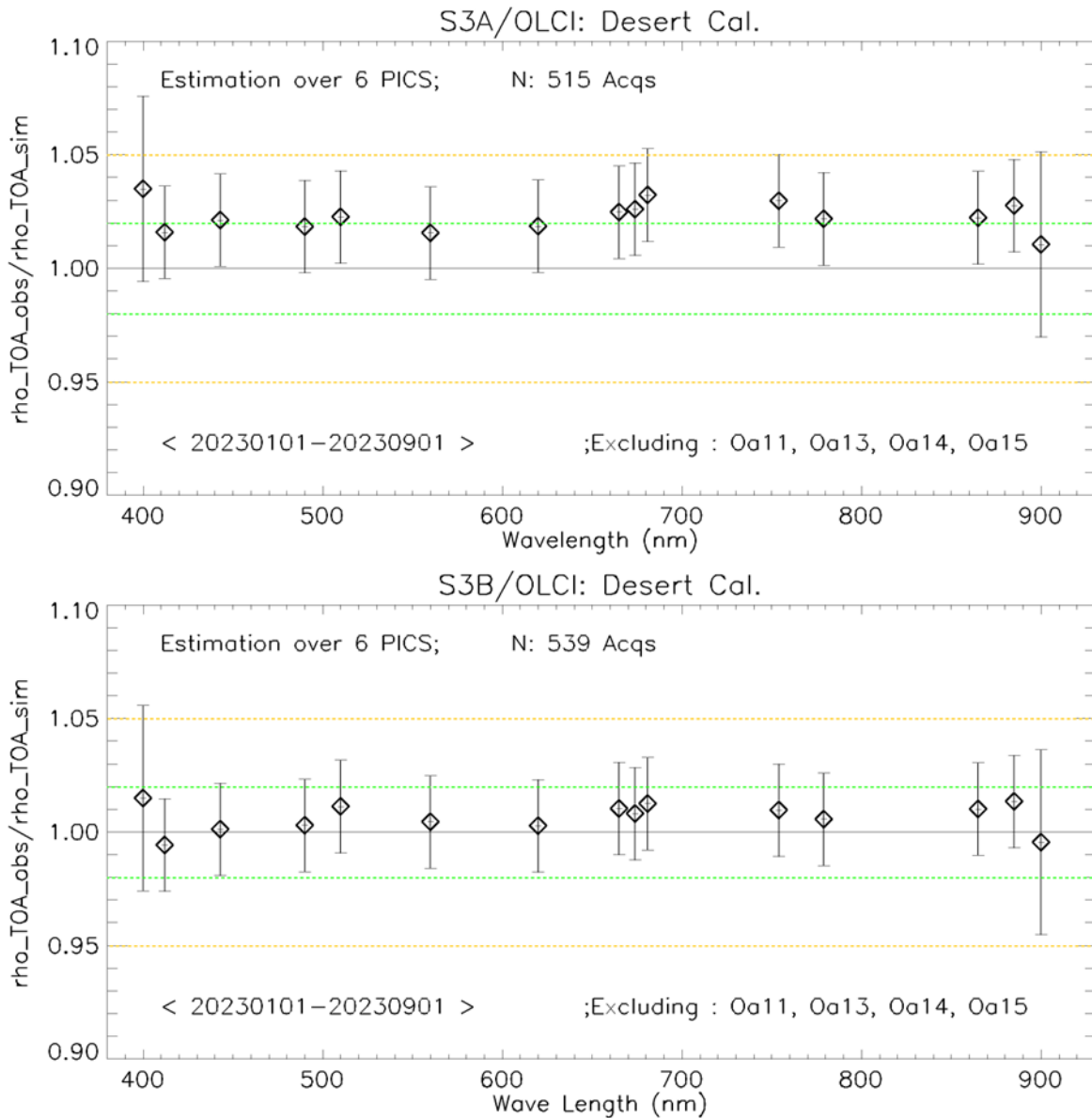


Figure 72: The estimated gain values for OLCI-A and OLCI-B over the 6 PICS sites identified by CEOS over the period January 2023- August 2023 as a function of wavelength. Dashed-green and orange lines indicate the 2% and 5% respectively. Error bars indicate the desert methodology uncertainty.

3.1.2.2 Validation over Rayleigh

Rayleigh method has been performed from the available mini-files over the period **January 2022 - End August 2023** for OLCI-A and OLCI-B. The results were produced with the configuration (ROI-AVERAGE). The gain coefficients of OLCI-A are consistent with the previous results. Bands Oa01-Oa05 display biases values between 3%-5% while bands Oa06-Oa09 exhibit biases about 2%, just within the mission requirement (Figure 73). The gain coefficients of OLCI-B are lower than OLCI-A ones, where bands Oa01-Oa05 display biases values about 2-5%, when bands Oa6-Oa9 exhibit biases within the 2% mission requirement (Figure 73).

3.1.2.3 Validation over Glint and synthesis

Glint calibration method has been performed over the period **January 2022 - end August 2023** for OLCI-A and OLCI-B. The outcome of this analysis shows a good consistency with the desert and Rayleigh outputs over the NIR spectral range Oa06-Oa09 for both sensors. Glint results from OLCI-A show that the NIR bands are within 3% (slightly above the 2% mission requirements), except Oa21 which shows higher biases more than ~5% for both sensors (see Figure 73). Again, the glint gain from OLCI-B looks slightly lower than OLCI-A one with most bands within the 2% mission requirement if ignoring the Rayleigh results in the blue-green region.

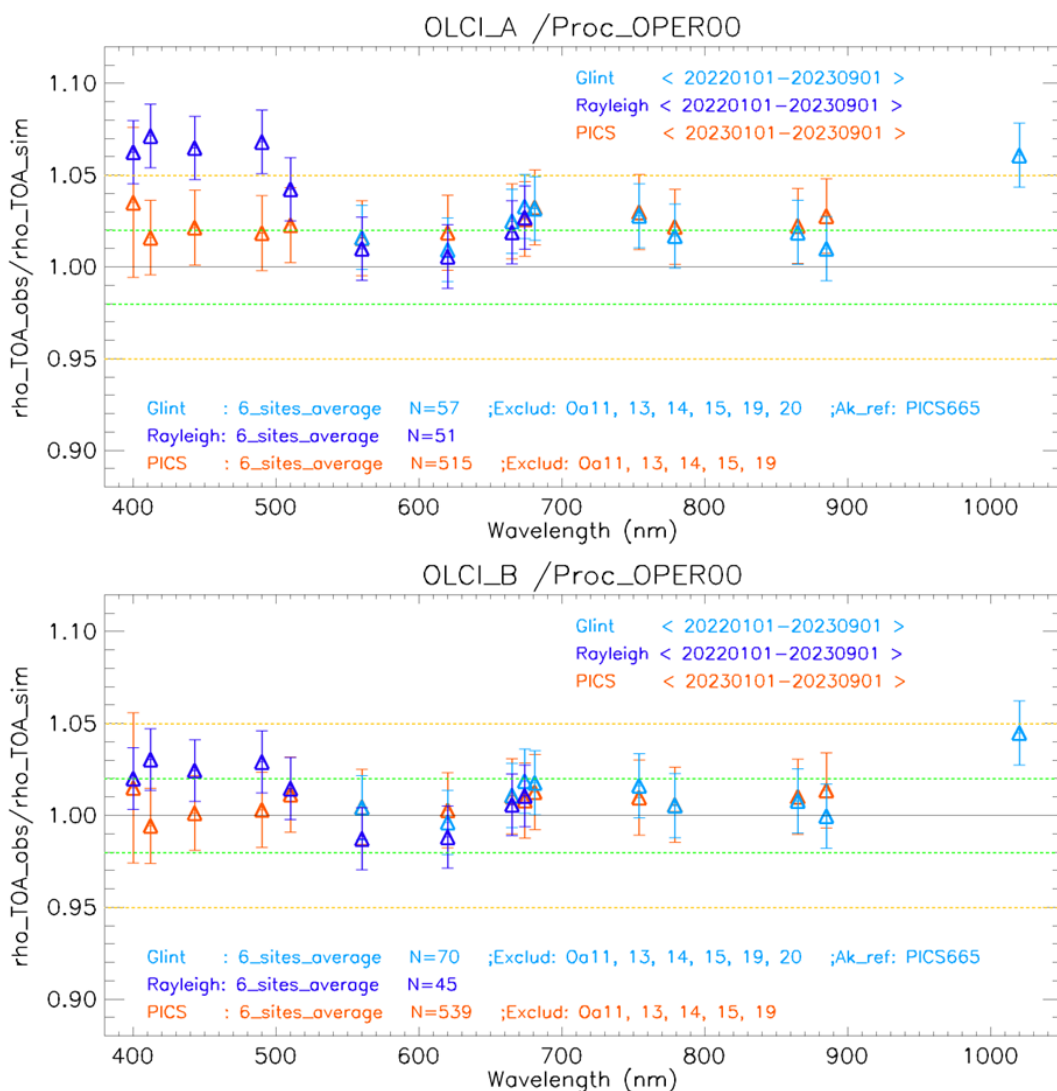


Figure 73: The estimated gain values for OLCI-A and OLCI-B from Glint, Rayleigh and PICS methods over the period January 2022- End August 2023 as a function of wavelength. We use the gain value of Oa8 from PICS-Desert method as reference gain for Glint method. Dashed-green and orange lines indicate the 2% and 5% respectively. Error bars indicate the method uncertainties.

3.1.2.4 Cross-mission Intercomparison over PICS:

X-mission Intercomparison between MERIS, MSI-A, MSI-B, OLCI-A, OLCI-B, SLSTR-A and SLSTR-B has been performed over the 6 PICS-test-sites.

Figure 74 shows the estimated gain over different time-series for different sensors over PICS. The spectral bands with significant absorption from water vapor and O₂ are excluded. OLCI-A seems to have higher gain wrt the other sensors (except SLSTR-A/B), and of about 1-3% higher gain wrt to OLCI-B over VNIR spectral range.

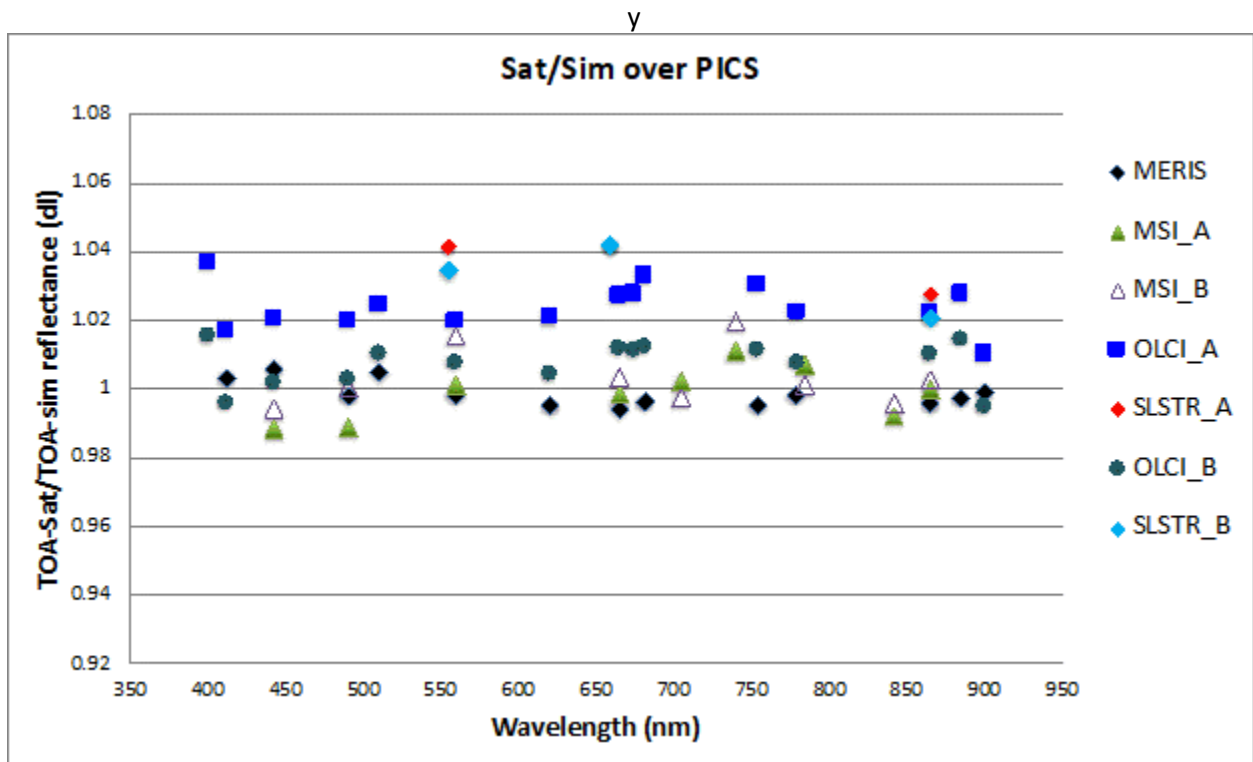


Figure 74: Ratio of observed TOA reflectance to simulated one for (black) MERIS, (pale-green) S2A/MSI, (white) S2B/MSI, (blue) S3A/OLCI, (green) S3B/OLCI, (red) S3A/SLSTR-NADIR, and (cyan) S3B/SLSTR-NADIR averaged over the six PICS test sites over different periods as a function of wavelength.

3.1.3 Radiometric validation with OSCAR

3.1.3.1 OSCAR Rayleigh results

The OSCAR Rayleigh have been applied to the S3A and S3B S3ETRAC data from the 6 oceanic calibration sites (Table 3) using a new chlorophyll climatology which has been derived from the CMEMS OLCI monthly CHL products from considering the years 2017, 2018 and 2019.

Table 3: S3ETRAC Rayleigh Calibration sites

Site Name	Ocean	North Latitude	South Latitude	East Longitude	West Longitude
PacSE	South-East of Pacific	-20.7	-44.9	-89	-130.2
PacNW	North-West of Pacific	22.7	10	165.6	139.5
PacN	North of Pacific	23.5	15	200.6	179.4
AtIN	North of Atlantic	27	17	-44.2	-62.5
AtIS	South of Atlantic	-9.9	-19.9	-11	-32.3
IndS	South of Indian	-21.2	-29.9	100.1	89.5

In Figure 75 the average OSCAR OLCI-A and OLCI-B Rayleigh results are given for August 2023. In Figure 76 and Table 4, the same results are given for all acquisitions of 2023.

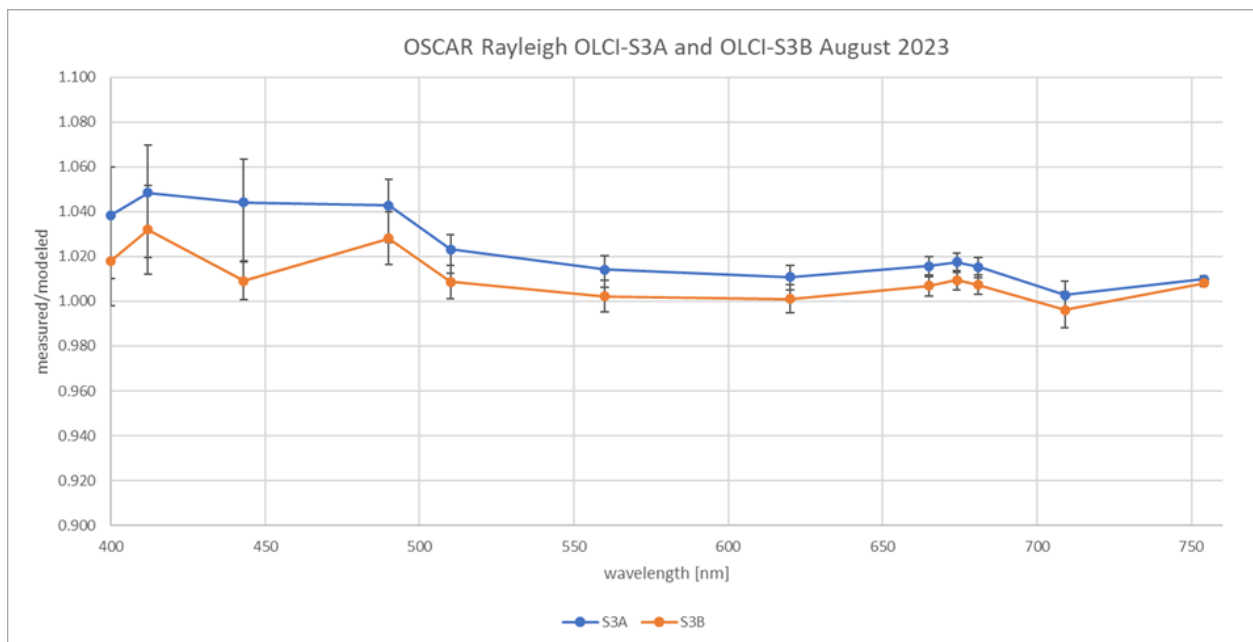


Figure 75: OSCAR Rayleigh S3A and S3B Calibration results as a function of wavelength for June 2023. The results are obtained with a new climatology derived from CMEMS OLCI monthly CHL products.

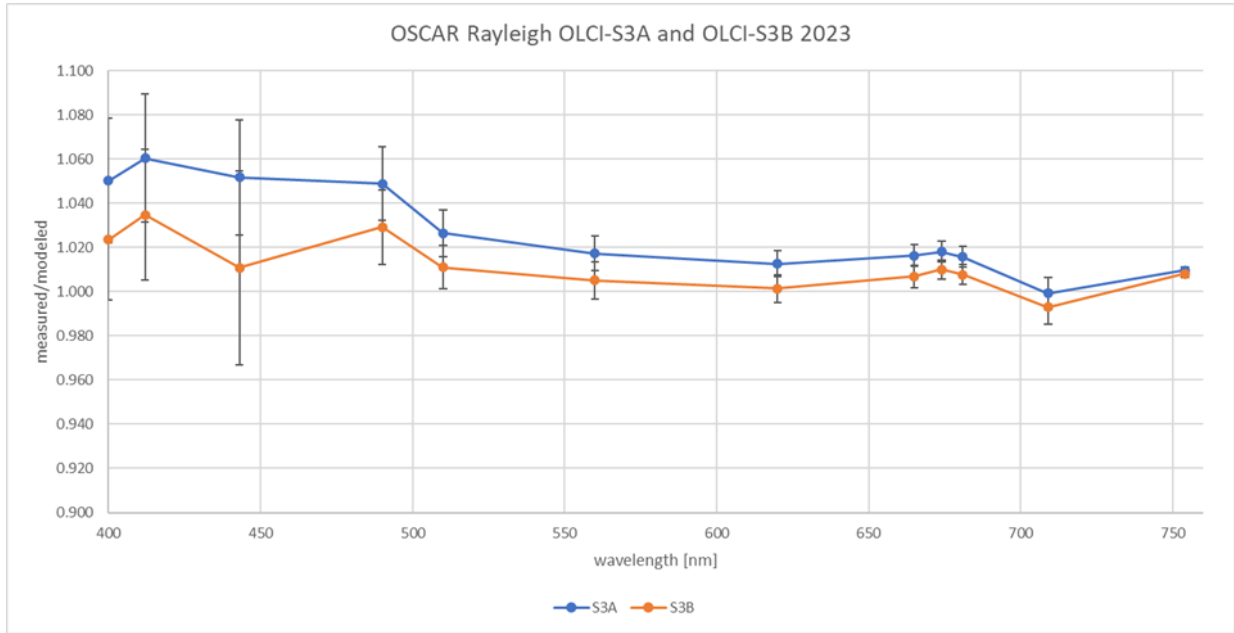


Figure 76: OSCAR Rayleigh OLCI-A and OLCI-B Calibration results as a function of wavelength for all acquisitions of 2023. The results are obtained with a new climatology derived from CMEMS OLCI monthly CHL products.

Table 4. OSCAR Rayleigh calibration results for S3A and S3B (average and standard deviation over all 2023 acquisitions) over all scenes currently (re)processed with the new climatology and observed difference (in %) between OLCIA and OLCIB

OLCI band	Wavelength	Oscar Rayleigh OLCIA		Oscar Rayleigh OLCIB		% difference OLCIA and OLCIB
	(nm)	avg	stdev	avg	stdev	
Oa01	400	1.050	0.028	1.024	0.027	2.54%
Oa02	412	1.060	0.029	1.035	0.030	2.41%
Oa03	443	1.052	0.026	1.011	0.044	3.89%
Oa04	490	1.049	0.017	1.029	0.017	1.88%
Oa05	510	1.026	0.011	1.011	0.010	1.51%
Oa06	560	1.017	0.008	1.005	0.008	1.20%
Oa07	620	1.013	0.006	1.001	0.006	1.10%
Oa08	665	1.016	0.005	1.007	0.005	0.93%
Oa09	674	1.018	0.005	1.010	0.004	0.80%
Oa10	681	1.016	0.005	1.008	0.004	0.79%
Oa11	709	0.999	0.007	0.993	0.008	0.62%
Oa12	754	1.010	0.001	1.008	0.002	0.16%

3.1.4 OSCAR Glitter results

The OSCAR Glitter have been applied to all S3ETRAC glitter data for August 2023. Both OLCI-A and OLCI-B data was processed. The plots in Figure 77 are the glitter results for OLCI-A and OLCI-B for the period of August 2023 and on Figure 78 for all results of 2023 (also provided in Table 5). The values are in absolute terms, since all bands are referenced to the Rayleigh result of band Oa8. The glitter method is a relative inter-band calibration method, since the Oa8 band is used to estimate windspeed. By multiplying all band results with the Rayleigh calibration factor for the same period, the results are referenced to the results of this method.

For all results of 2023, the difference between OLCI-A and OLCI-B (Table 5, in %) is below 1% for all bands, except for bands Oa04 and Oa05. It also indicates a brighter OLCI-A compared to OLCI-B.

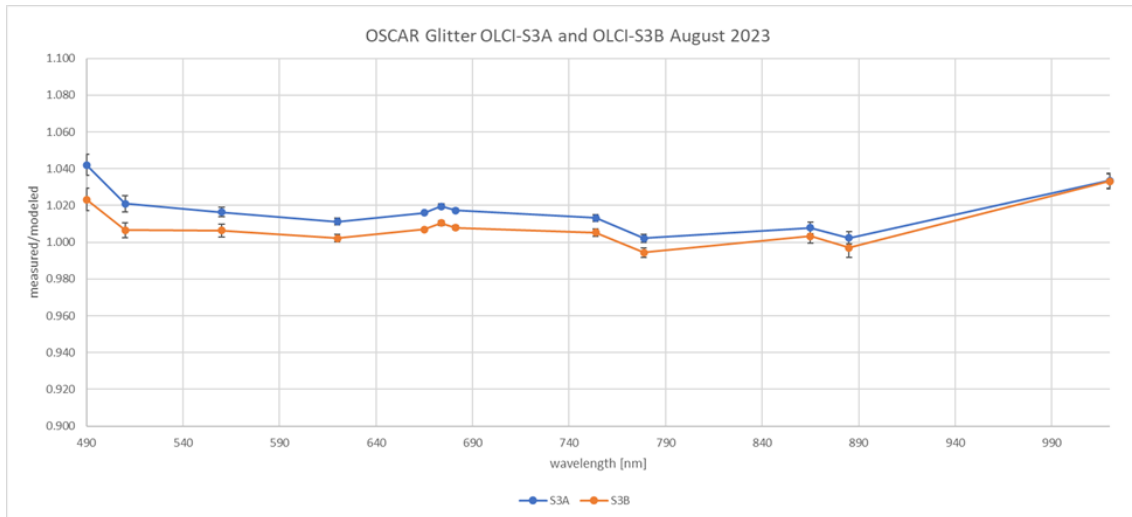


Figure 77: OSCAR Glitter OLCI-A & OLCI-B Calibration results as a function of wavelength for August 2023. The results are obtained with a new climatology derived from CMEMS OLCI monthly CHL products.

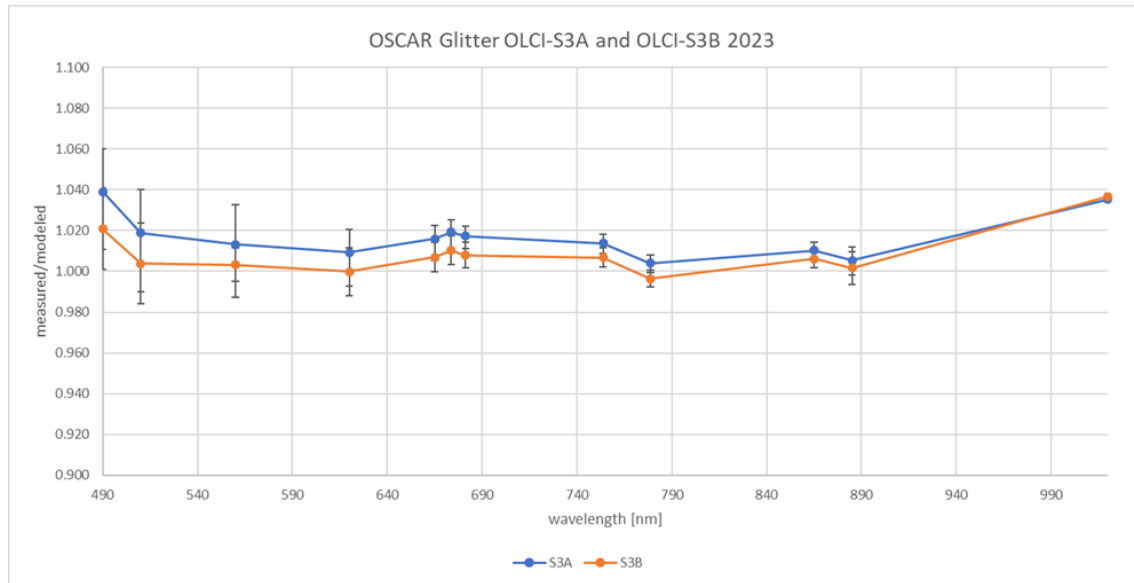


Figure 78: OSCAR Glitter OLCI-A & OLCI-B Calibration results as a function of wavelength for all acquisitions of 2023. The results are obtained with a new climatology derived from CMEMS OLCI monthly CHL products.

Table 5: OSCAR Glitter calibration results for OLCI-A and OLCI-B (average and standard deviation over all acquisitions of 2023) currently processed with the new climatology and observed difference (in %)

OLCI band	Wavelength (nm)	Oscar Glitter OLCIA		Oscar Glitter OLCIB		% difference OLCIA and OLCIB
		avg	stdev	avg	stdev	
Oa04	490	1.039	0.007	1.021	0.006	1.75%
Oa05	510	1.019	0.005	1.004	0.004	1.48%
Oa06	560	1.013	0.003	1.003	0.003	0.98%
Oa07	620	1.009	0.002	1.000	0.002	0.93%
Oa08	665	1.016	0.000	1.007	0.000	0.89%
Oa09	673.75	1.019	0.001	1.010	0.001	0.88%
Oa10	681.25	1.017	0.001	1.008	0.001	0.91%
Oa12	753.75	1.014	0.005	1.007	0.003	0.70%
Oa16	778.75	1.004	0.002	0.996	0.003	0.74%
Oa17	865	1.010	0.007	1.006	0.005	0.42%
Oa18	885	1.005	0.009	1.002	0.006	0.38%
Oa21	1020	1.035	0.011	1.037	0.007	-0.14%

3.1.5 Radiometric validation with Moon observations: LIME results

There has been no new result during the reporting period. The last figures (reported in [OLCI Data Quality Report covering June 2023](#)) are considered valid.

4 Level 2 Land products validation

4.1 [OLCI-L2LRF-CV-300]

4.1.1 Routine extractions

- ❖ The focus for this time period has been on the rolling archive Non Time Critical (NT) data until the 31st of July 2023. More data available for statistical analysis as a concatenation procedure for all available data in the MERMAID processing has been implemented.
- ❖ Concatenated time series of OLCI Global Vegetation Index and OLCI Terrestrial Chlorophyll Index have been regenerated on the current rolling archive availability including previous extractions since June 2016 and April 2018 for S3A and S3B respectively.

4.1.1.1 OLCI-A

Figure 79 to Figure 88 below present the Core Land Sites OLCI-A time series over the current period.

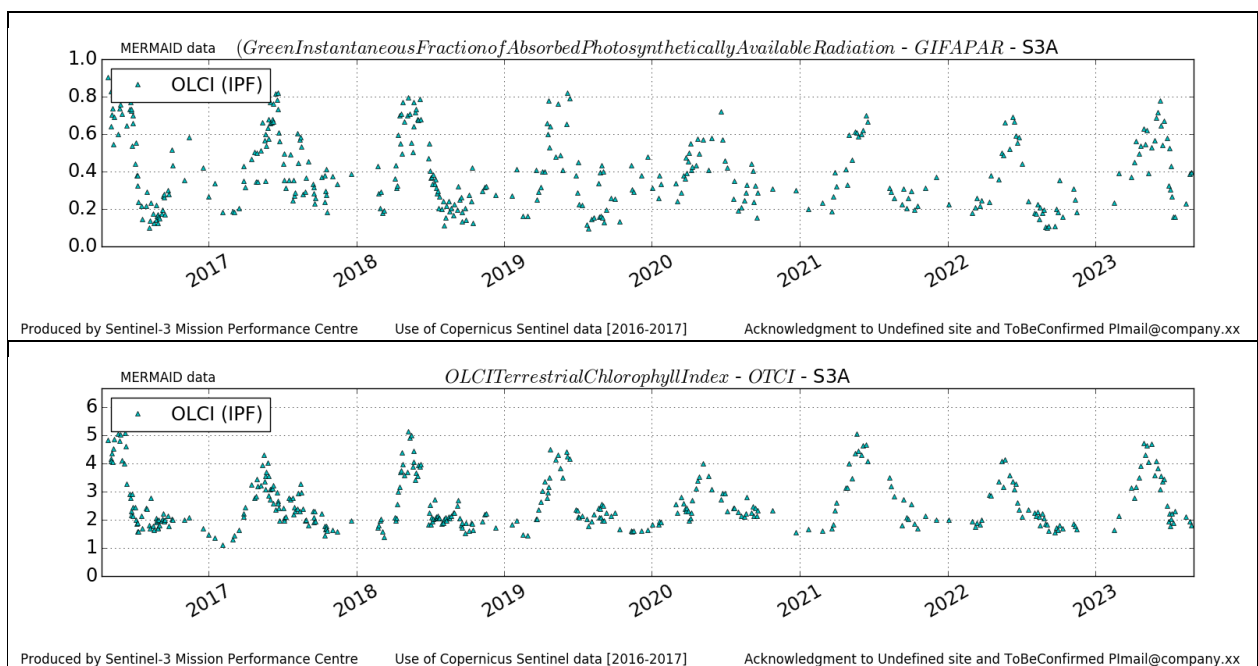


Figure 79: DeGeb time series over current report period

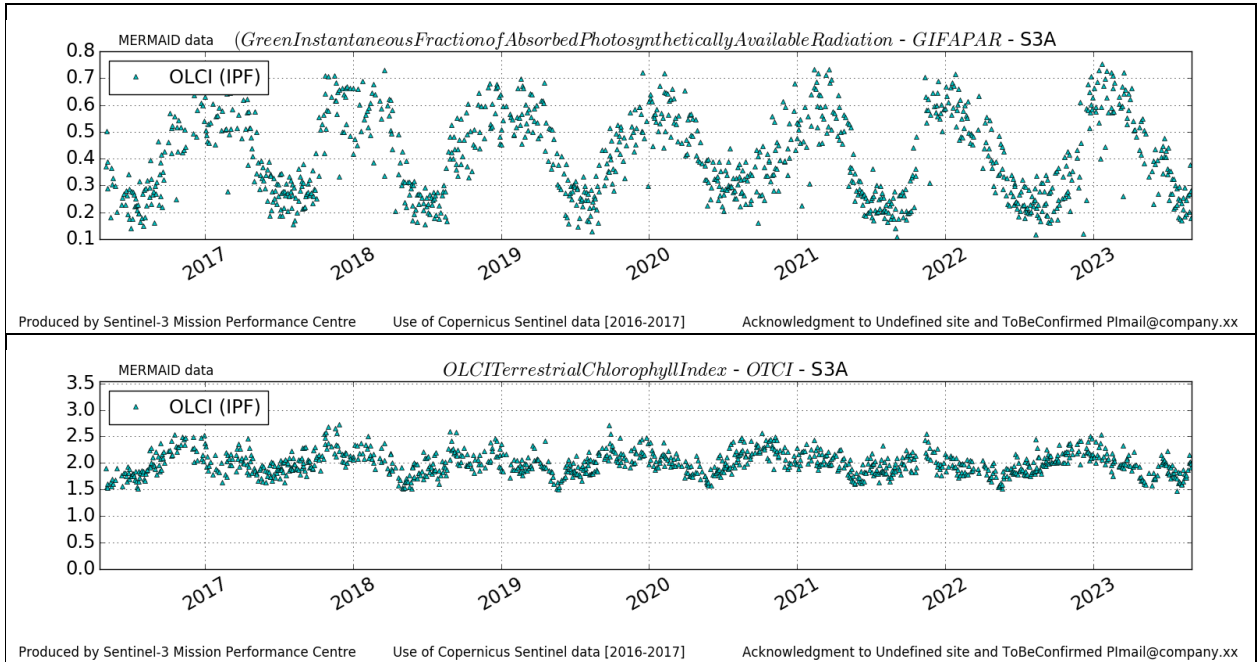


Figure 80: ITCat time series over current report period

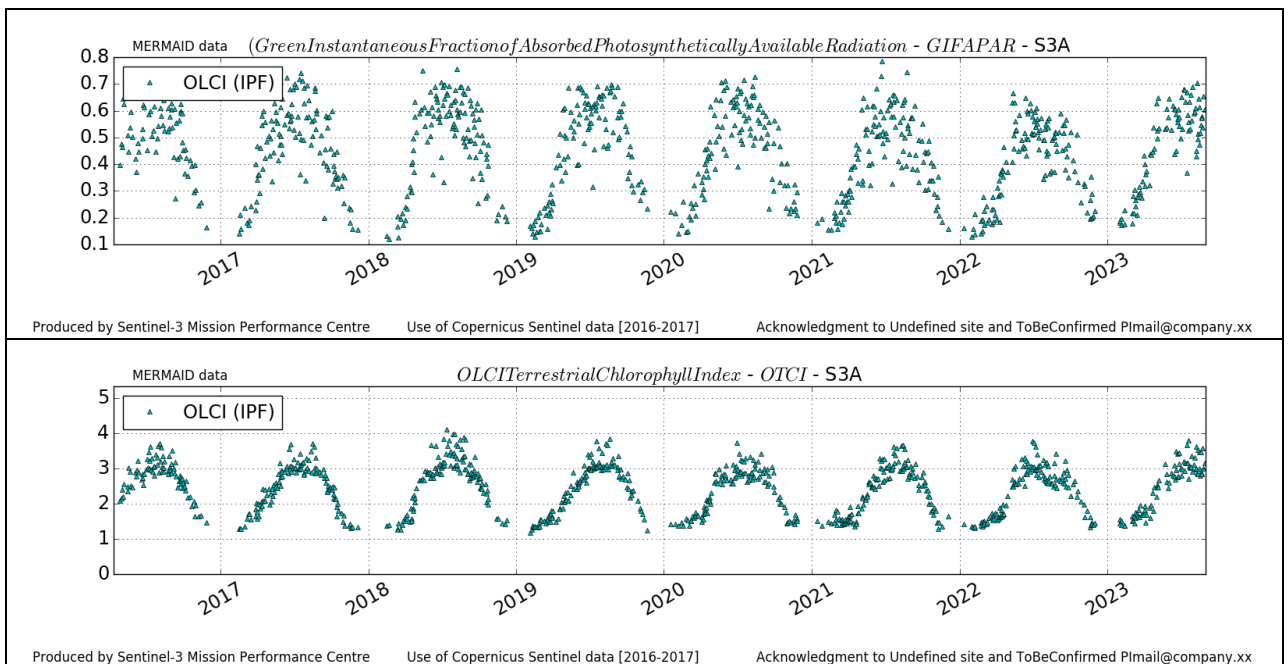


Figure 81: ITIs time series over current report period

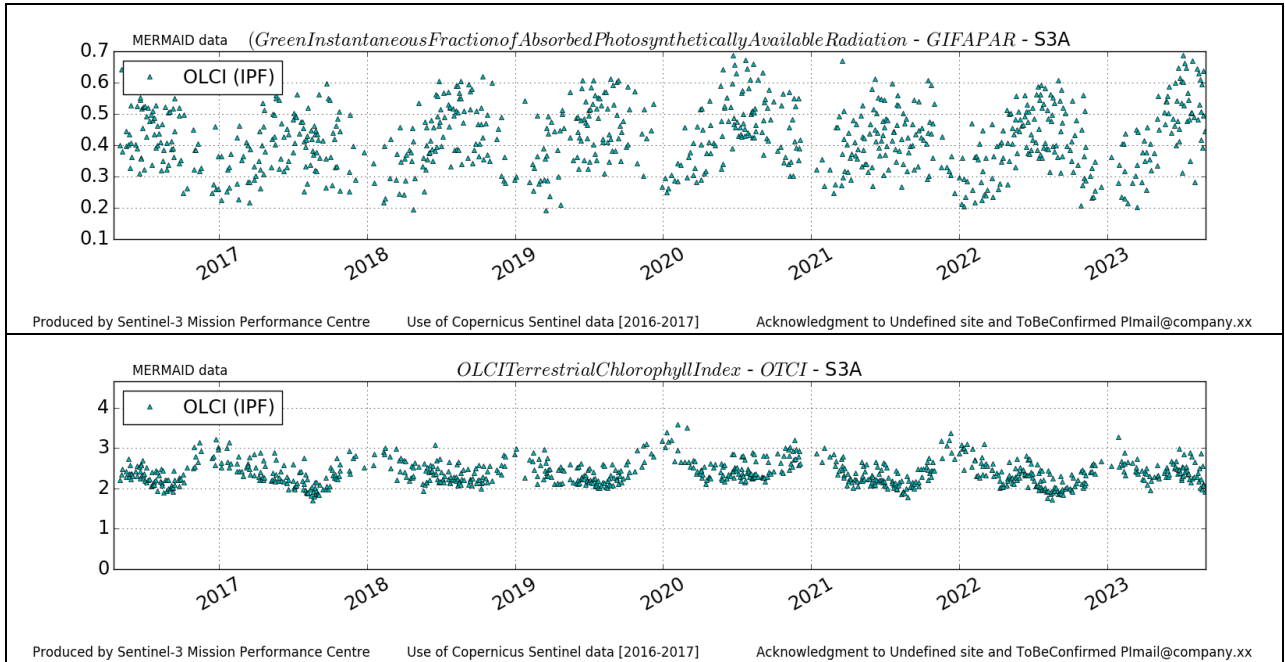


Figure 82: ITSro time series over current report period

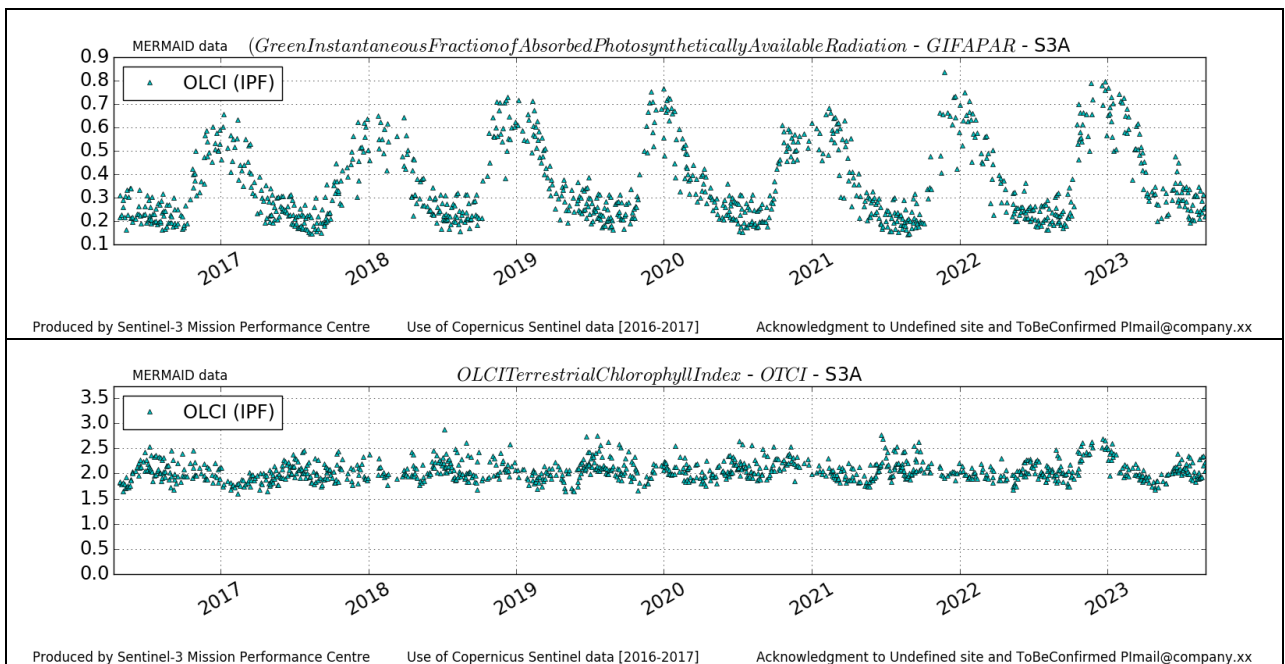


Figure 83: ITTra time series over current report period

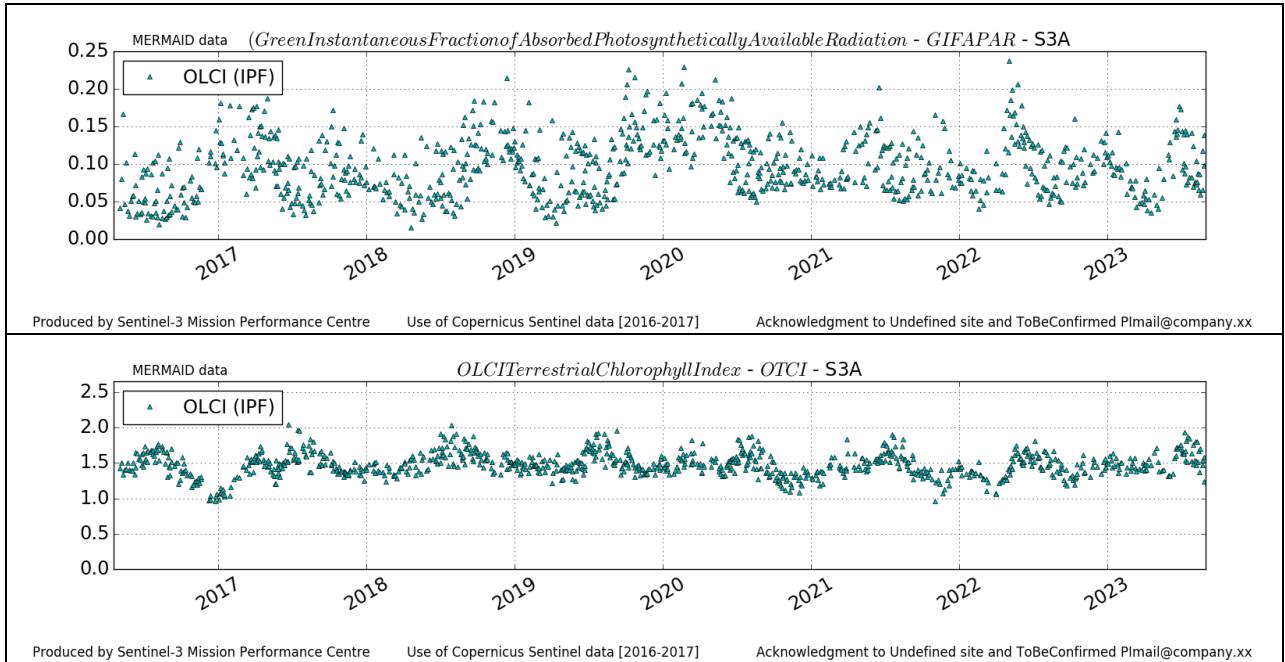


Figure 84: SPAl time series over current report period

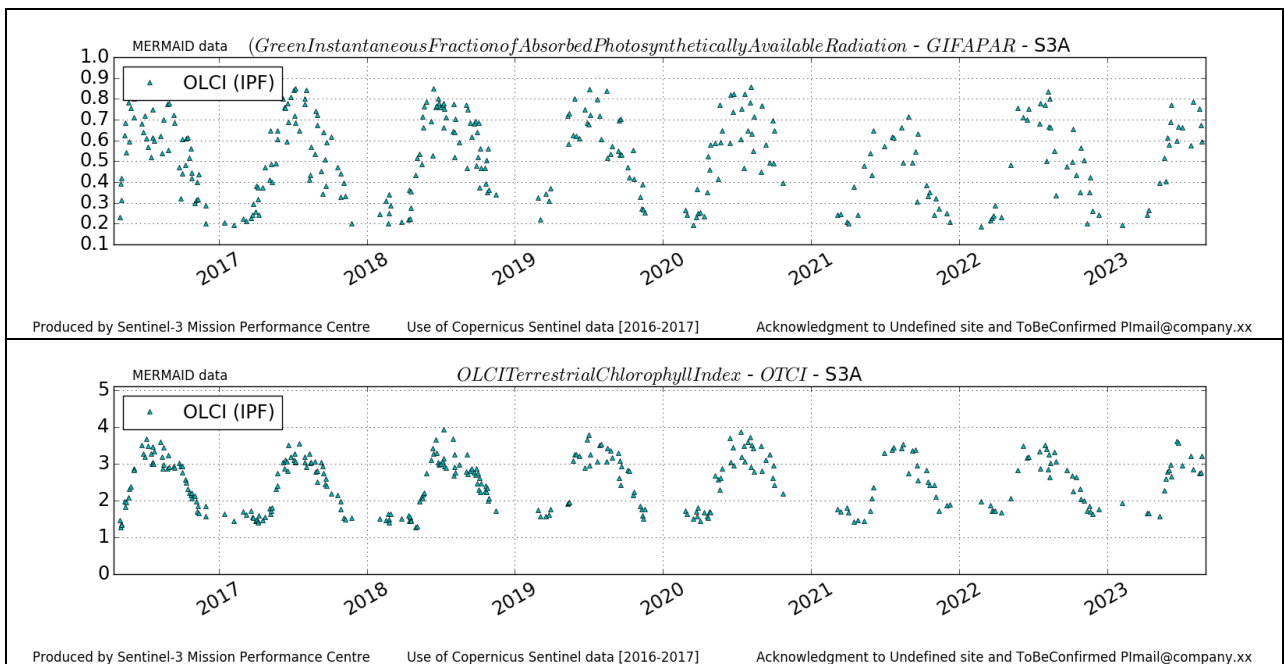


Figure 85: UKNfo time series over current report period

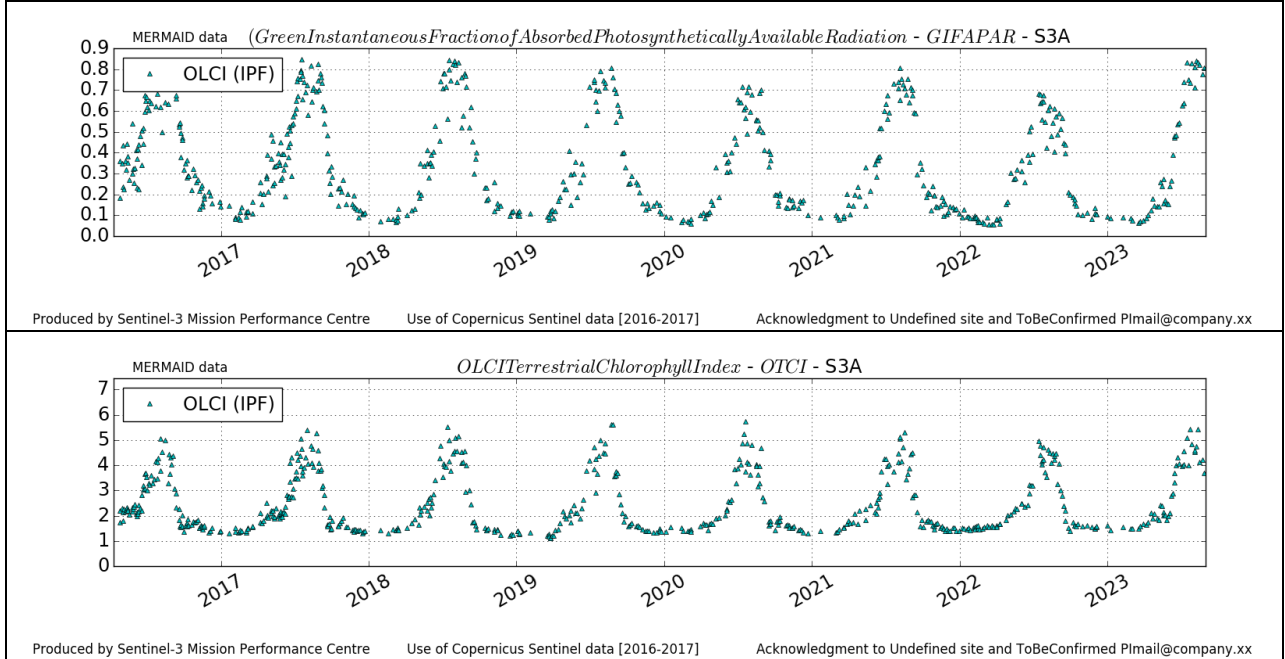


Figure 86: USNe1 time series over current report period

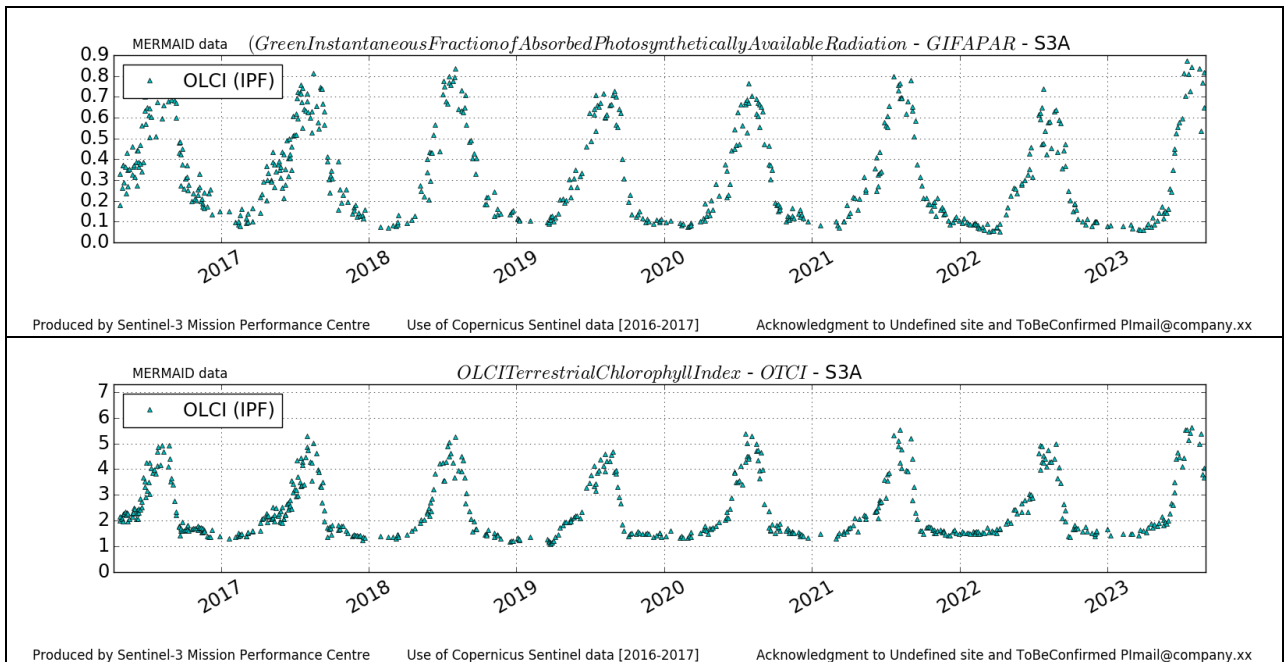


Figure 87: USNe2 time series over current report period

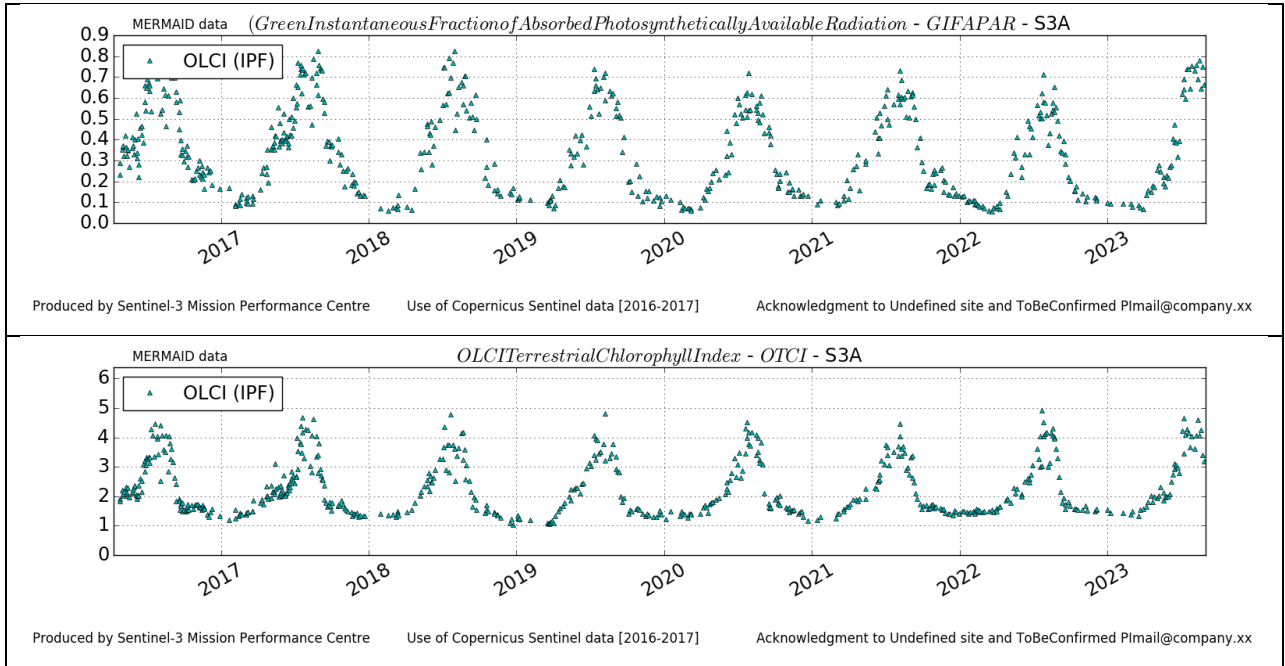


Figure 88: USNe3 time series over current report period

4.1.1.2 OLCI-B

Figure 89 to Figure 98 below present the Core Land Sites OLCI-B time series over the current period.

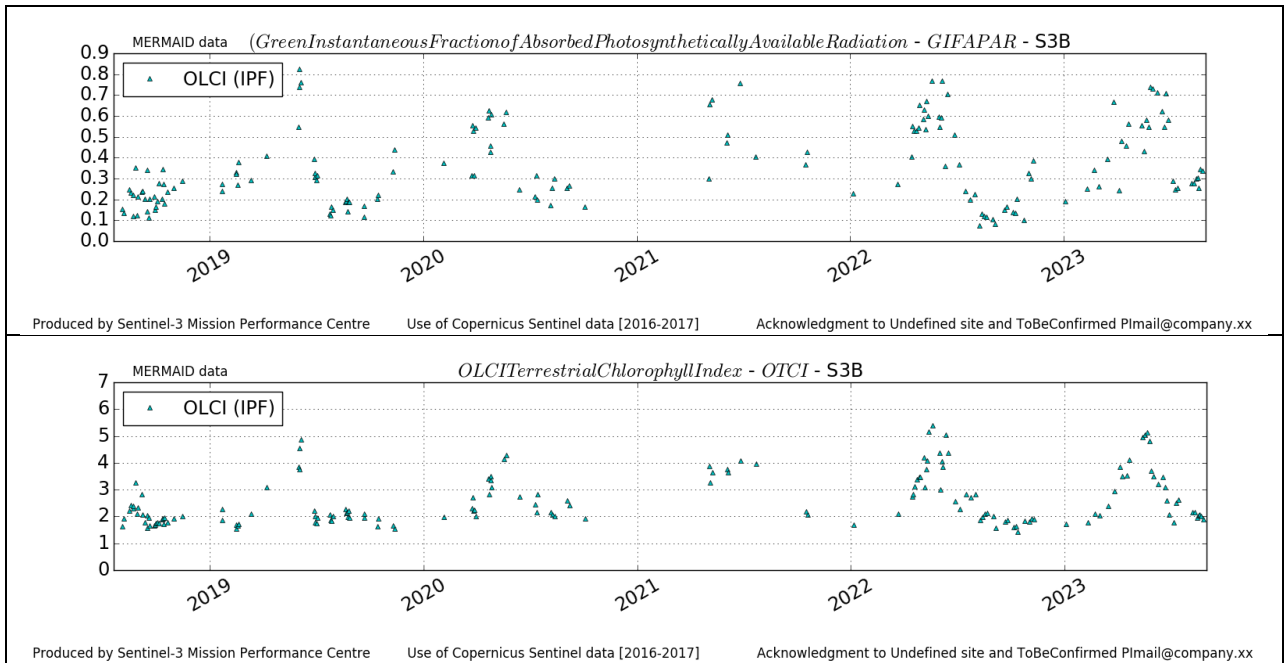


Figure 89: DeGeb time series over current report period

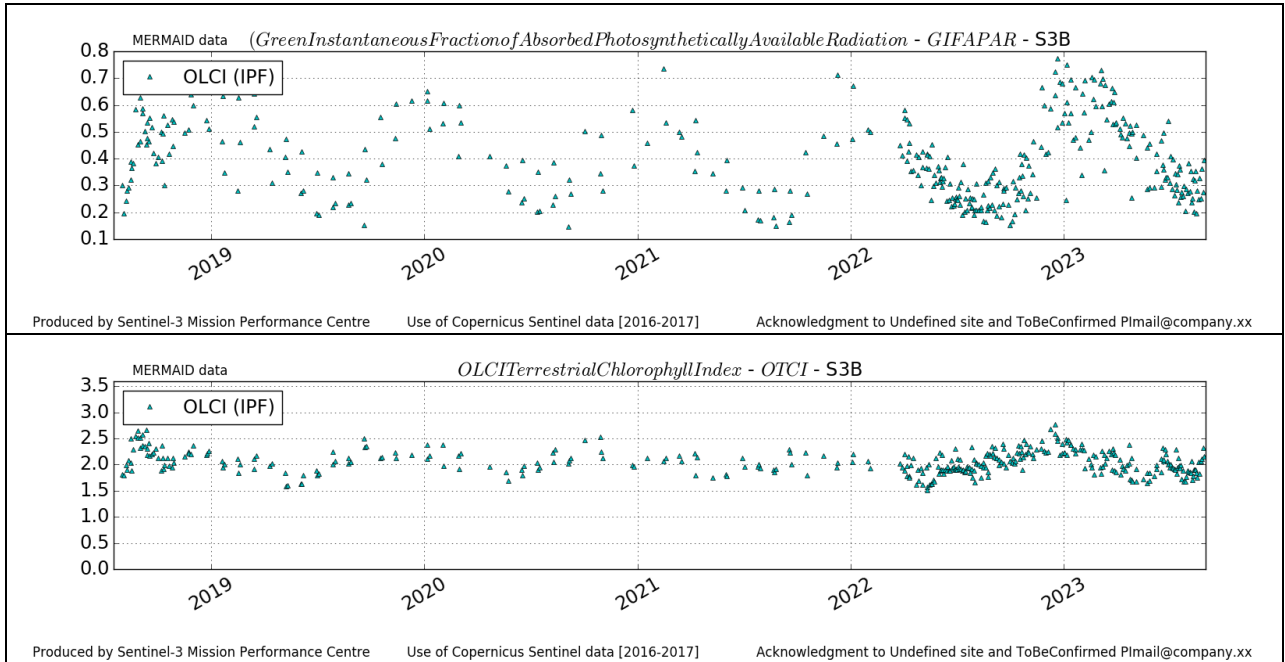


Figure 90: ITCat time series over current report period

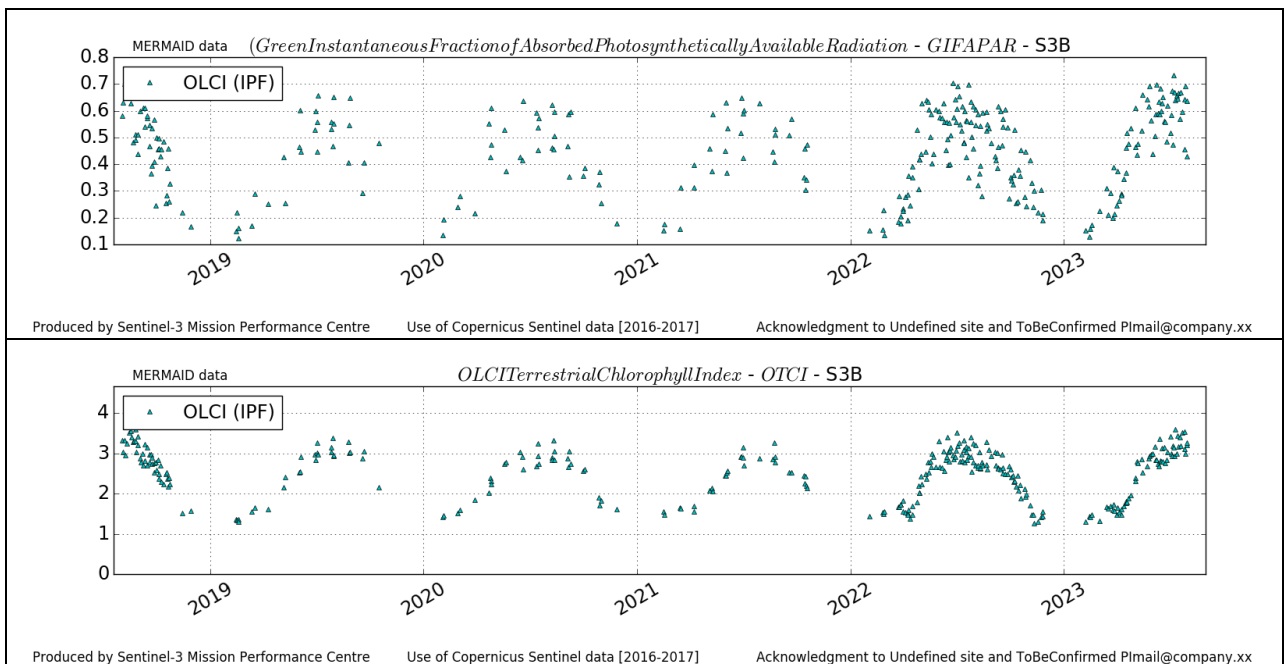


Figure 91: ITIsP time series over current report period

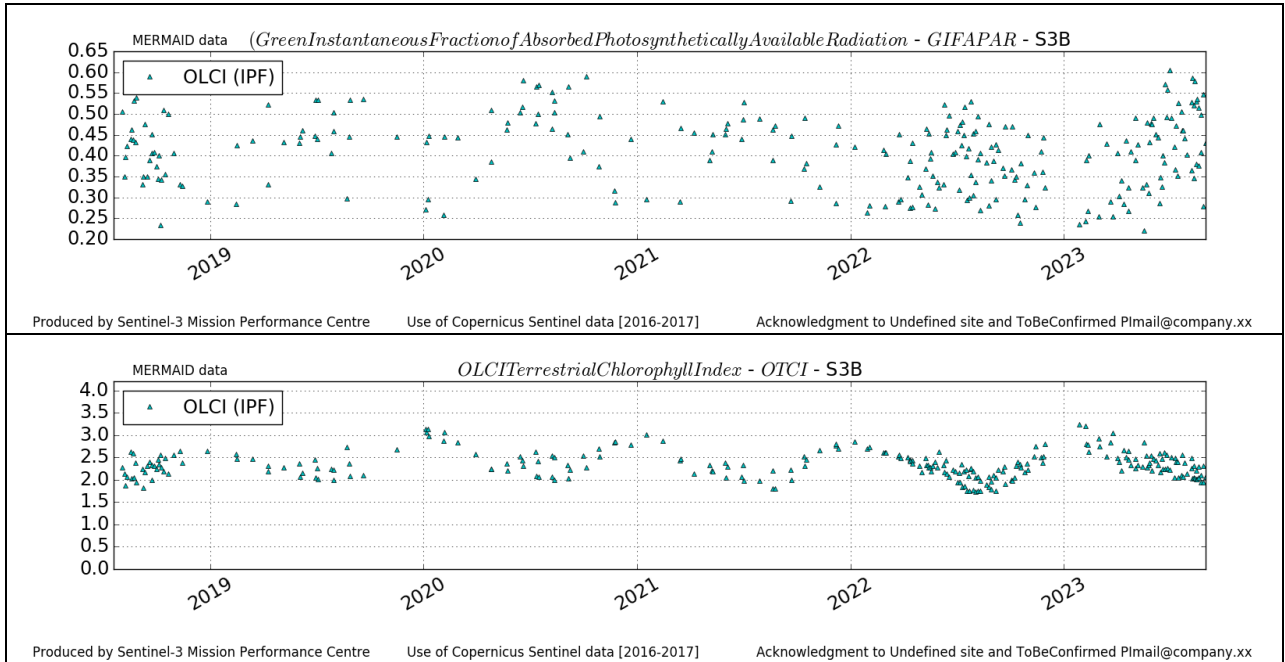


Figure 92: ITSro time series over current report period

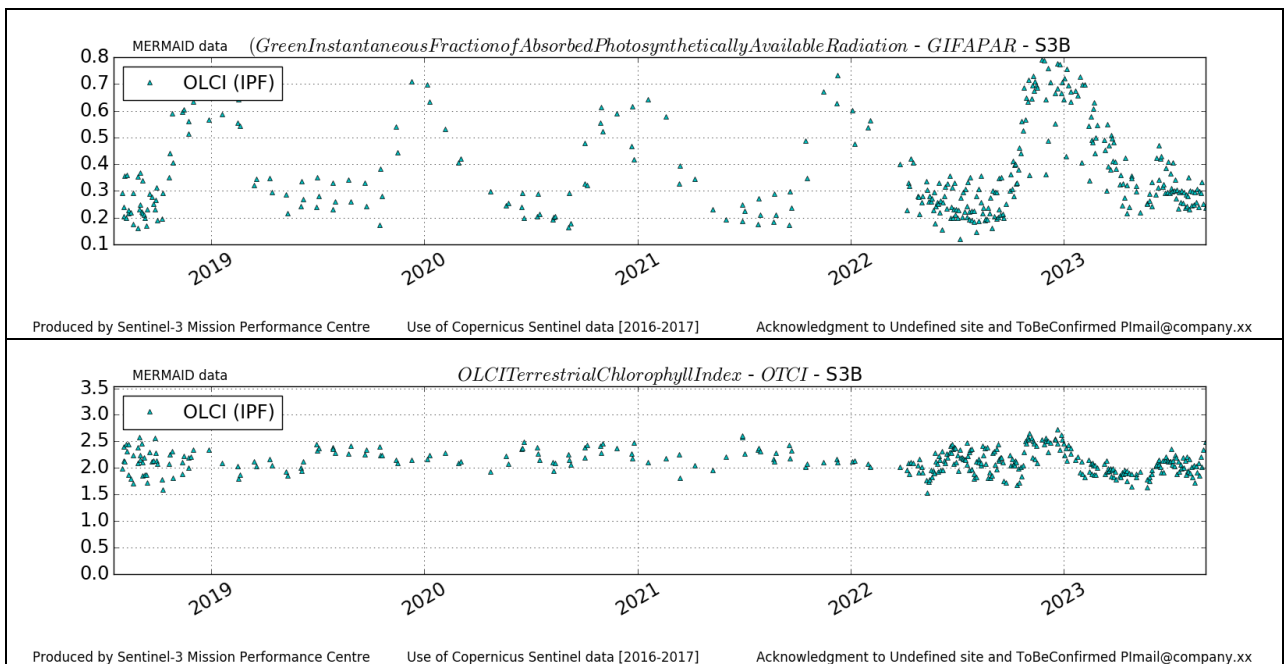


Figure 93: ITTra time series over current report period

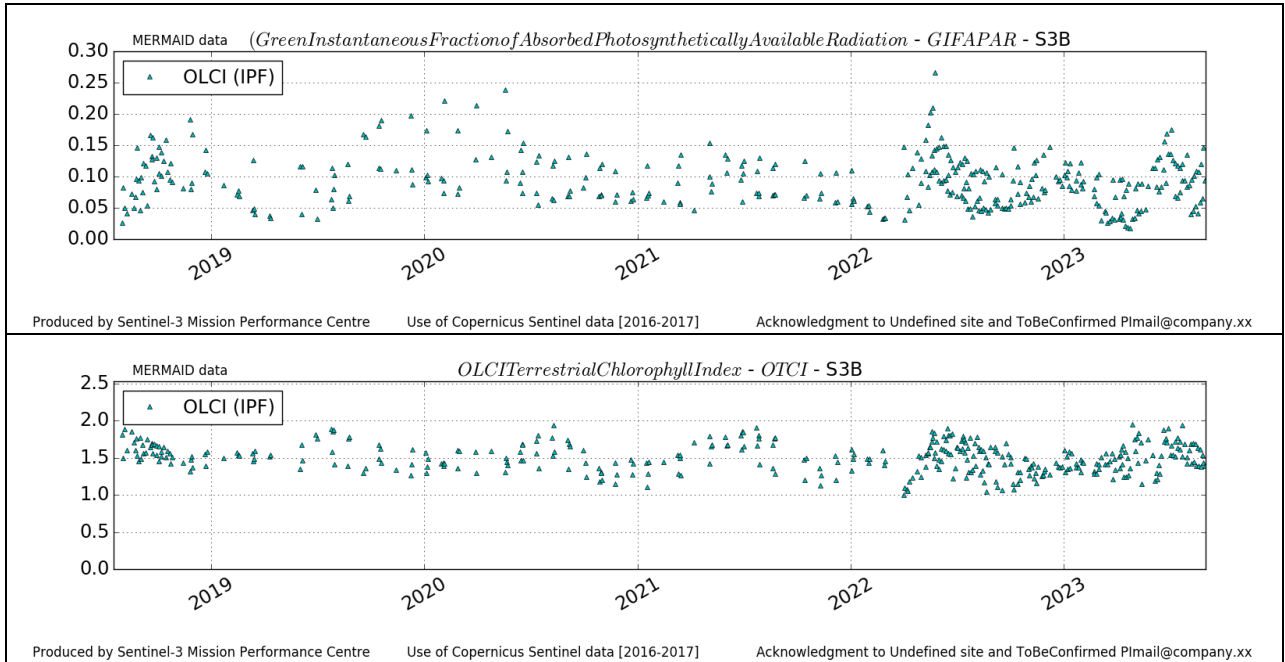


Figure 94: SPaI time series over current report period

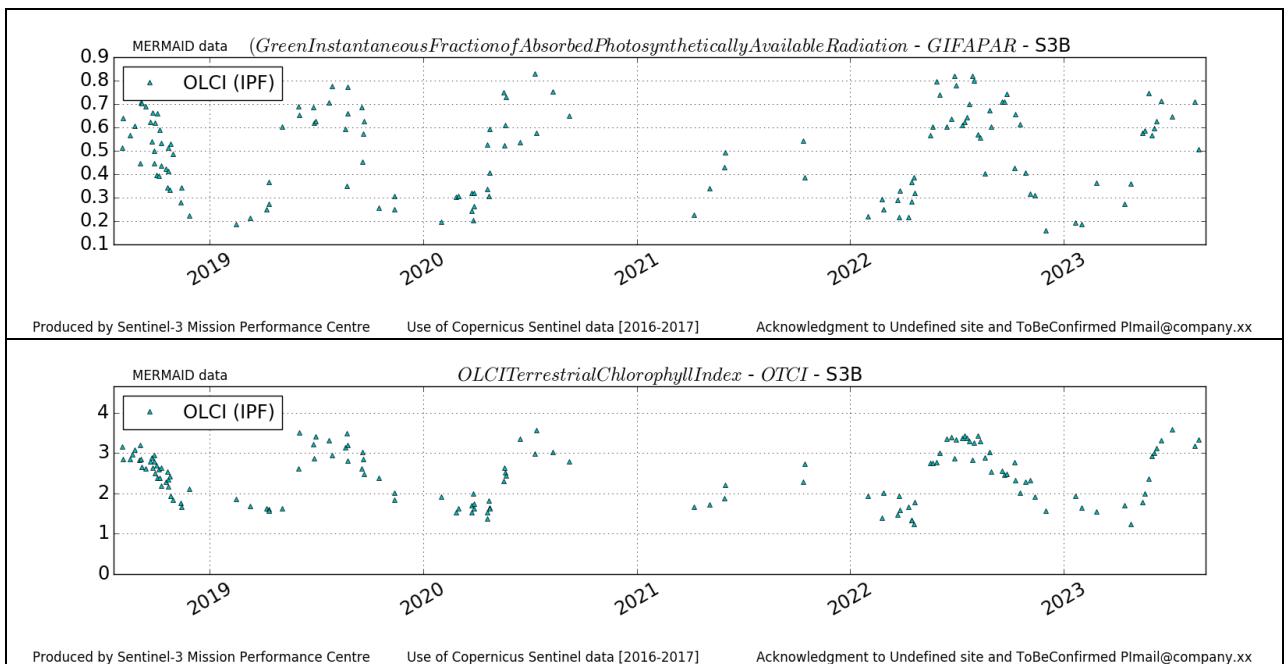


Figure 95: UKNfo time series over current report period

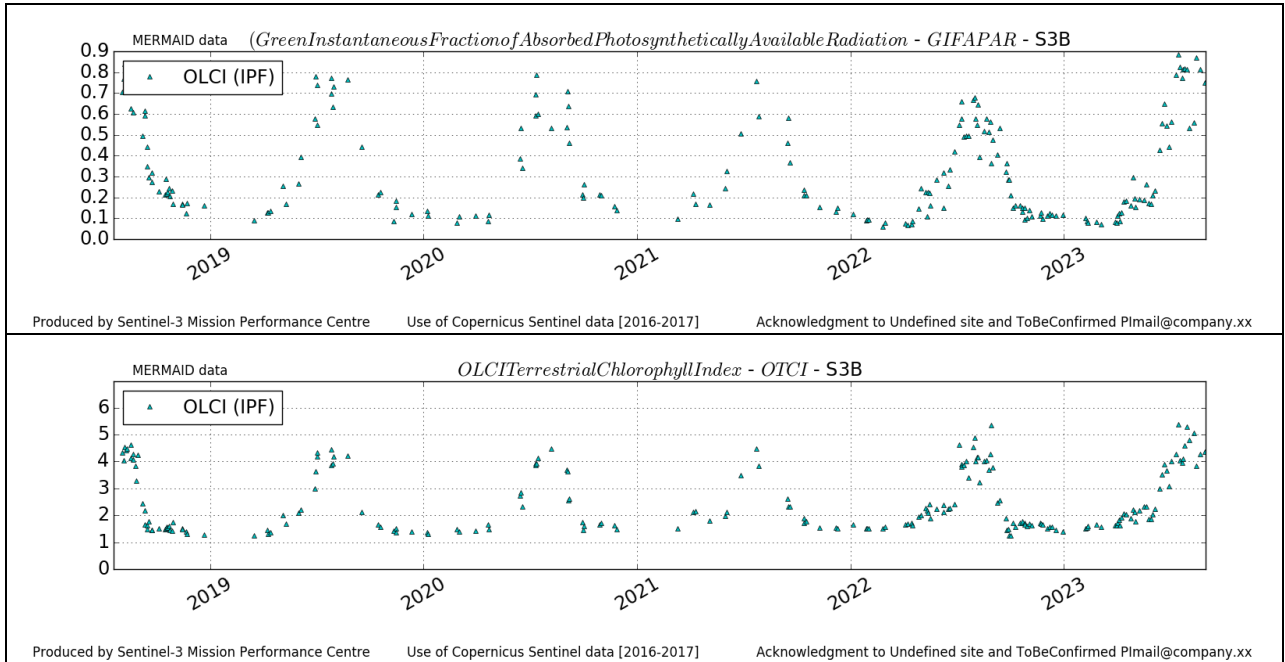


Figure 96: USNe1 time series over current report period

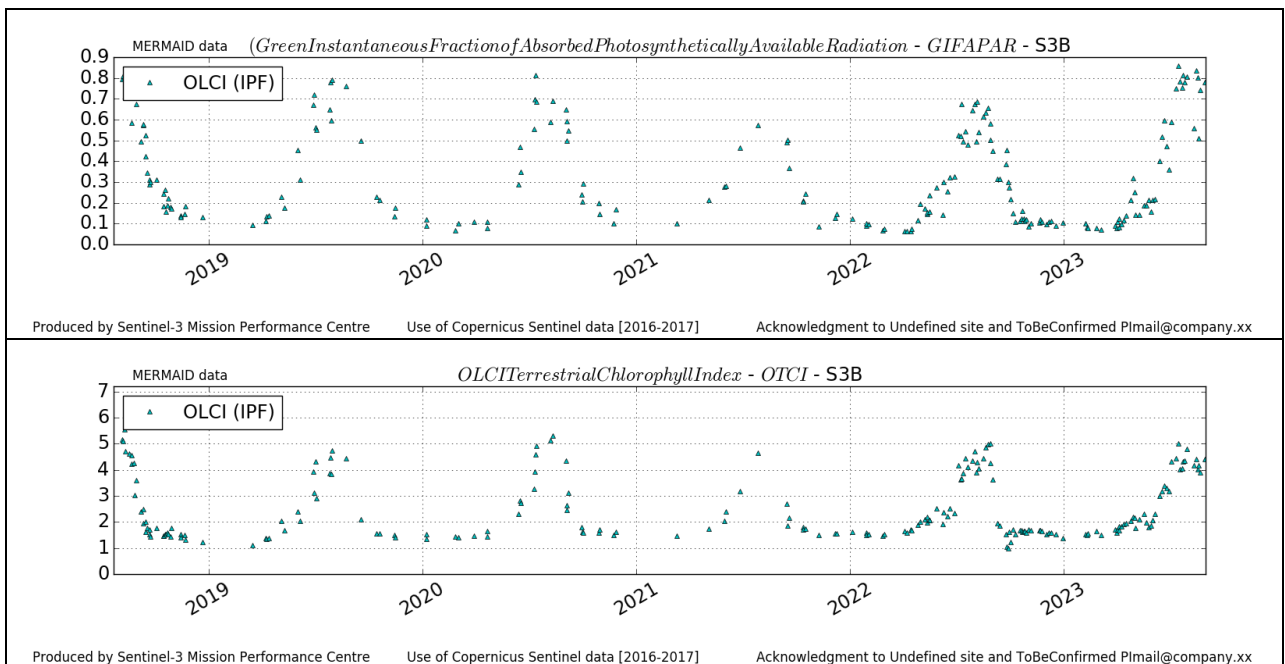


Figure 97: USNe2 time series over current report period

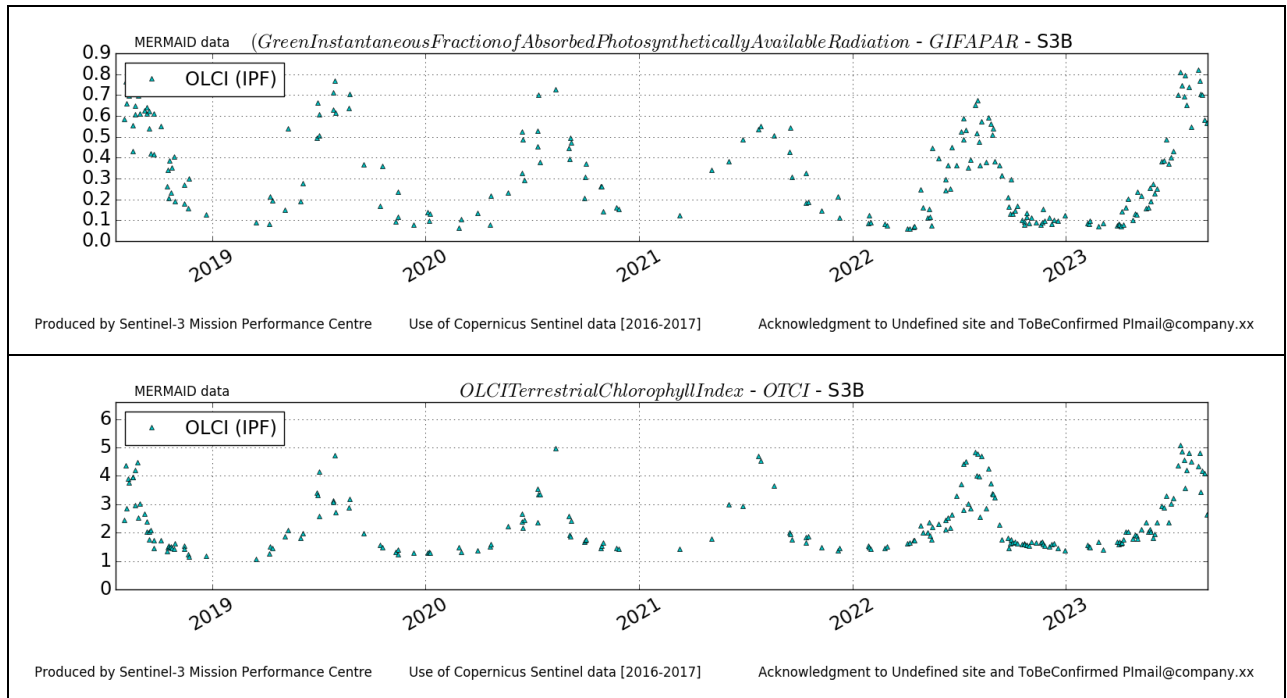


Figure 98: USNe3 time series over current report period

4.1.2 Comparisons with MERIS MGVI and MTCI climatology

There have been no new results during the reporting period. The latter figures (reported in [OLCI Data Quality Report covering July 2023](#)) are considered valid.

4.1.3 Comparisons with GBOV (Ground-Based Observations for Validation) data v3

This report compares the ground-based measurements from the Copernicus GBOV service and OLCI GIFAPAR products until 31st December 2021. Compared to the [May 2023](#) DQR, we have tested four protocols to improve the validation to match GBOV and Sentinel-3 data. The validation is conducted using the MERMAID extractions of Sentinel-3 (i.e., 81 for OLCI-A and 25 for OLCI-B) over twelve established validation sites and GBOV fAPAR land product (LP4). The selected sites are distributed across various geographical locations, representing different land cover types (Table 6).

Table 6: GBOV validation sites analysed in monthly reports

ID	Name	Country	LAT	LON	IGBP	GBOV Dates	Min - Max DOY
USA_BART	Bartlett Experimental Forest	USA	44.0639	-71.2873	Mixed Forest	20140104 - 20211217	8 - 349
USA_CPER	Central Plains Experimental Range	USA	40.81555	-104.7460	Grasslands	20140116 - 20211229	3 - 362
PRI_GUAN	Guanica Forest	Puerto Rico	17.9695	-66.8687	Evergreen Broadleaf	20150131- 20211228	8 - 349
GER-HAIN	Hainich	Germany	51.0792	10.4522	Mixed Forest	20200102 - 20211221	8-349
USA_HARV	Harvard	USA	42.5378	-72.1715	Mixed Forest	20140104 - 20211228	8 - 349
USA_JORN	Jornada	USA	32.5907	-106.842	Open Shrubland	20160106 - 20211229	3 - 362
USA_Moab	Moab	USA	38.2483	-109.388	Open Shrubland	20150108 - 20201220	3 - 362
USA_ORNL	Oak Ridge	USA	35.9641	-84.2826	Mixed Forest	20150117 - 20211230	8 - 349
USA_OSBS	Ordway Swisher Biological Station	USA	29.67615	-82.00847	Evergreen Needleleaf	20130328- 20211229	8 - 349
USA_SCBI	Smithsonian Conservation Biology	USA	38.8902	-78.1395	Mixed Forest	20150105 - 20211224	8 - 349
USA_STEI	Steigerwaldt Land Services	USA	45.5089	-89.5864	Deciduous Broadleaf	20160123 - 20211229	8 - 349
USA_TALL	Talladega National Forest	USA	32.9504	-87.3933	Evergreen Needleleaf	20150131 - 202112283	8 - 349
AUS_TUMB	Tumbarumba	AUS	-35.6565	148.1516	Evergreen Broadleaf	20200103- 20201230	8 - 349

The methodology involves 1) extracting the GBOV values of the corresponding Land Product (LP4) at 300 m resolution (WGS-84) overlapping the S3 pixels, 2) filtering OLCI-A/OLCI-B and GBOV data, and 3) plotting the temporal profiles. Sentinel data are filtered following the quality flags (i.e., GIFAPAR_FAIL, CLOUD, GIFAPAR_CLASS_BAD, GIFAPAR_CLASS_WS, GIFAPAR_CLASS_CSI, GIFAPAR_CLASS_BRIGHT, COSMETIC, SUSPECT, no valid values - 255), and GBOV data are filtered according to the project recommendations (<https://gbov.acri.fr/userSupport/>). Hence the values removed include 1) values with input or output out of range, 2) values outside the season used to establish the calibration function (Min DOY and Max DOY Table) and 3) threshold <50% on the percentage of valid native spatial resolution pixels.

Several protocols have been tested to match Sentinel-3 and GBOV data, including: 1) considering all the pixels extracted by MERMAID, 2) focusing on the central point of MERMAID extractions and the surrounding 3x3 window, 3) focusing on the tower and the 3x3 window and 4) focusing on the ESU measurements of each site.

4.1.4 OLCI-A

Figure 99 to Figure 111 shows the variability of both in situ values from GBOV and their corresponding OLCI-A matchups in time. OLCI-A reproduces the temporal variations of GBOV values for almost all sites satisfactorily. However, GBOV products provide systematically higher values than satellite products in forest classes. On the contrary, satellite products present higher values than GBOV for shrubland and grasslands. Results for 2021 (are similar to) follow the previous year's pattern. Preliminary results indicate that OLCI-A/OLCI-B satisfactorily reproduces the temporal variation of GBOV values for almost all sites.

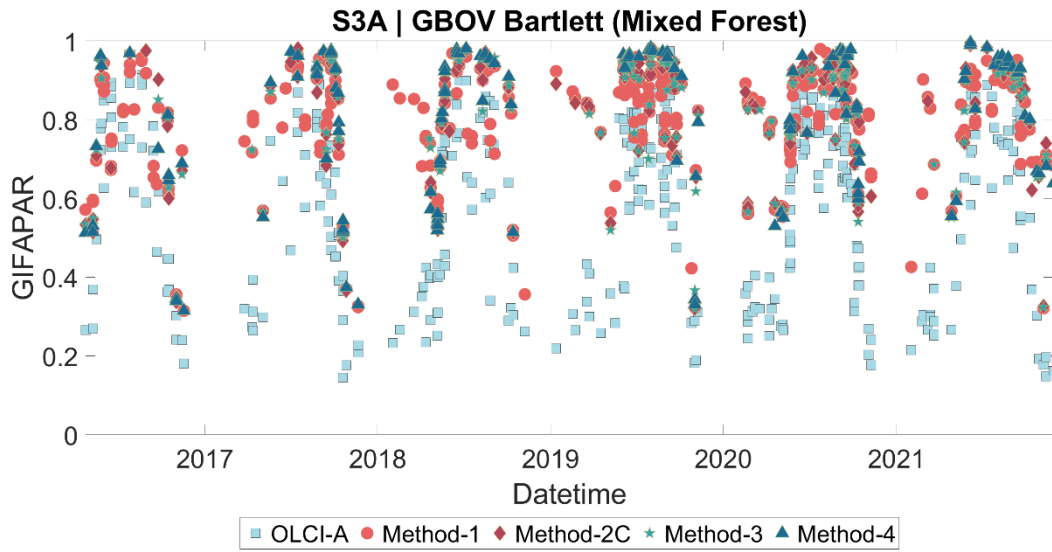


Figure 99: Time series of OLCI-A GIFAPAR (blue-sky) and four methods for the Bartlett site.

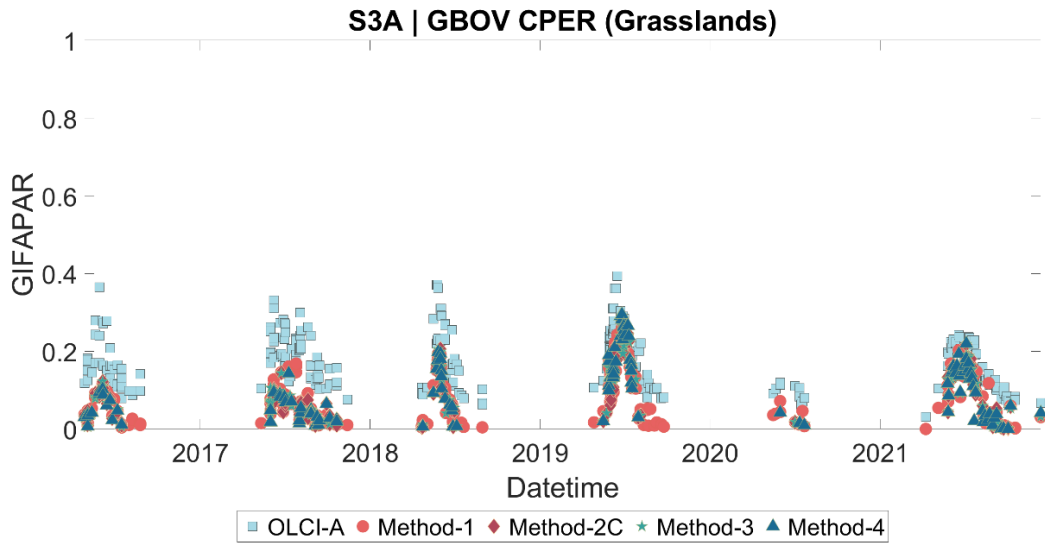


Figure 100: Time series of OLCI-A GIFAPAR (blue-sky) and four methods for the CPER site.

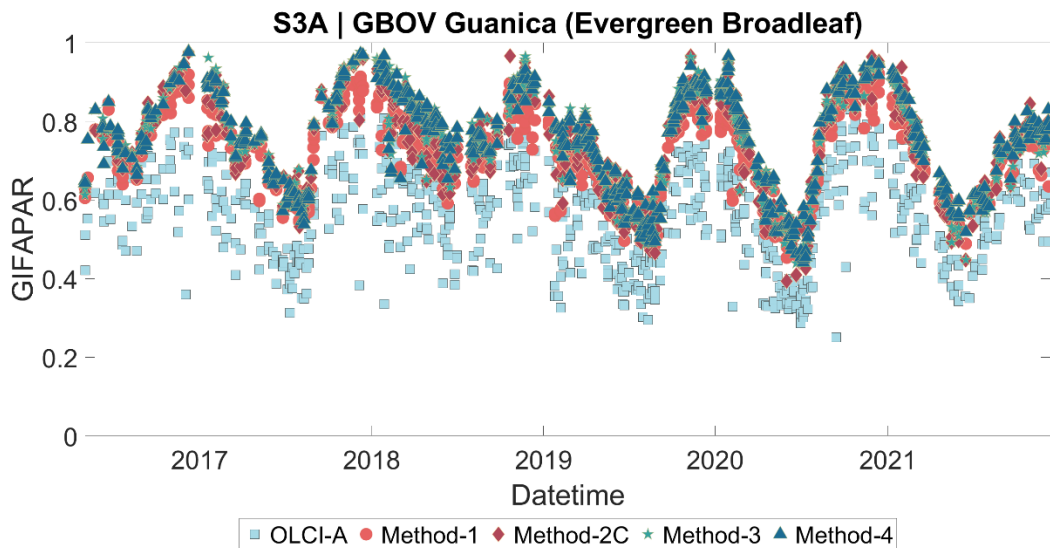


Figure 101: Time series of OLCI-A GIFAPAR (blue-sky) and four methods for the Guanica site.

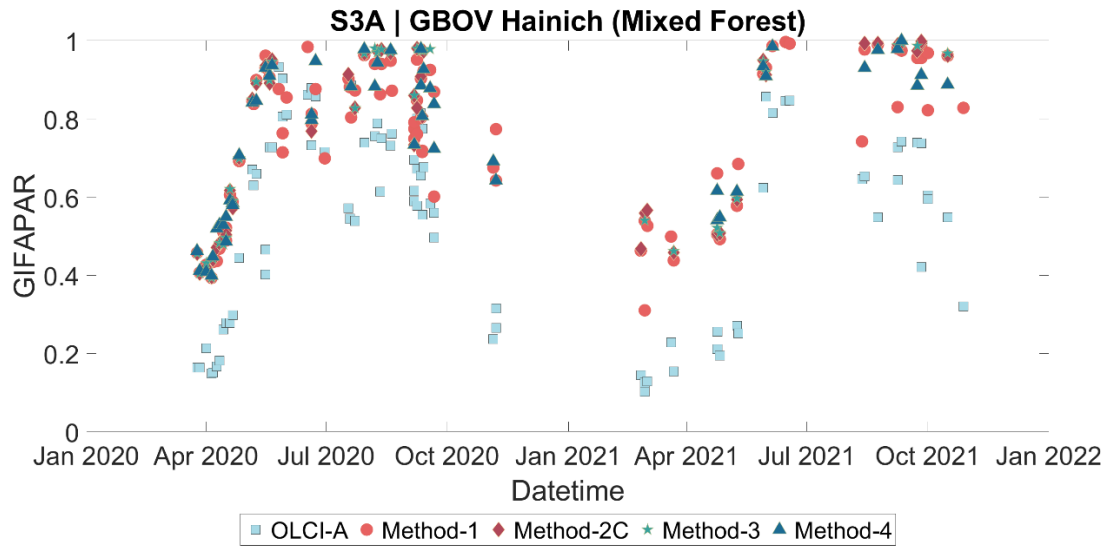


Figure 102: Time series of OLCI-A GIFAPAR (blue-sky) and four methods for the Hainich site.

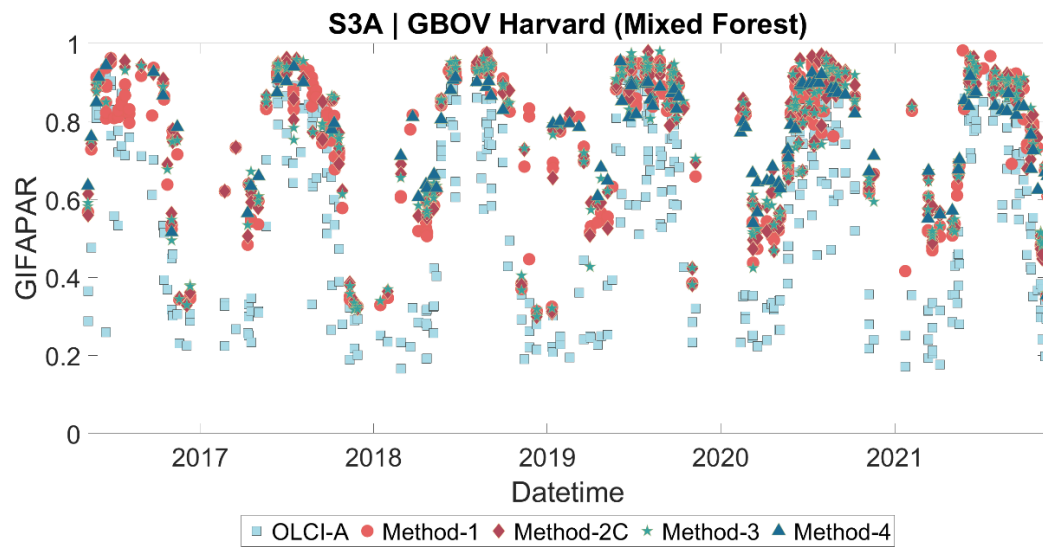


Figure 103: Time series of OLCI-A GIFAPAR (blue-sky) and four methods for the Harvard site.

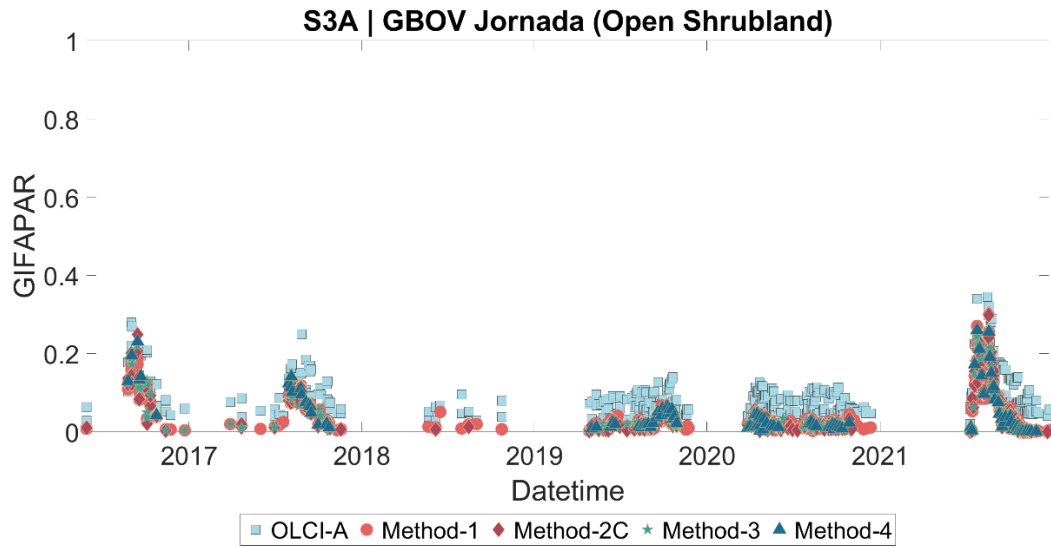


Figure 104: Time series of OLCI-A GIFAPAR (blue-sky) and four methods for the Jornada site.

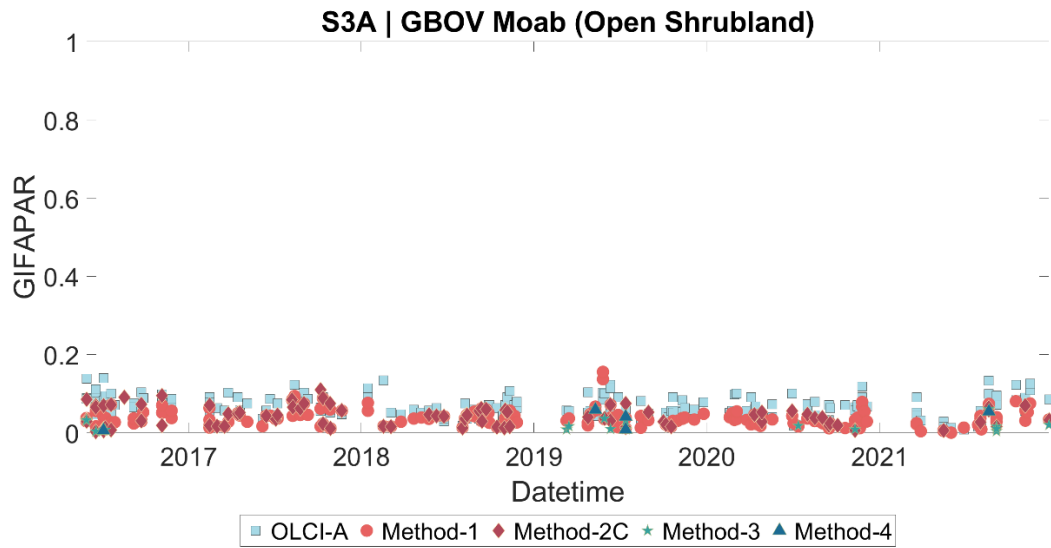


Figure 105: Time series of OLCI-A GIFAPAR (blue-sky) and four methods for the Moab site.

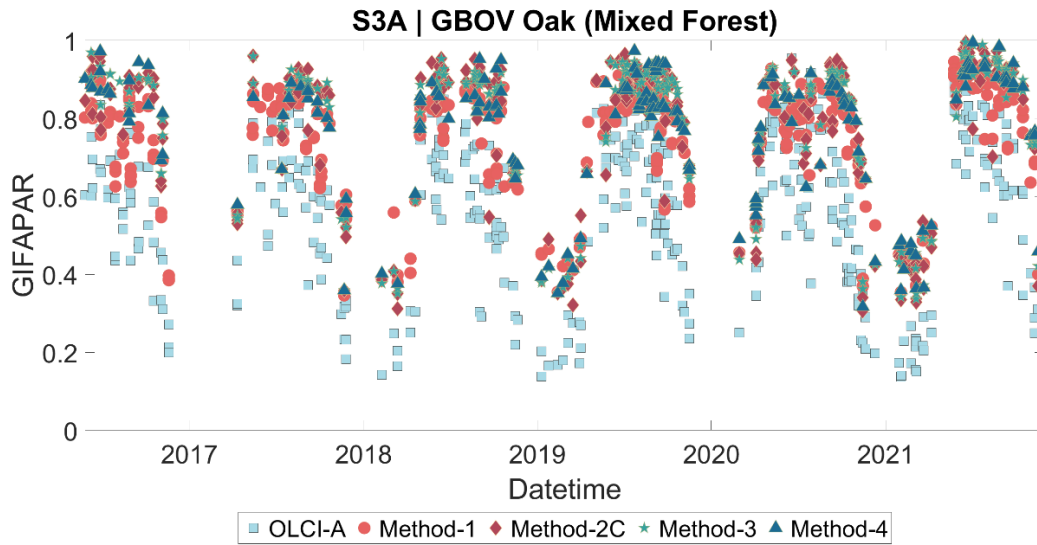


Figure 106: Time series of OLCI-A GIFAPAR (blue-sky) and four methods for the Oak site.

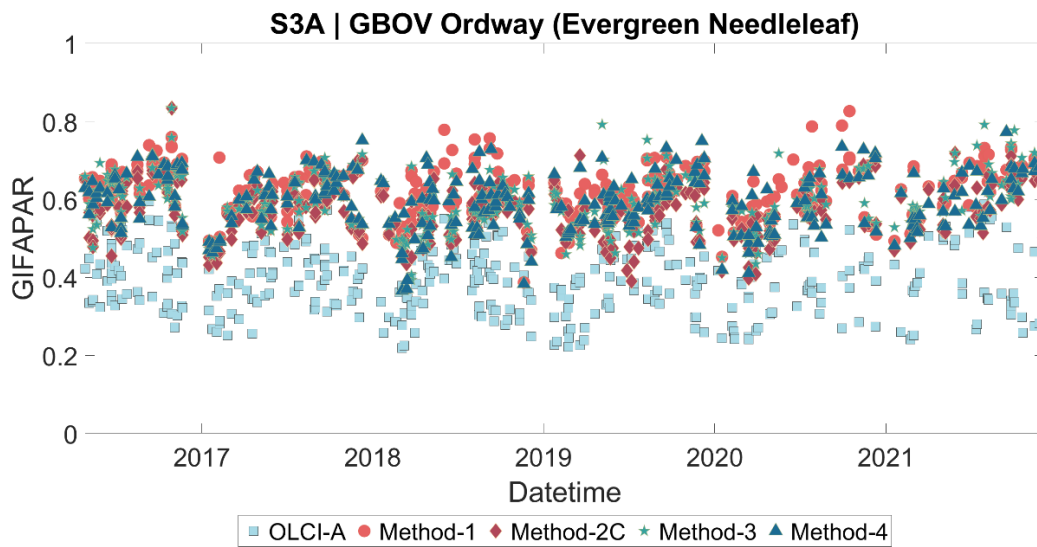


Figure 107: Time series of OLCI-A GIFAPAR (blue-sky) and four methods for the Ordway site.

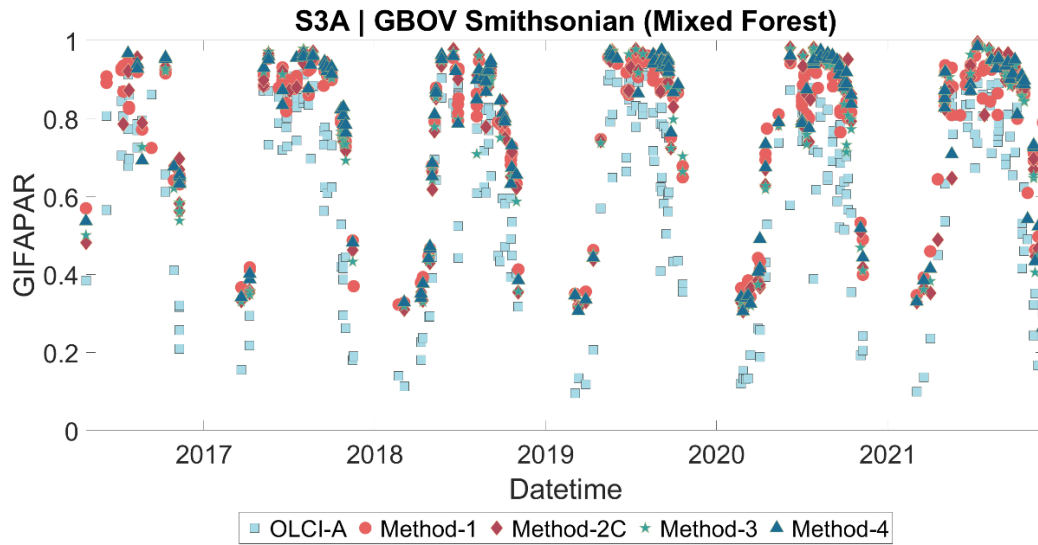


Figure 108: Time series of OLCI-A GIFAPAR (blue-sky) and four methods for the Smithsonian site.

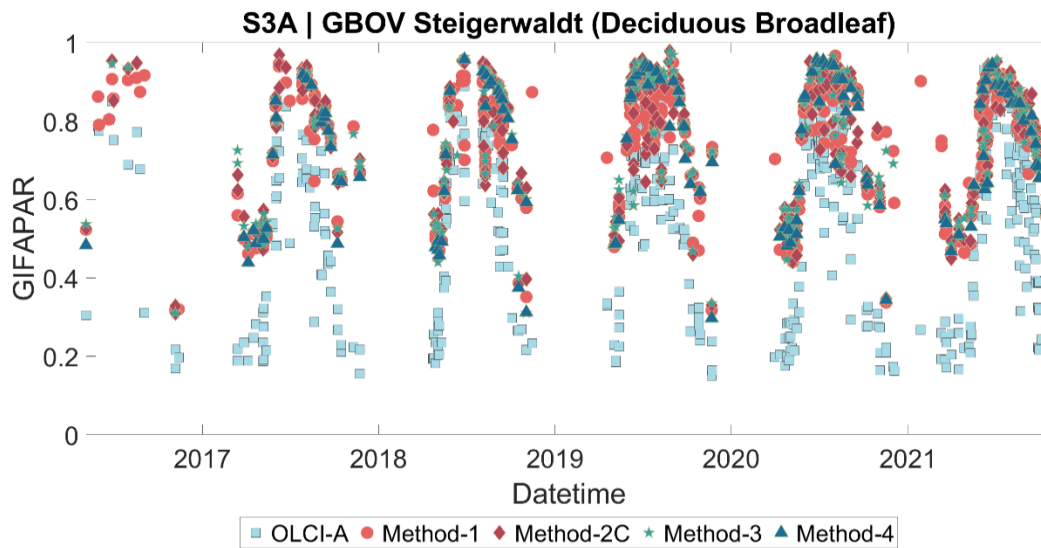


Figure 109: Time series of OLCI-A GIFAPAR (blue-sky) and four methods for the Steigerwaldt site.

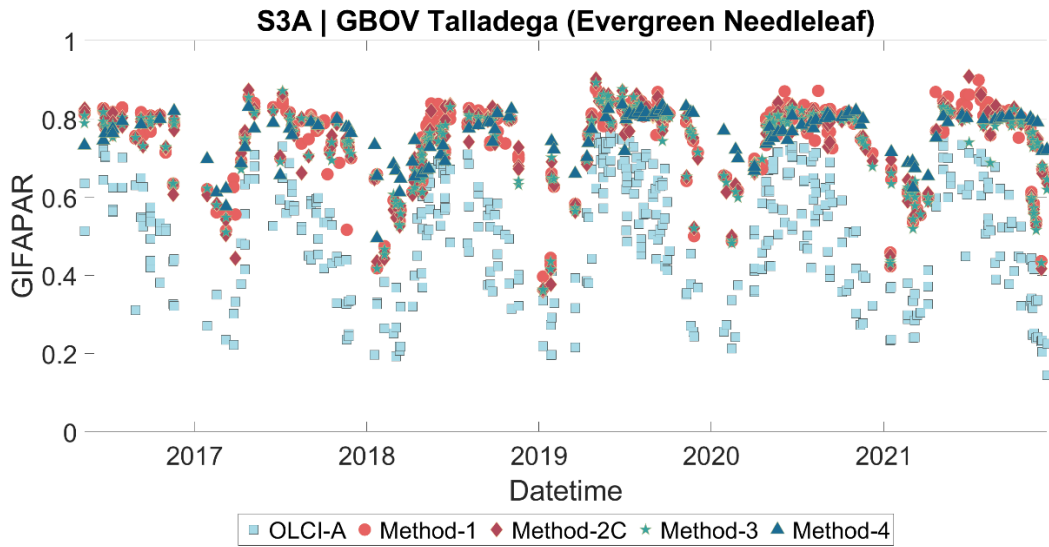


Figure 110: Time series of OLCI-A GIFAPAR (blue-sky) and four methods for the Talladega site.

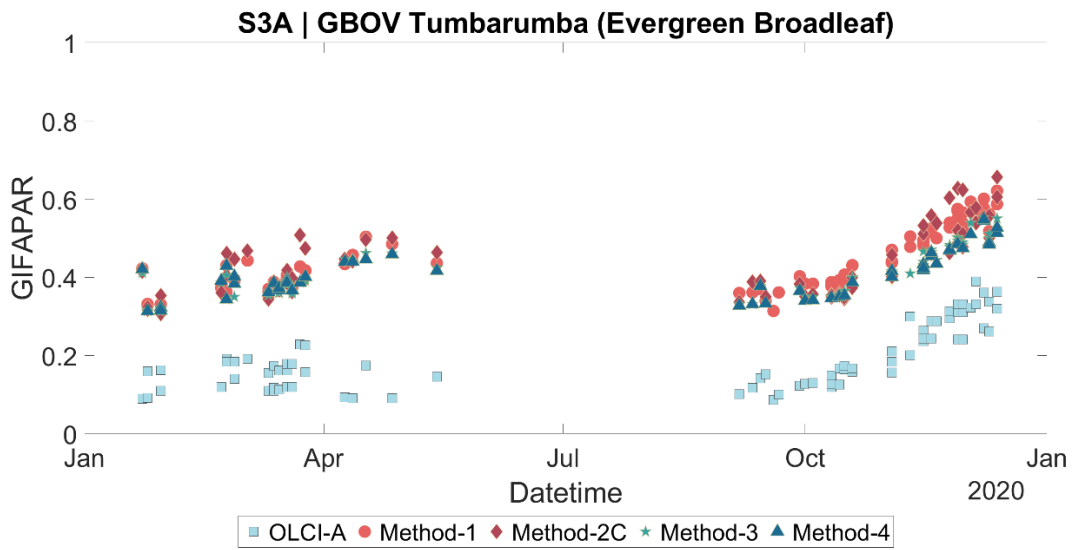


Figure 111: Time series of OLCI-A GIFAPAR (blue-sky) and four methods for the Tumbarumba site.

4.1.5 OLCI-B

Figure 112 to Figure 123 show the temporal profiles of GBOV LP4 against those of OLCI-B GIFAPAR. Overall, there are similar seasonal trajectories between OLCI-B and GBOV. The pattern is similar to OLCI-A, with higher values of GBOV than those of OLCI-B for forest classes. Similarly, grassland and shrubland classes show lower values than OLCI-B. Furthermore, the number of GBOV values after filtering must be increased to perform the validation, mainly in grasslands and shrublands sites (i.e., Moab, Central Plains).

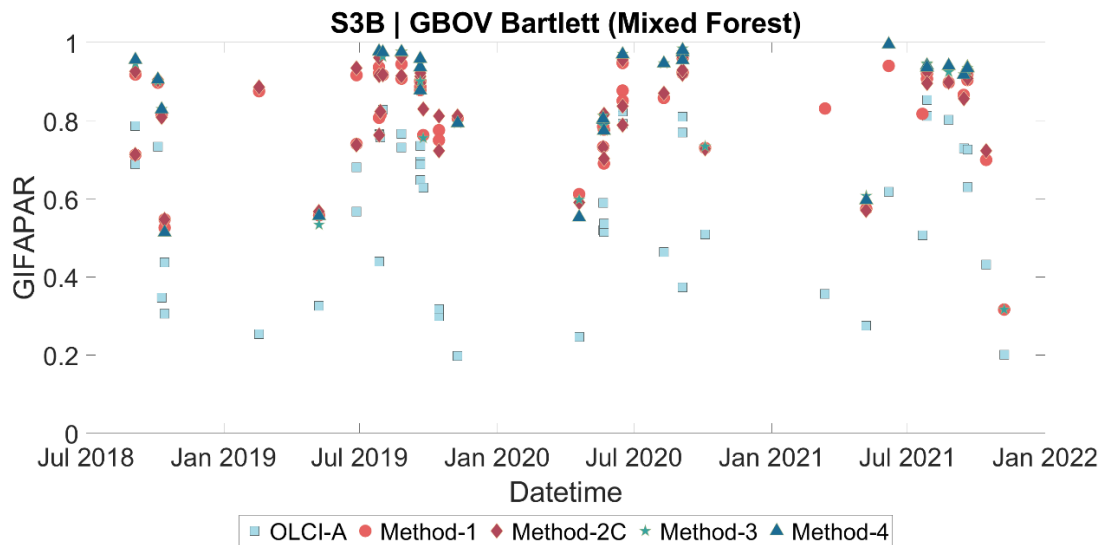


Figure 112: Time series of OLCI-B GIFAPAR (blue-sky) and four methods for the Bartlett site.

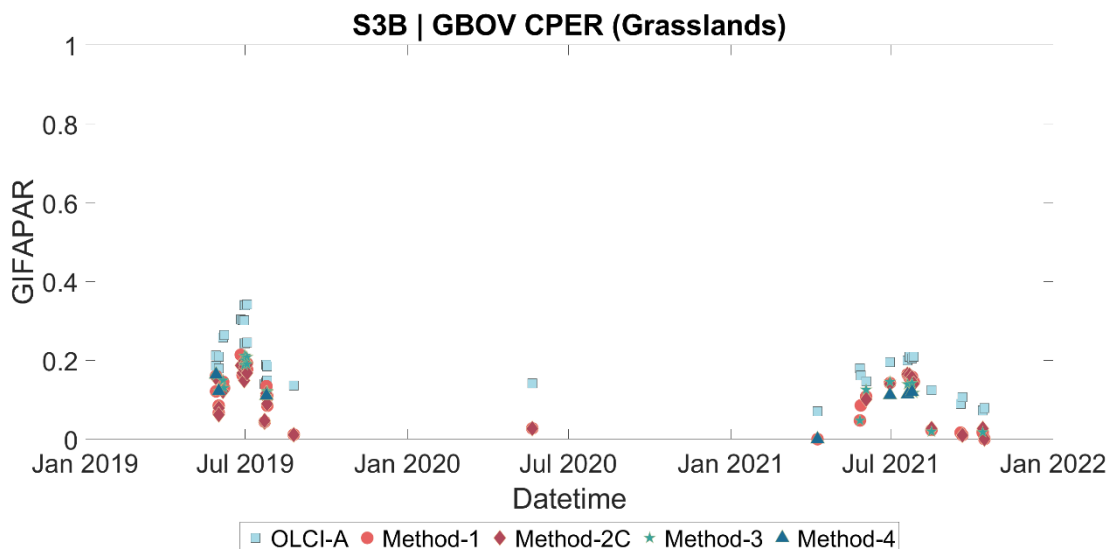


Figure 113: Time series of OLCI-B GIFAPAR (blue-sky) and four methods for the CPER site.

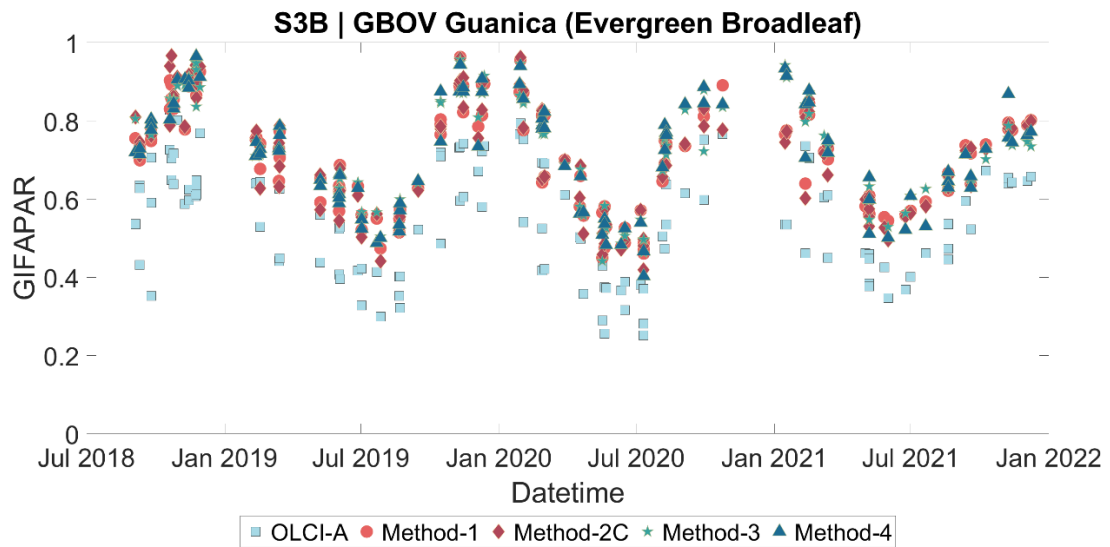


Figure 114: Time series of OLCI-B GIFAPAR (blue-sky) and four methods for the Guanica site.

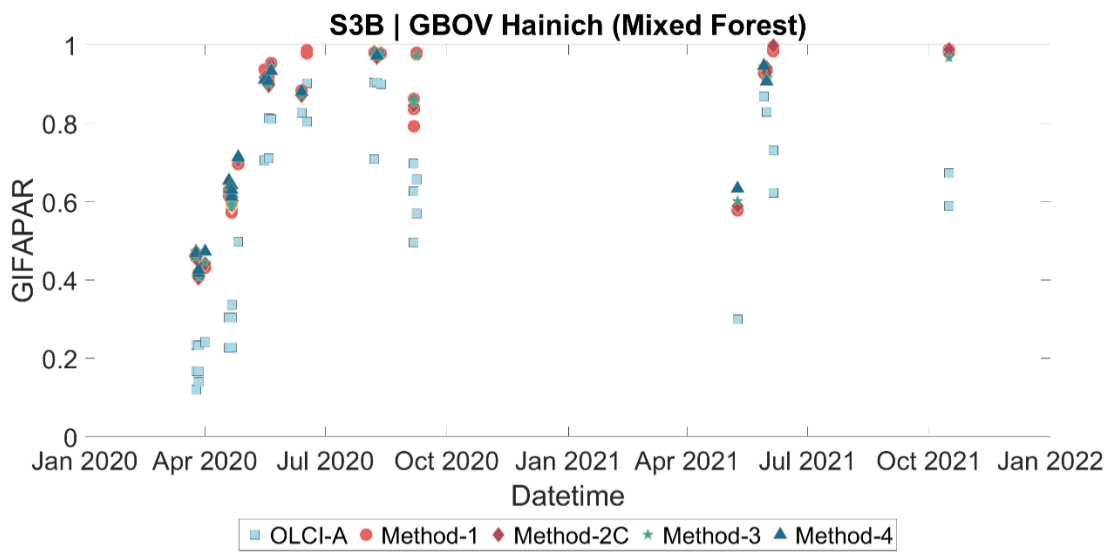


Figure 115: Time series of OLCI-B GIFAPAR (blue-sky) and four methods for the Hainich site.

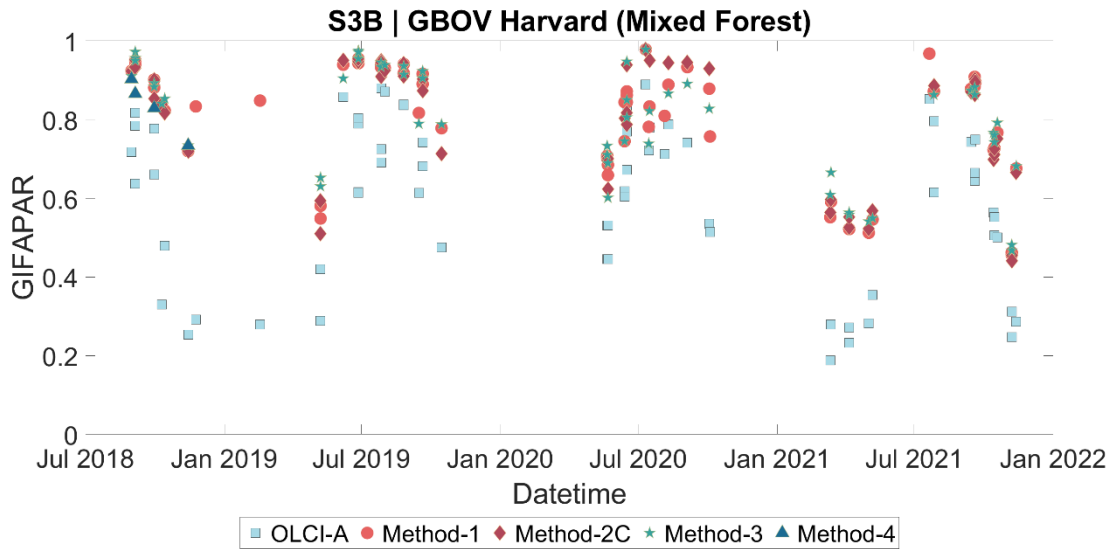


Figure 116: Time series of OLCI-B GIFAPAR (blue-sky) and four methods for the Harvard site.

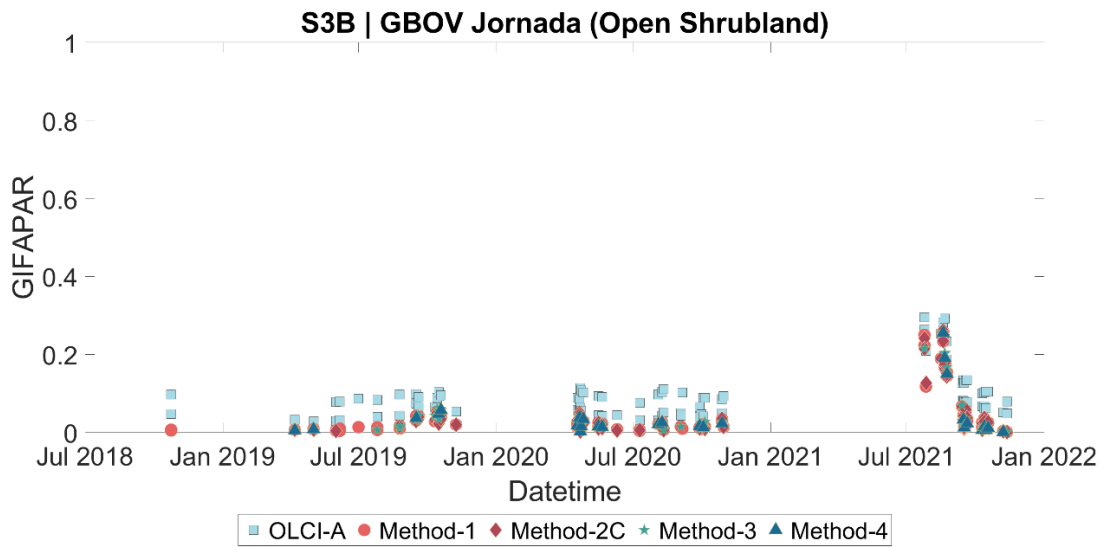


Figure 117: Time series of OLCI-B GIFAPAR (blue-sky) and four methods for the Jornada site.

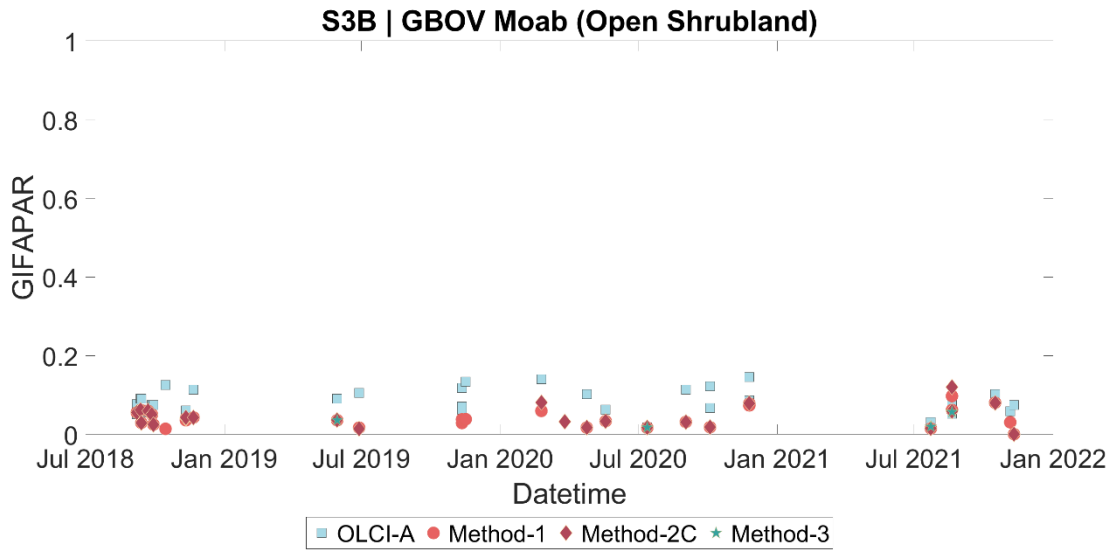


Figure 118: Time series of OLCI-B GIFAPAR (blue-sky) and four methods for the Moab site.

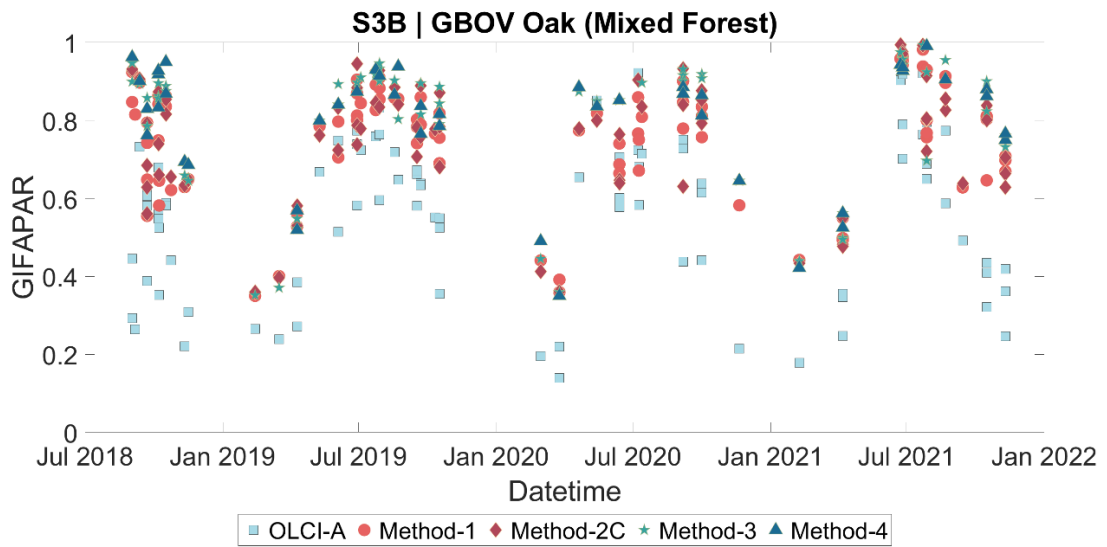


Figure 119: Time series of OLCI-B GIFAPAR (blue-sky) and four methods for the Oak site.

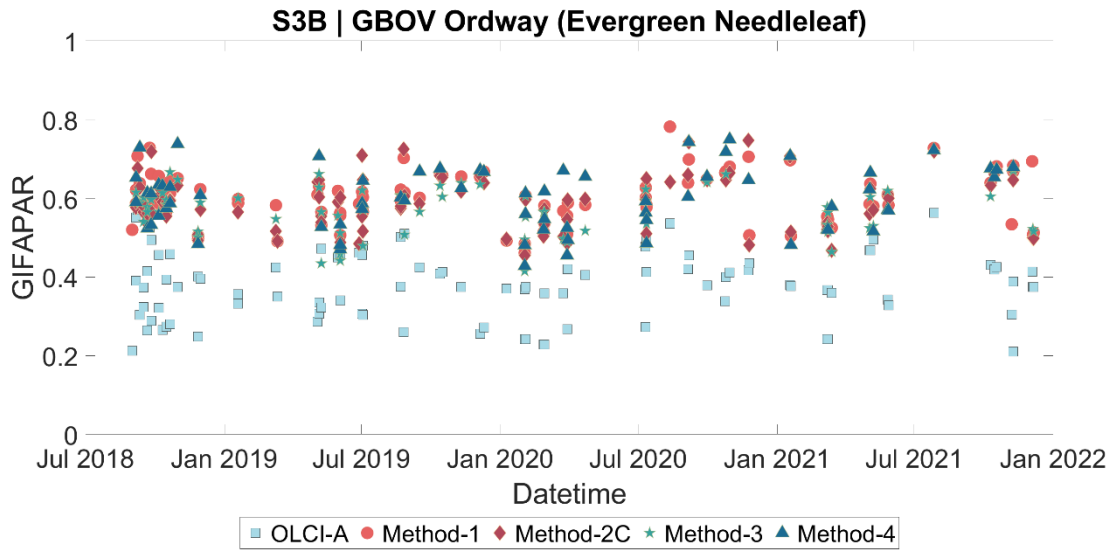


Figure 120: Time series of OLCI-B GIFAPAR (blue-sky) and four methods for the Ordway site.

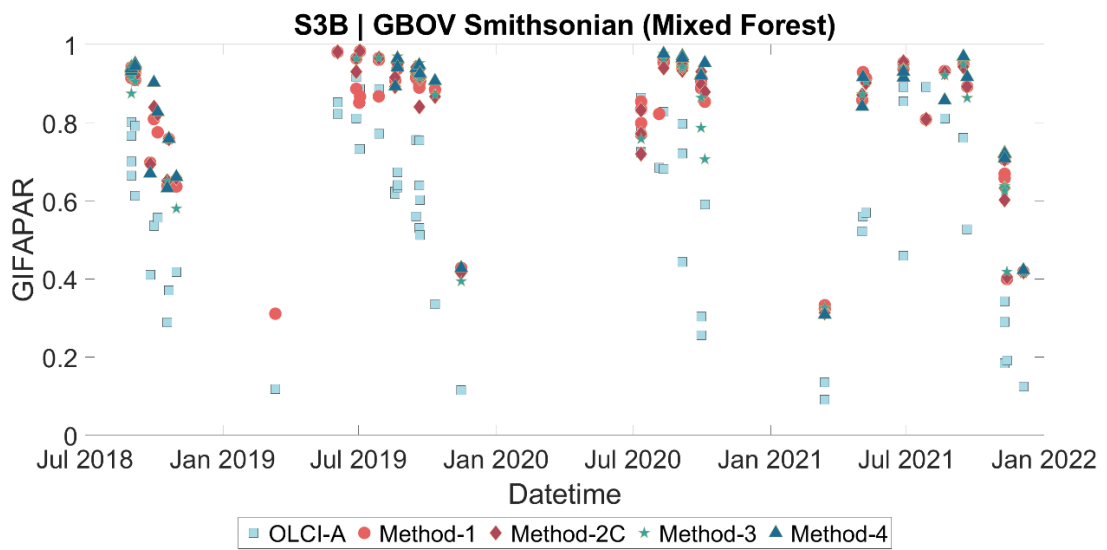


Figure 121: Time series of OLCI-B GIFAPAR (blue-sky) and four methods for the Smithsonian site.

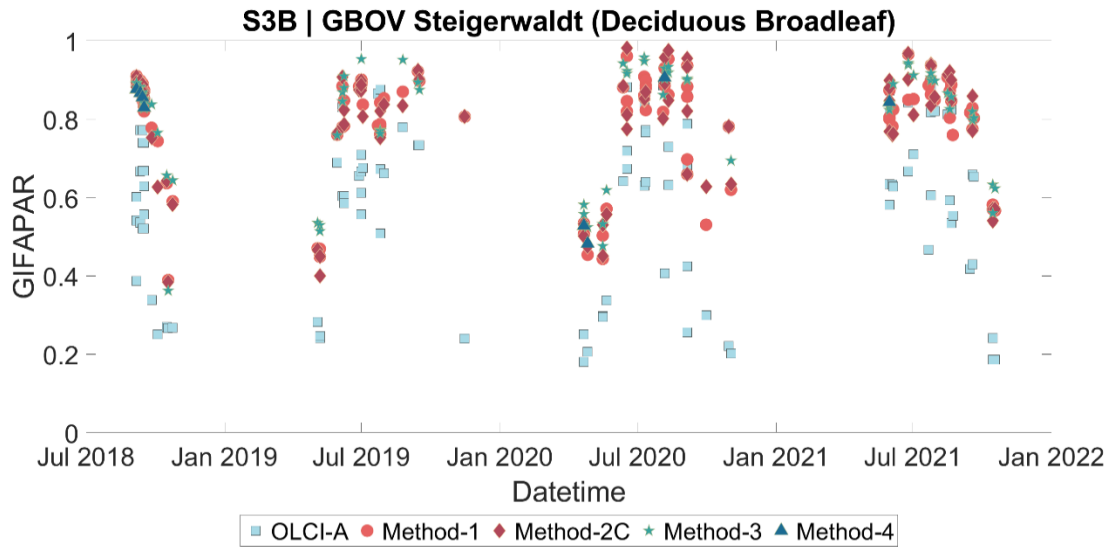


Figure 122: Time series of OLCI-B GIFAPAR (blue-sky) and four methods for the Steigerwaldt site.

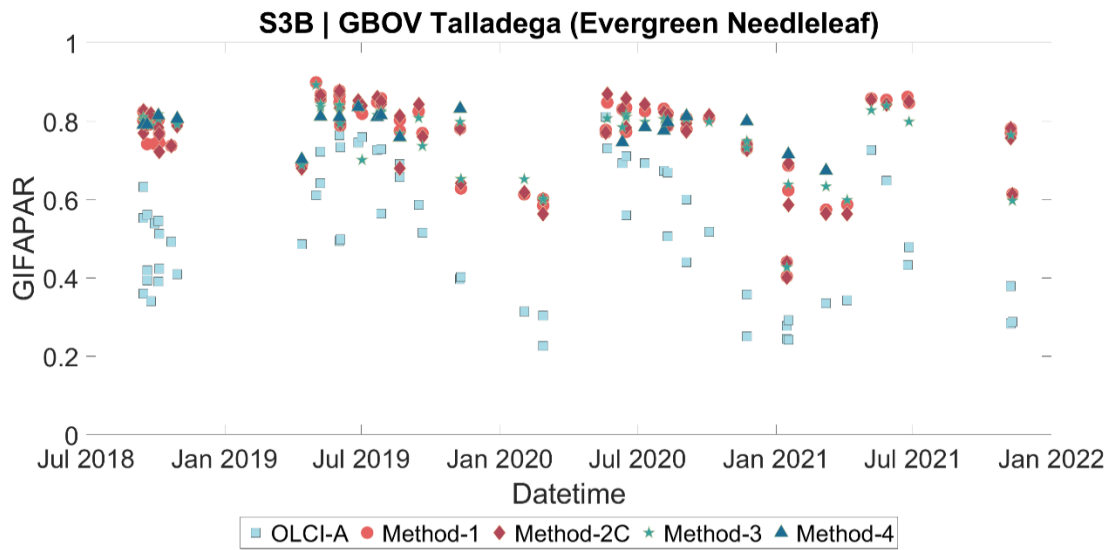


Figure 123: Time series of OLCI-B GIFAPAR (blue-sky) and four methods for the Talladega site.

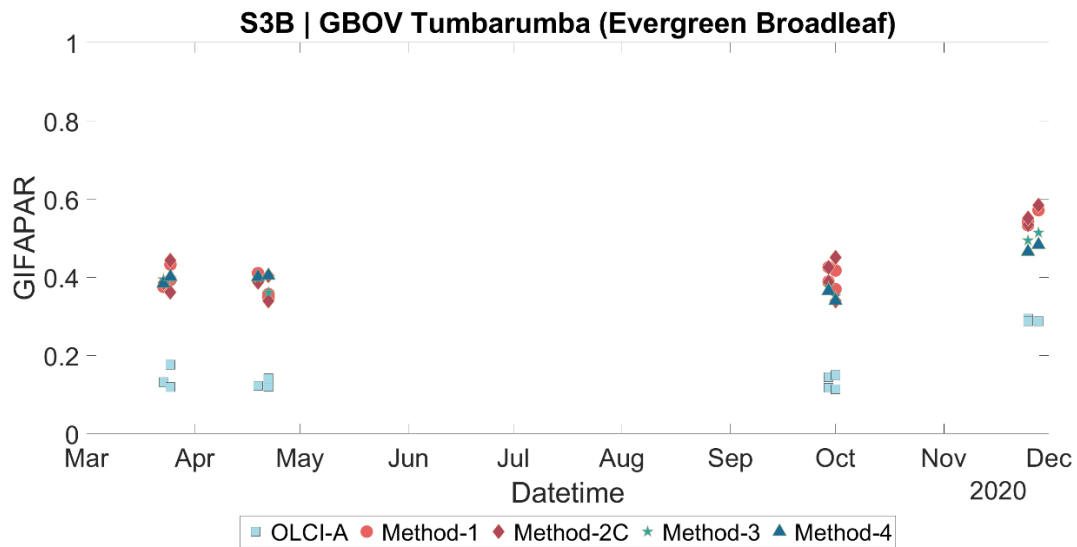


Figure 124: Time series of OLCI-B GIFAPAR (blue-sky) and four methods for the Tumbarumba site.

4.1.6 TAYLOR DIAGRAM RESULTS

The tables below represent the values of the Taylor diagram for the four evaluated methods, taking into consideration OLCI-A and OLCI-B for the 13 GBOV sites. Method 4 (focus on ESU measurement) provides better results, whilst method 1 (all MERMAID pixels) provides the worst results by considering the heterogeneity of the sites.

OLCI-A																
Sites	Method-1				Method-2				Method-3				Method-4			
	N	R ²	RMSE	BIAS	N	R ²	RMSE	BIAS	N	R ²	RMSE	BIAS	N	R ²	RMSE	BIAS
BART	363	0.43	0.27	-0.21	228	0.53	0.26	-0.20	220	0.53	0.27	-0.21	185	0.63	0.24	-0.19
CPER	280	0.54	0.11	0.10	174	0.45	0.11	0.10	169	0.66	0.10	0.09	159	0.58	0.10	0.09
GUAN	687	0.62	0.17	-0.16	638	0.64	0.18	-0.16	624	0.62	0.19	-0.17	644	0.66	0.18	-0.16
HAIN	87	0.64	0.27	-0.23	52	0.70	0.31	-0.28	43	0.81	0.29	-0.27	55	0.68	0.28	-0.24
HARV	427	0.65	0.24	-0.19	307	0.64	0.25	-0.20	296	0.61	0.25	-0.20	192	0.62	0.29	-0.25
JORN	490	0.62	0.06	0.05	353	0.66	0.06	0.05	330	0.66	0.06	0.05	211	0.69	0.06	0.05
MOAB	189	0.23	0.04	0.03	97	0.17	0.06	0.05	25	0.10	0.06	0.05	8	0.07	0.05	0.04
ORNL	411	0.69	0.21	-0.18	291	0.67	0.22	-0.17	282	0.69	0.23	-0.18	242	0.65	0.24	-0.19
OSBS	413	0.04	0.24	-0.22	346	0.02	0.22	-0.19	342	0.06	0.24	-0.21	333	0.02	0.25	-0.23
SCBI	290	0.72	0.21	-0.17	197	0.72	0.24	-0.19	182	0.73	0.24	-0.20	194	0.72	0.24	-0.20
STEI	514	0.63	0.24	-0.20	421	0.64	0.23	-0.17	397	0.60	0.24	-0.19	253	0.69	0.25	-0.21
TALL	437	0.49	0.27	-0.24	373	0.46	0.28	-0.25	366	0.42	0.28	0.26	217	0.17	0.32	-0.30
TUMB	79	0.76	0.25	-0.25	73	0.72	0.25	-0.25	72	0.54	0.24	-0.24	70	0.45	0.24	-0.24

OLCI-B																
Sites	Method-1				Method-2				Method-3				Method-4			
	N	R ²	RMSE	BIAS	N	R ²	RMSE	BIAS	N	R ²	RMSE	BIAS	N	R ²	RMSE	BIAS
BART	50	0.41	0.28	-0.23	45	0.28	0.28	-0.23	31	0.49	0.26	-0.16	32	0.58	0.24	-0.19
CPER	38	0.72	0.09	0.08	30	0.66	0.1	0.09	21	0.65	0.09	0.08	7	0.81	0.06	0.06
GUAN	124	0.81	0.18	-0.17	123	0.78	0.18	-0.16	116	0.66	0.19	-0.17	113	0.68	0.19	-0.17
HAIN	40	0.86	0.25	-0.23	35	0.8	0.28	-0.24	33	0.72	0.29	-0.25	26	0.93	0.26	-0.24
HARV	65	0.68	0.24	-0.21	57	0.71	0.23	-0.20	57	0.69	0.24	-0.21	6	0.59	0.31	-0.28
JORN	94	0.81	0.06	0.05	76	0.81	0.06	0.05	60	0.79	0.06	0.05	32	0.77	0.07	0.06
MOAB	33	0.01	0.06	0.04	28	0.03	0.06	0.04	4	0.29	0.03	0.02	-	-	-	-
ORNL	89	0.61	0.23	-0.19	79	0.56	0.22	-0.18	69	0.63	0.25	-0.21	61	0.55	0.27	-0.22
OSBS	99	0.13	0.24	-0.22	94	0.09	0.24	-0.22	65	0.01	0.25	-0.23	73	0.03	0.27	-0.25
SCBI	67	0.59	0.28	-0.24	60	0.57	0.29	-0.25	41	0.61	0.31	-0.27	41	0.54	0.35	-0.32
STEI	100	0.59	0.25	-0.21	88	0.66	0.25	-0.21	77	0.56	0.25	-0.20	12	0.58	0.29	-0.27
TALL	65	0.46	0.28	-0.25	59	0.52	0.27	-0.24	54	0.38	0.28	-0.26	22	0.14	0.28	-0.26
TUMB	13	0.91	0.26	-0.26	13	0.93	0.25	-0.25	8	0.91	0.27	-0.27	8	0.86	0.27	-0.26

4.1.7 Sentinel-3A and 3B biophysical variables inter-annual variability results

Monthly mean GIFAPAR and OTCI were computed from S3A and S3B MERMAID extractions for all years where data were available over the core CEOS, S3VT and GBOV sites (Table 6). Annual temporal profiles have been created to assess GIFAPAR and OTCI variability between years and compare the agreement between S3A and S3B.

The interannual variability of GIFAPAR and OTCI differs among the selected sites. Several locations, such as Smithsonian SCB, display a relatively steady pattern in values, seasonal patterns, and the timing of peak occurrences (Figure 125). Contrarily, several sites like Zigzag Creek exhibit more significant variability between years, with fluctuating peaks and valleys throughout the year (Figure 126). S3A and S3B exhibit similarities, with similar seasonal trends observed for GIFAPAR and OTCI and similar ranges of values.

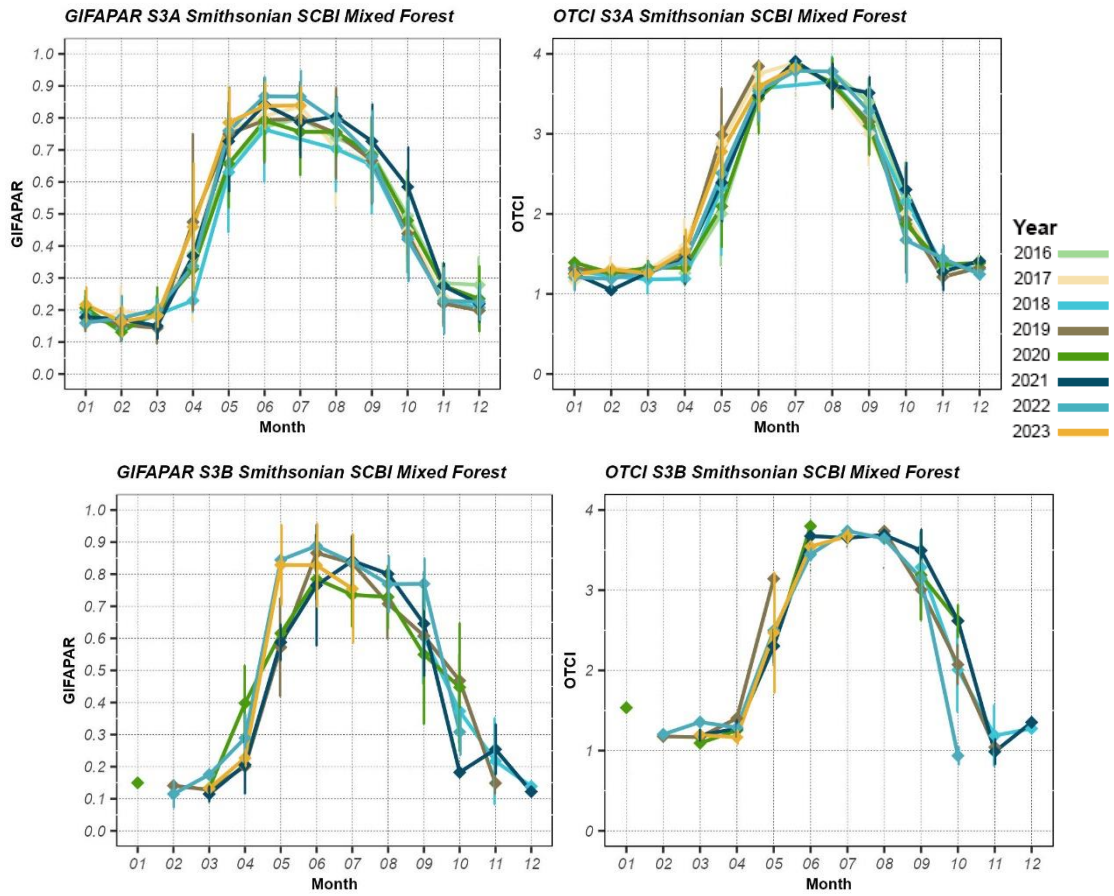


Figure 125: Time series of monthly mean GIFAPAR (left) and OTCI (right) for S3A (top) and S3B (bottom) for Smithsonian SCBI.

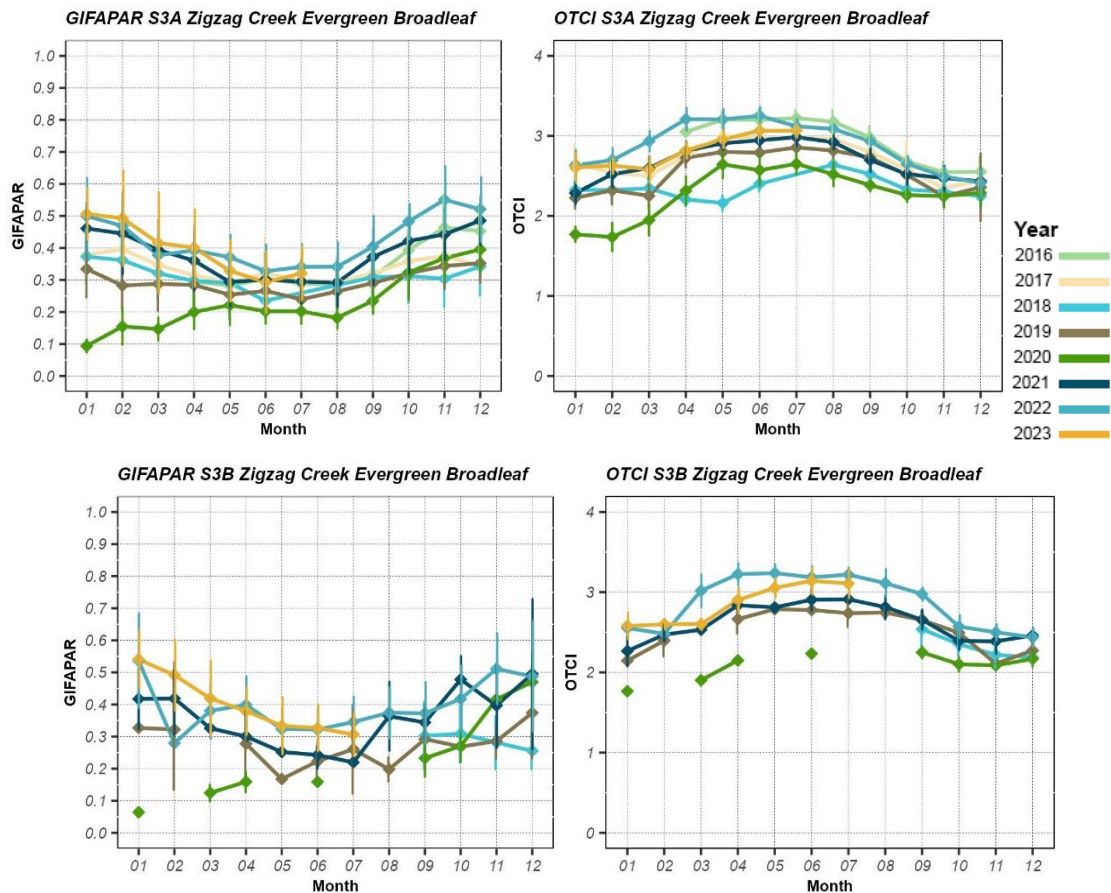


Figure 126: Time series of monthly mean GIFAPAR (left) and OTCI (right) for S3A (top) and S3B (bottom) for Zigzag Creek.

4.2 [OLCI-L2LRF-CV-410 & OLCI-L2LRF-CV-420] – Cloud Masking & Surface Classification for Land Products

For the August 2023 reporting the prototype validation results for OLCI cloud mask using sky cameras (SC) are based on two sites, currently validated independently. The two sites are located at La Sapienza University in Rome, Italy and at the University of Valencia in Spain.

For the Rome site the validation was switched to SC 2, due to some instabilities in azimuth location of SC1. Meaning, the camera rotated horizontally over time.

The coordinates of SC 2 at La Sapienza University are:

- ❖ Lat: 41.90148
- ❖ Lon: 12.51575

The coordinates of the location of SC 1 at University of Valencia are:

- ❖ Lat: 39.50832
- ❖ Lon: -0.42084

The sun being close to nadir in the SC image still leads to some overestimation of clouds in the SC data. A method to hopefully reduce this effect is currently still under development.

4.2.1 Sky Camera based validation – prototype results July 2023

4.2.1.1 Rome

Figure 131 and Figure 132 show the prototype validation results for the Rome site in August 2023. The weather in August around Rome is mostly dry, with occasional occurrence of cloudy days and rainfall on 6 days. (see Figure 127 and Figure 128).

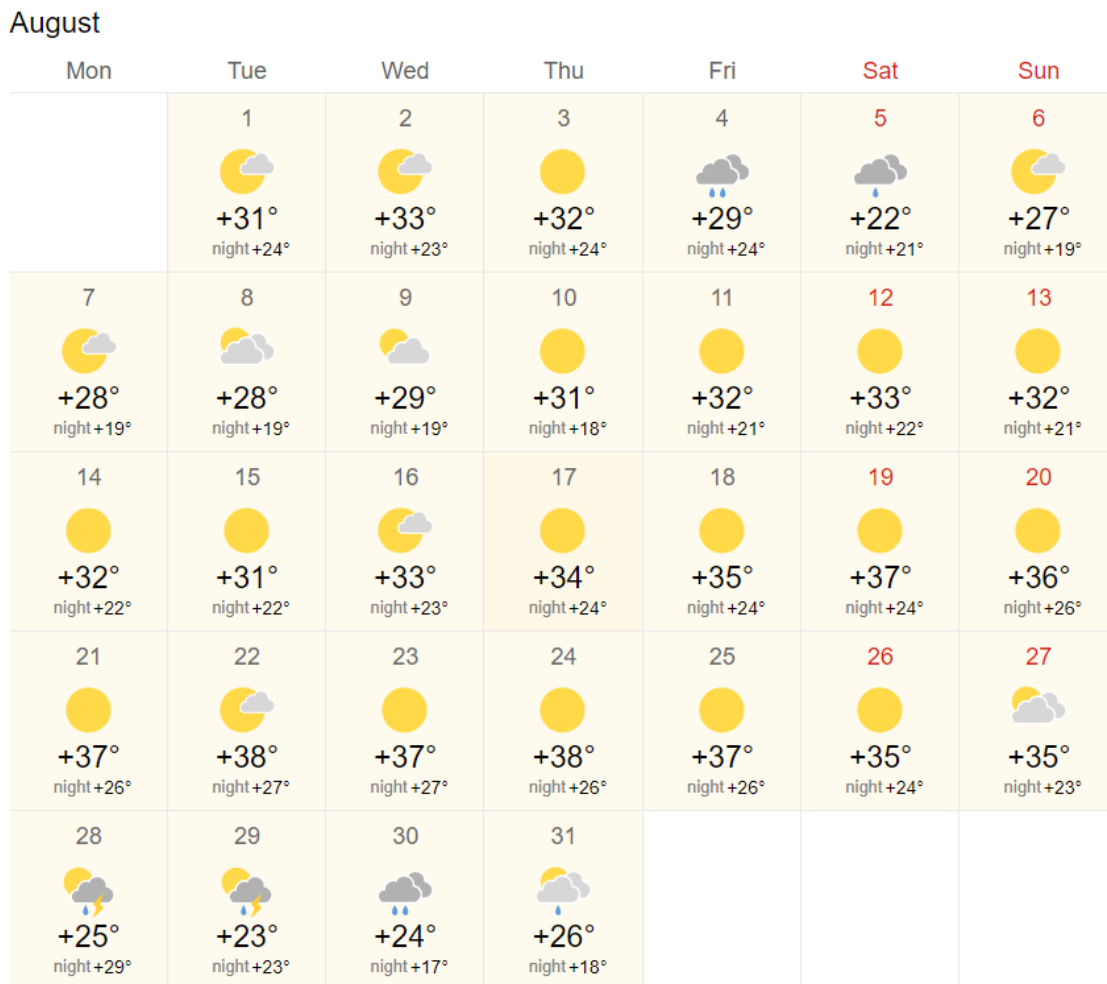


Figure 127: Temperature and cloud cover Rome, August 2023 (source: <https://world-weather.info/forecast/italy/rome/August-2023/>)

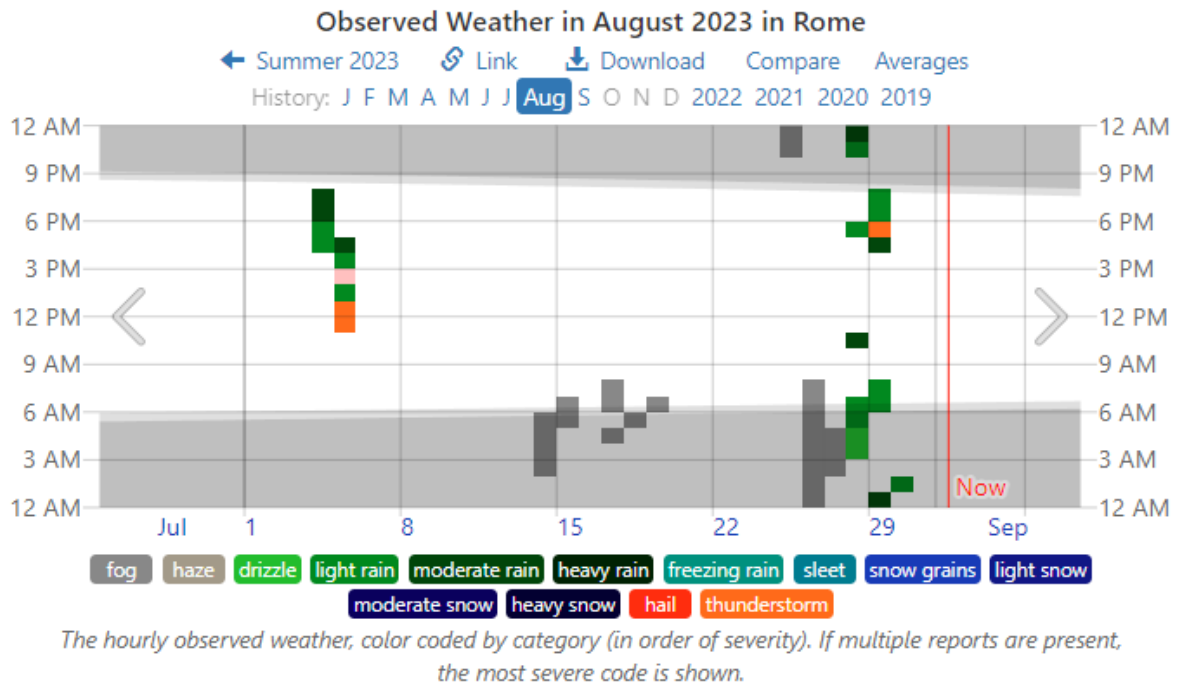
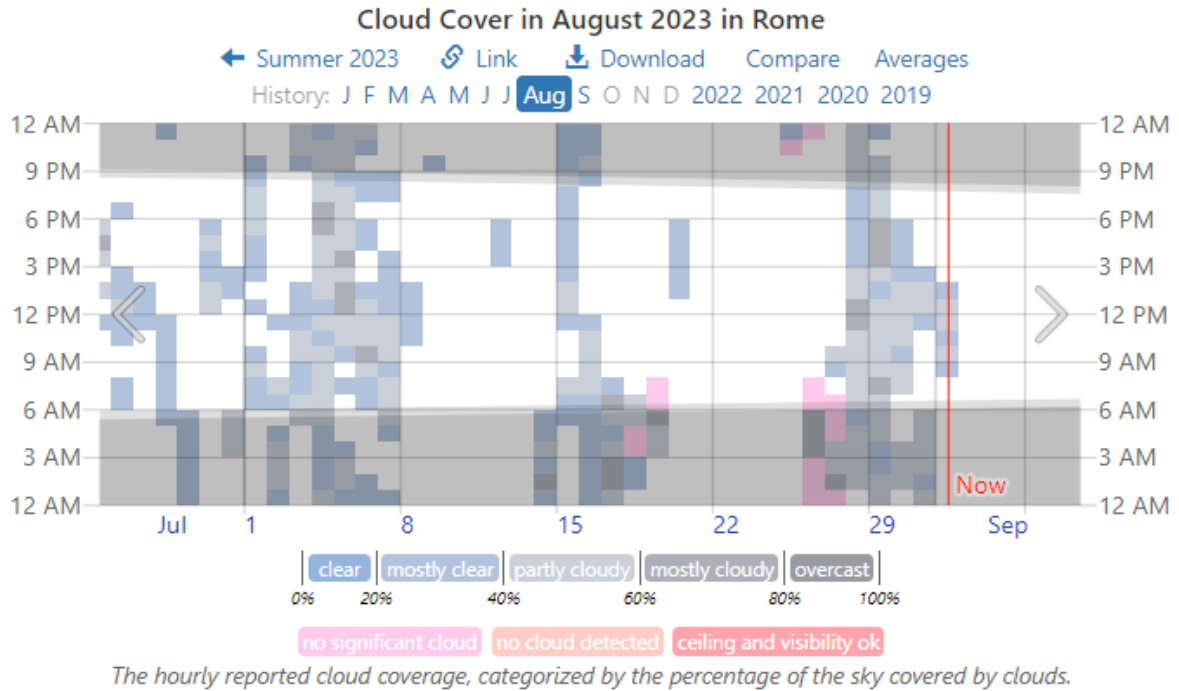


Figure 128: Cloud observations and precipitation Rome, August 2023 (source: <https://weatherspark.com/h/m/71779/2023/6/Historical-Weather-in-August-2023-in-Rome-Italy>)

Since March 2023 a new method was introduced to automatically remove all matchups between the SC images and the OLCI observation with OZA above 30°.

In August, there was an error of data transfer between University of Maryland and Brockmann Consult, therefore only sky camera (SC) images between first and twelfth of August were available. This led to only 9 acquisitions below 30 degree OZA matching the SC images. As shown in the previous months, the high sun elevations in combination with no physical shading device on the sky cameras leads to high sun interference. In August, this is again the case.

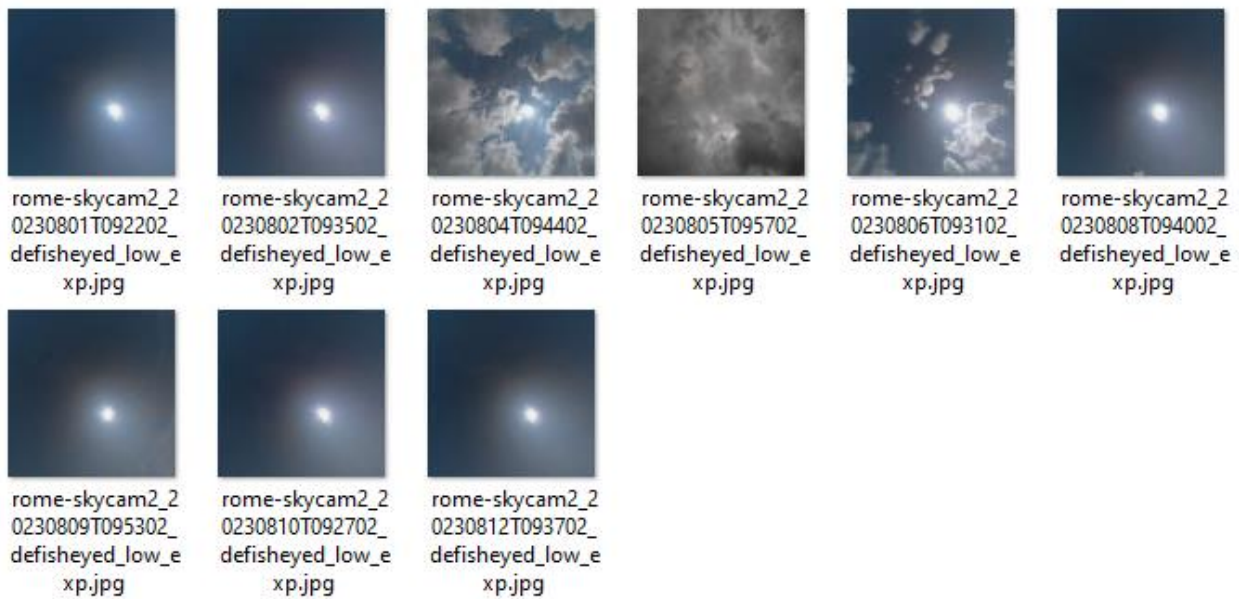


Figure 129: Sky camera acquisitions over Rome during Sentinel-3 OLCI overpass

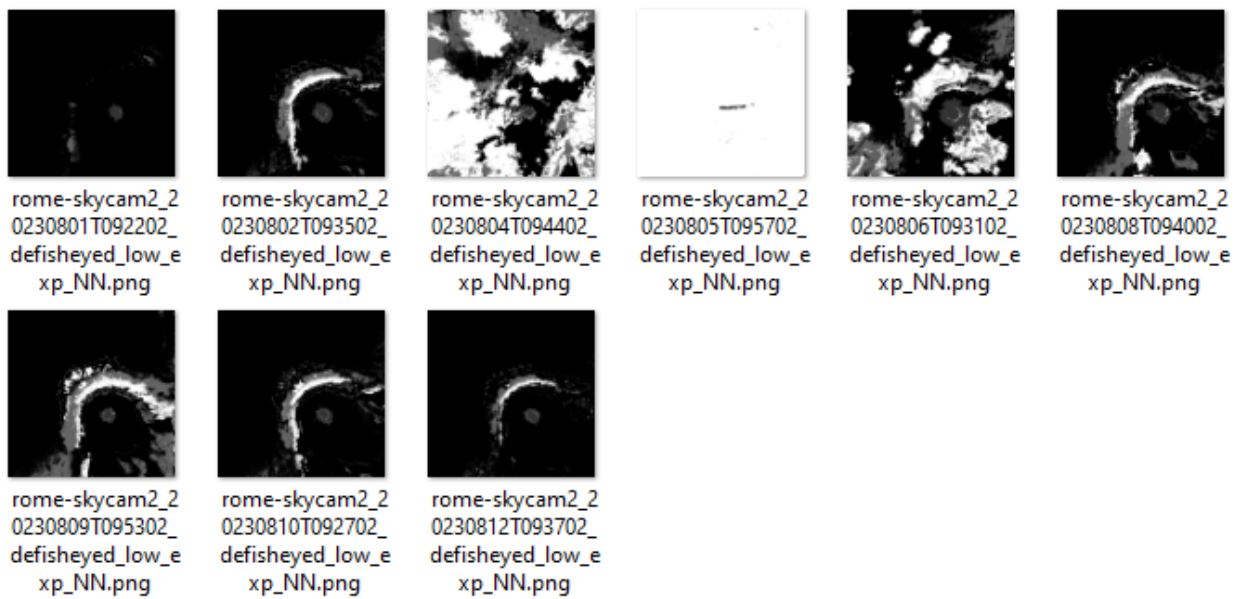


Figure 130: Classified sky camera acquisitions over Rome during Sentinel-3 OLCI overpass

The confusion matrices in Figure 131 and shows the validation results for the OLCI cloud flags including the margin. Only OLCI observations with a OZA below 30 have been considered to lower the influence of parallax between the OLCI observation and the SC observation. When comparing to the SC images, it is obvious that more than 3 observations are classified as cloud by the SC classification, which in turn leads to lower validation results than expected.

When neglecting the margin (see Figure 132) the margin this effect becomes stronger since less pixels are classified as cloud by the L2 cloud flag.

Overall, it can be stated that the L2 cloud flagging is stable, and deviations are caused by unreliable SC classifications, due to high sun elevations.

Rome SC 2 autom. classif. vs. OLCI L2 LFR Cloud & Ambiguous & Margin
August 2023
Sky Camera 1

Class		Clear	Cloud	Sum	U A	E
		CLEAR	4	2		
OLCI L2 LFR	CLOUD	0	3	3	100.0	0.0
	Sum	4	5	9		
	P A	100.0	60.0		OA:	77.78
	E	0.0	40.0		BOA:	80.0

Scotts Pi: 0.549
Krippendorfs alpha: 0.575
Cohens kappa: 0.571

Figure 131: Confusion matrix showing validation results for OLCI L2 cloud screening including margin against SC1 automated classification.

Rome SC 2 autom. classif. vs. OLCI L2 LFR Cloud & Ambiguous
August 2023
Sky Camera 1

Class		Clear	Cloud	Sum	U A	E
		CLEAR	4	4		
OLCI L2 LFR	CLOUD	0	1	1	100.0	0.0
	Sum	4	5	9		
	P A	100.0	20.0		OA:	55.56
	E	0.0	80.0		BOA:	60.0

Scotts Pi: 0.0
Krippendorfs alpha: 0.055
Cohens kappa: 0.181

Figure 132: Confusion matrix showing validation results for OLCI L2 cloud screening excluding margin against SC1 automated classification

4.2.1.2 Valencia

Figure 131 and Figure 132 show the prototype validation results for the Valencia site in August 2023. The weather in August around Valencia is very arid, with very occasional cloud covered days (see Figure 133).

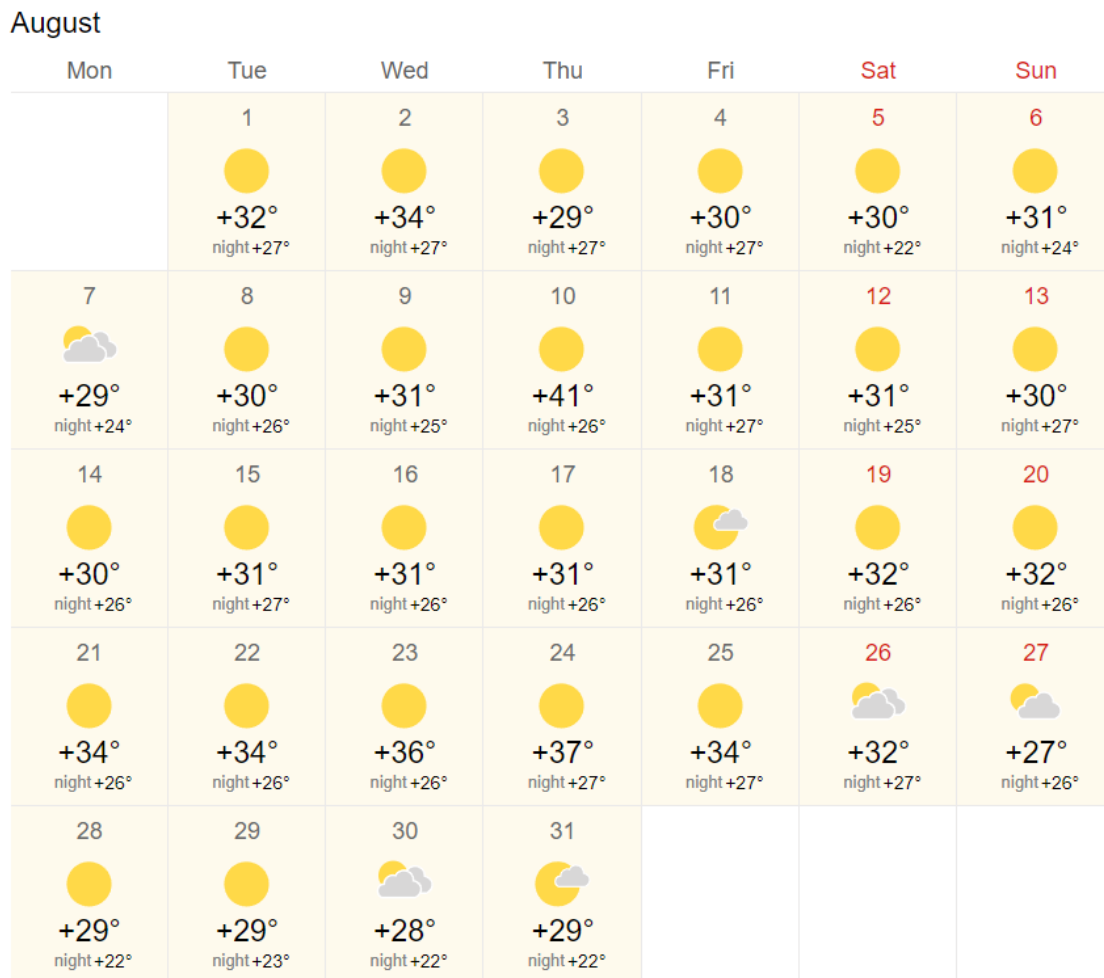


Figure 133: Temperature and cloud cover Valencia, August 2023 (source: <https://world-weather.info/forecast/spain/valencia/August-2023/>)

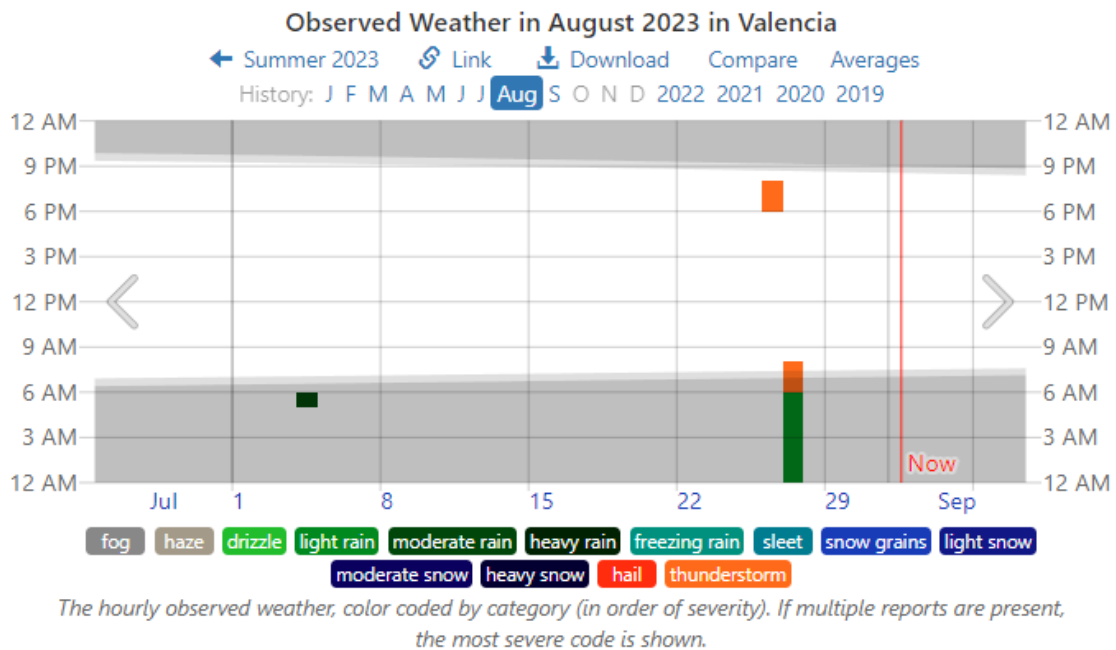
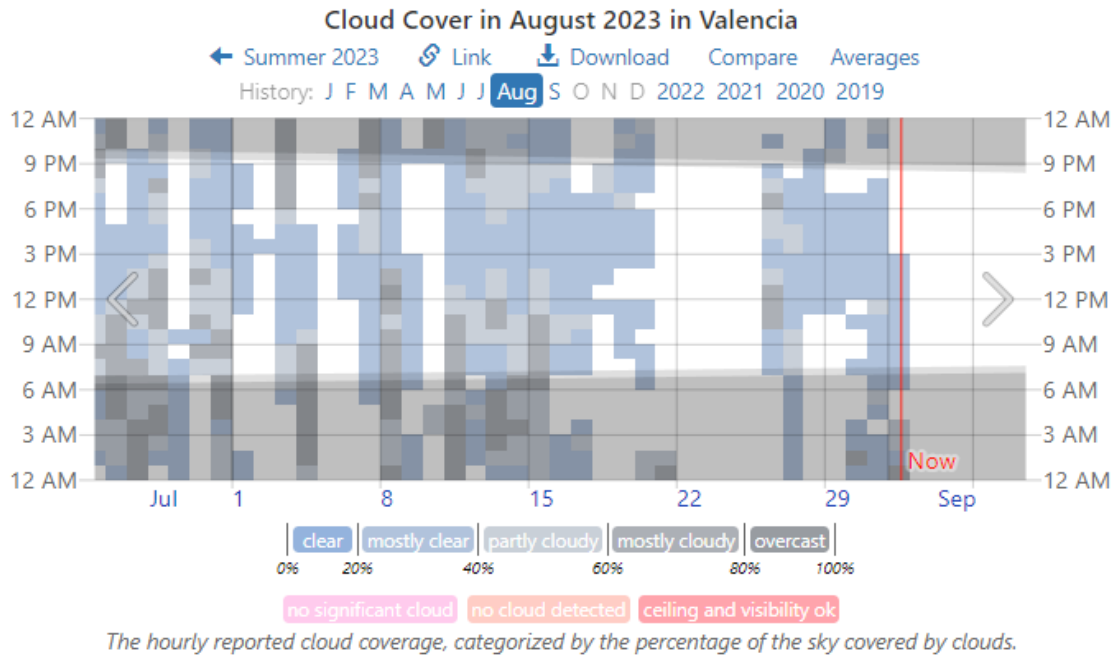


Figure 134: Cloud observations and precipitation Valencia, August 2023 (source: <https://weatherspark.com/h/m/42614/2023/6/Historical-Weather-in-August-2023-in-Valencia-Spain#Figures-CloudCover>)

As already stated for the Rome site, in August, there was an error of data transfer between University of Maryland and Brockmann Consult, therefore only SC images between first and twelfth of August were available. This led to only 8 acquisitions below 30 degree OZA matching the SC images.

Only 5 of the SC observation show clear sky conditions (see Figure 135). Since the sun is close to the centre of all acquisitions, the SC classification (see Figure 136) show a bit of cloud bias. When the majority of the

reference window, used for the classification, is classified as sun, those observations are not used for the comparison. Leading to only 11 out of 15 comparable matches.

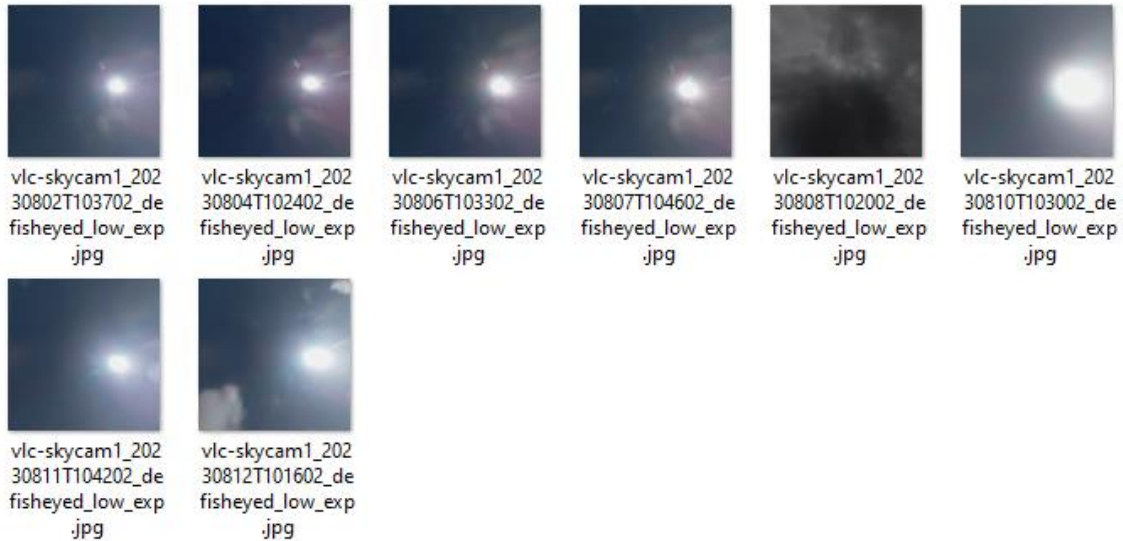


Figure 135: Sky camera acquisitions over Valencia during Sentinel-3 OLCI overpass

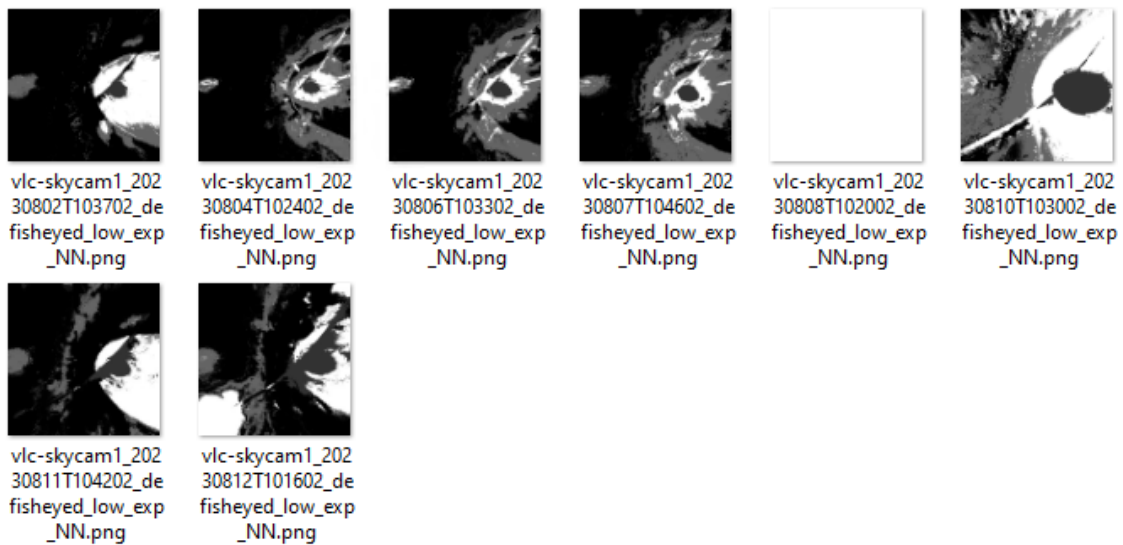


Figure 136: Classified sky camera acquisitions over Valencia during Sentinel-3 OLCI overpass

Figure 137 shows the validation results for the OLCI cloud flags including the margin. Only OLCI observations with a OZA below 30 have been considered to lower the influence of parallax between the OLCI observation and the SC observation.

The SC classification of the Valencia SC is better trained to identify the sun in the images therefore, the interference of sun is a bit better, leading to less false classifications. If pixels of the SC image are classified as sun, and the majority of the used window of the SC image shows mostly sun, those acquisitions are neglected for the comparison. Therefore, the reference is lowered to only 5 matchups.

The number of matchups is too low to draw sound conclusions.

Valencia SC 1 autom. classif. vs. OLCI L2 LFR Cloud & Ambiguous & Margin
August 2023
Sky Camera 1

OLCI L2 LFR	Class	Clear	Cloud	Sum	U A	E
	CLEAR	3	1	4	75.0	25.0
	CLOUD	0	1	1	100.0	0.0
	Sum	3	2	5		
	P A	100.0	50.0		OA:	80.0
	E	0.0	50.0		BOA:	75.0

Scotts Pi: 0.523
Krippendorfs alpha: 0.571
Cohens kappa: 0.545


Figure 137: Confusion matrix showing validation results for OLCI L2 cloud screening including margin against SC1 automated classification

Valencia SC 1 autom. classif. vs. OLCI L2 LFR Cloud & Ambiguous
August 2023
Sky Camera 1

OLCI L2 LFR	Class	Clear	Cloud	Sum	U A	E
	CLEAR	3	1	4	75.0	25.0
	CLOUD	0	1	1	100.0	0.0
	Sum	3	2	5		
	P A	100.0	50.0		OA:	80.0
	E	0.0	50.0		BOA:	75.0

Scotts Pi: 0.523
Krippendorfs alpha: 0.571
Cohens kappa: 0.545

Figure 138: Confusion matrix showing validation results for OLCI L2 cloud screening excluding margin against SC1 automated classification

	<p>Optical MPC</p> <p>Data Quality Report –Sentinel-3 OLCI</p> <p>August 2023</p>	<p>Ref.: OMPC.ACR.DQR.03.08-2023</p> <p>Issue: 1.0</p> <p>Date: 11/09/2023</p> <p>Page: 107</p>
---	--	---

5 Validation of Integrated Water Vapour over Land & Water

We continuously investigate the temporal evolution of quality measures of integrated water vapour, when comparing SUOMI NET (Ware et al. 2000) with reduced resolution data of OLCI L2 non-time-critical. All data until March 2022 has been acquired from EUMETSAT CODA, all data from Apr 2022 on has been downloaded from EUMETSAT’s datastore (collection id: EO:EUM:DAT:0410).

741.000 (OLCI-A) and 429.800 (OLCI-B) potential matchups within the period of June 2016 (OLCI-A) January 2019 (OLCI-B) to end of August 2023 have been analysed. The global service of SUOMI-NET has been reduced at the end of 2018; thus OLCI-B colocations are less frequent outside North America.

For the cloud detection, the standard L2 cloud-mask has been applied (including the cloud ambiguous and cloud margin flags). The comparison of OLCI and GNSS shows a very high agreement (Figure 139). The correlation between both quantities is around 0.98. The root-mean-squared-difference is 1.9 -2.1 kg/m². The systematic overestimation by OLCI is 11%-12%. The bias corrected *rmsd* is around 1.3 kg/m².

The temporal evolution of several quality measures (Figure 140), indicates small seasonal variations, which are certainly related to retrieval assumptions.

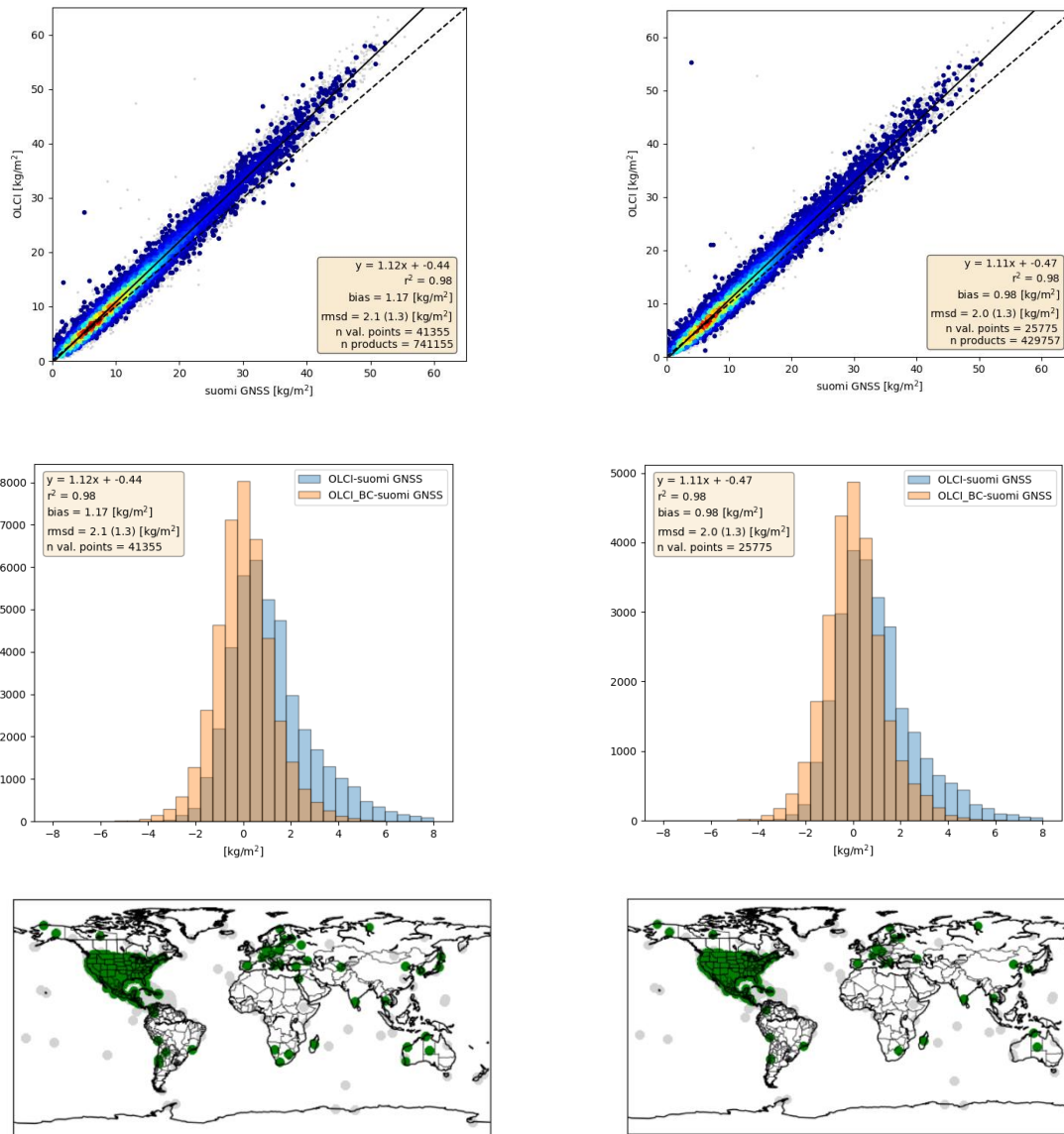


Figure 139: Upper: Scatter plot of the IWV products, derived from OLCI (A left, B right) above land and from SUOMI NET GNSS measurements. Middle: Histogram of the difference between OLCI (A: left, B: right) and GNSS (blue: original OLCI, orange: bias corrected OLCI). Lower: Positions of the GNSS (A: left, B: right).

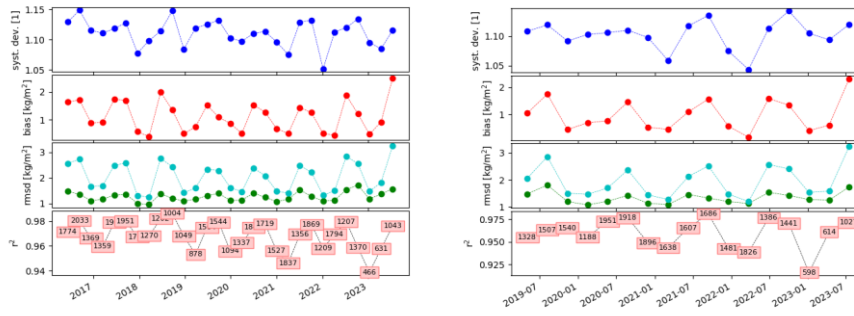



Figure 140: Temporal evolution of different quality measures for OLCI A (left) and OLCI B (right) with respect to SUOMI Net. From top to bottom: systematic deviation factor, bias, root mean squared difference (with and without bias correction), explained variance (number in boxes are the numbers of matchups)

	Optical MPC Data Quality Report –Sentinel-3 OLCI August 2023	Ref.: OMPC.ACR.DQR.03.08-2023 Issue: 1.0 Date: 11/09/2023 Page: 110
---	---	--

6 Level 2 SYN products validation

6.1 SYN L2 SDR products

There has been no new result during the reporting period. The last figures (reported in [OLCI Data Quality Report covering June 2023](#)) are considered valid.

6.2 SY_2_VGP, SY_2_VG1 and SY_2_V10 products

The similarity of SYN VGT like products with the PROBA-V archive is evaluated through intercomparison of 10-daily composites extractions over LANDVAL [1] sites. Since there is no overlap with the PROBA-V nominal operational phase and no PROBA-V Collection 2 climatology is available yet, direct comparison is done by comparing the SY_2_V10 NTC products starting January/2021 with those of PROBA-V S10-TOC since January/2017.

The temporal evolution of statistics results below are based on intercomparison over the entire periods up to August/2023. The scatterplots are based on intercomparison between SY_2_V10 products of July/2023 with PROBA-V Collection 2 S10-TOC products of July/2019.

Products availability

Availability of SY_2_VG1 and SY_2_V10 products is checked through an automated query and download via the Copernicus Data Space Ecosystem feeding the products database Belgian Collaborative Ground Segment (Terrascope, www.terrascope.be). For the month August/2023, there are missing data or empty files for:

- ❖ S3A_SY_2_VG1____20230801T000000_20230801T235959_*
- ❖ S3A_SY_2_VG1____20230807T000000_20230807T235959_*
- ❖ S3A_SY_2_VG1____20230808T000000_20230808T235959_*
- ❖ S3B_SY_2_VG1____20230824T000000_20230824T235959_*

Statistical consistency

The scatter density plots with geometric mean regression equation, coefficient of determination (R^2) and APU statistics based on intercomparison between SY_2_V10 products of August/2023 with PROBA-V Collection 2 products of August/2019 are shown in Figure 141. The APU statistics are defined as: Accuracy (A) or average bias, Precision (P) or the standard deviation of the bias, and Uncertainty (U) or the Root Mean Squared Distance. Accuracy is best for BLUE and SWIR (< 1%) and slightly less good for RED and NIR (< 2%). The relatively large values for Precision (large scatter, low R^2) are caused by the fact that products of two different years are compared. From 18/07/2023 (for S3B) and 25/07/2023 (for S3A) an updated processing baseline is in operations, including application of SLSTR calibration factors, and aligning the spectral resampling to PROBA-V. As a result, the statistical consistency for RED, NIR and SWIR has improved in comparison to previous periods, which were affected by erroneous spectral resampling and the SLSTR calibration offset (in bands S5 and S6).

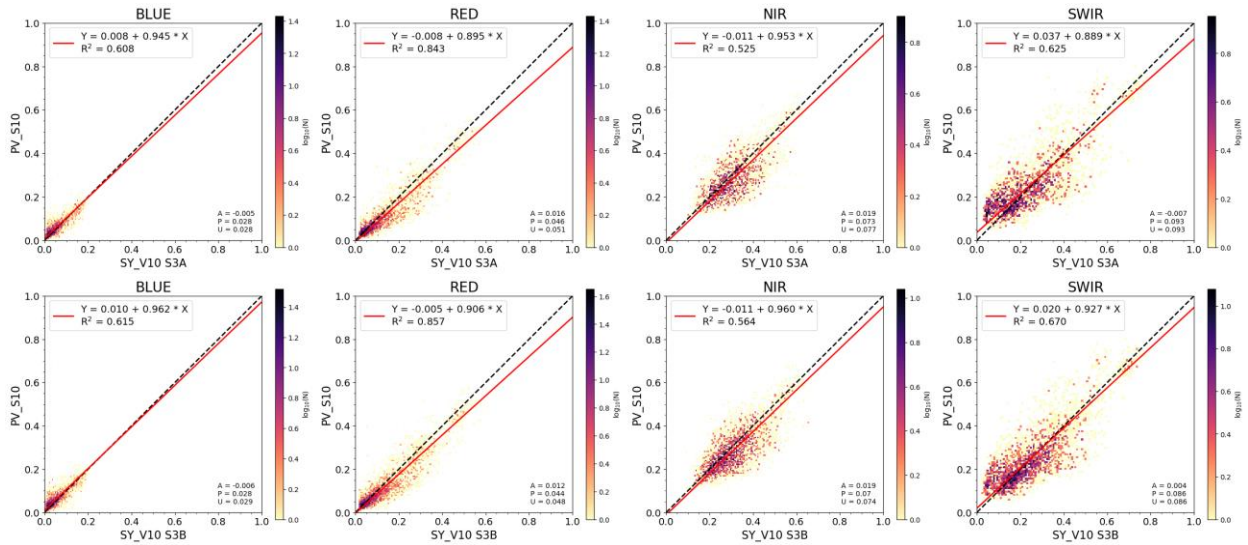


Figure 141: Scatter density plots between SY_V10 S3A (top) or S3B (bottom) and PROBA-V C2 S10-TOC for BLUE, RED, NIR and SWIR bands (left to right), August/2023 vs. August/2019

Temporal consistency

The temporal evolution of APU statistics derived from intercomparison of SY_2_V10 NTC products January/2021 –August/2023 with those of PROBA-V S10-TOC January/2017 – August/2019 (Figure 142). The APU statistics show stable evolution over time, although some seasonal pattern is observed for the mainly the SWIR channel, and to a lesser extent the RED and NIR channel. The temporal behaviour is stable, except for a strong discontinuity for the SWIR band, with improved statistics at the end of July/2023, related to the updated processing baseline with improved SWIR calibration (see above).

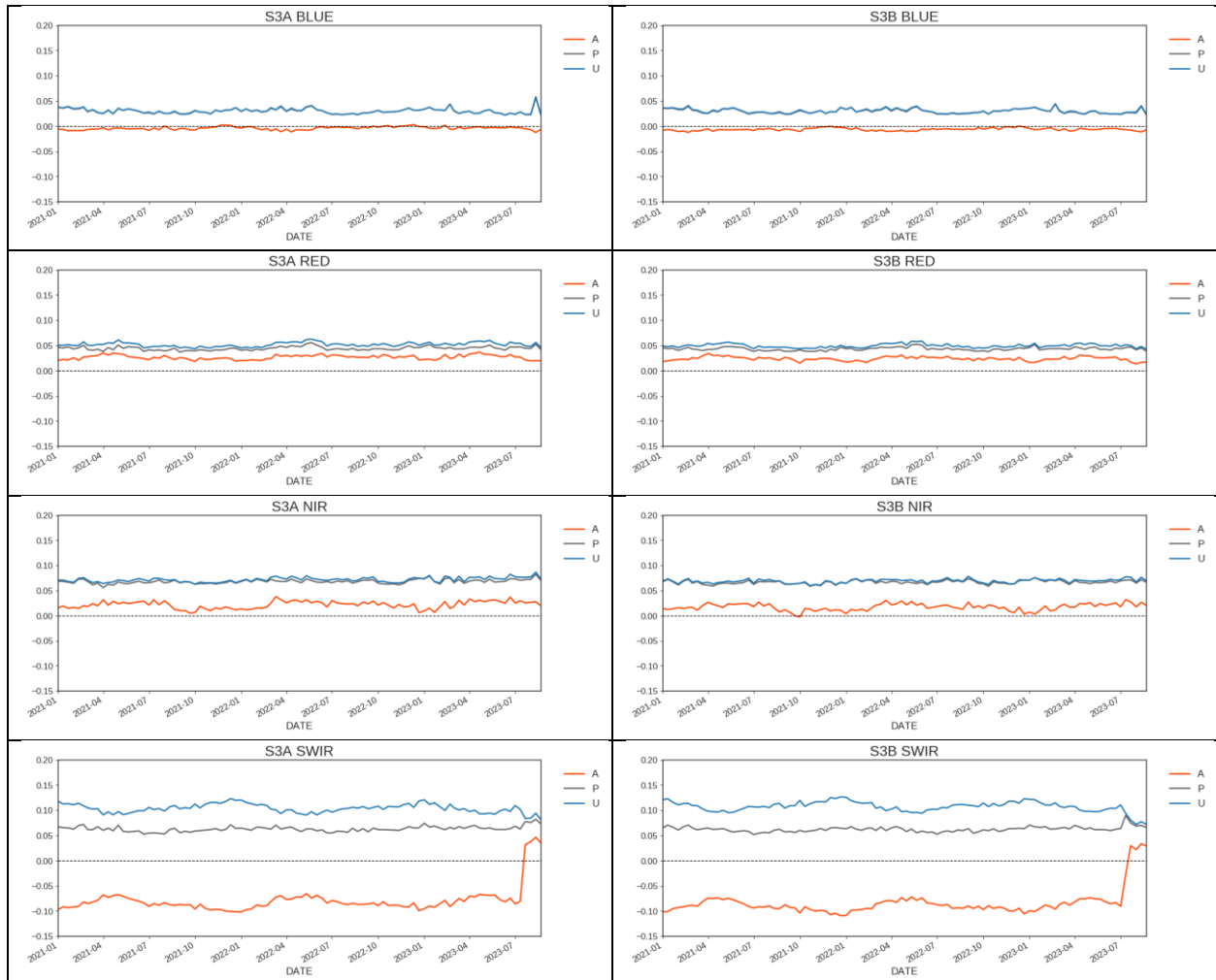


Figure 142: Temporal evolution of APU statistics between SY_2_V10 S3A (left) or S3B (right) and PROBA-V S10-TOC for BLUE, RED, NIR and SWIR bands (top to bottom), January/2021 - June/2023 (S3 SYN VGT) vs. January/2017 - August/2019 (PROBA-V)

Figure 143 shows the temporal evolution of APU statistics derived from the intercomparison of SY_2_V10 NTC products based on S3A with those based on S3B January/2021 –August/2023. The APU statistics show a stable temporal evolution, except for a strong discontinuity for SWIR, related to the different timing of the processing baseline update for S3A resp. S3B (see above).

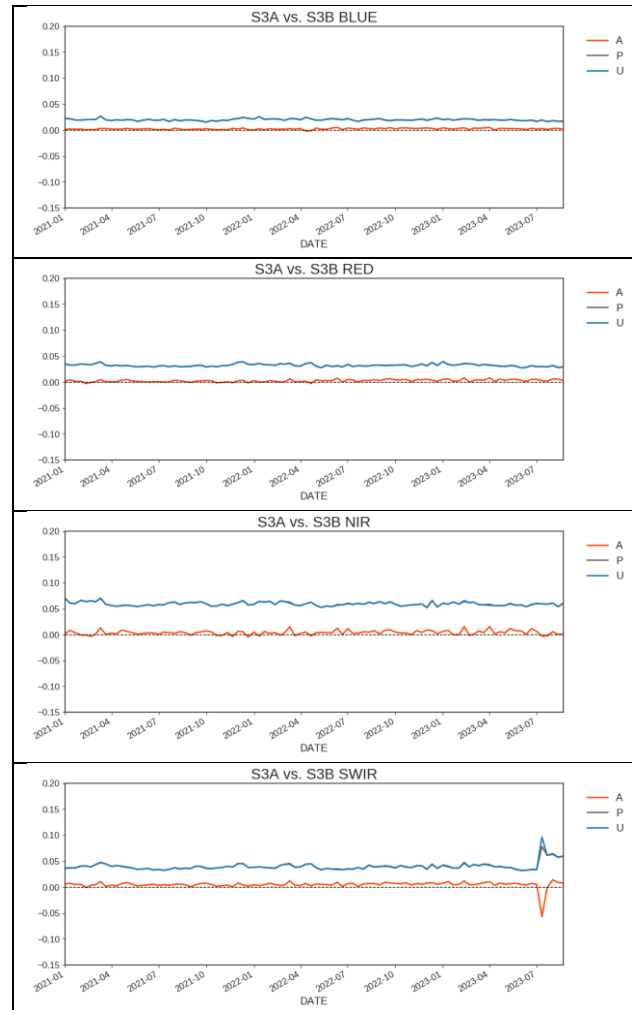


Figure 143: Temporal evolution of APU statistics between S3A_SY_2_V10 and S3B_SY_2_V10 for BLUE, RED, NIR and SWIR bands (top to bottom), January/2021 - August/2023

References

- [1] B. Fuster *et al.*, “Quality Assessment of PROBA-V LAI, fAPAR and fCOVER Collection 300 m Products of Copernicus Global Land Service,” *Remote Sens.*, vol. 12, no. 6, p. 1017, Mar. 2020, doi: 10.3390/rs12061017.

6.3 SYN L2 AOD NTC products

For the current report, matchups for May and June 2023 have been added into the analysis.

Validation results for May-June separately for years 2020, 2021, 2022 and 2023 are shown in Figure 144. There are year-to-year variations in the results, which are determined mostly by the outliers (as it was suggested in the previous report). However, lower GCOS fraction in 2023 may be results from the higher bias (need to be checked with additional analysis).

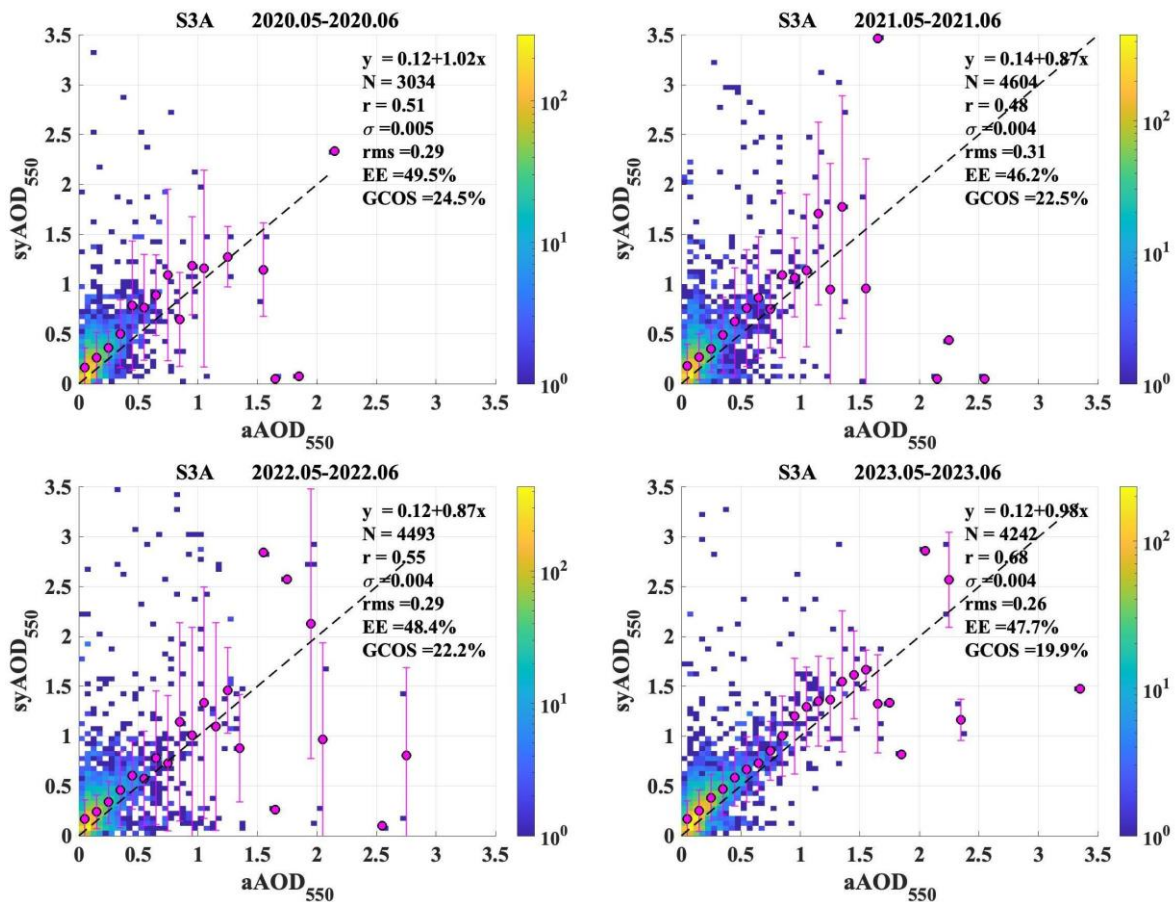


Figure 144: For S3A, for the period May-June, for years 2020 to 2023 separately, scatter density plots for aAOD and syAOD and corresponding validation statistics.

Adding two months (May-June 2023) do not change overall validation results for the whole mission (Figure 145).

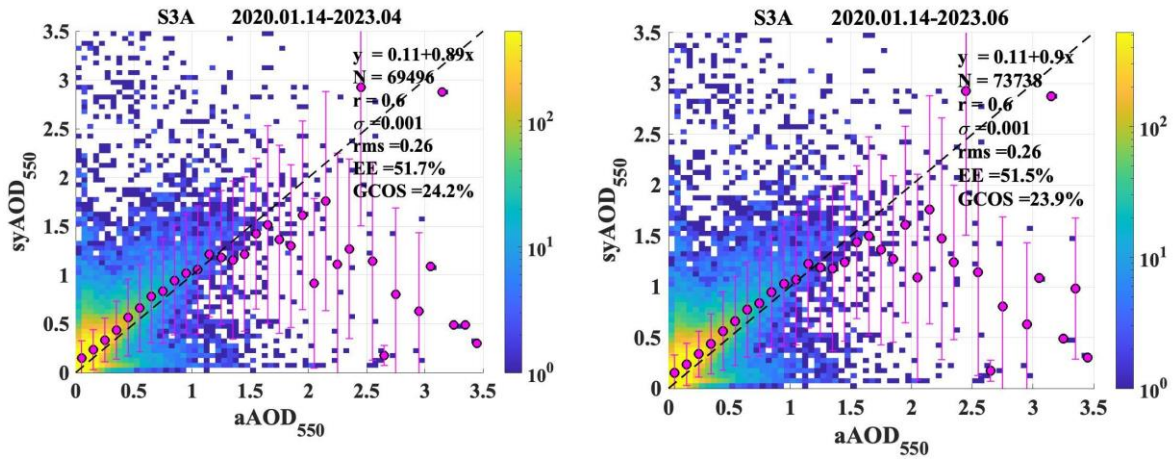



Figure 145: Globally, for S3A, scatter density plots for matchups between syAOD and aAOD for the period 2020.01-2023.04 (left) and 2020.01-2023.06 (right) for matchups with SZA>78.

 <p>OPT-MPC Optical Mission Performance Cluster</p>	<p>Optical MPC</p> <p>Data Quality Report –Sentinel-3 OLCI</p> <p>August 2023</p>	<p>Ref.: OMPC.ACR.DQR.03.08-2023 Issue: 1.0 Date: 11/09/2023 Page: 116</p>
---	--	---

7 Events

For OLCI-A, two Radiometric Calibration sequences have been acquired during the reported period:

- ❖ S01 sequence (diffuser 1) on 09/08/2023 00:15 to 00:17 (absolute orbit 38931)
- ❖ S01 sequence (diffuser 1) on 28/08/2023 18:55 to 18:57 (absolute orbit 39213)

For OLCI-B, one Radiometric Calibration sequence have been acquired during the reported period:

- ❖ S01 sequence (diffuser 1) on 11/08/2023 10:31 to 10:33 (absolute orbit 27572)

There has been one S02+S03 Spectral Calibration for OLCI-A in the current reported period:

- ❖ S02 sequence (diffuser 1) on 11/08/2023 11:10 to 11:12 (absolute orbit 38966)
- ❖ S03 sequence (Erbium doped diffuser) on 11/08/2023 12:51 to 12:53 (absolute orbit 38967)

and one Spectral calibration S09:

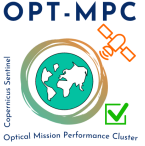
- ❖ S09 sequence on 11/08/2023 09:04:44 to 09:04:49 (absolute orbit 38965)

There has been one S02+S03 Spectral Calibration for OLCI-B in the reporting period:

- ❖ S02 sequence (diffuser 1) on 21/08/2023 11:13 to 11:15 (absolute orbit 27715)
- ❖ S03 sequence (Erbium doped diffuser) on 21/08/2023 12:54 to 12:56 (absolute orbit 27716)

and one Spectral calibration S09:

- ❖ S09 sequence on 21/08/2023 09:07:00 to 09:07:06 (absolute orbit 27714)

 <p>OPT-MPC Optical Mission Performance Cluster</p>	<p>Optical MPC Data Quality Report –Sentinel-3 OLCI August 2023</p>	<p>Ref.: OMPC.ACR.DQR.03.08-2023 Issue: 1.0 Date: 11/09/2023 Page: 117</p>
---	--	--

8 Appendix A

All Data Quality Reports, as well as past years Data Quality Reports and Annual Performance Reports, are available on dedicated pages in Sentinel Online website, at:

- ❖ <https://sentinel.esa.int/web/sentinel/technical-guides/sentinel-2-msi/data-quality-reports>
- ❖ <https://sentinel.esa.int/web/sentinel/technical-guides/sentinel-3-olci/data-quality-reports>
- ❖ <https://sentinel.esa.int/web/sentinel/technical-guides/sentinel-3-slstr/data-quality-reports>
- ❖ [OPT Annual Performance Report Year 2022 \(PDF document\)](#)

End of document